

DISSERTATION

submitted to the

Combined Faculty of Mathematics, Engineering and Natural Sciences
of Heidelberg University, Germany

for the degree of

Doctor of Natural Sciences

Put forward by

Alina Sophie Elter, M.Sc.

Born in Germersheim, Germany

Oral examination: February 16th, 2022

Development of end-to-end tests for online adaptive magnetic resonance- guided radiotherapy

Referees:

Prof. Dr. Joao Seco

Prof. Dr. Christian P. Karger

DEVELOPMENT OF END-TO-END TESTS FOR ONLINE ADAPTIVE MAGNETIC RESONANCE-GUIDED RADIOTHERAPY

Magnetic resonance (MR)-guided radiotherapy (MRgRT) enables new treatment procedures such as online treatment plan adaption based on daily imaging of the patient. This allows for the delivery of high radiation doses to the tumor while optimally sparing surrounding healthy tissue. However, such complex workflows require thorough quality assurance including dedicated end-to-end tests to validate the feasibility and overall accuracy of each specific treatment workflow. In this thesis, end-to-end tests for online adaptive MRgRT in presence of inter-fractional anatomy changes were developed. For this, a standardized protocol for 3D polymer gel (PG) dosimetry and new anthropomorphic materials simulating the image contrast of real patients in computed tomography and MR imaging were developed. These methods were validated resulting in uncertainties $< 5\%$ for PG dose measurements and $< 3.5\%$ for the imaging parameters of the phantom materials. Finally, two end-to-end tests were developed and implemented at a 0.35 T MRgRT device using (i) a highly reproducible geometric phantom and (ii) an anthropomorphic and deformable pelvis phantom. These tests resulted in γ -index passing rates (3 %/3 mm) of 93.1 % (i) and 98.9 % (ii) for the PG-filled targets and demonstrated the feasibility of online adapted MRgRT in presence of inter-fractional anatomical changes.

The thesis is presented in cumulative format and comprises six peer-reviewed publications.

ENTWICKLUNG VON END-TO-END TESTS FÜR DIE ONLINE ADAPTIVE MAGNETRESONANZ-GEFÜHRTE STRAHLENTHERAPIE

Die Magnetresonanz (MR)-geführte Strahlentherapie (MRgRT) ermöglicht neue Behandlungsverfahren, wie die Online-Adaption des Bestrahlungsplans durch tägliche Bildgebung des Patienten. Dies ermöglicht die Applikation hoher Strahlendosen im Tumor bei optimaler Schonung des umliegenden Normalgewebes. Solche komplexen Arbeitsabläufe erfordern jedoch umfassende Qualitätssicherungsmaßnahmen, einschließlich spezieller End-to-End-Tests zur Validierung der Durchführbarkeit und Gesamtgenauigkeit jedes einzelnen Behandlungsablaufes. In dieser Arbeit wurden End-to-End-Tests für die online adaptive MRgRT bei interfraktionellen Anatomieänderungen entwickelt. Hierfür wurden ein standardisiertes Protokoll für die 3D-Polymergel (PG)-Dosimetrie und neue anthropomorphe Materialien, die den Bildkontrast von realen Patienten in der Computertomographie und MR-Bildgebung simulieren, entwickelt. Diese Methoden wurden validiert und ergaben Unsicherheiten $< 5\%$ für PG-Dosismessungen und $< 3,5\%$ für die Bildgebungsparameter der Phantommaterialien. Schließlich wurden zwei End-to-End-Tests entwickelt und an einem 0,35 T MRgRT-Gerät durchgeführt, wobei (i) ein hoch reproduzierbares geometrisches Phantom und (ii) ein anthropomorphes deformierbares Beckenphantom verwendet wurden. Die Tests ergaben γ -Index Akzeptanzraten ($3\%/3\text{ mm}$) von 93.1% (i) beziehungsweise 98.9% (ii) für die jeweilige PG-gefüllte Zielstruktur und belegen die Durchführbarkeit von online adaptierter MRgRT in Gegenwart von interfraktionellen anatomischen Veränderungen.

Die vorliegende Dissertation wurde kumulativ angefertigt und umfasst sechs von Experten begutachtete Veröffentlichungen.

CONTENTS

1	Introduction	1
1.1	Radiotherapy.....	1
1.1.1	Treatment planning	2
1.1.2	Treatment delivery.....	3
1.2	Imaging for radiotherapy	4
1.2.1	Computed tomography	5
1.2.2	Magnetic resonance imaging.....	6
1.3	Image-guided radiotherapy	9
1.3.1	Position verification	10
1.3.2	Motion compensation.....	11
1.3.3	Offline plan adaption	12
1.3.4	Online plan adaption	12
1.4	Online adaptive MR-guided radiotherapy	13
1.4.1	Offline treatment preparation.....	13
1.4.2	Online treatment workflow	14
1.5	Implementation of new MR-guided treatment procedures.....	15
1.5.1	Machine-related quality assurance.....	15
1.5.2	Patient-specific quality assurance.....	16
1.5.3	End-to-end testing	17
1.6	Aim of the thesis.....	18
2	Publications	19
2.1	Thematic overview.....	21
2.1.1	Methodological developments	21
2.1.2	Validation of methods.....	23
2.1.3	End-to-end tests.....	24
2.2	Publication I	27
2.3	Publication II.....	43
2.4	Publication III	63
2.5	Publication IV.....	75

2.6	Publication V.....	81
2.7	Publication VI.....	97
3	Discussion.....	117
3.1	Methodological developments.....	117
3.1.1	3D dose verification	117
3.1.2	Phantoms with anthropomorphic attenuation and imaging contrast	118
3.1.3	Simulation of anatomical changes in phantoms	119
3.2	Validation of methods.....	119
3.2.1	Phantoms with anthropomorphic attenuation and imaging contrast	119
3.2.2	Advanced dosimetry in an anthropomorphic pelvis phantom.....	121
3.3	End-to-end tests.....	121
3.3.1	3D polymer dosimetry gel in clinical QA phantoms	122
3.3.2	Online adaptive MRgRT using a highly reproducible geometric phantom.....	122
3.3.3	Multi-fractional online adaptive MRgRT using a pelvis phantom.....	123
4	Conclusion.....	125
	List of figures	127
	List of publications.....	129
	Bibliography.....	135
	Acknowledgements	145

LIST OF ABBREVIATIONS

ADAM	<i>anthropomorphic, deformable and multimodality</i>
ADAM-PETer	<i>ADAM pelvis phantom with PET extension for radiotherapy</i>
AQUARIUM	<i>anthropomorphic QA phantom to study interfractional uncertainties in MRgRT</i>
bSSFP	<i>balanced steady state free precession</i>
CBCT	<i>cone beam CT</i>
CT	<i>computed tomography</i>
CTV	<i>clinical target volume</i>
DECT	<i>dual-energy CT</i>
DIR	<i>deformable image registration</i>
DKFZ	<i>German Cancer Research Center</i>
FID	<i>free induction decay</i>
GTV	<i>gross target volume</i>
HLUT	<i>Hounsfield lookup table</i>
IgRT	<i>image-guided RT</i>
IMRT	<i>intensity modulated RT</i>
ITV	<i>internal target volume</i>
K ₂ HPO ₄	<i>dipotassium phosphate</i>
KCl	<i>potassium chloride</i>
Linac	<i>linear accelerator</i>
MLC	<i>multi leaf collimator</i>
MR	<i>magnetic resonance</i>
MRgRT	<i>MR-guided RT</i>
MRI	<i>MR imaging</i>
MSE	<i>multiple spin echo</i>
Ni-DTPA	<i>nickel diethylenetriaminepentaacetic acid</i>
OAR	<i>organ at risk</i>
PAGAT	<i>polyacrylamide gelatin gel fabricated at atmospheric conditions</i>
PET	<i>positron emission tomography</i>
PG	<i>polymer gel</i>
PTV	<i>planning target volume</i>
QA	<i>quality assurance</i>
RF	<i>radiofrequency</i>
RT	<i>radiotherapy</i>
SPR	<i>stopping power ratio</i>
TE	<i>echo time</i>
TI	<i>inversion time</i>
TLD	<i>thermoluminescence detector</i>
TPS	<i>treatment planning system</i>

LIST OF ABBREVIATIONS

TR.....	<i>repetition time</i>
TSE.....	<i>turbo spin echo</i>
UKHD.....	<i>Heidelberg university hospital</i>

1 INTRODUCTION

The increasing life expectancy in the modern world is accompanied by an increasing risk of developing cancer [1, 2]. In Germany, the lifetime risk of a cancer diagnosis was $> 40\%$ in 2016 with numbers constantly rising [3]. Thus, almost one out of two people develops cancer in the course of his or her life today. The term cancer is generally defined as an uncontrolled proliferation of cells leading to a malignant tissue formation (the *tumor*), whereas pathological cells may spread to distant parts of the body (so-called *metastasis*) and invade healthy tissue. Individual cancer therapy depends primarily on tumor type, site and grade of spreading, but typically employs a combination of the three main pillars of cancer therapy: surgery, chemotherapy and radiotherapy.

Radiotherapy (RT), which applies ionizing radiation to damage cancerous cells while aiming to optimally spare surrounding healthy tissue, allows for an individual treatment based on anatomical patient information [4]. Approximately 50% of all cancer patients today receive RT treatment throughout the course of their disease [5]. Radiation exposure to tissue induces DNA damage by single- or double strand breaks, which eventually leads to cell death and a prevention of further tumor growth [6]. However, one of the main challenges in RT is to precisely hit an ‘invisible’ target with an ‘invisible’ radiation beam. Although the target may be visualized for treatment planning using medical imaging modalities such as computed tomography (CT) or magnetic resonance (MR) imaging (MRI), an accurate and precise delivery of the radiation is still limited by anatomical changes that may arise during the treatment (intra-fractional motion) or between two radiotherapy sessions (inter-fractional motion). In modern RT, medical imaging techniques are therefore often installed directly at the treatment site to visualize the patient anatomy directly before or during the actual irradiation. Nevertheless, the radiation must penetrate healthy tissue and so-called organs at risk (OARs) in order to reach deep-seated tumor regions. Hence, a main limitation for achieving tumor control by RT is the risk of damaging healthy tissue. As different tissue types are differently sensitive to radiation damage, tolerance levels of normal tissues can be found in literature [7, 8]. These may be used to define clinical recommendations of applied radiation doses for local tumor control with an acceptable risk of possible side effects of the treatment.

1.1 Radiotherapy

External RT is a non-invasive method of cancer treatment that applies ionizing radiation to deliver high amounts of energy to the tumor while aiming to optimally spare adjacent healthy tissue. The amount of energy is typically described by the radiation dose D defining the mean absorbed energy \bar{E} per mass m in units of *Gray* ($1\text{ Gy} = 1\text{ J/kg}$) using water as reference material:

$$D = \frac{d\bar{E}}{dm}. \quad (1)$$

However, many parameters associated with the patient anatomy influence the accurate dose deposition. These have to be considered in treatment planning and delivery, which will be discussed in the following sections.

1.1.1 Treatment planning

Treatment planning relies on anatomical images of the patient (section 1.2) allowing for a delineation of the so-called gross tumor volume (GTV) as well as adjacent OARs. The GTV is the macroscopic part of the tumor visible in conventional imaging techniques. To account for geometric and dosimetric uncertainties during treatment planning and delivery, several margins are conventionally added to the GTV [9-11]. The clinical target volume (CTV) contains, as an extent to the GTV, infiltrating tumor cells that may not be visible in conventional images used for treatment planning. In case of moving tumors, the internal target volume (ITV) may be introduced to account for physiological motion of the tumor in between or during treatment fractions. Finally, the planning target volume (PTV) additionally covers machine- and patient positioning related uncertainties. The extent of these margins is chosen based on international recommendations as well as site-specific experience and may vary for different treatment techniques. To ensure a homogenous coverage of the entire tumor and hence, to achieve a local tumor control, all margins are prescribed the same high radiation dose as the GTV. This consequently leads to an increased dose in adjacent healthy tissue, which may cause severe side effects of the treatment. Therefore, new developments in RT aim at decreasing the size of the applied margins, which significantly decreases the irradiated volume of healthy tissue. This is schematically visualized in figure 1.

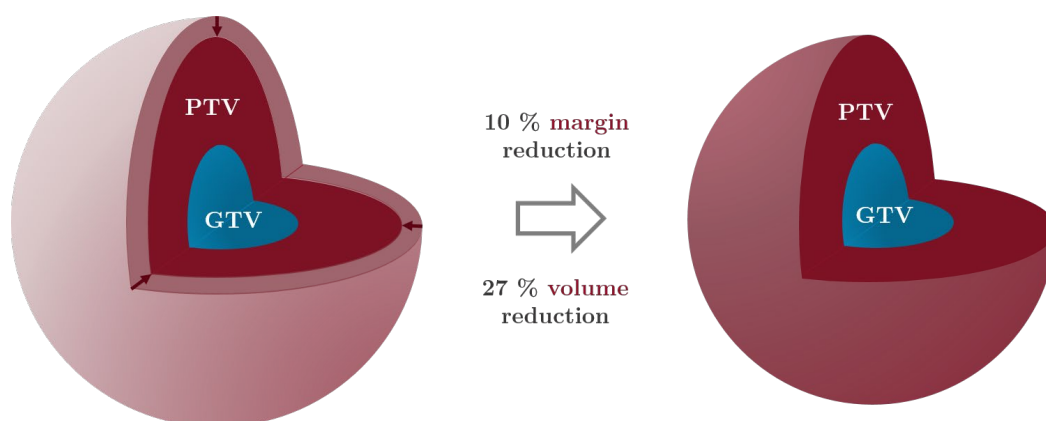


Figure 1: Schematic visualization of a margin reduction for a spherical GTV (blue) with an isotropic margin leading to an extended PTV (red). For simplicity, CTV and ITV are not shown. A reduction of the margin by 10 % (light red shell) leads to a reduction of the irradiated volume by 27 % and thereby to a significant sparing of healthy tissue.

While an irradiation of OARs may generally not be avoided, several approaches exist to minimize radiation damage. These are mainly related to (i) a fractionation of the applied dose and (ii) geometric tissue sparing. Dose fractionation exploits the typically better capability of healthy tissue compared to tumor cells to repair sub-lethal cell damage [12]. Spreading the total dose of the treatment over several days (e.g. 30 daily fractions of 2 Gy in six weeks, excluding the weekends) allows the healthy tissue to repair potential radiation damage before the next fraction. A geometric tissue sparing may be achieved by using specific beam arrangements and treatment techniques (e.g. intensity modulated RT (IMRT) [13]), by choosing different ions beams instead of photons (e.g. proton therapy, section 1.1.2) or by so-called image-guided treatment procedures (section 1.3).

In IMRT, non-uniform fluence distributions of the irradiation are applied with multiple radiation beams of different orientation to achieve a highly conformal coverage of the target volume [13].

Technically, this is realized by a multi leaf collimator (MLC, section 1.1.2) to adjust the shape of the beams. Several individual MLC apertures (so-called *segments*) of different dose levels are then superimposed for each beam to achieve the non-uniform fluence distribution. The fluence profile and the resulting dose distribution are optimized in an iterative process using a so-called inverse planning algorithm with the dose prescription and constraints to PTV and OARs as input parameters [14, 15]. IMRT is the state-of-the art treatment technique conventionally applied in clinical practice [4]. The entire process of treatment planning is performed in the treatment planning system (TPS).

1.1.2 Treatment delivery

For treatment delivery, the patient is positioned on the treatment couch of the treatment device and may be immobilized to ensure the same geometry as present in the images used for treatment planning. In conventional RT, the treatment is delivered using high energetic photons generated by a medical linear accelerator (Linac) [16, 17]. The Linac initially accelerates electrons to typical energies of 6 – 18 MeV. These hit a target of high atomic number (e.g. tungsten) resulting in bremsstrahlung and characteristic X-rays. Due to a directional dependence of the bremsstrahlung and resulting beam profiles with spatially varying intensity, a flattening filter may be included to homogenize the radiation field. However, most modern RT devices omit the flattening filter to avoid a significant loss in radiation intensity (so-called *flattening filter free* irradiation). The beam is afterwards collimated to a specific field size and shape using an MLC. The MLC consists of a large number of tungsten leaves (e.g. 2×80 leaves) with a typical width of 0.5 cm, that are arranged in opposing pairs. Independent spatial shifting of the leaves enables the generation of arbitrarily shaped radiation fields required for advanced treatment techniques such as IMRT. For varying beam orientations, the main parts of a Linac are mounted on a gantry that rotates the beam around the patient.

As photons have no electric charge, they act indirectly ionizing. They deposit their energy in tissue mainly via secondary electrons that are released by interaction processes of the photons with the traversed tissue. In the RT energy range (MeV), these interactions are dominated by Compton scattering. Subsequently, Coulomb interactions of the released secondary electrons with other charged particles of the tissue lead to a local dose deposition. The dose deposited by photons decreases exponentially with depth in tissue after a short build-up region due to increasingly generated secondary electrons [18]. Several beams from different directions are required to achieve a homogeneous dose distribution of deep-sited targets. Although a medical Linac is typically used for photon irradiation, the tungsten target may be replaced by a scatter foil [19] for a direct irradiation with the accelerated electrons. These have, however, only a short range within tissue (< 5 cm at 6 MeV [20]) corresponding to the mean stopping point of the particles.

For a precise dose deposition in deep-sited tumors, also protons and light ions are used [21, 22]. These charged and hence directly ionizing particles lose their energy mainly via electromagnetic interactions with orbital electrons of tissue atoms when traversing tissue, leading to an energy transfer inversely proportional to their velocity. The ions have therefore a finite range in tissue with the resulting depth-dose profile being denoted as Bragg-peak (figure 2) [23]. Hence, healthy tissue along the beam path as well as beyond the maximum range can be optimally spared.

However, the finite range also leads to a decreased robustness of treatment plans in presence of anatomical changes in the entrance region of the beam.

The range of the ions depends on the beam energy as well as on the traversed material. Thereby, the mean energy loss $d\bar{E}$ within a path dx is given by the stopping power S :

$$S = -\frac{d\bar{E}}{dx}. \quad (2)$$

For treatment planning, the stopping power of a specific material is typically related to the stopping power in water resulting in the so-called stopping power ratio (SPR):

$$[\text{SPR}] = \frac{S}{S_{\text{water}}}. \quad (3)$$

Characteristic depth-dose profiles of a photon, electron and proton beam are given in figure 2.

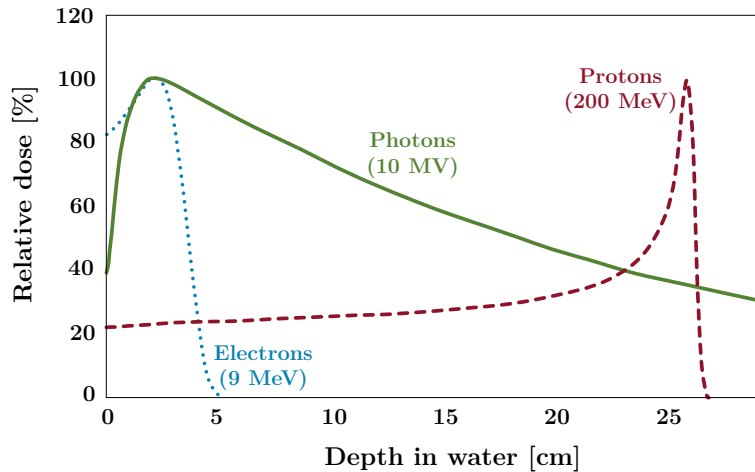


Figure 2: Characteristic relative depth-dose profiles generated by a 10 MV photon (solid green), 9 MeV electron (dotted blue) and 200 MeV proton (dashed red) beam in water normalized to the respective dose maximum. Recreated from [24].

1.2 Imaging for radiotherapy

Imaging of anatomical structures is an essential part of RT in order to ensure an accurate delivery of the applied radiation. From the initial diagnostics to treatment planning, setup and motion control during treatment and the final monitoring of the treatment success (so-called *follow-up*), non-invasive 2D and 3D imaging is crucial. CT imaging is most widely used for treatment planning today as it provides information of the tissue's electron density required for dose calculation. Additional imaging modalities (e.g. MRI or positron emission tomography (PET)) may provide further morphological or functional information to facilitate the differentiation of internal structures. If several imaging modalities are combined, the acquired images have to be transferred to a single coordinate system using rigid or deformable (DIR) image registration [25-27]. In modern RT, additional imaging of the patient's anatomy is typically performed directly before or even during the treatment to correct the positioning or to compensate for inter-fractional anatomical changes or intra-fractional motion of tissues within the patient (section 1.3). This is conventionally

done using X-ray based planar imaging techniques with more advanced systems applying 3D imaging (e.g. CT, MRI). The following section describes the principles of CT and MRI as the most relevant imaging techniques within the scope of this thesis in more detail.

1.2.1 Computed tomography

Computed tomography is based on the measurement of the photon attenuation within tissue to obtain information about the anatomical structure [28]. A conventional CT scanner applies a rotating X-ray tube with a typical voltage of 80 – 140 kV together with an opposing set of detectors. This setup is used to generate attenuation profiles from many different directions, which are then reconstructed to a 3D image. The extent of X-ray attenuation due to tissue interaction along a line element dx can be described by *Lambert-Beer's law*. Here, the relation is given for the specific case of a mono-energetic X-ray beam:

$$I = I_0 \cdot e^{-\int \mu(x) dx}, \quad (4)$$

with I being the intensity of the transmitted photons as a function of the incident intensity I_0 and the photon attenuation coefficient $\mu(x)$, which may vary within inhomogeneous objects.

The CT-values represented in a CT image as grey values relate the attenuation coefficient of the respective tissue linearly to water and are given in Hounsfield units (HU):

$$[\text{CT-value}] = \frac{\mu_{\text{tissue}} - \mu_{\text{water}}}{\mu_{\text{water}}} \cdot 1000 \text{ HU}. \quad (5)$$

Hence, the denser a material the higher is the CT-value with water having a CT-value of 0 HU. Without attenuation (i.e. in vacuum) the CT-value corresponds to -1000 HU. Fatty tissues have a lower density than water and CT-values in the order of -100 HU, while most soft tissues are slightly denser than water with values in the range of $20 - 70$ HU. Cortical bones reach CT-values of up to 2000 HU [29].

CT imaging benefits from very short acquisition times in the order of a few seconds and a sub-millimeter resolution with a high geometric accuracy. However, the images lack soft tissue contrast compared to other 3D imaging modalities such as MRI (section 1.2.2) and expose the patient with additional radiation dose [30]. While the dose exposure of a CT scan varies largely with scan protocols and imaged organ site, the effective dose describing the associated radiation risk in units of mSv of a typical abdomen and pelvis scan is in the range of $8 - 11$ mSv [31].

Nevertheless, CT imaging is an integral part of almost all RT planning procedures providing the electron density information required for dose calculation. Electron densities can be deduced from CT-values using a CT specific Hounsfield lookup table (HLUT). Similarly, CT-values may be transformed to SPRs for ion therapy planning [32]. However, there is no direct relationship between CT-values and SPR. An uncertainty of the transformation of $1 - 3$ % based on the experimental determination of the lookup table was estimated [33-35]. Therefore, alternative methods for SPR prediction, such as the use of dual-energy CT (DECT), have recently been introduced [36]. DECT applies two X-ray beams with separated energy spectra simultaneously, allowing to directly extract

radiological tissue parameters as for example the electron density or the effective atomic number. Using these parameters the uncertainty of the SPR prediction can be reduced to $< 1\%$ [36-38].

1.2.2 Magnetic resonance imaging

Magnetic resonance imaging is a tomographic imaging modality that generates 3D images of the scanned object based on the interaction of its nuclear magnetic moments with an external magnetic field B . In contrast to CT, MRI includes no additional dose exposure to the patient as no ionizing radiation is used for image acquisition. Furthermore, an excellent soft tissue contrast may be achieved, facilitating the differentiation of pathological structures such as the tumor and surrounding OARs [39]. Image acquisition is based on the deflection of the magnetic moments within the body by the main magnetic field B_0 as well as a combination of additional magnetic field gradients and radiofrequency (RF) pulses. While a short introduction to the principles of MRI is given in this section, a detailed description of the technique and underlying physical principles can be found in literature [39-41].

Basic principle

Atomic nuclei with an odd number of nucleons (protons and neutrons) possess a non-zero nuclear spin quantum number I and hence a non-zero magnetic moment. This allows the nuclei to interact with an external magnetic field. The simplest case is the hydrogen (^1H) nucleus consisting of a single proton with $I = 1/2$. The typically high abundance and mobility of hydrogen in biological systems as well as the high gyromagnetic ratio γ of protons ($\gamma = 42.58\text{ MHz/T}$) leads to an increased MR signal as compared to other nuclei [39, 42]. Therefore, MRI based on hydrogen nuclei is most widely spread in clinical applications today and this section will focus on hydrogen MRI.

Without an external magnetic field ($B_0 = 0$) the nuclear spins of the tissue have no preferred orientation. However, if a non-zero magnetic field is applied, a slight preference in the order of ppm is found for spins aligned parallel to B_0 compared to the anti-parallel direction due to Boltzmann statistics. This leads to a static macroscopic net magnetization M_z in z-direction. Due to conservation of angular momentum, the individual spins precess around the direction of B_0 with the Larmor frequency ω_0 :

$$\omega_0 = \gamma B_0. \quad (6)$$

In MRI, this equilibrium state is disturbed by the application of a time-dependent RF pulse $B_1(t)$ with a frequency equal to ω_0 and oriented perpendicular to B_0 to tilt the net magnetization from the longitudinal z-direction (M_z) into the transversal x-y-plane (M_{xy}). The resulting flip angle α of the rotation depends on the duration t_p of the RF pulse:

$$\alpha = \int_0^{t_p} \gamma B_1(\tau) d\tau. \quad (7)$$

The tilted net magnetization then precesses around the direction of B_0 with the same frequency ω_0 as the individual nuclear spins. After RF excitation, the magnetization decays towards its equilibrium state. This relaxation process is called *free induction decay* (FID) and is induced by interaction of the spins with the environment as well as with the magnetic moments of other spins.

To detect an MR signal, *Faraday's law* is exploited according to which the time-dependent transversal magnetization induces an oscillating electric signal in a receiver coil with an amplitude proportional to $|M_{xy}|$.

Relaxation processes

The interaction with the environment (the *lattice*) induces a relaxation of the longitudinal magnetization M_z and is called the longitudinal or spin-lattice relaxation characterized by the material-specific relaxation time T_1 :

$$M_{z,0}(t) = M_{z,0} \cdot \left(1 - e^{-t/T_1}\right). \quad (8)$$

The interaction of the spins between one another induces a dephasing of individual spins and hence a relaxation of the transverse magnetization M_{xy} . This process is called transverse or spin-spin relaxation and is characterized by the corresponding material-specific relaxation time T_2 :

$$M_{xy,0}(t) = M_{xy,0} \cdot e^{-t/T_2}. \quad (9)$$

While natural dephasing is induced by the interaction of neighboring spins, the measured transversal decay is typically enhanced by local field inhomogeneities. These lead to varying Larmor frequencies of the individual spins and thus an acceleration of the transverse dephasing. The field distortions mainly result from inhomogeneities of the main magnetic field, but may also be induced by different magnetic susceptibilities of the imaged materials. This effect is taken into account by the time constant $T_2^* < T_2$, which may replace T_2 in equation (9). In contrast to the natural dephasing characterized by T_2 , influences leading to the shorter relaxation time T_2^* may be reversed by special imaging techniques. The tissue specific time constants together with the density of the nuclear spins (here proton density) are mainly responsible for different signal intensities and image contrasts in MRI. Characteristic profiles of longitudinal and transversal relaxation are depicted in figure 3.

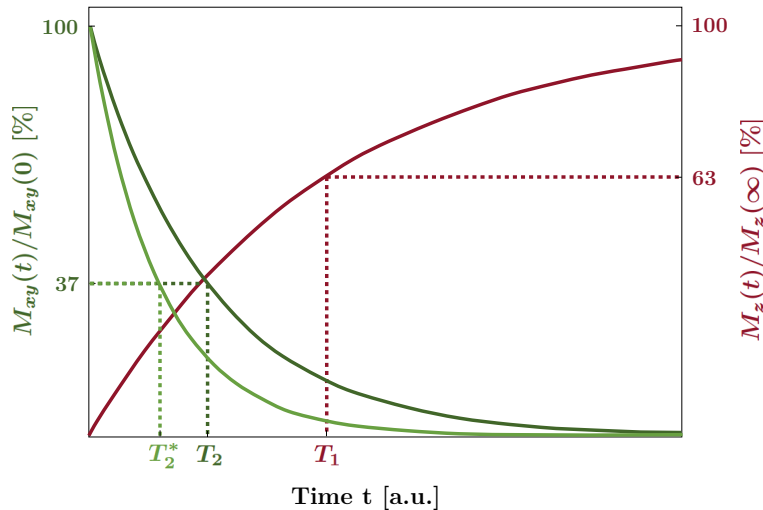


Figure 3: Characteristic profiles of longitudinal ($M_z(t)$, red) and transversal ($M_{xy}(t)$, green) relaxation described by equations (8) and (9). T_1 is defined as the time after which the longitudinal magnetization has recovered to 63 % of the equilibrium value and T_2 and T_2^* as the times when the signal has decayed to 37 % of its initial value, respectively.

Image acquisition

To generate an MR image, a sequence of RF pulses and additional magnetic field gradients with varying timing, duration, strength and direction, called pulse sequence, is applied. First, a spatial encoding of the signal is required to reconstruct a 3D image of the scanned object. This is implemented by superimposing magnetic field gradients in the three spatial directions to the main magnetic field B_0 . A slice selective gradient allows to exclusively excite the spins in a certain slice of the transversal plane by the initial RF pulse, which deflects the magnetization from its equilibrium state. For a spatial encoding of the signal within the selected slice, so-called phase and frequency encoding gradients are applied in the remaining spatial directions. While the phase encoding gradient is active only shortly prior to read-out, the frequency encoding gradient remains active during signal read-out. As the additional gradients change the local magnetic field and thus the Larmor frequency, the recorded signal can be assigned to a specific location. For each slice, this procedure is repeated while changing the phase encoding gradient stepwise until the entire volume can be reconstructed.

For signal acquisition, additional pulses are applied after the initial RF pulse. Without further measures, the signal would present a FID caused by longitudinal and transversal relaxation of the spins. Therefore, the pulse sequence is used to generate a so-called *echo* of the signal, which is recorded by the receiver coil. The pulse sequence is mainly characterized by the so-called echo time (TE), repetition time (TR) and the flip angle. While TE defines the time from the initial excitation to the generation of the echo, TR describes the time between two consecutive excitations of the longitudinal magnetization into the transversal plane. Pulse sequences used for MR image acquisition can generally be divided into two groups categorized by the method of echo generation: (i) spin echo and (ii) gradient echo sequences. In a standard spin echo sequence, the initial 90° pulse to flip the longitudinal magnetization into the transversal plane is followed by a 180° RF pulse at TE/2 that reverses the dephasing of the spins due to local field inhomogeneities leading to a signal echo at time TE. In a gradient echo sequence, the dephasing of the spins after the initial excitation is enhanced by an additional magnetic dephasing gradient. The gradient echo is generated by switching the polarity of this gradient resulting in a rephasing of the spins and a signal echo at TE. For both sequence types, different MRI contrasts may be achieved by varying TE, TR and flip angle, which changes the signal intensity of tissues having different intrinsic relaxation properties and proton densities. Based on these standard sequences a large variability of sequences is available in modern MRI allowing for different image contrasts and acquisition times. In addition, quantitative measurements of tissue properties (e.g. T_1 and T_2 [43]) and the representation of biological activities (e.g. diffusion-weighted MRI [44], functional MRI [45, 46]) is possible. A few examples relevant for the scope of this thesis are given here.

A common variant of the gradient echo sequence is the so-called (*balanced*) *steady state free precession* (bSSFP) sequence, which benefits from short acquisition times with a high signal-to-noise ratio [47-49]. The bSSFP as well as most clinically applied sequences qualitatively represent different tissues as different signal intensities. While this qualitative imaging is sufficient for most clinical purposes, certain applications may require to quantify the tissue-specific properties (i.e. T_1 and T_2) in order to further characterize the imaged materials. For this purpose, special pulse sequences have to be applied to enable quantitative imaging. For a quantitative measurement of

the T_1 relaxation time, a series of so-called *inversion- or saturation recovery* sequences can be used, in which the actual sequence (both spin echo and gradient echo sequences are in principle applicable) is preceded by a 180° or 90° preparation pulse, respectively. Here, the inversion time TI defines the time between the preparation pulse and the beginning of the actual sequence. During TI the magnetization relaxes longitudinally towards its equilibrium state until the image acquisition starts. Hence, the signal of the FID measured is directly proportional to the longitudinal magnetization that has recovered after the preparation pulse. By acquiring a series of pulse sequences with varying TI the profile of the longitudinal relaxation process (see eq. (8) and figure 3) can be measured. The gold standard to quantitatively measure the T_2 relaxation time is a *Carr-Purcell-Meiboom-Gill* sequence [50] also known as a *multiple spin echo* (MSE) sequence. This sequence is based on a standard spin echo sequence with the 90° excitation pulse being followed by multiple 180° refocusing pulses. With the refocusing pulses restoring signal decay due to local field inhomogeneities, their signal decreases with an exponential function of the transversal relaxation time T_2 (see Eq. (9) and figure 3). Hence, T_2 can be measured by acquiring the signal at each of the refocusing pulses and applying an exponential fit to the signal. Similarly, series of other spin echo sequences with different TEs may be applied to quantitatively measure T_2 . The *turbo spin echo* (TSE) sequence, for instance, also applies multiple 180° pulses, but uses varying field gradients between the pulses for an accelerated image acquisition [51].

1.3 Image-guided radiotherapy

Modern RT typically applies additional on-site imaging directly before or during the irradiation to validate and correct the patient's position and to account for possible anatomical changes or organ motion. These treatment concepts are known as image-guided RT (IgRT) [52-55]. In the simplest case the images are used to ensure the correct position of the patient but more advanced techniques are available today allowing for motion compensation of moving tumors and an adaption of the treatment plan according to additionally acquired images. However, all image-guided techniques increase the complexity of the treatment. An overview of the workflow development from conventional RT to more advanced image-guided treatment procedures as displayed in figure 4 will be given in this section. While the section will focus on image-guided photon therapy, most of the presented techniques are available or under development for RT using protons and ions as well. Due to the finite range of ions and the resulting steep dose gradients (figure 2), proton and ion therapy are especially sensitive to anatomical changes and therefore largely benefit from image-guided treatment techniques [56, 57]. Position correction and some motion compensation techniques are often already defined as adaptive radiotherapy in the literature. In the context of this thesis, however, only the actual recalculation of the treatment plan during the course of the treatment is considered a plan adaption.

In conventional RT, images are acquired solely for treatment planning with a CT scan being required for dose calculation. Other imaging modalities may be used in addition to acquire further information relevant for planning purposes (section 1.2). The conventional treatment planning and delivery procedure is described in section 1.1. The same patient position for imaging and treatment delivery is typically ensured using external markers on the patient surface together with a laser system in the treatment room. Furthermore, positioning can be facilitated using different

positioning and immobilization aids such as thermoplastic masks and vacuum mattresses [58]. For each treatment fraction, the patient is repositioned and immobilized in the same manner before irradiation.

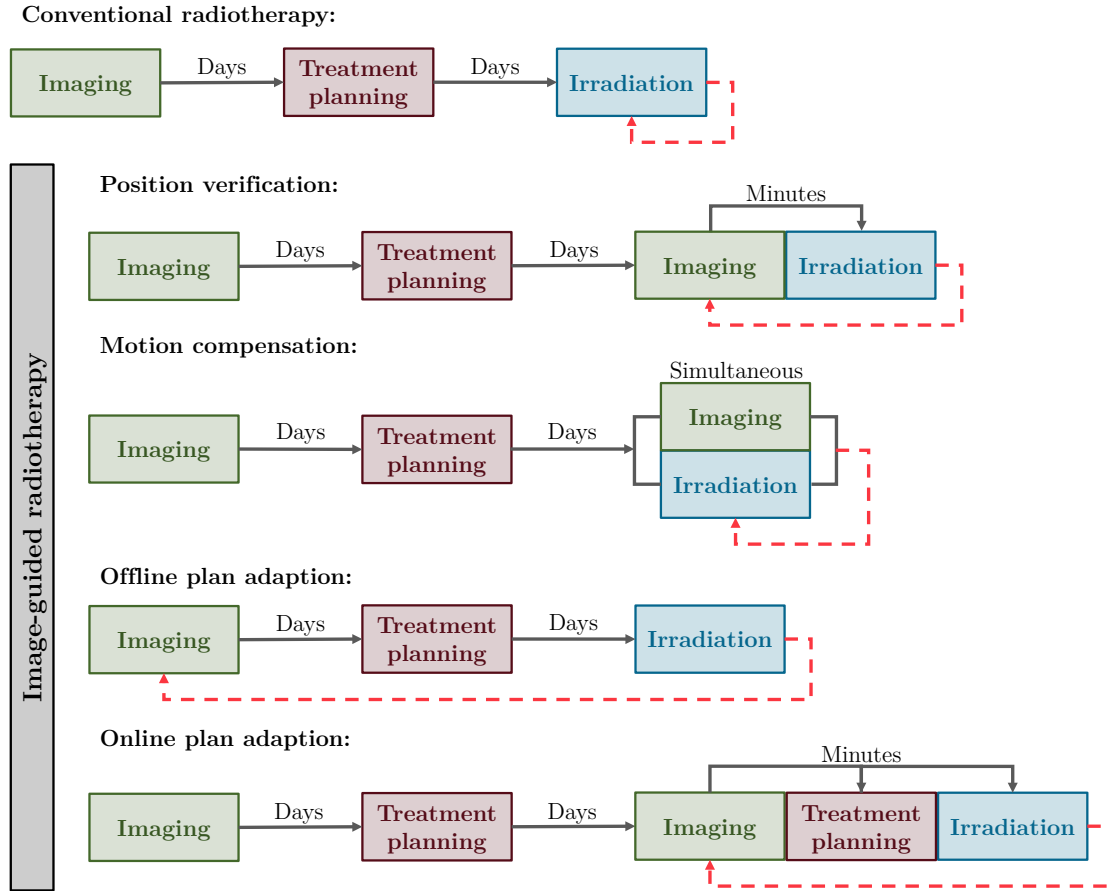


Figure 4: Workflow development from conventional radiotherapy to image-guided radiotherapy techniques including position verification, motion compensation, offline and online treatment plan adaption. The dashed red arrow represents the workflow that is repeated for each treatment fraction, respectively. Adapted from [59].

1.3.1 Position verification

In most IgRT procedures, the on-site images are used for a position verification prior to each treatment fraction. Mostly X-ray based systems are clinically available using either the treatment beam itself (MV beam) or an additional kV imaging system. For MV imaging, a flat panel detector is mounted on the Linac gantry opposite the beam exit. However, due to the high photon energy in the MV range, this so-called portal imaging lacks soft tissue contrast compared to conventional kV imaging [60, 61]. For kV imaging, a kV source is typically mounted on the Linac gantry perpendicular to the beam with an opposing flat panel detector to acquire planar (2D) or tomographic (3D CT) images using the gantry rotation for multiple beam directions. As this on-board imaging applies a cone beam instead of a standard fan beam geometry, the CT reconstruction is termed (kV-) cone beam CT (CBCT) [62]. While the image contrast of kV CBCT is higher than for MV imaging it still lags behind conventional fan beam CT imaging (section 1.2.1). Hence, some treatment sites additionally apply a mobile CT scanner (‘CT-on-rails’) for

positioning verification. The implantation of metal markers in or near to the target can increase the accuracy of an X-ray based correction, which otherwise relies primarily on the representation of bony structures.

Today, position verification may also be performed using MRI in so-called MR-guided RT (MRgRT), which benefits from a better soft tissue contrast without additional radiation exposure compared to X-ray based imaging (section 1.2). MR-guidance is available in an offline and online setting. In offline MRgRT, dedicated shuttle systems for patient transportation between MRI scanner and treatment device in treatment position may be used as well as special mobile MRI systems ('MRI-on-rails') [63-65]. For online MRgRT, special hybrid systems have recently been introduced combining an MRI scanner and a therapeutic Linac in a single device, so-called *MR-Linacs* [66-69]. Currently, two of these systems are commercially available, the 1.5 T "Unity" (Elekta AB, Stockholm, Sweden) and the 0.35 T "MRIdian Linac" (ViewRay, Inc., Oakwood Village, USA). The main difficulty in combining MRI and irradiation devices is shielding the Linac and its electronics from influences of the MRI's magnetic field and RF pulses as well as the MRI from the electronic noise generated by the Linac. Furthermore, since the main magnetic field of the MRI is always present, its influence on the dose distribution and on the response of radiation detectors has to be accounted for by the treatment planning algorithm. Although the photons themselves are not affected by the magnetic field, secondary electrons will be forced into circular trajectories due to Lorentz force, which shifts and deforms the entire dose distribution. At soft tissue interfaces with air, low density tissue (e.g. lung) or bone, secondary electrons entering the low-density material may be directed back to the dense material leading to an increased dose in the denser material. This is also known as the *electron return effect*.

1.3.2 Motion compensation

A precise and accurate dose deposition becomes especially challenging in case of tumors that significantly move within a single treatment fraction, i.e. in case of intra-fractional motion (e.g. due to breathing). To nevertheless ensure a homogenous coverage of the entire tumor, an extended ITV leading to a significantly increased PTV is typically introduced (section 1.1.1). The increase in treatment volume, however, involves a significant dose increase to healthy tissue possibly leading to severe side effects of the treatment (figure 1). Therefore, a reduction of the ITV by compensating the motion with the support of continuous imaging is highly desirable. Motion compensating may be realized by so-called tumor gating [70, 71] or tumor tracking [72, 73]. In a gated treatment, the beam is only turned on as long as the tumor is in a certain position and is automatically turned off as soon as it moves out of the so-called gating window. In contrast, tracking techniques attempt to follow the tumor motion with the beam. In both cases, an accurate and continuous knowledge of the tumor position is essential. Gating techniques may for example be implemented using X-ray tubes mounted in the treatment room [74-76], surface imaging using optical camera systems [77] or robotic ultrasound imaging systems [78]. Furthermore, the recent clinical introduction of MR-Linacs allows for MRI-based gating techniques using the much better soft tissue contrast of MRI [79, 80]. Fast imaging sequences (e.g. bSSFP or TSE sequences) with the possibility to acquire several frames per second enables real-time imaging of the patient's anatomy and hence an accurate tracing of the tumor motion without additional exposure. Tumor tracking, which includes a real-

time adaption of the treatment beam to the actual tumor position, is technically much more complex to implement. In first studies, this has been realized using an electromagnetic transponder-guided dynamic MLC response [81] or by robotic tumor tracking [82, 83]. However, an online reoptimization of the treatment plan to account for intra-fractional tumor motion, has not yet found its way into clinical practice.

1.3.3 Offline plan adaption

For slowly moving targets that may change position or shape between several treatment fractions (i.e. inter-fractional motion) an adaption of the treatment plan to take these changes into account is of high interest [84]. An inter-fractional motion may for example occur in abdominal tumors due to different bladder and rectum fillings as well as in case of tumor growth or shrinkage. In offline adaptive treatment techniques the treatment planning process, including imaging for planning purposes of conventional RT, is repeated between treatment fractions. Replanning may be done between single fractions or only after a number of fractions if the deviation becomes clinically relevant. Furthermore, online imaging techniques for position verification (section 1.3.1) may be combined with an offline recalculation of the treatment plan. Thus, it is possible to create several treatment plans based on different anatomical geometries already before treatment start and to select the most suitable plan for each fraction based on the online acquired image (so-called *plan of the day* concept). If the quality of the image acquired at the treatment device itself is sufficient, the new plan may also be calculated based on the online image directly without the need of further offline image acquisition [85].

1.3.4 Online plan adaption

An online adaption of treatment plans requires high-resolution 3D images of the patient anatomy acquired directly in treatment position. While CT imaging is typically used for treatment planning and also allows for a fast image acquisition, no hybrid device combining a diagnostic CT scanner with a treatment Linac is available today [85]. Hence, only with the introduction of hybrid MRgRT devices, an online plan adaption became clinically relevant [86-88]. The online MRI provides high-resolution images of the actual patient geometry but lacks the electron density information required for dose calculation. Therefore, electron density maps have to be created e.g. by using a DIR of pre-treatment CT images and/or by an assignment of bulk densities to specific tissue types [87]. Since dose recalculation is performed while the patient lies on the treatment couch, fast algorithms capable of accounting for magnetic field effects (section 1.3.1) have to be applied. Both hybrid MR-Linac systems available today employ a Monte-Carlo based dose calculation [89, 90]. A further time consuming component of the online plan adaption process is the manual correction of target and OAR structures, which are transferred to the online MRI from the pre-treatment plan using a DIR. In total, long treatment times in the order of 45 min are required for online adaptive MR-guided treatment procedures today compared to a total treatment time of a few minutes in conventional RT [91]. However, automated segmentation and advanced planning tools may accelerate the workflow in the future. A detailed description of the online adaptive treatment workflow performed at the MRIdian Linac will be given in section 1.4.

While the image quality of CBCTs has been mostly too low for online plan adaptations (low soft tissue contrast), new approaches are now available that allow fast online plan adaptation using artificial intelligence-driven CBCT-guided systems [92, 93]. However, if several CBCT images are acquired, a significant additional dose exposure may be accumulated.

1.4 Online adaptive MR-guided radiotherapy

The basic principles of MRgRT and online plan adaptation have already been discussed in section 1.3. Online adaptive MR-guided treatments are clinically implemented at a limited number of centers worldwide using the two commercially available MR-Linac systems [87, 88, 94-96]. While first centers currently develop prototypes to demonstrate the future integration of MR-guidance into proton therapy [97, 98], no system is, however, clinically available yet.

In this work, the online adaptive treatment workflow at the MRIdian Linac was investigated. The system combines a 0.35 T MRI scanner with a 6 MV Linac mounted on a ring gantry between the two superconducting magnet halves (double donut) of the MRI scanner [99]. The online adaptive treatment workflow performed with the MRIdian Linac at the Heidelberg university hospital (UKHD) in case of inter-fractional anatomy changes (figure 5) will be explained in this section.

The workflow can be divided into an offline and an online part. Treatment preparation including pre-treatment imaging and treatment planning is performed offline several days before the first irradiation. The online workflow is performed while the patient is positioned on the treatment couch and is repeated for each treatment fraction.

1.4.1 Offline treatment preparation

Treatment planning is based on an external pre-treatment CT. In addition, a pre-treatment MRI is acquired directly at the MRIdian Linac using a bSSFP imaging sequence with imaging parameters being pre-set in clinical mode depending on the chosen field of view. Both images are acquired in treatment position. The entire treatment planning is then performed at the TPS of the MR-Linac (ViewRay, Inc., Oakwood Village, USA). For this, the CT and MRI as well as potential additional images (e.g. high-field MRI) are deformably registered to the coordinate of the pre-treatment MRI using the integrated intensity-based registration algorithm of the TPS [100]. Once the images are sufficiently aligned, planning volumes such as the PTV and OARs are delineated based on the pre-treatment MRI while the CT image may support the delineation of bony structures. In addition, the registered CT image is used together with a HLUT to generate an electron density map representing the anatomical geometry of the pre-treatment MRI for dose calculation. Based on dose prescriptions for the PTV and OARs an IMRT plan is calculated and optimized iteratively. Before treatment, the accurate registration of pre-treatment images, the delineated structure set as well as the final dose distribution have to be approved by the physician in charge.

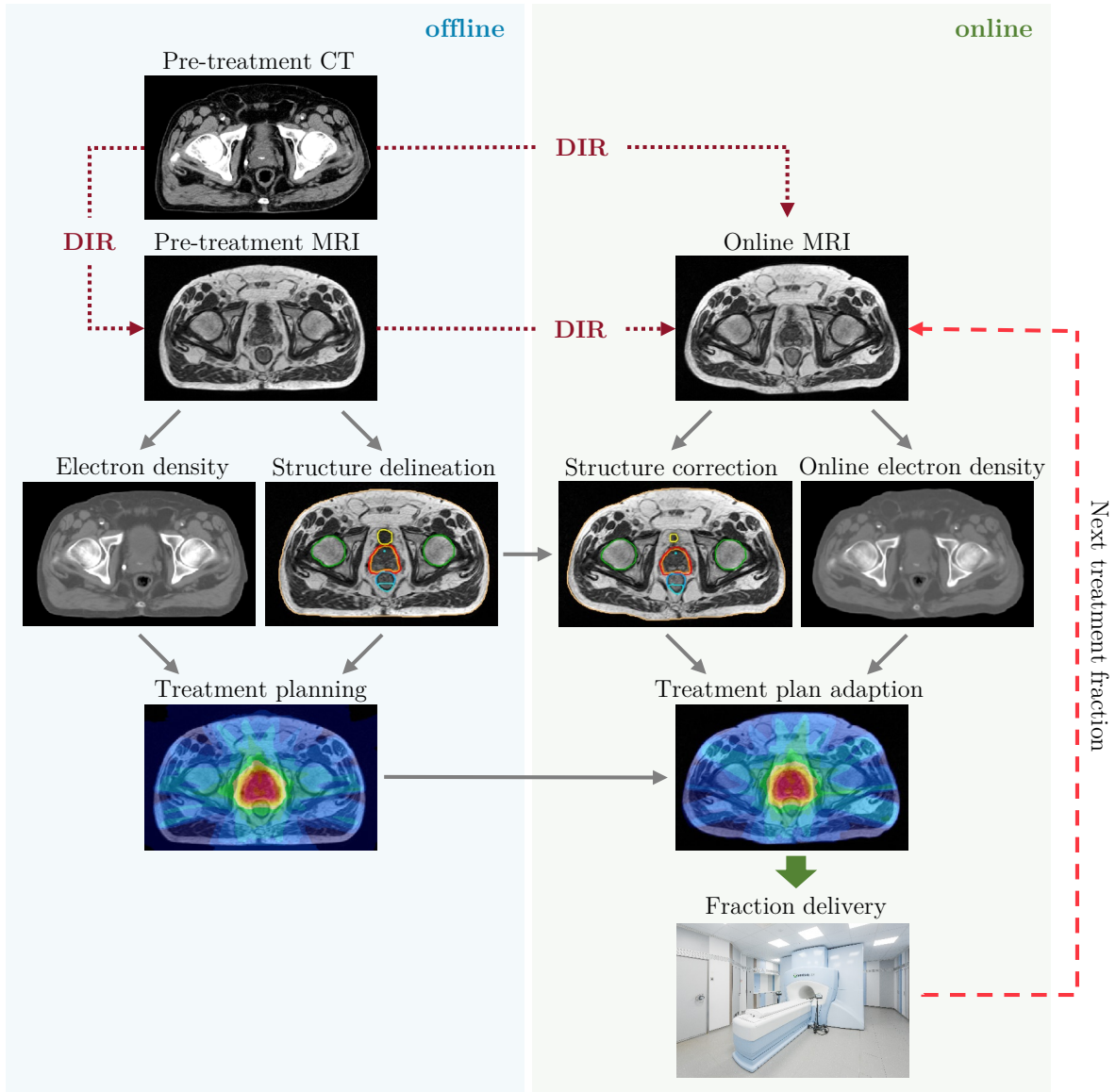


Figure 5: Online adaptive treatment workflow at the MRIdian Linac as performed at the UKHD in case of inter-fractional anatomy changes including initial treatment preparation performed offline.

1.4.2 Online treatment workflow

On the day of irradiation, the patient is positioned on the treatment couch using an external laser system and an online MRI is acquired with the same field of view and sequence parameters as for the pre-treatment MRI. The pre-treatment MRI is then transformed to the coordinate system of the online MRI using a DIR and the resulting vector field is applied to deform the delineated structures accordingly. A new electron density map is created via a second DIR of the pre-treatment CT to the online MRI. In a first step, the patient position is corrected by transferring the translation vector of the MRI-MRI registration (corresponding to a primary rigid registration) as a spatial shift to the treatment couch. The treatment structures transferred to the online MRI are then validated and, if necessary, manually corrected to ensure a precise alignment with the actual anatomy. To save time, this manual correction is typically limited to a volume that extends the PTV by 2 – 3 cm [87]. In a next step, the original treatment plan is recalculated on the new

geometry without a plan adaption. This is used to decide whether it can be directly applied to the patient or whether an online plan adaption is necessary. In case of an online adaption, the treatment plan is reoptimized in an iterative procedure similar to the offline planning procedure while the patient is waiting on the treatment couch. Once the plan satisfies the prescription, an online quality assurance (QA) tool including a secondary dose calculation (section 1.5.2) is performed and, if accepted, the adapted plan may be delivered to the patient. To further assure a correct dose delivery, an additional online MRI may be acquired directly before treatment delivery to exclude significant anatomical changes during the replanning procedure. Furthermore, an online adaption of the treatment plan may be combined with motion compensation procedures accounting for intra-fractional motion (e.g. gating, section 1.3.2).

1.5 Implementation of new MR-guided treatment procedures

The introduction of complex new treatment techniques such as online adaptive MRgRT into clinical practice requires a thorough quality assurance of all included steps. As MRgRT is clinically only available for photon beams, this section will focus on QA tests being applied in MRgRT with photons. To ensure a correct functioning of the treatment device and a precise dose delivery, both machine-related as well as patient-specific QA procedures are essential. These are based on standard QA procedures that have to be performed routinely to provide the foundation for the introduction of new techniques exceeding standard applications. A particular challenge of QA in MRgRT is the combination of two devices. This means that all safety aspects of a conventional Linac as well as those of an MRI device have to be tested separately. In addition, it requires validation of all interfaces of the two devices. Furthermore, all measurement equipment must be MR compatible and all procedures involving imaging must use phantoms providing MR contrast. Finally, to demonstrate the possibility and accuracy of a new treatment technique, so-called end-to-end tests are required that investigate not only all single components of a given workflow, but also their interaction and accumulated uncertainty.

1.5.1 Machine-related quality assurance

Machine-related QA routinely validates technical aspects of a treatment device to ensure a correct functioning of all components. In case of hybrid MR-Linacs, this includes both the Linac and the MRI scanner as well as dedicated tests that validate the correct interaction of the two devices [87]. A routine implementation of these QA procedures meeting reliably predefined quality standards provides the basis for the introduction of more advanced treatment techniques.

Machine-QA of the Linac comprises mainly dosimetric investigations such as the measurement of depth and lateral dose profiles as well as the measurement of the so-called output of the Linac. For dosimetric measurements, the MR compatibility of the equipment is essential. Reference dosimetry is mainly performed using ionization chambers that allow for absolute dosimetry at a certain reference point. However, their specific measurement setup, i.e. orientation within the magnetic field, as well as specific dose correction factors have to be considered [101-103]. Comparative measurements may be performed using other point-like dosimeters such as thermoluminescence detectors (TLDs) that are able to detect the absolute applied dose with the aid of specific

calibration procedures. Besides dosimetric measurements other components of the Linac such as the MLC calibration have to be checked regularly. Tolerance limits, test frequencies and measurement specifications of these QA procedures are typically oriented to international recommendations (e.g. [104, 105]).

On the imaging side, dedicated QA procedures ensuring high-quality and artifact-free patient imaging are required. This includes quality checks of the magnetic field homogeneity, the signal-to-noise ratio and the geometric accuracy of acquired images. For the use of MR images in the treatment planning process the investigation of geometric distortions and possible corrections are of special importance to ensure the accurate geometric representation of the patient's anatomy [106, 107]. These tests may be performed using dedicated QA phantoms for MRI [108-110].

In MRgRT, it is furthermore crucial that both systems work correctly together without deteriorating the quality of the other. QA procedures of the combined system are therefore necessary. Most importantly, the correct alignment of reference points, i.e. isocenters, of radiation delivery and imaging has to be validated [111, 112]. Furthermore, specific QA tests are recommended to investigate the interference of the two systems. This includes for example the measurement of the magnetic field homogeneity as a function of the Linac's gantry angle and the image quality during irradiation and MLC movements [113].

1.5.2 Patient-specific quality assurance

Patient-specific QA predominantly refers to a dosimetric treatment plan verification for individual patients. This verification became especially important with the introduction of complex dose distributions using IMRT techniques (section 1.1.1) [114]. In clinical practice, a patient plan may typically be verified using (i) a single- or multipoint dose measurement within a dedicated QA phantom or (ii) an independent dose calculation [115].

To detect the entire dose distribution with a physical measurement, 2D- or 3D dosimetry systems are particularly suitable. Several 2D- or 3D MR-compatible arrays of ionization chambers or diode systems are commercially available for dose verifications [116-120]. However, these systems consist of a finite set of dose measurement points with limited spatial resolution, which have to be interpolated to receive full 2D- or 3D dose distributions. The interpolation may lead to a loss of information in regions with steep dose gradients, which are especially sensitive to uncertainties in the dose delivery. For a spatially continuous dose measurement, radiochromic films may be used. Due to their high spatial resolution, films are routinely used in clinical practice to display complex radiation fields. However, they only allow for 2D measurements. Today, only few dosimeters allow for an accurate measurement of continuous 3D dose distributions. One such type of dosimeters are polymer gels (PGs) [121-124]. Polymer gels employ radiosensitive chemicals that polymerize after irradiation and the degree of polymerization depends on the absorbed dose. These chemicals are typically embedded in a water-based gelatin matrix to ensure geometric stability. Hence, PGs are radiologically equivalent to soft tissues. The gel's polymerization leads to a local change in mass density and the material specific T_2 relaxation rate, which allows for a read-out of the dose distribution by either (optical-) CT [121, 125, 126], MRI [121, 127, 128] or ultrasound imaging [129]. Within this thesis, PAGAT (PolyAcrylamide Gelatin gel fabricated at ATmospheric

conditions) dosimetry gel being evaluated in MRI was employed [130]. Using a dedicated calibration procedure together with a quantitative MRI evaluation of T_2 relaxation times (e.g. using a MSE sequence) allows to generate absolute dose maps in 3D. A detailed description of the experimental workflow from gel production to evaluation can be found in publication I of this thesis (section 2.2) [131].

If the patient is lying on the treatment couch during online plan adaption, a measurement-based dose verification is not feasible. In these cases, the dose distribution may be verified by a comparison with a secondary independent dose calculation. With the MRIdian Linac system a so-called adaptive QA tool may be applied during online adaption. This tool performs a secondary Monte Carlo-based dose calculation of the adapted plan for comparison with the original treatment plan. Furthermore, additional comparisons are performed including a check of the total machine output of the Linac (the so-called *monitor units*) and of the number of plan segments [132]. In addition, adapted treatment plans may be verified retrospectively using measurements already performed during treatment with so-called log file analyses [133] or portal dosimetry systems. Such a portal dosimetry system is available at the Unity system but not at the MRIdian Linac [134].

For a quantitative evaluation of measured 3D dose distributions, the so-called γ -index analysis [135] is typically used to assess the geometric and dosimetric accuracy of the measurement. The analysis tests if a measured dose value at a certain point in space can be assigned a dose value in the reference distribution, e.g. the treatment plan, that lies within a radius Δd of the evaluation point and has a maximum dose deviations of ΔD . If this is true for a certain criterion of relative deviations ($\Delta D/\Delta d$), the corresponding measurement point passes the analysis. By evaluating all measurement points of the volume, a passing rate of the γ -index analysis can be determined as the rate of measurement points passing the respective criterion.

1.5.3 End-to-end testing

To implement new treatment techniques a correct functioning of not only each component but the entire treatment chain is crucial. Hence, end-to-end tests simulating the treatment workflow from pre-treatment imaging to dose delivery with the possibility to accurately measure the applied dose are recommended. While standard QA procedures (section 1.5.1) estimate the uncertainty of single components, the uncertainty accumulated over the entire treatment may only be detected using end-to-end tests. Hence, such tests may demonstrate the feasibility to clinically implement complex treatment procedures and quantify remaining uncertainties and limitations. To perform end-to-end tests dedicated phantoms are necessary, which have to meet several requirements depending on the tested treatment workflow. For the implementation of new MR-guided treatment procedures, the phantom should ideally fulfill the following requirements:

- (i) possibility of accurate dose measurements at selected spatial points as well as in 2D/3D,
- (ii) anthropomorphic attenuation properties for the beam and anthropomorphic image contrast in CT and MRI, and
- (iii) precise and realistic simulation of anatomical structures as well as inter- and/or intra-fractional anatomy changes.

End-to-end tests are especially important for the commissioning of new devices and the introduction of new treatment workflows. A routine performance on a daily or weekly basis is typically neither feasible nor intended, but a repetition after longer periods (e.g. yearly) are highly recommended to ensure the stability of the workflow. However, only few end-to-end tests of online adaptive MR-guided treatments have been reported yet [136-138]. These employ mostly static phantoms, which are not able to simulate inter- or intra-fractional motion. Furthermore, the dose was mostly measured only at some selected spatial points or in 2D. So far, 3D dose measurement systems with high geometric and dosimetry accuracy, e.g. PGs, have been applied only in few cases for end-to-end tests of MRgRT [136, 139]. PGs are typically highly sensitive to chemical interactions with oxygen or the container material, temperature gradients during different steps of the experimental workflow or magnetic field inhomogeneities during MRI evaluation [121, 140]. Therefore, end-to-end tests require highly standardized PG workflows as well as the possibility to use PG in arbitrary geometries. A recent study demonstrated the compatibility of PAGAT dosimetry gel with a 3D printing technique to produce PG containers [141]. This opens up new possibilities for the development of anthropomorphic phantoms for end-to-end tests capable of validating delivered 3D dose distributions. First end-to-end tests using a standardized PAGAT dosimetry protocol have been performed at a conventional Linac [142-144].

1.6 Aim of the thesis

This thesis investigated, developed and implemented dedicated end-to-end tests to validate the overall accuracy of an MR-guided radiotherapy workflow. The ultimate aim was to demonstrate the feasibility of online adaptive MRgRT in case of inter-fractional anatomy changes. To this end, existing methods were further improved, aiming for a standardized 3D dose evaluation with PG as well as to produce anthropomorphic phantom materials with individually adjustable soft tissue contrast in CT and MRI. These methods were validated by investigating the feasibility to perform PG dosimetry in a deformable anthropomorphic pelvis phantom and by investigating the radiological tissue equivalence of the developed phantom materials. The PG application in a set of clinical QA phantoms was then explored. Finally, two end-to-end tests of an online adaptive MRgRT treatment were developed and successfully implemented at the 0.35 T MRIdian Linac. The tests include the simulation of inter-fractional motion and apply PG for 3D dose measurements.

2 PUBLICATIONS

The thesis is written in a cumulative format in accordance with the regulation of the Department of Physics and Astronomy of Heidelberg University. The thesis comprises four manuscripts published in international peer-reviewed journals, one additional manuscript being accepted for publication in an international peer-reviewed journal as well as one manuscript being submitted and peer-reviewed to be published as a conference paper. The manuscripts will be referred to by roman numerals. I am the first and main author of publications I, II, IV, V & VI. In case of publication III, which was written by Mathieu Marot, I am the second author.

None of the publications have been used in other dissertations.

List of publications

Publication I

Alina Elter, Stefan Dorsch, Sarina Thomas, Clemens M. Hentschke, Ralf O. Floca, Armin Runz, Christian P. Karger and Philipp Mann (2021) 'PAGAT gel dosimetry for everyone: gel production, measurement and evaluation', *Biomed. Phys. Eng. Express* **7** 057001

Publication II

Alina Elter, Emily Hellwich, Stefan Dorsch, Martin Schäfer, Armin Runz, Sebastian Klüter, Benjamin Ackermann, Stephan Brons, Christian P. Karger and Philipp Mann (2021) 'Development of phantom materials with independently adjustable CT- and MR-contrast at 0.35, 1.5 and 3 T', *Phys. Med. Biol.* **66** 045013

Publication III

Mathieu Marot, Alina Elter, Philipp Mann, Andrea Schwahofer, Clemens Lang, Wibke Johnen, Stefan A. Körber, Bettina Beuthien-Baumann and Clarissa Gillmann (2021) 'Technical Note: On the feasibility of performing dosimetry in target and organ at risk using polymer dosimetry gel and thermoluminescence detectors in an anthropomorphic, deformable, and multimodal pelvis phantom', *Med. Phys.*, 48:5501– 5510

Publication IV

Alina Elter, Dorsch Stefan, Mathieu Marot, Clarissa Gillmann, Wibke Johnen, Armin Runz, C. Katharina Spindeldreier, Sebastian Klüter, Christian P. Karger and Philipp Mann 'Gel dosimetry as a tool for clinical implementation of image-guided radiotherapy', *peer-reviewed as conference paper of the 2021 IC3DDose virtual meeting, publication pending*

Publication V

Alina Elter, Dorsch Stefan, Philipp Mann, Armin Runz, Wibke Johnen, C. Katharina Spindeldreier, Sebastian Klüter and Christian P. Karger (2019) 'End-to-end test of an online adaptive treatment procedure in MR-guided radiotherapy using a phantom with anthropomorphic structures', *Phys. Med. Biol.* **64** 225003

Publication VI

Alina Elter, Carolin Rippke, Wibke Johnen, Philipp Mann, Emily Hellwich, Andrea Schwahofer, Stefan Dorsch, Carolin Buchele, Sebastian Klüter and Christian P. Karger (2021) 'End-to-end test for fractionated online adaptive MR-guided radiotherapy using a deformable anthropomorphic pelvis phantom', *accepted, Phys. Med. Biol.*, <https://doi.org/10.1088/1361-6560/ac3e0c>

2.1 Thematic overview

The major aim of the thesis was the development and implementation of end-to-end tests for online adaptive MRgRT techniques in presence of inter-fractional motion. For this purpose, the projects of the thesis can be divided into methodological developments, the validation of these methods and final end-to-end tests. A thematic overview and an assignment of the publications to these categories is presented in figure 6. In addition, the major results of these publications are summarized. The original manuscripts are presented in sections 2.2 to 2.7.

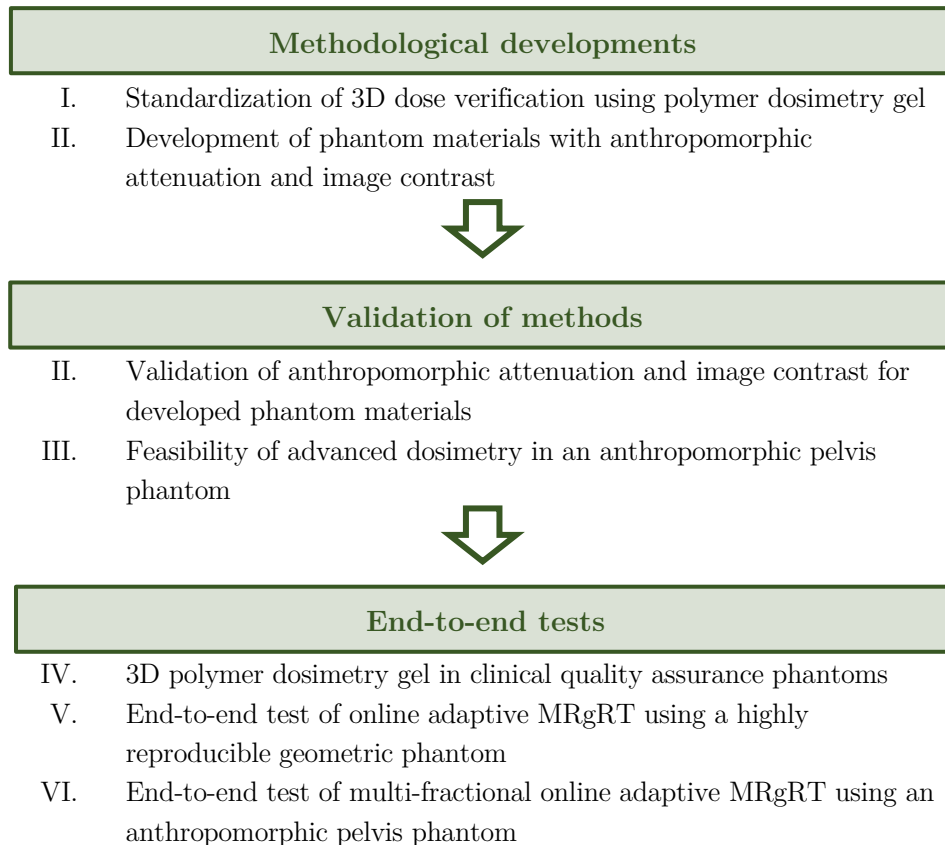


Figure 6: Thematic overview of the six publications (I-VI).

2.1.1 Methodological developments

Dedicated phantoms are required for the implementation of specific end-to-end tests. For end-to-end tests of online adaptive MRgRT in presence of inter-fractional motion, the phantom should ideally comprise (section 1.5.3):

- (i) the possibility of accurate dose measurements at selected spatial points as well as in 2D/3D,
- (ii) anthropomorphic radiologic attenuation properties and imaging contrast in CT and MRI, and
- (iii) precise and realistic simulation of anatomy changes.

Only few end-to-end tests of online adaptive MRgRT have been presented in literature yet [136-138], which typically fulfill only parts of requirements (i)-(iii). Hence, several methods have been developed within the scope of this thesis to be implemented in new as well as already existing end-to-end testing phantoms.

3D dose verification

A standardized workflow to perform highly accurate 3D dosimetry using PGs is presented in publication I. For 3D dose verification with high geometric and dosimetric accuracy, PGs provide a promising tool to be implemented in end-to-end tests of MRgRT techniques [139]. However, due to the high costs of commercial gels and the complex workflows that are required to perform PG experiments using in-house produced gels, only few centers apply PGs for clinical QA purposes worldwide. Therefore, the entire workflow of PG experiments using PAGAT gel from production to evaluation was described in great detail in publication I. The highly standardized workflow has been implemented at the German Cancer Research Center (DKFZ) within a preceding dissertation by Philipp Mann [144] and was already applied in several studies [112, 141-143, 145, 146]. In publication I, the existing knowledge was summarized and supplemented with further literature consultations to make the experimental workflow widely accessible to both experienced and unexperienced PG users. In addition, a plugin for the post-processing of gel experiments was developed within an open source image processing tool. This tool is provided free of charge as a supplement to the publication and allows for a highly standardized and reproducible evaluation of PG experiments. For the application of PAGAT gel in end-to-end tests, its use in anthropomorphic shapes is highly desirable. Therefore, I previously demonstrated the compatibility of the PG with a 3D printing material in my master thesis [141, 147]. This results in the possibility to produce anthropomorphically-shaped PG containers by 3D printing. The technique was applied in publications III-VI together with the gel production and evaluation workflow presented in publication I. Furthermore, the use of TLDs to renormalize the gel's dose response for absolute dosimetry was previously described in literature [145, 146]. TLDs were used in publication IV to independently measure the dose at selected positions and to validate the PG measurements (section 2.1.2). In addition, they were used in publication VI as an external reference measurement to renormalize the PG dose response (section 2.1.3).

Phantoms with anthropomorphic attenuation and imaging contrast

In publication II, phantom materials were developed that represent anthropomorphic and independently adjustable attenuation as well as imaging contrast in CT and MRI. In conventional RT, end-to-end testing phantoms are typically produced from solid materials, which show anthropomorphic radiation attenuation properties and CT contrast due to different material densities (e.g. Alderson Radiation Therapy Phantom, Radiology Support Devices, Inc., Long Beach, USA). However, these phantoms are not visible in conventional MRI sequences due to the very short relaxation times of solid materials. Phantoms for MRgRT therefore require materials that additionally exhibit anthropomorphic MRI contrast, i.e. T_1 and T_2 relaxation times, such as different liquids or gels. In publication II, phantom materials with individually adjustable CT and MRI contrast in the soft tissue range were developed for three different magnetic field strengths (0.35, 1.5 and 3.0 T). These materials are based on potassium chloride (KCl) and nickel diethylenetriaminepentaacetic acid (Ni-DTPA)-doped agarose gels. The concentration of KCl is

mainly responsible for different CT-values, while the concentrations of Ni-DTPA and agarose predominantly affect the changes in T_1 and T_2 , respectively. Within the scope of publication II, I developed a set of equations relating the required concentrations of KCl, Ni-DTPA and agarose with CT-, T_1 and T_2 values and vice versa. These equations were implemented in a software tool to automatically convert given imaging parameters into required chemical concentrations as well as in the opposite direction. This enables also other groups to easily produce phantom materials with anthropomorphic image contrast. Using this method, anthropomorphic phantom materials in the soft tissue range with positive CT-values can be produced. Similar materials, in combination with petroleum jelly (also known as ‘Vaseline’) and oil for fatty tissues as well as dipotassium phosphate (K_2HPO_4) and gypsum for bony structures [148], have been applied in the so-called AQUARIUM (Anthropomorphic QUality Assurance phantom to study Interfractional Uncertainties in MRgRT) and ADAM-PETer (Anthropomorphic, Deformable and Multimodality pelvis phantom with PET Extension for Radiotherapy) phantoms used in publications IV-VI in order to represent anthropomorphic imaging contrast.

Simulation of anatomical changes in phantoms

In this thesis, several phantoms were applied to simulate inter- or intra-fractional anatomy changes. Inter-fractional motion, which refers to anatomical changes in between two consecutive treatment fractions, may result from varying positioning, organ fillings (e.g. bladder, rectum) or tumor growth and shrinkage. Both the AQUARIUM (publications IV & V) and the ADAM-PETer (publications III, IV & VI) allow to simulate inter-fractional motion. The AQUARIUM enables for highly reproducible changes of several geometrical structures. On the other hand, the ADAM-PETer realistically represents the male pelvis including pelvic bones, bladder, rectum, prostate, fatty as well all muscle tissues and allows for the simulation of realistic anatomical changes induced by different bladder and rectum fillings [149, 150]. While benefitting from anthropomorphic geometries, the anatomical changes in the ADAM-PETer are, however, less reproducible than those of the AQUARIUM.

In contrast to inter-fractional motion, intra-fractional motion refers to anatomical changes during the course of a treatment fraction such as breathing or swallowing. As part of publication IV, two additional phantoms are presented, which simulate intra-fractional breathing motion. This includes a highly reproducible geometrical motion phantom and a realistic, but less reproducible, porcine lung phantom.

2.1.2 Validation of methods

In a second step towards the implementation of new end-to-end tests, the developed methods (section 2.1.1) were validated in a clinical environment.

Phantoms with anthropomorphic attenuation and imaging contrast

The developed phantom materials (publication II) may be adjusted to different CT, T_1 and T_2 values. To validate their anthropomorphic properties, nine specific soft tissue samples were produced according to literature values at 1.5 T and measured contrast parameters were compared with predictions at all three magnetic field strengths (0.35, 1.5 and 3.0 T). The comparison revealed a good agreement of predicted and measured values with mean deviations of less than

3.5 %. Furthermore, their long-term stability was confirmed by an additional acquisition of image parameters (MRI at 1.5 T) in the same samples after five months. This measurement resulted in only small mean deviations of -0.8 ± 1.6 %, -0.2 ± 1.5 % and -5.2 ± 1.1 % for CT, T_1 and T_2 values, respectively. However, the developed gels contain components of high atomic number ($Z_{\text{Ni}} = 28$) as compared to materials being naturally present in the human body. Since HLUTs, transferring CT-values to radiological attenuation properties, are typically optimized for materials with $Z < 20$, anthropomorphic radiological attenuation can therefore not be guaranteed for the developed phantom materials with a corresponding anthropomorphic CT-value. This is especially pronounced in ion therapy due to the different interaction processes of X-rays and ions within tissue. To be able to use the developed phantom materials also for future MR-guided ion therapy applications, the SPR of the specific soft tissue samples was experimentally determined and compared to predictions from both single- and dual-energy CT measurements. While the use of single-energy CT together with a conventional HLUT applied in clinical practice overestimated the SPR of the soft tissue samples, DECT predictions agreed well with measurements, with a mean deviation of only 0.2 ± 0.3 %. These results are presented in publication II.

Advanced dosimetry in an anthropomorphic pelvis phantom

The use of PAGAT dosimetry gel and TLDs for dose measurements in the anthropomorphic pelvis phantom (ADAM-PETer) was validated in publication III. The phantom was equipped with a 3D printed and PG-filled prostate as well as nine TLDs being placed in the rectum using a dedicated 3D printed holder. A prostate treatment was performed at a conventional Linac (Artiste, Siemens Healthineers, Erlangen, Germany) using a treatment plan based on an in-room CT-on-rails image. In addition, a position verification was performed with the integrated CBCT system. The PG evaluation resulted in a good agreement with the treatment plan, as demonstrated by a passing rate of the 3D γ -index analysis (3 %/3 mm criterion) of 97.7 %. Furthermore, TLD measurements deviated in mean only by 1.78 % from the respective planned values. This demonstrated the feasibility to perform accurate PG and TLD measurements within the ADAM-PETer phantom. The study presents important preliminary work for the end-to-end test of an online adaptive MRgRT treatment presented in publication VI (section 2.1.3), where the same phantom was used.

2.1.3 End-to-end tests

Several end-to-end tests of general IgRT as well as specific MRgRT treatments have been developed and implemented within the scope of this thesis. Publication IV presents an overview of QA phantoms that employ PG for 3D dose measurements being clinically applied at DKFZ and UKHD. An end-to-end test of an online adaptive MRgRT treatment within one treatment fraction using the highly reproducible AQUARIUM is described in publication V. Finally, an end-to-end test of a multi-fractional online adaptive MRgRT treatment was performed using the anthropomorphic ADAM-PETer with different bladder and rectum fillings (publication VI).

3D polymer dosimetry gel in clinical QA phantoms

As PGs allow for 3D dose verification, they provide a promising tool to be applied in clinical QA phantoms allowing for both hardware and end-to-end workflow tests of new IgRT treatment techniques. Within publication IV, the phantoms that are equipped with PG and are applied for clinical QA procedures at DKFZ and UKHD are summarized. This includes one machine-QA

phantom capable of measuring the 3D isocenter alignment accuracy in MRgRT devices [112], two motion phantoms to be used for end-to-end tests in case of intra-fractional breathing motion [142] as well as the two deformable phantoms AQUARIUM and ADAM-PETer used for end-to-end tests in case of inter-fractional motion.

Online adaptive MRgRT using a highly reproducible geometric phantom

In publication V, the AQUARIUM phantom is presented, which includes reproducibly rotatable and shiftable inserts. These inserts are placed within a water-filled cylinder and may be filled with anthropomorphic imaging contrast materials or PG. The phantom was used to perform an end-to-end test of an online adaptive treatment at the MRIdian Linac. For this, two phantom inserts were filled with PG to simulate a tumor and OAR, respectively. Three inserts contained different MRI contrast materials and two further inserts represented different image contrasts in CT. In total, the phantom was irradiated under three different conditions: (i) A static reference setup without changes of internal structures between treatment planning and irradiation. A position correction was performed according to the online MRI. (ii) Inter-fractional anatomy changes were simulated by rotations and shifts of the phantom inserts. However, the online MRI was used for a position correction only, the treatment plan was not adapted to the new phantom geometry. (iii) The same rotations and shifts of phantom structures as in case (ii) were applied in order to simulate inter-fractional anatomy changes. This time, however, an online adaption of the treatment plan was performed according to the online MRI. The end-to-end test validated that the treatment plan adaption resulted in very similar dose distributions of PG-filled tumor and OAR structures compared to the static case (i), where no plan adaption was necessary. While a significant under-dosage of the tumor and over-dosage of the OAR was found in case (ii), the dose was homogeneously distributed in the target and the OAR was well spared in both irradiations (i) and (iii).

Multi-fractional online adaptive MRgRT using a pelvis phantom

A final end-to-end test of a multi-fractional online adaptive MRgRT treatment is presented in publication VI. Here, the ADAM-PETer was used, equipped with 3D printed and PG-filled prostate and rectum inserts positioned at the same height. In addition, three TLDs were placed at the center and on the surface of the prostate for additional dose measurements and an external renormalization of the PG dose response. A total of five prostate treatment fractions were applied in sequence with different bladder and rectum fillings. For each fraction, the treatment plan was online adapted according to the online MRI. A good agreement of measured dose distributions in prostate and the rectum inserts with the accumulated adapted treatment plans of the single fractions was found. This was demonstrated by passing rates of the 3D γ -index analysis (3 %/3 mm criterion) of 98.9 % and 93.7 % for the prostate and rectum insert, respectively. TLD measurements revealed only minor deviations (mean -2.8 %). The end-to-end test validated the feasibility and accuracy of multi-fractional online adaptive MR-guided prostate irradiations in case of inter-fractional anatomy changes.

2.2 Publication I

PAGAT GEL DOSIMETRY FOR EVERYONE: GEL PRODUCTION, MEASUREMENT AND EVALUATION

Authors: [Alina Elter](#), Stefan Dorsch, Sarina Thomas, Clemens M. Hentschke, Ralf O. Floca, Armin Runz, Christian P. Karger and Philipp Mann

Status (12/2021): Published

Journal reference: *Biomedical Physics & Engineering Express*, **7** (2021) 057001

DOI: 10.1088/2057-1976/ac12a5

Copyright: © Institute of Physics and Engineering in Medicine. Reproduced with permission. All rights reserved.

This Accepted Manuscript is available for reuse under a CC BY-NC-ND 4.0 licence (<https://creativecommons.org/licenses/by-nc-nd/4.0/>) after the 12 month embargo period provided that all the terms of the licence are adhered to. This is the Accepted Manuscript version of an article accepted for publication in *Biomedical Physics & Engineering Express*. IOP Publishing Ltd is not responsible for any errors or omissions in this version of the manuscript or any version derived from it. The Version of Record is available online at <https://doi.org/10.1088/2057-1976/ac12a5>. No changes have been made.

Contribution: This work presents an introduction to perform highly standardized 3D dosimetric polymer gel experiments using PAGAT dosimetry gel. The manuscript describes the conduction of polymer gel experiments in great detail including the gel production, treatment planning, irradiation, MRI evaluation and post-processing procedure. The general workflow was first established by Philipp Mann in his dissertation in 2017 and has been widely used within the working group since then. The publication comprises furthermore a plugin in an open source image processing tool for post-processing. The manuscript focuses on the workflow description rather than new results and was published as a note. As main and first author, I have summarized the existing knowledge within our group as well as in literature and was responsible for the scientific input in the development of the post-processing tool. I have written the manuscript, prepared all graphics and revised the manuscript based on the reviewer's comments with support from Prof. Christian P. Karger and Dr. Philipp Mann.

ACCEPTED MANUSCRIPT

PAGAT gel dosimetry for everyone: gel production, measurement and evaluation

To cite this article before publication: A Elter *et al* 2021 *Biomed. Phys. Eng. Express* in press <https://doi.org/10.1088/2057-1976/ac12a5>

Manuscript version: Accepted Manuscript

Accepted Manuscript is “the version of the article accepted for publication including all changes made as a result of the peer review process, and which may also include the addition to the article by IOP Publishing of a header, an article ID, a cover sheet and/or an ‘Accepted Manuscript’ watermark, but excluding any other editing, typesetting or other changes made by IOP Publishing and/or its licensors”

This Accepted Manuscript is © 2021 IOP Publishing Ltd.

During the embargo period (the 12 month period from the publication of the Version of Record of this article), the Accepted Manuscript is fully protected by copyright and cannot be reused or reposted elsewhere.

As the Version of Record of this article is going to be / has been published on a subscription basis, this Accepted Manuscript is available for reuse under a CC BY-NC-ND 3.0 licence after the 12 month embargo period.

After the embargo period, everyone is permitted to use copy and redistribute this article for non-commercial purposes only, provided that they adhere to all the terms of the licence <https://creativecommons.org/licenses/by-nc-nd/3.0>

Although reasonable endeavours have been taken to obtain all necessary permissions from third parties to include their copyrighted content within this article, their full citation and copyright line may not be present in this Accepted Manuscript version. Before using any content from this article, please refer to the Version of Record on IOPscience once published for full citation and copyright details, as permissions will likely be required. All third party content is fully copyright protected, unless specifically stated otherwise in the figure caption in the Version of Record.

View the [article online](#) for updates and enhancements.

PAGAT gel dosimetry for everyone: gel production, measurement and evaluation

A Elter^{1,2,3}, S Dorsch^{1,3}, S Thomas⁴, C M Hentschke⁴, R Floca^{3,4}, A Runz^{1,3}, C P Karger^{1,3} and P Mann^{1,3}

¹ Division of Medical Physics in Radiation Oncology, German Cancer Research Center (DKFZ), Heidelberg, Germany

² Faculty of Physics and Astronomy, University of Heidelberg, Heidelberg, Germany

³ National Center for Radiation Research in Oncology (NCRO), Heidelberg Institute for Radiation Oncology (HIRO), Heidelberg, Germany

⁴ Division of Medical Image Computing, German Cancer Research Center (DKFZ), Heidelberg, Germany

E-mail: a.elter@dkfz.de

Received xxxxxx

Accepted for publication xxxxxx

Published xxxxxx

Abstract

Polymer gel (PG) dosimetry is a valuable tool to measure complex dose distributions in 3D with a high spatial resolution. However, due to complex protocols that need to be followed for in-house produced PGs and the high costs of commercially available gels, PG gels are only rarely applied in quality assurance procedures worldwide. In this work, we provide an introduction to perform highly standardized dosimetric PG experiments using PAGAT (PolyAcrylamide Gelatine gel fabricated at ATmospheric conditions) dosimetry gel. PAGAT gel can be produced at atmospheric conditions, at low costs and is evaluated using magnetic resonance imaging (MRI). The conduction of PG experiments is described in great detail including the gel production, treatment planning, irradiation, MRI evaluation and post-processing procedure. Furthermore, a plugin in an open source image processing tool for post-processing is provided free of charge that allows a standardized and reproducible analysis of PG experiments.

Keywords: 3D dosimetry, gel dosimetry, PAGAT, dosimetry gel production, dosimetry gel evaluation

1. Introduction

With techniques and workflows of radiation therapy (RT) treatment devices becoming more and more advanced, the use of radiation detectors that can validate the applied doses with a high geometric and dosimetric accuracy in three dimensions (3D) are of great interest. Polymer gel (PG) dosimeters (Baldock et al. 2010) provide a promising method to measure complex dose distributions for different treatment techniques (e.g. within magnetic fields (Dorsch et al. 2018), in intensity-modulated RT (Sandilos et al. 2004; Vergote et al. 2003), intensity-modulated arc therapy (Vergote et al. 2004) and stereotactic radiosurgery (Ertl et al. 2000; Novotný et al. 2002)) with a high spatial resolution. However, only few centers worldwide use PGs for quality assurance (QA). This is mostly related to the high costs of commercially available dosimetry gels and the lack of expertise in the use of in-house developed gels as the application requires highly standardized and complex workflows to gain high geometric and dosimetric accuracy. The large variety of gel dosimeters in literature combined with their individual workflows for production, application and evaluation poses a challenge to the inexperienced user. Not considering seemingly unimportant or

not mentioned details in literature may lead to inaccurate or even unusable results. This hinders establishing and widely using gel dosimetry for validation of complex treatment techniques in radiotherapy.

In this work, we present a detailed description of all relevant steps to obtain highly accurate and reproducible results in PAGAT (PolyAcrylamide Gelatine gel fabricated at ATmospheric conditions) dosimetry gel measurements. PAGAT gel benefits from a small dose rate dependence (De Deene et al. 2006), can be produced at atmospheric conditions at low costs and is evaluated using magnetic resonance imaging (MRI). We provide detailed protocols for gel preparation, treatment planning, irradiation, gel evaluation using MRI and post-processing using the in-house developed image processing platform Medical Imaging Interaction toolkit (MITK), which is made publicly available free of charge. The presented workflow is intended for applications with small PG volumes ($\sim 20 - 100 \text{ ml}$) inserted into larger QA phantoms, where the PG container represents for example a tumour or an organ at risk within an anthropomorphic end-to-end testing phantom.

2. General workflow of a PG experiment

A schematic overview of the time course of a PG experiment together with the temperature required at each step is displayed in figure 1. Typically, four days are needed from gel production to evaluation in MRI. After PG production on the first day (section 3), the gel samples are stored in a refrigerator at 4°C until 4 h before irradiation. This storage time may be used to acquire images for treatment planning and to generate a treatment plan (section 4). Approximately 24 h after gel production, the irradiation is performed (section 5) and the gel samples are stored at room temperature. Gel evaluation is then performed 48 h after irradiation using MRI (section 6). Finally, post-processing is performed to determine the dose distribution (section 7).

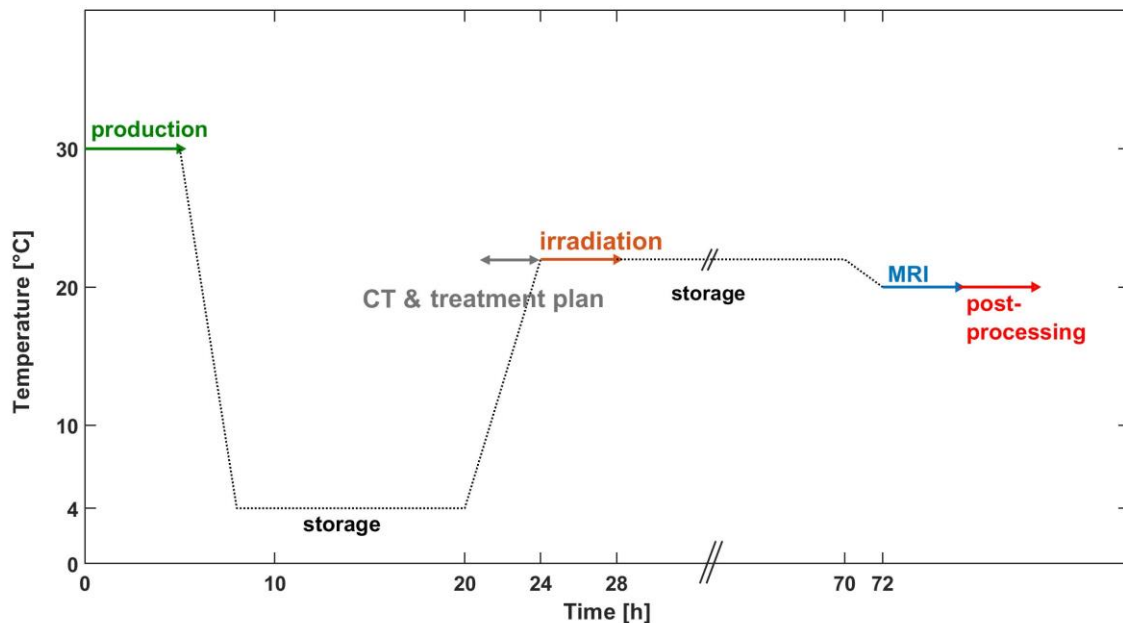


Figure 1: Schematic overview of the workflow of a typical gel dosimetry experiment giving the timeline and temperature profile.

3. Gel preparation

PAGAT dosimetry gel is based on two monomers (acrylamide and N,N-methylene-bis-acrylamide) embedded in a gelatine matrix and can be produced under atmospheric conditions. The following production workflow, which is based on De Deene et al. 2006, allows to produce the PG in-house at very low costs, exhibits no significant influence of penetrating oxygen and shows accurate ($< 4\%$ (De Deene and Jirasek 2015; Mann, Schwahofer, and Karger 2019)) results under temperature-controlled conditions when evaluated with MRI. The entire production process can be divided into three steps: (i) preparation of monomer and gelatine solutions, (ii) mixing and (iii) filling procedure. For each step, specific temperatures are required. A schematic overview of the temperature profile during the production procedure is displayed in figure 2 and a detailed list of ingredients and equipment required can be

found in the supplementary material via http://suppl.dkfz.de/E040_210305/Supplementaries_GelDosimetry.7z. The production procedure described was tested for gel volumes up to 1.5 l. For the production, a chemical fume hood should be used due to potential health hazards of the chemicals used (Baldock et al. 2010).

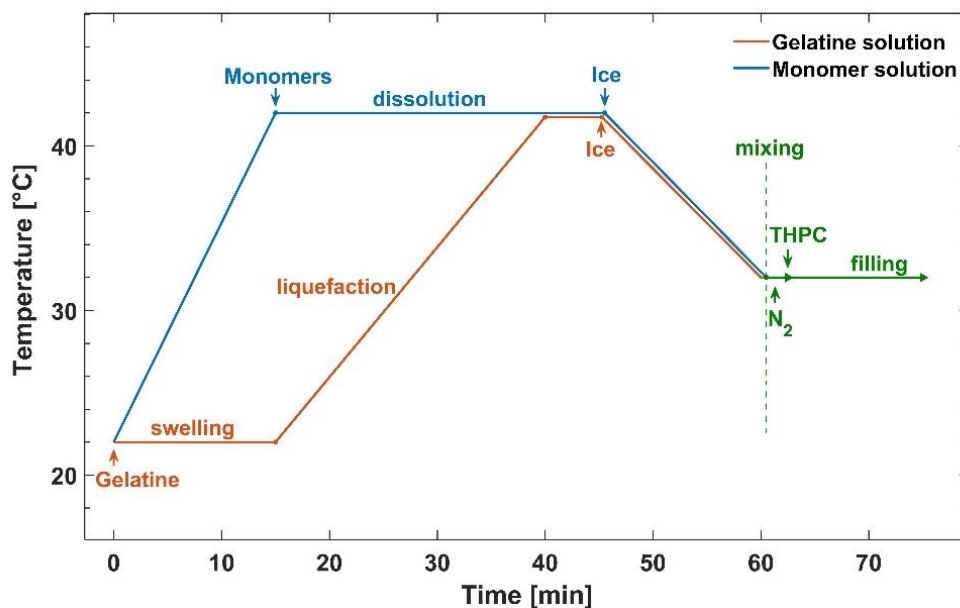


Figure 2: Schematic overview of the workflow of the dosimetry gel production. Monomers (blue, section 3.1.1) and gelatine (orange, section 3.1.2) solutions are prepared separately at the same time and are then mixed for the final dosimetry gel (green, section 3.2) using a highly standardized protocol (sections 3.1-3.3).

3.1 Preparation of monomer and gelatine solutions

Monomer and gelatine solutions are prepared at the same time in beakers inside a water reservoir using temperature controlled magnetic hot-plate stirrers, respectively. A metallic placeholder under the beakers is used to prevent the beakers from overheating. Magnetic stirrers are placed in both the water reservoirs and the beakers. The beakers are covered with aluminium foil to prevent water loss due to evaporation. A picture of the setup is shown in figure 3. For preparation, both water reservoirs are heated to a temperature of 42 °C.

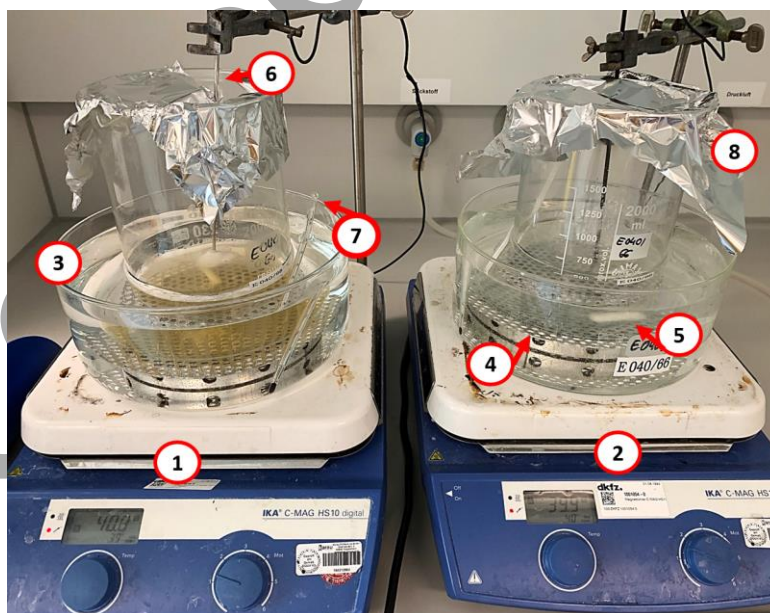


Figure 3: Picture of the gel production setup: magnetic hot-plate stirrer for the preparation of the gelatine (1) and monomer (2) solution, respectively, water reservoirs (3), metallic placeholders (4), magnetic stirrers (5), thermometer for temperature control of both magnetic hot-plate stirrers (6), thermometer for temperature control of both water reservoirs (7) and aluminium foil to seal the beakers (8). All components depicted (3)-8) are used for the gelatine as well as for the monomer solution.

3.1.1 *Monomer solution.* 60 % of the deionized water is given into the first beaker and heated to 42 °C. At this temperature, the acrylamide is poured into the water followed by the bis-acrylamide. A continuous stirring using the magnetic stirrer ensures a uniform distribution of the chemical components. The acrylamide dissolves within 1 *min* and leads to a temperature decrease of about 1 – 2 °C, while the bis-acrylamide takes up to 30 *min* to dissolve completely. When working with the monomer solution, a lab coat, protection gloves, glasses and a P2 respiratory mask should be worn.

3.1.2 *Gelatine solution.* The remaining 40 % of deionized water is placed in the second beaker together with a magnetic stirrer and followed by the gelatine. After a swelling process of at least 12 *min* at room temperature outside a water reservoir, the beaker is placed into the second water reservoir and heated to 42 °C.

3.2 *Mixing procedure*

Once the monomers and the gelatine are completely dissolved, the two solutions (both beakers) are cooled down to a temperature of 32 °C, e.g. by adding ice cubes to the water reservoirs. However, the temperature should not drop below 30 °C to assure the gelatine solution to stay fluid. When both solutions have reached the temperature of 32 °C, the monomer solution is carefully poured into the gelatine beaker to obtain the final dosimetry gel. It is very important to pour the monomers into the gelatine and not vice versa to prevent the gelatine from solidifying due to a fast cooling of the beaker when removing it from the water bath. To reduce the amount of dissolved oxygen (De Deene et al. 2002), nitrogen is flushed for approximately 2 *min* with a pressure of 1.5 *bar* into the gel using e.g. a Tygon® tubing connected to a large cannula. It is recommended to move the cannula slowly through the entire gel as to assure the nitrogen is homogeneously distributed within the solution. Finally, the bis[tetrakis(hydroxymethyl)phosphonium] chloride (THPC) is added as an antioxidant and stirred for 1 – 2 *min*. The THPC is an oxygen scavenger and allows for a gel production at atmospheric conditions in contrast to so-called hypoxic PAG-type gels that need to be produced in a nitrogen environment (De Deene et al. 2002; Venning et al. 2005).

3.3 *Filling procedure*

After adding THPC, the gel thickens quickly and should therefore be directly filled into containers, which were previously flushed with nitrogen. Due to the high reactivity of the polymer gel with oxygen and other contaminations (De Deene et al. 2006), containers that are impermeable to oxygen should be used, e.g. Barex™, glass (De Deene and Vandecasteele 2013) or VeroClear™ 3D printing material without using support material on inner walls during the printing process (Elter et al. 2019). In addition to the primary PG volume to be evaluated (from now on called *test containers*), a minimum of eight calibration containers having a volume similar to the test containers (e.g. Barex™ flasks, VELOX GmbH, Hamburg, Germany) are filled with PG, if absolute dose is to be measured. Using the same container size is recommended to minimize any uncertainties related to different volumes between test and calibration containers. To avoid dose uncertainties up to 25 % in the peripheral regions of larger phantoms reported elsewhere (Vandecasteele and De Deene 2013b) small container sizes (~20 – 100 *ml*) are recommended. Furthermore, the same batch of gel production is to be used for both the test and calibration containers to avoid uncertainties due to inter-batch variations (De Deene and Vandecasteele 2013). For renormalization of the calibration curve by an ionization chamber (IC) measurement, an additional test container being filled with a gelatine solution (monomers may be omitted) is required that allows inserting the IC into the gel volume. PG-filled containers are wrapped in aluminium foil to avoid light influencing the polymerization (Koeva et al. 2009) and stored within a nitrogen-flushed desiccator inside a refrigerator at 4 °C.

4. **Treatment planning**

For treatment planning, a CT image of the investigated phantom is acquired using an established clinical protocol. For this, the PGs are removed from the refrigerator, stored at room temperature and the test container is placed within the phantom of choice. This should be done approximately 4 *h* prior to irradiation. The applied CT dosage is negligible compared to the applied irradiation dose with regard to the accuracy of the gel experiment. To visualize the orientation of the test container within the phantom, which is later required for proper alignment of the measured dose distribution to the CT-image of the phantom (section 7.3), up to three external markers (e.g. PinPoint® #128

Multi-Modality Fiducial Markers, Beekly Medical, Bristol, USA) are attached to the test container. A treatment plan is then generated using a standard treatment planning system. Typically, a dose grid resolution of $1 \times 1 \times 1 \text{ mm}^3$ is used matching the image resolution of the MRI evaluation (section 6). Due to saturation of the calibration curve at higher doses and the resulting reduction in PG sensitivity (Jirasek et al. 2009), the maximum planned dosage within the evaluated gel volume should be in the range of 4 – 5 Gy.

5. Irradiation

Approximately 24 h after gel production, the PG can be irradiated using photons with beam energies of 6 – 25 MV (De Deene et al. 2006). If not yet done, the containers have to be removed from the refrigerator 4 h prior to irradiation to adapt to room temperature at the irradiation site. Test containers are then irradiated according to the treatment plan. In case of absolute dosimetry, the calibration containers have to be irradiated under reference conditions, e.g. within a water phantom, with known doses covering the range being irradiated in the gel evaluation volume (e.g. 0 – 7 Gy in steps of 1 Gy). In case of renormalization of the measured dose distribution, a reference measurement with an IC or thermoluminescence detectors (TLD) may be additionally performed (Mann et al. 2019; Vandecasteele and De Deene 2013a). After irradiation, all PG containers are wrapped in aluminium foil.

6. MRI evaluation

After irradiation, the gels are stored at room temperature for approximately 48 h to ensure that there is no further polymerization within the PG (De Deene and Vandecasteele 2013). However, if the gel shall be evaluated only geometrically rather than dosimetrically, MRI evaluation may also be performed directly after irradiation (Dorsch et al. 2018). For the subsequent PG evaluation, a quantitative T_2 measurement is carried out to acquire $R_2 = 1/T_2$ -maps that can then be translated to dose. For this, a multiple spin-echo sequence is used. To gain optimal results and to minimize uncertainties related to (i) temperature variations during the scan, (ii) magnetic field inhomogeneities or (iii) the choice of MR scanner and the applied sequence parameters, a dedicated measurement protocol needs to be applied. We achieved very good results with the following protocol (sections 6.1 – 6.3), however, suitable protocols may not be limited to this suggestion.

6.1 Temperature stability

Temperature variations may be induced by energy absorption during long MR measurements (De Deene and De Wagter 2001), temperature differences between gel containers of different sizes (e.g. test vs. calibration container) or within a large gel container. For temperature stability during MR scanning, the gels are inserted into a water-flow phantom (e.g. 3D-printed, a construction file can be found in the supplementary material via http://suppl.dkfz.de/E040_210305/Supplementaries_GelDosimetry.7z) attached to a water reservoir via a circulation pump (e.g. refrigerated circulator F6/C25, Thermo Haake GmbH, Karlsruhe, Germany) to maintain a temperature stability within $\pm 0.1 \text{ }^\circ\text{C}$. Approximately 2 h prior to MR scanning (Mann et al. 2017), the gel containers should be inserted into the flow phantom with the temperature being adjusted to that of the scanner bore (e.g. 20 $^\circ\text{C}$). The gel containers should be fixed by dedicated (e.g. 3D printed) holders so that they do not move when the water flow is operated. To reduce motion artifacts in the image caused by the continuous water flow, a contrast agent (e.g. 4 mmol/l GADOVIST® (Bayer AG, Leverkusen, Germany) (Rohrer et al. 2005)) is substituted to the water resulting in T_1 and T_2 relaxations times $< 50 \text{ ms}$. To avoid temperature differences between test and calibration containers, both container types are imaged in the same scan. Temporal stability should be checked by acquiring a calibration curve at the beginning and at the end of the MR evaluation (see section *Calibration* in the documentary of the of the provided gel evaluation plugin in MITK).

6.2 Magnetic field inhomogeneities

To reduce dose uncertainties resulting from magnetic field inhomogeneities of both the static field B_0 and the time-dependent field B_1 , the use of small test containers is recommended (Vandecasteele and De Deene 2013c). Furthermore, a manual B_0 shim should be applied prior to each measurement sequence.

6.3 MR scanner and scanning parameters

Since final dose resolution depends on the signal-to-noise ratio (SNR) of the MR images (De Deene and Baldock 2002), which increases with the magnetic field strength of the MR scanner, the use of an MR scanner with higher main field strength (e.g. 3 T) as well as a signal acquisition coil with as many receiver channels as possible is of advantage. Furthermore, the choice of imaging parameters is essential to acquire high-resolution images (down to $1 \times 1 \times 1 \text{ mm}^3$ voxel size) with large SNR while minimizing the total measurement time. Ideally, a standard Carr-Purcell-Meiboom-Gill (CPMG) sequence (Meiboom and Gill 1958) with 32 equidistant echoes is used, where the repetition time (TR), echo time (TE) and voxel size (VS) are optimized for the type of irradiation performed: (i) TR should be chosen to be long enough to avoid influences in the signal intensities from longitudinal relaxation (T_1), e.g. $TR \geq 3 \text{ s}$; (ii) T_2 of the PG decreases with higher radiation doses and hence, shorter TE should be selected. Ideally, TE is chosen such that the signal intensity has decreased to 20 % of its initial value at the last acquired echo, e.g. $TE = 22.5 \text{ ms}$. It is important that the signal of the last echo has not yet decreased to the noise level as this would result in an inaccurate fit to determine $R_2 = 1/T_2$ values. Furthermore, no background signal of the contrast agent-enhanced water of the water-flow phantom should be present after the third echo. If this cannot be achieved, the concentration of the contrast agent has to be increased further; (iii) finally, VS should be adjusted to match the dose grid resolution of the treatment plan, e.g. $VS = 1 \times 1 \times 1 \text{ mm}^3$. The number of image slices is adjusted to the irradiated PG volume, whereas the acquisition of a single transversal slice is sufficient for the calibration containers. It is important to select identical acquisition parameters for the calibration and test containers. Additionally, a high-resolution ($0.5 \times 0.5 \times 0.5 \text{ mm}^3$) 3D image of the test containers is acquired, e.g. by using a standard true fast imaging sequence with steady state precession (TrueFISP) (Chavhan et al. 2008; Scheffler and Hennig 2003), to allow the alignment of the measured dose distribution with the planning CT. A detailed list of all sequence parameters at a diagnostic 3 T Magnetom Prisma^{fit} MRI scanner (Siemens Healthineers, Erlangen, Germany) can be found in the supplementary material via http://suppl.dkfz.de/E040_210305/Supplementaries_GelDosimetry.7z.

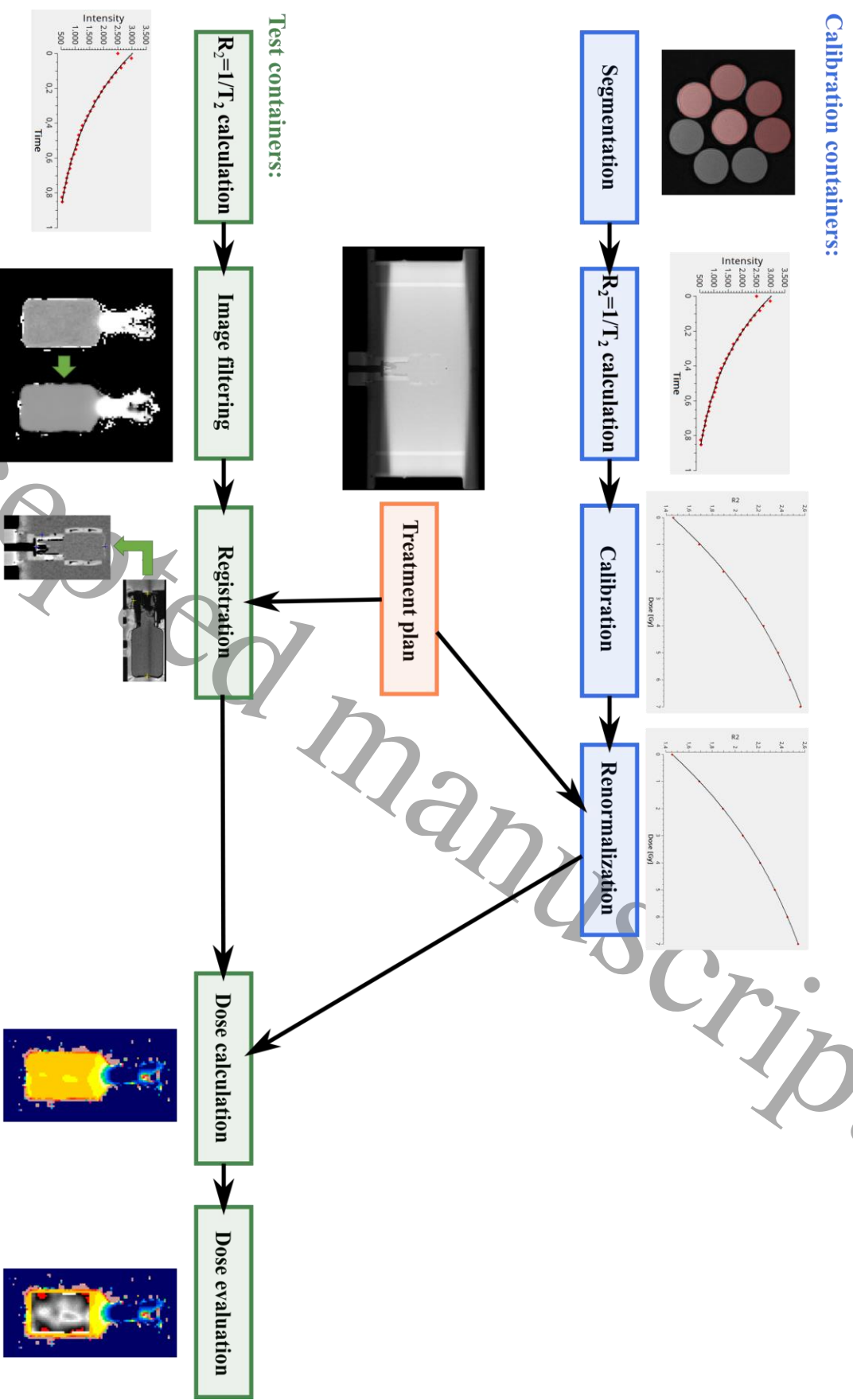


Figure 4: Schematic overview of the post-processing workflow for gel evaluation being provided in the supplementary materials. Steps performed using the image of the calibration containers, the treatment plan and the test container are marked in blue, orange and green, respectively.

7. Post-processing

Post-processing of the acquired data for PG evaluation requires several steps that can be executed in a dedicated plugin of the image processing platform MITK (Debus et al. 2019; Nolden et al. 2013). This plugin is provided for interested users for free via https://www.mitk.org/wiki/MITK_Geldosimetry together with an example data set in the supplementary material via http://suppl.dkfz.de/E040_210305/Supplementaries_GelDosimetry.7z. A detailed description on the usage of the evaluation tool can be found in its documentary. The post-processing workflow is summarized in figure 4.

7.1 Calibration

From calibration container measurements, the R_2 -dose calibration curve is established. For this, quantitative $R_2 = 1/T_2$ values are calculated for each calibration container. After defining regions of interest (ROI) in the container images, the mean R_2 value of each container is determined by fitting a mono-exponential curve to 29 of the 32 acquired MR images using a Levenberg-Marquard X^2 -minimization algorithm (Marquardt 1963). Image 1 – 3 are excluded to minimize any influence of stimulated echoes on the fitting process (Hennig 1991). The calibration curve is then established by fitting the mean relaxation rates R_2 against the known doses, D , by a mono-exponential function (Vandecasteele and De Deene 2013a):

$$R_2(D) = R_{2,sat} - \Delta R_2 e^{-\alpha D}, \quad (1)$$

With $R_{2,sat}$ corresponding to the saturation relaxation rate, ΔR_2 to the range of R_2 and the fit coefficient α .

7.2 Test container and image filtering

After calculating a T_2 map of the PG-filled test container (section 7.1) an edge-conserving total variation filter is applied (Rudin, Osher, and Fatemi 1992). The filter reduces the noise level within regions of constant intensities while preserving steep dose gradients.

7.3 Image registration

As irradiation and MR evaluation of the gel containers are generally performed in different phantoms, a spatial alignment of the measured and planned dose distribution is required. This is done by a rigid co-registration of the planning CT- and the high-resolution MR image. Using the three landmarks (e.g. Beekly markers, sections 4 and 6) on the surface of the test container, the high-resolution MR image is registered to the CT image using the MITK registration algorithm *RigidClosedForm3D* (a point-based closed-form solution approach to deduce the rigid registration matrix). The generated registration is subsequently applied together with a b-Spline 3rd order interpolation algorithm to align the T_2 -, R_2 - or dose map of the gel evaluation volume with the planned dose of the treatment plan.

7.4 Renormalization

Various factors during PG production (Vandecasteele and De Deene 2013a), storage and irradiation (Vandecasteele and De Deene 2013b) or evaluation may influence the gel response (De Deene and Vandecasteele 2013). Therefore, a renormalization of the calibration curve is usually performed, if absolute dose values are of interest. This renormalization may use (i) the treatment plan or (ii) a reference measurement (e.g. with an IC or TLD). In general, a renormalization is performed using either the known doses at two points in uniform low- and high-dose regions (*2-point-renormalization*) or one known dose at a single point in the high-dose region (*1-point-renormalization*), if no low-dose region is present in the irradiated gel volume or if only a single reference measurement was performed (Vandecasteele and De Deene 2013a).

7.4.1 2-point-renormalization. For a 2-point-renormalization, the mean R_2 values in a low- ($R_{2,1}$) and a high- ($R_{2,2}$) dose ROI within the test container are determined. Known dose values (D_1, D_2) are assigned to these R_2 values based on (i) corresponding ROIs in the treatment plan or (ii) given reference measurements. Employing the fit coefficient α of equation 1, $R_{2,sat}$ and ΔR_2 are recalculated (Vandecasteele and De Deene 2013a):

$$R'_{2,sat} = R_{2,1} - \Delta R'_2 \cdot e^{-\alpha D_1} \quad (2)$$

$$\Delta R'_2 = \frac{R_{2,2} - R_{2,1}}{e^{-\alpha D_2} - e^{-\alpha D_1}}. \quad (3)$$

Using these recalculated instead of the original parameters in equation 1 leads to the renormalized R_2 -dose calibration curve.

7.4.2 1-point-renormalization. If only a high-dose region is available for dose renormalization, the calibration curve remains fixed at the R_2 value measured for 0 Gy (Tremblay et al. 2011). Following the procedure in section 7.4.1, $R_{2,sat}$ and ΔR_2 are recalculated using:

$$R'_{2,sat} = \Delta R'_2 + R_{2,0} \quad (4)$$

$$\Delta R'_2 = \frac{R_{2,2} - R_{2,0}}{e^{-\alpha D_2} - 1}, \quad (5)$$

With $R_{2,0} = R_{2,sat} - \Delta R_2$ being the intersection of the original calibration curve with the y-axis. Replacing the original by the recalculated parameters in equation 1 results in the renormalized calibration curve.

7.5 3D dose calculation

To receive the final dose distribution, the R_2 map of the test container is converted into a dose map using the renormalized calibration curve created in section 7.4.

7.6 Gamma index analysis

To evaluate the measured dose distribution within the PG-filled test container, a comparison with the treatment plan is recommended. For quantitative evaluation of dose distribution differences a γ -index analysis (Low et al. 1998) is typically performed. In gel dosimetry, passing criteria of $\Delta D_M = 3\%$ and $\Delta d_M = 3\text{ mm}$ for the γ -index are generally applied. The γ -index analysis can also be performed in MITK using the RTToolbox (Zhang et al. 2013).

8. Discussion

In this work, a detailed overview on the conduction of high quality PG experiments using PAGAT gel is presented including gel production, treatment planning, irradiation, MRI evaluation and post-processing procedures. This allows performing 3D dosimetry of complex dose distributions applied with different treatment techniques in a highly standardized and reproducible way without having prior experience in the field of gel dosimetry. Furthermore, the free post-processing tool offers an easy and accurate evaluation of the experiments.

PAGAT gel was chosen due to its comparably low costs and low dose-rate dependence (De Deene et al. 2006). However, a large variety of different dosimetry gels and corresponding protocols exist in literature (Baldock et al. 2010) that might also be suitable to perform 3D dosimetry depending on the specific application.

The presented workflow was optimized to minimize uncertainties of the PG experiment that might occur during gel production, irradiation and MR evaluation. However, remaining uncertainties during production may result from small chemical variations due to an inhomogeneous mixing, remaining impurities in the gel or in the containers or oxygen penetration effects (De Deene and Jirasek 2015). During irradiation and storage it is usually not feasible to perform a temperature control as done for the MR evaluation. Hence, temperature variations between test and calibration containers may lead to differences in the gel response and it is therefore advised to store all gel containers of one experiment in the same room and to use similar gel volumes for test and calibration containers. Furthermore, variations in the dose rate and energy spectrum of the irradiation may lead to variations in the gel response and have to be avoided (De Deene and Jirasek 2015). Applying the proposed MR evaluation protocol using a water-flow phantom keeps the temperature stable and to reduces the uncertainties of the MR evaluation to a minimum. However, small remaining temperature variations as well as B_0 - and B_1 - field inhomogeneities and other scanner-related error sources may have an influence on the gel response (Vandecasteele and De Deene 2013c). While a general uncertainty analysis in PG dosimetry can be found elsewhere (De Deene and Jirasek 2015; De Deene and Vandecasteele 2013; Mann 2017), a similar overall uncertainty of $< 4\%$ has been found applying the presented PG workflow (Mann et al. 2019).

Although PAGAT gel can be produced under atmospheric conditions, its handling is still challenging as it is strongly reactive with oxygen and other contaminations (De Deene et al. 2006). This limits the choice of suitable container materials. Furthermore, a PG experiment is time-consuming (approximately one week for a single experiment) and requires a well-equipped laboratory and access to an MRI device for gel evaluation. Therefore, PG experiments as described in this work might not be feasible for daily or weekly QA procedures in clinical routine. However, they optimally complement the process of commissioning new treatment devices, end-to-end testing of new treatment workflows prior to clinical implementation and repeated QA-tests on an intermediate- or long-term time scale (Baldock, Karger, and Zaidi 2020).

9. Conclusion

In this work, instructions for 3D gel dosimetry experiments using PAGAT gel are presented in such detail that especially inexperienced users have all necessary information to establish highly accurate measurements. All relevant steps and technical details from gel production to evaluation are explained and supplementary material is provided including a detailed list of ingredients, the required lab equipment as well as a post-processing tool.

References

- Baldock, C., Y. De Deene, S. Doran, G. Ibbott, A. Jirasek, M. Lepage, K. B. McAuley, M. Oldham, and L. J. Schreiner. 2010. "Polymer Gel Dosimetry." *Physics in Medicine and Biology* 55(5):R1-63.
- Baldock, Clive, Christian P. Karger, and Habib Zaidi. 2020. "Gel Dosimetry Provides the Optimal End-to-End Quality Assurance Dosimetry for MR-Linacs." *Medical Physics* 47(8):3259–62.
- Chavhan, G. B., P. S. Babyn, B. G. Jankharia, H. M. Cheng, and M. M. Shroff. 2008. "Steady-State MR Imaging Sequences: Physics, Classification, and Clinical Applications." *RadioGraphics* 28(4):1147–60.
- Debus, Charlotte, Ralf Floca, Michael Ingrisich, Ina Kompan, Klaus Maier-Hein, Amir Abdollahi, and Marco Nolden. 2019. "MITK-ModelFit: A Generic Open-Source Framework for Model Fits and Their Exploration in Medical Imaging - Design, Implementation and Application on the Example of DCE-MRI." *BMC Bioinformatics* 20(1):31.
- De Deene, Y. and C. Baldock. 2002. "Optimization of Multiple Spin-Echo Sequences for 3D Polymer Gel Dosimetry." *Physics in Medicine and Biology* 47(17):3117–41.
- De Deene, Y., C. Hurley, A. Venning, K. Vergote, M. Mather, B. J. Healy, and C. Baldock. 2002. "A Basic Study of Some Normoxic Polymer Gel Dosimeters." *Physics in Medicine and Biology* 47(19):3441–63.
- De Deene, Y., K. Vergote, C. Claeys, and C. De Wagter. 2006. "The Fundamental Radiation Properties of Normoxic Polymer Gel Dosimeters: A Comparison between a Methacrylic Acid Based Gel and Acrylamide Based Gels." *Physics in Medicine and Biology* 51(3):653–73.
- De Deene, Y. and C. De Wagter. 2001. "Artefacts in Multi-Echo T2 Imaging for High-Precision Gel Dosimetry: III. Effects of Temperature Drift during Scanning." *Physics in Medicine and Biology* 46(10):2697–2711.
- De Deene, Yves and Andrew Jirasek. 2015. "Uncertainty in 3D Gel Dosimetry." *Journal of Physics: Conference Series* 573:012008.
- De Deene, Yves and Jan Vandecasteele. 2013. "On the Reliability of 3D Gel Dosimetry." in *Journal of Physics: Conference Series*. Vol. 444.
- Dorsch, S., P. Mann, C. Lang, P. Häring, A. Runz, and C. P. Karger. 2018. "Feasibility of Polymer Gel-Based Measurements of Radiation Isocenter Accuracy in Magnetic Fields." *Physics in Medicine & Biology* 63(11):11NT02.
- Elter, A., S. Dorsch, P. Mann, A. Runz, W. Johnen, and C. P. Karger. 2019. "Compatibility of 3D Printing Materials and Printing Techniques with PAGAT Gel Dosimetry." *Physics in Medicine and Biology* 64(4):04NT02.

- 1
2
3 Ertl, A., A. Berg, M. Zehetmayer, and P. Frigo. 2000. "High-Resolution Dose Profile Studies Based on MR
4 Imaging with Polymer BANG(TM) Gels in Stereotactic Radiation Techniques." *Magnetic Resonance*
5 *Imaging* 18(3):343–49.
- 6
7 Hennig, J. 1991. "Echoes—How to Generate, Recognize, Use or Avoid Them in MR-Imaging Sequences. Part II:
8 Echoes in Imaging Sequences." *Concepts in Magnetic Resonance* 3(4):179–92.
- 9
10 Jirasek, A., M. Hiltz, A. Berman, and K. B. McAuley. 2009. "Effects of Glycerol Co-Solvent on the Rate and
11 Form of Polymer Gel Dose Response." *Physics in Medicine and Biology* 54(4):907–18.
- 12
13 Koeva, V. I., T. Olding, A. Jirasek, L. J. Schreiner, and K. B. McAuley. 2009. "Preliminary Investigation of the
14 NMR, Optical and x-Ray CT Dose–Response of Polymer Gel Dosimeters Incorporating Cosolvents to
15 Improve Dose Sensitivity." *Physics in Medicine and Biology* 54(9):2779–90.
- 16
17 Low, D. A., W. B. Harms, S. Mutic, and J. A. Purdy. 1998. "A Technique for the Quantitative Evaluation of Dose
18 Distributions." *Medical Physics* 25(5):656–61.
- 19
20 Mann, P. 2017. "Development and Implementation of 3D-Dosimetric End-to-End Tests in Adaptive Radiation
21 Therapy of Moving Tumors." Ruperto-Carola University of Heidelberg.
- 22
23 Mann, P., A. Schwahofer, and C. P. Karger. 2019. "Absolute Dosimetry with Polymer Gels—a TLD Reference
24 System." *Physics in Medicine and Biology* 64(4):45010.
- 25
26 Mann, P., M. Witte, T. Moser, C. Lang, A. Runz, W. Johnen, M. Berger, J. Biederer, and C. P. Karger. 2017. "3D
27 Dosimetric Validation of Motion Compensation Concepts in Radiotherapy Using an Anthropomorphic
28 Dynamic Lung Phantom." *Physics in Medicine and Biology* 62(2):573–95.
- 29
30 Marquardt, Donald W. 1963. "An Algorithm for Least-Squares Estimation of Nonlinear Parameters." *Journal of*
31 *the Society for Industrial and Applied Mathematics* 11(2):431–41.
- 32
33 Meiboom, S. and D. Gill. 1958. "Modified Spin-Echo Method for Measuring Nuclear Relaxation Times." *Review*
34 *of Scientific Instruments* 29:688–91.
- 35
36 Nolden, M., S. Zelzer, A. Seitel, D. Wald, M. Müller, A. M. Franz, Daniel Maleike, Markus Fangerau, Matthias
37 Baumhauer, Lena Maier-Hein, Klaus H. Maier-Hein, Hans-Peter Meinzer, and Ivo Wolf. 2013. "The
38 Medical Imaging Interaction Toolkit: Challenges and Advances." *International Journal of Computer*
39 *Assisted Radiology and Surgery* 8(4):607–20.
- 40
41 Novotný, Josef, Pavel Dvůrák, Václav Špeváček, Jaroslav Tintera, Josef Novotný, Tomáš Cechák, and Roman
42 Liscák. 2002. "Quality Control of the Stereotactic Radiosurgery Procedure with the Polymer-Gel
43 Dosimetry." *Radiotherapy and Oncology : Journal of the European Society for Therapeutic Radiology and*
44 *Oncology* 63(2):223–30.
- 45
46 Rohrer, Martin, Hans Bauer, Jan Mintorovitch, Martin Requardt, and Hanns-Joachim Weinmann. 2005.
47 "Comparison of Magnetic Properties of MRI Contrast Media Solutions at Different Magnetic Field
48 Strengths." *Investigative Radiology* 40(11):715–24.
- 49
50 Rudin, L. I., S. Osher, and E. Fatemi. 1992. "Nonlinear Total Variation Based Noise Removal Algorithms." *Physica D: Nonlinear Phenomena* 60(1–4):259–68.
- 51
52 Sandilos, P., A. Angelopoulos, P. Baras, K. Dardoufas, P. Karaiskos, P. Kipouros, M. Kozicki, J. M. Rosiak, L.
53 Sakelliou, I. Seimenis, and L. Vlahos. 2004. "Dose Verification in Clinical IMRT Prostate Incidents." *International Journal of Radiation Oncology, Biology, Physics* 59(5):1540–47.
- 54
55
56 Scheffler, K. and J. Hennig. 2003. "Is TrueFISP a Gradient-Echo or a Spin-Echo Sequence?" *Magnetic*
57 *Resonance in Medicine* 49(2):395–97.
- 58
59 Tremblay, Nicolas M., Vincent Hubert-Tremblay, Rachel Bujold, A. Sam Beddar, Luc Beaulieu, and Martin
60 Lepage. 2011. "Accurate Calibration of a Polymer Gel Dosimeter with a Plastic Scintillation Detector."

1
2
3
Medical Physics 38(5):2754–61.

4 Vandecasteele, Jan and Yves De Deene. 2013a. “On the Validity of 3D Polymer Gel Dosimetry: I.
5 Reproducibility Study.” *Physics in Medicine and Biology* 58(1):19–42.

6
7 Vandecasteele, Jan and Yves De Deene. 2013b. “On the Validity of 3D Polymer Gel Dosimetry: II. Physico-
8 Chemical Effects.” *Physics in Medicine and Biology* 58(1):43–61.

9
10 Vandecasteele, Jan and Yves De Deene. 2013c. “On the Validity of 3D Polymer Gel Dosimetry: III. MRI-Related
11 Error Sources.” *Physics in Medicine and Biology* 58(1):63–85.

12
13 Venning, A. J., B. Hill, S. Brindha, B. J. Healy, and C. Baldock. 2005. “Investigation of the PAGAT Polymer Gel
14 Dosimeter Using Magnetic Resonance Imaging.” *Physics in Medicine and Biology* 50(16):3875–88.

15
16 Vergote, K., Y. De Deene, W. Duthoy, W. De Gersem, W. De Neve, E. Achten, and C. De Wagter. 2004.
17 “Validation and Application of Polymer Gel Dosimetry for the Dose Verification of an Intensity-Modulated
18 Arc Therapy (IMAT) Treatment.” *Physics in Medicine and Biology* 49(2):287–305.

19
20 Vergote, Koen, Yves De Deene, Filip Claus, Werner De Gersem, Bart Van Duyse, Leen Paelinck, Eric Achten,
21 Wilfried De Neve, and Carlos De Wagter. 2003. “Application of Monomer/Polymer Gel Dosimetry to Study
22 the Effects of Tissue Inhomogeneities on Intensity-Modulated Radiation Therapy (IMRT) Dose
23 Distributions.” *Radiotherapy and Oncology : Journal of the European Society for Therapeutic Radiology
24 and Oncology* 67(1):119–28.

25
26 Zhang, Lanlan, Martina Hub, Sarah Mang, Christian Thieke, Oliver Nix, Christian P. Karger, and Ralf O. Floca.
27 2013. “Software for Quantitative Analysis of Radiotherapy: Overview, Requirement Analysis and Design
28 Solutions.” *Computer Methods and Programs in Biomedicine* 110(3):528–37.

2.3 Publication II

DEVELOPMENT OF PHANTOM MATERIALS WITH INDEPENDENTLY ADJUSTABLE CT- AND MR-CONTRAST AT 0.35, 1.5 AND 3 T

Authors: Alina Elter, Emily Hellwich, Stefan Dorsch, Martin Schäfer, Armin Runz, Sebastian Klüter, Benjamin Ackermann, Stephan Brons, Christian P. Karger and Philipp Mann

Status (12/2021): Published

Journal reference: *Physics in Medicine & Biology*, **66** (2021) 045013

DOI: 10.1088/1361-6560/abd4b9

Copyright: © Institute of Physics and Engineering in Medicine. Reproduced with permission. All rights reserved.

This Accepted Manuscript is available for reuse under a CC BY-NC-ND 3.0 licence (<https://creativecommons.org/licenses/by-nc-nd/3.0/>) after the 12 month embargo period provided that all the terms of the licence are adhered to. This is the Accepted Manuscript version of an article accepted for publication in *Physics in Medicine and Biology*. IOP Publishing Ltd is not responsible for any errors or omissions in this version of the manuscript or any version derived from it. The Version of Record is available online at <https://doi.org/10.1088/1361-6560/abd4b9>. No changes have been made.

Contribution: In this study, phantom materials with independently adjustable anthropomorphic image contrast in CT and MRI were developed. These materials are based on a method available in literature to independently adjust T_1 - and T_2 -relaxation times being the main contrast parameters in MRI using Ni-DTPA doped agarose gels. I have extended the existing method to (i) three different magnetic field strengths as T_1 and T_2 are field strength dependent and (ii) to additionally include CT image contrast by the addition of potassium chloride. Furthermore, I have measured the SPR of the materials using carbon ions and compared them with predictions from single- and dual-energy CT. I have conducted all experiments including gel production, CT and MR imaging as well as SPR measurements with support of the co-authors. Furthermore, I have developed a system of equations that describes the material specific imaging parameters in dependence on the chemical concentration of the ingredients as well as vice versa. Finally, I wrote the manuscript, prepared all graphics and revised the manuscript based on the reviewer's comments with support from Dr. Philipp Mann and Prof. Christian P. Karger.

ACCEPTED MANUSCRIPT

Development of phantom materials with independently adjustable CT- and MR-contrast at 0.35, 1.5 and 3T

To cite this article before publication: Alina Elter *et al* 2020 *Phys. Med. Biol.* in press <https://doi.org/10.1088/1361-6560/abd4b9>

Manuscript version: Accepted Manuscript

Accepted Manuscript is “the version of the article accepted for publication including all changes made as a result of the peer review process, and which may also include the addition to the article by IOP Publishing of a header, an article ID, a cover sheet and/or an ‘Accepted Manuscript’ watermark, but excluding any other editing, typesetting or other changes made by IOP Publishing and/or its licensors”

This Accepted Manuscript is © 2020 Institute of Physics and Engineering in Medicine.

During the embargo period (the 12 month period from the publication of the Version of Record of this article), the Accepted Manuscript is fully protected by copyright and cannot be reused or reposted elsewhere.

As the Version of Record of this article is going to be / has been published on a subscription basis, this Accepted Manuscript is available for reuse under a CC BY-NC-ND 3.0 licence after the 12 month embargo period.

After the embargo period, everyone is permitted to use copy and redistribute this article for non-commercial purposes only, provided that they adhere to all the terms of the licence <https://creativecommons.org/licenses/by-nc-nd/3.0>

Although reasonable endeavours have been taken to obtain all necessary permissions from third parties to include their copyrighted content within this article, their full citation and copyright line may not be present in this Accepted Manuscript version. Before using any content from this article, please refer to the Version of Record on IOPscience once published for full citation and copyright details, as permissions will likely be required. All third party content is fully copyright protected, unless specifically stated otherwise in the figure caption in the Version of Record.

View the [article online](#) for updates and enhancements.

Development of phantom materials with independently adjustable CT- and MR-contrast at 0.35, 1.5 and 3T

A Elter^{1,2,3}, E Hellwich^{1,2}, S Dorsch^{1,2}, M Schäfer⁴, A Runz^{1,2}, S Klüter^{2,5}, B Ackermann⁶, S Brons⁶, C P Karger^{1,2} and P Mann^{1,2,7}

¹ Department of Medical Physics in Radiation Oncology, German Cancer Research Center (DKFZ), INF 280, 69120 Heidelberg, Germany

² National Center for Radiation Research in Oncology (NCRO), Heidelberg Institute for Radiation Oncology (HIRO), Heidelberg, Germany

³ Faculty of Physics and Astronomy, University of Heidelberg, Heidelberg, Germany

⁴ Department of Radiology, German Cancer Research Center (DKFZ), INF 280, 69120 Heidelberg, Germany

⁵ Department of Radiation Oncology, University Hospital Heidelberg, INF 400, 69120 Heidelberg, Germany

⁶ Heidelberg Ion-Beam Therapy Center, Im Neuenheimer Feld 450, Heidelberg, Germany

⁷ HQ-Imaging GmbH, Heidelberg, Germany

E-mail: a.elter@dkfz.de

Received xxxxxx

Accepted for publication xxxxxx

Published xxxxxx

Abstract

Quality assurance in magnetic resonance (MR)-guided radiotherapy (RT) lacks anthropomorphic phantoms that represent tissue-equivalent imaging contrast in both computed tomography (CT) and MR imaging. In this study, we developed phantom materials with individually adjustable CT value as well as T_1 - and T_2 -relaxation times in MR imaging at three different magnetic field strengths. Additionally, their experimental stopping power ratio (SPR) for carbon ions was compared with predictions based on single- and dual-energy CT.

Ni-DTPA doped agarose gels were used for individual adjustment of T_1 and T_2 at 0.35, 1.5 and 3.0 T. The CT value was varied by adding potassium chloride (KCl). By multiple linear regression, equations for the determination of agarose, Ni-DTPA and KCl concentrations for given T_1 , T_2 and CT values were derived and employed to produce nine specific soft tissue samples. Experimental T_1 , T_2 and CT values of these soft tissue samples were compared with predictions and additionally, carbon ion SPR obtained by range measurements were compared with predictions based on single- and dual-energy CT.

The measured CT value, T_1 and T_2 of the produced soft tissue samples agreed very well with predictions based on the derived equations with mean deviations of less than 3.5 %. While single-energy CT overestimates the measured SPR of the soft tissue samples, the dual-energy CT-based predictions showed a mean SPR deviation of only (0.2 ± 0.3) %.

To conclude, anthropomorphic phantom materials with independently adjustable CT values as well as T_1 and T_2 relaxation times at three different magnetic field strengths were developed. The derived equations describe the material specific relaxation times and the CT value in dependence on agarose, Ni-DTPA and KCl concentrations as well as the chemical composition of the materials based on given T_1 , T_2 and CT value. Dual-energy CT allows accurate prediction of the carbon ion range in these materials.

Keywords: phantom materials, magnetic resonance imaging (MRI) and Computed tomography (CT) contrast, MR-guided radiotherapy (MRgRT), end-to-end tests, quality assurance

1. Introduction

Modern radiotherapy (RT) systems used in clinical practice usually combine a treatment beam, consisting of photons or ions, with an imaging modality, e.g. X-rays (computed tomography (CT), fluoroscopy and cone beam CT) or magnetic resonance (MR)-imaging. Especially hybrid MR-guided RT devices combining an MRI with a linear accelerator (MR-Linac) for treatment with high energetic photons (MRgXT) became popular in the last years. This is especially due to the superior soft tissue contrast and the reduction of radiation dose to normal tissue allowing for inter- and intrafractional motion management (Paganelli et al. 2018). However, the use of MRI for online adaptive irradiation procedures poses new demands on phantoms for quality assurance and end-to-end tests that reflect the complexity of real patient treatments.

Conventional phantoms as routinely used in radiotherapy are mostly optimized with respect to X-ray based imaging at a Linac and are therefore mostly not visible in MRI due to the absence of liquids. Furthermore, tissue-equivalent materials are usually optimized in terms of photon attenuation by adding substitutes of variable electron densities; however, these materials typically do not show anthropomorphic imaging contrast in MRI. Therefore, phantoms with a correct representation of anthropomorphic contrast in CT as well as in MRI are currently not available, but are needed to validate MRgXT treatment strategies.

Various studies addressed the requirements of contrast materials that can be used in MRI as well as in RT. These studies characterized potential phantom materials for their applicability in MRgXT end-to-end tests by determining their CT value and visibility in different MRI sequences (Steinmann et al. 2018), characterized different materials quantitatively in CT and MRI to simulate anthropomorphic image contrast in the pelvic region (Niebuhr et al. 2016) or in the general soft tissue range (Kim et al. 2020). Furthermore, anthropomorphic MRI phantom materials with individually adjustable T_1 and T_2 relaxation times at a magnetic field of 1.5 T are available using Nickel- or Gadolinium diethylenetriaminepentaacetic acid (Ni-, GD-DTPA) (Tofts et al. 1993). Ideally, contrast parameters in both imaging modalities (X-ray and MRI) should be individually adjustable. This issue was already addressed in a recently published study that introduces phantom materials with individually adjusted CT- and MR contrast at 3.0 T using carrageenan-based gels doped with gadolinium, agarose, glass microspheres and calcium carbonate (Singhrao et al. 2020a; Singhrao et al. 2020b) which are based on Hattori and Yoshimura (Hattori et al. 2013; Yoshimura et al. 2003). However, MRI contrast parameters (T_1 and T_2 relaxation times) depend on the magnetic field strength B_0 and the presented fit-models can therefore not be transferred to other field strengths. To our knowledge no individual adjustment of both CT value and T_1 and T_2 relaxation times at different magnetic field strengths has yet been published. All field strengths that are potentially included in the MR-guided treatment process (e.g. pre-RT at a diagnostic MRI and online imaging at the MR-Linac for daily plan adaption) should be included in the development of new phantom materials. In principle, it is desirable to use such materials also in phantoms for end-to-end tests in recently proposed MR-guided ion therapy (MRgIT) treatments (Hoffmann et al. 2020; Oborn et al. 2017; Raaymakers, Raaijmakers, and Lagendijk 2008). Due to the different interaction processes of X-rays and ions, however, the ion range in these materials has to be verified and in the optimal case tissue-equivalence may be obtained in terms of the stopping power ratio (SPR).

In this study, we first improved a previously developed method (Tofts et al. 1993) to produce phantom materials with individually adjustable T_1 - and T_2 - relaxation rates using Ni-DTPA-doped agarose gels and present equations to obtain tissue-equivalent material with predefined T_1 - and T_2 -relaxation times at three different field strengths (0.35, 1.5 and 3 T) as well as the not necessarily tissue-equivalent CT -value of these materials. In a second step, we extended the method to independently adjust the CT value of the gels by adding potassium chloride (KCl) and equations are derived to determine the concentrations of agarose, Ni-DTPA and KCl to achieve a specific soft tissue contrast in both imaging modalities. Finally, we produced a set of nine specific soft tissues (kidney medulla, kidney cortex, prostate, spleen, grey matter, white matter, muscle, liver and pancreas) with adjusted T_1 -, T_2 - and CT -values and validated these values by quantitative MR and CT measurements. In addition, carbon (^{12}C) ion range predictions based on single- and dual-energy CT were compared with measurements of the stopping power ratio (SPR).

2. Materials and Methods

2.1 Contrast Materials

It has been shown that the contrast of Ni-DTPA doped agarose gel may be individually adjusted to given T_1 - and T_2 - relaxation times in MRI by selecting appropriate Ni-DTPA and agarose concentrations (Tofts et al. 1993). Here, Ni-DTPA is mainly responsible for a reduction in T_1 while an increasing agarose concentration mainly decreases T_2 . In our study, Ni-DTPA was produced in-house following the same method (Tofts et al. 1993) and was chosen as quantitative T_1 values show a reduced temperature and B_0 dependence as compared to other frequently used contrast materials that are based on Copper, Manganese or Gadolinium (Tofts et al. 1993). Additionally, potassium chloride (KCl) was added to increase CT values. In total, three sets of phantom material samples were produced: (a) Ni-DTPA doped agarose gels without the addition of KCl used solely for MR contrast adjustment (termed as MR contrast calibration), (b) Ni-DTPA- and KCl-doped agarose gels for a combined adjustment of MR and CT contrast (termed as MR/CT contrast calibration), and (c) adjustment of Ni-DTPA, KCl and agarose concentrations to obtain specific tissue contrasts based on results found in (a) and (b) (termed as tissue-specific samples using the MR/CT contrast calibration). The separate MR contrast calibration (a) was performed to allow application of the method also for MR-only users who are not interested in reproducing also tissue-specific CT-values.

For gel preparation, agarose (Agarose HEEO Ultra-Quality, Carl Roth GmbH & Co. KG, Karlsruhe, Germany), in-house prepared Ni-DTPA and, if required, KCl ($\geq 99,5\%$, Carl Roth GmbH & Co. KG, Karlsruhe, Germany) were solved in water (HPLC Gradient grade) and heated under continuous stirring to $(75 - 80)^\circ\text{C}$. After filling test tubes, gels were stored for at least 4 h in the refrigerator for hardening. As gel containers for MR and CT measurements, plastic conical centrifuge tubes (50 ml, diameter: 28 mm, FalconTM, Thermo Fisher Scientific Inc., Waltham, USA) were used (experiments I and II), whereas the stopping power ratios (SPR) of the material relative to water for ion beams were measured in single 3D printed containers consisting of 14 serially aligned cuboidal subvolumes (inner volume: $15 \times 17.8 \times 17.8 \text{ mm}^3$) described in (Möhler et al. 2018) (experiment III).

Table 1 displays the chemical compositions of the samples used for the MR (a) and MR/CT (b) contrast calibration. The range of Ni-DTPA and agarose concentrations is based on the concentrations in (Tofts et al. 1993). However, this range was extended in this study to achieve a greater variability in T_1 and T_2 . The KCl concentration was increased up to its solubility. The MR/CT-calibration was then used to produce 9 specific soft tissue contrasts (c) with relaxation times optimized to match literature values at 1.5 T given in (de Bazelaire et al. 2004) and (Bottomley et al. 1984) and CT values in (Schneider, Bortfeld, and Schlegel 2000).

Filled centrifuge tubes were well sealed by means of superglue, sealing tube and gluing tubes and stored at room-temperature for long-term stability measurements after the main experiments have been performed.

Tab. 1. Chemical composition of the produced samples. Agarose concentration ([Ag]) is given in mass percent (%)^a, Ni-DTPA ([Ni]) in mM^b and KCl ([KCl]) in mass permille (‰)^c.

a) MR contrast calibration														
	AgNi-1	AgNi-2	AgNi-3	AgNi-4	AgNi-5	AgNi-6	AgNi-7	AgNi-8	AgNi-9	AgNi-10	AgNi-11	AgNi-12	AgNi-13	AgNi-14
[Ag]	1.0	2.0	1.5	4.4	2.5	2.0	1.0	8	8	10	10	15	20	35
[Ni]	2	2	4	6	6	8	8	8	10	10	15	20	25	35
b) MR/CT contrast calibration														
	KCl-1	KCl-2	KCl-3	KCl-4	KCl-5	KCl-6	KCl-7	KCl-8	KCl-9	KCl-10	KCl-11	KCl-12		
[Ag]	1.0	3.5	2.5	0.5	2.0	3.0	5.0	1.5	4.0	1.5	1.5	3.0	1.0	1.0
[Ni]	6	4	2	6	20	8	10	15	4	6	6	4	10	10
[KCl]	5	5	10	10	15	15	20	20	25	25	25	30	30	30
c) tissue-specific samples using the MR/CT contrast calibration at 1.5 T														
	KCl-13	KCl-14	KCl-15	KCl-16	KCl-17	KCl-18	KCl-19	KCl-20	KCl-21	KCl-22				
[Ag]	2.5	1.5	4.5	0.5	2.0	1.0	3.0	2.5	3.5	2.0				
[Ni]	12	6	2	8	4	4	2	8	10	4				
[KCl]	35	35	40	40	45	50	60	100	140	260				

^arelative to water
^brelative to the agarose solution
^crelative to the agarose/Ni-DTPA solution

2.2 Experiments

Using the different samples, three different experiments were performed:

- I. **CT measurements:** Single-energy CT (SECT) measurements were performed on a clinical Somatom Confidence RT Pro scanner (Siemens Healthineers, Erlangen, Germany) at a tube voltage of 120 kV to assess the x-ray attenuation (CT values). For realistic beam hardening conditions, samples in centrifuge tubes were placed in a water-filled phantom (diameter: 12 cm) (Mann et al. 2017). The 3D printed containers used for SPR measurements were placed at the center of a cylindrical PMMA cylinder (diameter: 16 cm). Additionally, dual-energy CT (DECT) measurements of the 3D printed containers were acquired on a Somatom Definition Flash (Siemens Healthineers, Erlangen, Germany) at a voltage pair of 80/Sn 140 kV (Sn: with additional tin filtration) to determine the electron density relative to water ($\hat{\rho}_e$) and the effective atomic number (Z_{eff}) of the phantom materials. All images were reconstructed with the D34s reconstruction kernel on a cubic grid of 1.0 mm edge length. To investigate the long-term stability of the developed materials SECT measurements of the specific soft tissue samples (table 1c) in the centrifuge tubes were repeated after 5 months.
- II. **MRI measurements:** Quantitative T_1 - and T_2 measurements were carried out at (i) a clinical 0.35 T MR-Linac (MRIdian Linac, Viewray Inc., Oakwood, USA), (ii) a diagnostic 1.5 T (Magnetom Aera) and (iii) a diagnostic 3 T MRI (Magnetom Prisma^{fit}) (Siemens Healthineers, Erlangen, Germany). For (i), a surface flex coil with 12 channels was used whereas measurements for (ii) and (iii) were carried out with a 20- and 64-channel head/neck coil, respectively. For quantitative T_1 measurement, a saturation recovery sequence was applied using at least 32 inversion times. For T_2 measurement, either a set of 5 turbo-spin echo sequences with 3 equidistant echoes for (i) or a multi-spin echo sequence with 32 equidistant echoes (ii and iii) was used. To keep the temperature constant within ± 0.5 °C during MRI acquisitions for (ii) and (iii), the samples were put into a water-flow phantom with $T = 20.0$ °C (Mann et al. 2017). At 0.35 T, samples were measured at room temperature of $T = 20.8$ °C, since sample temperature is not expected to rise significantly during measurements at such a low field strength. To investigate the long-term stability of the developed materials T_1 and T_2 of the specific soft tissue samples (table 1c) were re-acquired at 1.5 T after 5 months.
- III. **SPR measurements:** Ion ranges, defined as the 80 % isodose at the distal fall-off of the Bragg-peak, were measured at the Heidelberg Ion Beam Therapy Center (HIT, Germany) using a 200.28 MeV/u carbon (^{12}C) ion pencil beam with a nominal full width at half maximum (FWHM) of 5.1 mm. For this, the PeakFinder (PTW, Freiburg, Germany) was employed with a step size of 0.1 mm as described previously (Möhler et al. 2018). For this, the cubic subvolumes of the 3D printed containers used were filled with the 9 specific soft tissue samples, three additional subvolumes were water-filled and two remained air-filled. The experimental SPR was then calculated from the measured ranges for each sample according to

$$SPR = \frac{r_a - r_s}{r_a - r_w}, \quad (1)$$

with the indices a, w, and s referring to air, water and the sample, respectively.

2.3 Evaluation

SECT values were evaluated as the mean of a circular region of interest (ROI) placed to the center of the sample using the image processing platform MITK (Nolden et al. 2013). The respective stopping power ratios (SPR^{SECT}) were then determined from the Hounsfield look-up table (HLUT, (Schneider, Pedroni, and Lomax 1996)) clinically implemented at HIT. DECT images were evaluated in the image processing software syngo.via (Siemens Healthineers, Erlangen, Germany) and $\hat{\rho}_e$ and Z_{eff} were calculated using the syngo.CT DE Rho/Z application (Hünemohr et al. 2014) based on a circular ROI at the center of the sample. The stopping power was then determined according to the parametrization given in (Hünemohr et al. 2014):

$$SPR_{DECT} = \hat{\rho}_e \frac{12.77 - (a \cdot Z_{eff} + b)}{8.45}, \quad (2)$$

With

$$\begin{aligned} a &= 0.125, b = 3.378 \text{ for } Z_{eff} \leq 8.5 \\ a &= 0.098, b = 3.376 \text{ for } Z_{eff} > 8.5. \end{aligned} \quad (3)$$

MR data was processed using an in-house developed Matlab (The Mathworks Inc., Natick, USA) evaluation tool (Mann et al. 2017) and mono-exponential fits performed to determine T_1 and T_2 , respectively.

For the MR contrast calibration, a multi-linear regression (MLR) using the linear least square method was performed to describe the measured T_1 , T_2 and CT values as a function of the material concentrations listed in Tab. 1a:

$$x = a_x + b_x[Ag] + c_x[Ni], \quad (4)$$

with x standing for $\frac{1}{T_1}$ or $\frac{1}{T_2}$ or CT value, a_x , b_x , and c_x being the fit parameters that depend on the magnetic field strength B_0 , respectively, and with the concentrations of agarose $[Ag]$ in mass percent (%) relative to water and Ni-DTPA $[Ni]$ in mM relative to the agarose solution. It needs to be kept in mind that for this calibration method CT values refer to the intrinsic attenuation of the contrast materials as no KCl was added. In the same way, a multi-linear system may be used to describe the concentrations $[Ag]$ and $[Ni]$ as a function of T_1 and T_2 :

$$y_{B_0} = e_y + f_y \frac{1}{T_1} + g_y \frac{1}{T_2}, \quad (5)$$

with y_{B_0} standing for $[Ag]$ or $[Ni]$ and the fit parameters e_y , f_y and g_y depending on B_0 . Repeating this for all three field strengths B_0 . In total, this leads to 7 equations predicting the contrast parameters (T_1 and T_2 for 0.35 T, 1.5 T and 3.0 T plus the CT contrast, Eq. 4) and 6 equations for the determination of the concentrations ($[Ag]$ and $[Ni]$ at 0.35 T, 1.5 T and 3.0 T, Eq. 5).

For the combined MR/CT contrast calibration, the above method was extended by the adding KCl to modify the CT value of the contrast materials. Using the samples listed in Tab. 1a and 1b together, the parameters a_x , b_x , c_x and d_x of the linear system of equations were fitted:

$$x = a_x + b_x[Ag] + c_x[Ni] + d_x[KCl], \quad (6)$$

again, with x standing for $\frac{1}{T_1}$, $\frac{1}{T_2}$ or the CT value. Eq. 6 additionally includes the concentration of KCl, $[KCl]$, in mass permille (‰) being added to the agarose/Ni-DTPA-solution. In the same way as for the MR contrast calibration, equations for $[Ag]$, $[Ni]$ and $[KCl]$ were derived as a function of the measured T_1 , T_2 and CT values:

$$y_{B_0} = e_y + f_y \frac{1}{T_1} + g_y \frac{1}{T_2} + h_y CT, \quad (7)$$

with y_{B_0} standing for $[Ag]$, $[Ni]$ or $[KCl]$ and the additional fit parameter h . Repeating this fitting procedure for all three field strengths B_0 . In total, this leads to 7 equations predicting the contrast parameters (T_1 and T_2 at 0.35 T, 1.5 T and 3.0 T plus the CT contrast, Eq. 6) and 9 equations for the determination of the concentrations ($[Ag]$, $[Ni]$ and $[KCl]$ at 0.35 T, 1.5 T and 3.0 T, Eq. 7).

3. Results

3.1 MR contrast calibration

Measured T_1 , T_2 and CT values of the MR contrast calibration samples in Tab. 1a are listed in Tab. 2a. T_1 values cover a range of 226 ms – 1665 ms (331 ms – 1769 ms, 165 ms – 1868 ms) and T_2 values from 27 ms – 239 ms (29 ms – 283 ms, 30 ms – 241 ms) at 1.5 T (0.35 T, 3 T). Without modifying the CT value by adding KCl, CT values in the range of (8 – 74) HU were found. The resulting fit parameters of Eq. 4 and 5 are listed in Tab. 3a. A software tool to convert T_1 - and T_2 - values into agarose and Ni-DTPA concentrations and vice versa is provided via this link: <http://suppl.dkfz.de/AE/ParameterCalculation.7z>.

Tab. 2. Measurement results of contrast calibration. T_1 and T_2 times are given in *ms*, CT values in Hounsfield units (*HU*).

a) MR contrast calibration		$AgNi-1$	$AgNi-2$	$AgNi-3$	$AgNi-4$	$AgNi-5$	$AgNi-6$	$AgNi-7$	$AgNi-8$	$AgNi-9$	$AgNi-10$	$AgNi-11$	$AgNi-12$	$AgNi-13$	$AgNi-14$
0.35 T	T_1	1769 ± 9	1519 ± 8	1359 ± 4	909 ± 4	1066 ± 3	989 ± 5	1073 ± 6	1059 ± 8	735 ± 4	567 ± 2	553 ± 2	418 ± 2	331 ± 2	363 ± 1
	T_2	155 ± 5	86 ± 2	104 ± 2	33 ± 2	58 ± 2	79 ± 3	136 ± 3	283 ± 7	47 ± 2	40 ± 2	140 ± 8	46 ± 2	29 ± 2	188 ± 4
1.5 T	T_1	1665 ± 5	1566 ± 4	1197 ± 2	850 ± 2	900 ± 2	780 ± 2	821 ± 2	765 ± 8	672 ± 1	485 ± 1	414 ± 2	317 ± 1	226 ± 1	253 ± 4
	T_2	151 ± 4	81 ± 1	101 ± 2	32 ± 1	54 ± 1	76 ± 2	130 ± 3	239 ± 6	45 ± 1	39 ± 1	119 ± 3	43 ± 1	27 ± 1	143 ± 3
3 T	T_1	1868 ± 20	1734 ± 9	1241 ± 7	844 ± 1	877 ± 2	734 ± 2	761 ± 4	691 ± 7	591 ± 1	392 ± 1	329 ± 2	254 ± 1	165 ± 1	216 ± 2
	T_2	163 ± 4	88 ± 1	106 ± 1	35 ± 1	59 ± 1	80 ± 1	135 ± 2	241 ± 2	49 ± 1	42 ± 1	119 ± 3	45 ± 1	30 ± 1	128 ± 1
CT value		8 ± 3	11 ± 3	13 ± 3	24 ± 3	19 ± 3	20 ± 3	17 ± 3	18 ± 3	25 ± 3	36 ± 4	36 ± 4	50 ± 3	74 ± 3	59 ± 3
b) MR/CT contrast calibration															
0.35 T	T_1	KCl-1	KCl-2	KCl-3	KCl-4	KCl-5	KCl-6	KCl-7	KCl-8	KCl-9	KCl-10	KCl-11	KCl-12		
	T_2	1210 ± 7	1031 ± 6	1421 ± 7	1305 ± 8	575 ± 4	836 ± 4	722 ± 5	733 ± 4	1007 ± 7	1108 ± 4	1155 ± 4	887 ± 3		
1.5 T	T_1	145 ± 7	42 ± 2	64 ± 2	219 ± 7	75 ± 5	50 ± 2	32 ± 2	100 ± 5	39 ± 2	119 ± 4	45 ± 1	140 ± 5		
	T_2	975 ± 3	1031 ± 4	1581 ± 2	998 ± 3	420 ± 1	812 ± 1	656 ± 1	523 ± 1	1066 ± 3	984 ± 3	1097 ± 4	703 ± 2		
3 T	T_1	159 ± 4	40 ± 1	63 ± 1	266 ± 9	67 ± 1	46 ± 1	30 ± 2	93 ± 2	37 ± 1	110 ± 2	46 ± 1	128 ± 3		
	T_2	1066 ± 11	1106 ± 5	1460 ± 4	978 ± 8	375 ± 3	723 ± 2	589 ± 1	502 ± 2	1161 ± 6	958 ± 5	1210 ± 7	646 ± 4		
CT value		172 ± 4	45 ± 1	69 ± 1	270 ± 9	71 ± 1	52 ± 1	34 ± 2	98 ± 2	43 ± 1	118 ± 2	51 ± 1	133 ± 3		
0.35 T	T_1	KCl-13	KCl-14	KCl-15	KCl-16	KCl-17	KCl-18	KCl-19	KCl-20	KCl-21	KCl-22				
	T_2	707 ± 4	1179 ± 6	1221 ± 6	1106 ± 5	1324 ± 7	1480 ± 8	1393 ± 7	877 ± 4	769 ± 5	1453 ± 14				
1.5 T	T_1	61 ± 3	168 ± 9	39 ± 2	311 ± 13	88 ± 4	170 ± 5	53 ± 2	59 ± 2	60 ± 3	147 ± 6				
	T_2	629 ± 1	991 ± 3	1332 ± 6	876 ± 4	1302 ± 3	1313 ± 4	1552 ± 4	828 ± 2	699 ± 2	1242 ± 4				
3 T	T_1	57 ± 1	159 ± 3	38 ± 1	296 ± 3	91 ± 2	181 ± 4	53 ± 1	56 ± 1	56 ± 1	185 ± 4				
	T_2	520 ± 1	893 ± 5	1527 ± 6	776 ± 6	1347 ± 10	1156 ± 5	1470 ± 5	638 ± 3	531 ± 4	861 ± 9				
CT value		62 ± 1	166 ± 4	43 ± 1	294 ± 2	96 ± 1	195 ± 4	58 ± 1	62 ± 2	63 ± 2	205 ± 8				
		86 ± 3	71 ± 3	79 ± 5	78 ± 4	84 ± 4	91 ± 4	110 ± 4	170 ± 4	219 ± 4	354 ± 4				

Tab. 3. Resulting fit parameters of Eq. 4-7 based on measured data in Tab. 2 given together with the respective standard error and the adjusted R^2 (R^2_{adj}) value.

a) MR contrast calibration		b) MR/CT contrast calibration									
x	a_x [ms^{-1}] or [HU]	b_x [$\text{ms}^{-1}\%$] ⁻¹ or [HU % ⁻¹]	c_x [$\text{ms}^{-1}\text{mM}^{-1}$] or [HU mM^{-1}]	d_x [$\text{ms}^{-1}\%$] ⁰⁻¹ or [HU % ⁰⁻¹]	R^2_{adj}	y	e_y [%], [mM] or [%ol]	f_y [% ms], [mM ms] or [mM ms]	g_y [% ms], [mM ms] or [mM ms]	h_y [% HU ⁻¹], [mM HU ⁻¹] or [%o HU ⁻¹]	R^2_{adj}
0.35 T	T_1^{-1}	$(331.1 \pm 41.6) \times 10^{-6}$	$(90.5 \pm 14.7) \times 10^{-6}$	$(67.5 \pm 1.9) \times 10^{-6}$	0.991	0.35 T	(0.139 ± 0.069)	(-143.1 ± 43.0)	(149.0 ± 3.5)	0.994	
	T_2^{-1}	$(-529.1 \pm 442.0) \times 10^{-6}$	$(6764.9 \pm 156.1) \times 10^{-6}$	$(64.2 \pm 19.7) \times 10^{-6}$	0.994	1.5 T	(0.120 ± 0.066)	(-134.7 ± 28.3)	(143.3 ± 3.4)	0.994	
1.5 T	T_1^{-1}	$(254.0 \pm 29.0) \times 10^{-6}$	$(80.1 \pm 10.3) \times 10^{-6}$	$(105.6 \pm 1.3) \times 10^{-6}$	0.998	3 T	(-0.011 ± 0.080)	(-126.8 ± 26.6)	(164.3 ± 4.9)	0.990	
	T_2^{-1}	$(-541.7 \pm 434.8) \times 10^{-6}$	$(7009.4 \pm 153.6) \times 10^{-6}$	$(102.1 \pm 19.4) \times 10^{-6}$	0.994	0.35 T	(-4.936 ± 0.64)	(14895.0 ± 396.9)	(-199.8 ± 32.3)	0.992	
3 T	T_1^{-1}	$(-90.4 \pm 108.3) \times 10^{-6}$	$(166.3 \pm 38.2) \times 10^{-6}$	$(141.9 \pm 4.8) \times 10^{-6}$	0.987	1.5 T	(-2.496 ± 0.312)	(9551.4 ± 133.1)	(-106.2 ± 15.7)	0.998	
	T_2^{-1}	$(23.0 \pm 419.6) \times 10^{-6}$	$(6149.5 \pm 148.2) \times 10^{-6}$	$(118.3 \pm 18.7) \times 10^{-6}$	0.993	3 T	(0.649 ± 0.822)	(7071.8 ± 275.0)	(-175.0 ± 50.3)	0.983	
CT value		(0.686 ± 0.466)	(3.180 ± 0.165)	(1.611 ± 0.021)	0.998						
b) MR/CT contrast calibration											
x	a_x [ms^{-1}] or [HU]	b_x [$\text{ms}^{-1}\%$] ⁻¹ or [HU % ⁻¹]	c_x [$\text{ms}^{-1}\text{mM}^{-1}$] or [HU mM^{-1}]	d_x [$\text{ms}^{-1}\%$] ⁰⁻¹ or [HU % ⁰⁻¹]	R^2_{adj}	y	e_y [%], [mM] or [%ol]	f_y [% ms], [mM ms] or [%o ms]	g_y [% ms], [mM ms] or [%o ms]	h_y [% HU ⁻¹], [mM HU ⁻¹] or [%o HU ⁻¹]	R^2_{adj}
0.35 T	T_1^{-1}	(336.4 ± 24.8)	(92.3 ± 8.1)	(66.6 ± 1.3)	0.989	0.35 T	(0.109 ± 0.074)	(-186.6 ± 49.8)	(149.9 ± 3.3)	(2.022 ± 0.411)	0.984
	T_2^{-1}	(-162.2 ± 435.1)	(6645.0 ± 141.7)	(61.9 ± 22.4)	0.985	1.5 T	(0.142 ± 0.074)	(-181.4 ± 34.0)	(141.9 ± 3.3)	(2.426 ± 0.441)	0.982
1.5 T	T_1^{-1}	(286.8 ± 23.8)	(61.0 ± 7.8)	(105.0 ± 1.2)	0.996	3 T	(0.010 ± 0.072)	(-173.4 ± 26.5)	(163.6 ± 3.9)	(2.891 ± 0.455)	0.981
	T_2^{-1}	(-505.8 ± 471.5)	(6951.9 ± 153.6)	(112.8 ± 24.3)	0.984	0.35 T	(-4.989 ± 0.388)	(15084.0 ± 163.3)	(-210.3 ± 17.5)	(-1.17 ± 2.17)	0.990
3 T	T_1^{-1}	(-12.5 ± 71.8)	(106.0 ± 23.4)	(141.6 ± 3.7)	0.978	1.5 T	(-2.794 ± 0.247)	(9559.5 ± 114.0)	(-81.72 ± 10.99)	(0.797 ± 1.476)	0.995
	T_2^{-1}	(0.9 ± 412.9)	(6057.7 ± 134.5)	(131.2 ± 21.3)	0.984	3 T	(0.243 ± 0.529)	(7101.6 ± 193.4)	(-111.2 ± 28.6)	(-9.01 ± 3.32)	0.976
CT value		(6.449 ± 2.205)	(3.310 ± 0.718)	(1.441 ± 0.113)	0.993						

3.2 MR/CT contrast calibration

T_1 , T_2 and CT values measured for the combined MR/CT contrast calibration samples in Tab. 1a and 1b are listed in Tab. 2b. Here, T_1 values range from 420 ms – 1581 ms (575 ms – 1480 ms, 375 ms – 1470ms) and T_2 values from 30 ms – 296 ms (32 ms – 311 ms, 34 ms – 294 ms) at 1.5 T (0.35 T, 3 T). CT values up to (354 ± 4) HU were achieved. The resulting fit parameters of Eq. 6 and 7 are given in Tab. 3b. A software tool to convert T_1 -, T_2 - and CT values into agarose, Ni-DTPA and KCl concentrations and vice versa is provided via this link: <http://suppl.dkfz.de/AE/ParameterCalculation.7z>.

3.3 Specific soft tissues

MRI and CT measurement results of the specific soft tissue samples (Tab. 1c) are listed in Tab. 4 together with predicted values (Eq. 6 and 7). Deviations between predicted and measured contrast parameters averaged over all samples were (1.6 ± 1.4) % for the CT value, (-1.7 ± 3.3) % ((0.3 ± 3.6) %, (1.6 ± 4.6) %) for T_1 and (3.4 ± 1.9) % ((1.7 ± 3.6) %, (3.0 ± 2.1) %) for T_2 , respectively, at 1.5 T (0.35 T, 3.0 T). Fig. 1 visualizes the MRI and CT contrast and the distribution of the contrast parameters T_1 , T_2 and the CT value for 7 representative soft tissue samples. Tab. 5 displays results of the SECT and DECT measurements together with the predicted and measured SPR. While SPR^{SECT} deviates significantly from the experimental SPR by a mean of (-2.3 ± 0.4) %, SPR^{DECT} is in good agreement with the experimental SPR with a mean error of (0.2 ± 0.3) %.

Long-term stability measurements of the specific soft-tissue samples resulted in mean deviations of all samples of (-0.8 ± 1.6) %, (-0.2 ± 1.5) % and (-5.2 ± 1.1) % for the CT value, T_1 and T_2 , were found after 5 months, respectively.

Tab. 4. MRI and CT contrast parameters determined for specific soft tissue samples compared with predicted values. T_1 and T_2 times are given in *ms* and *CT* values in Hounsfield units (*HU*). Predicted values were calculated using Eq. 6 and fit parameters given in Tab. 3b. Differences between measured and predicted values ($\Delta T_1, \Delta T_2, \Delta CT$) are given in per cent (%), respectively.

		<i>Kidney medulla</i>	<i>Kidney cortex</i>	<i>Prostate</i>	<i>Spleen</i>	<i>Grey matter</i>	<i>White matter</i>	<i>Muscle</i>	<i>Liver</i>	<i>Pancreas</i>
6	T_1	1448 ± 8	1121 ± 6	1383 ± 5	1178 ± 5	1051 ± 5	907 ± 6	797 ± 4	764 ± 5	770 ± 4
7	T_1^{pred}	1428 ± 60	1108 ± 36	1372 ± 54	1166 ± 41	1085 ± 34	962 ± 28	846 ± 36	714 ± 20	714 ± 19
8	ΔT_1	1.4	1.4	0.8	1.0	-3.1	-5.7	-5.8	7.0	7.8
9	T_2	85 ± 2	87 ± 3	86 ± 2	82 ± 4	110 ± 5	101 ± 7	30 ± 2	50 ± 3	51 ± 3
10	T_2^{pred}	87 ± 4	90 ± 4	90 ± 4	81 ± 4	104 ± 5	96 ± 5	28 ± 1	49 ± 2	49 ± 2
11	ΔT_2	-2.3	-3.3	-4.4	1.1	5.8	5.2	7.1	2.0	4.1
12	T_1	1373 ± 3	916 ± 3	1243 ± 3	1004 ± 3	882 ± 2	801 ± 2	857 ± 2	609 ± 1	598 ± 1
13	T_1^{pred}	1412 ± 56	965 ± 26	1314 ± 48	1056 ± 32	920 ± 23	790 ± 18	853 ± 35	586 ± 13	584 ± 12
14	ΔT_1	-2.8	-5.1	-5.4	-4.9	-4.1	1.4	0.5	3.9	2.4
15	T_2	87 ± 2	88 ± 1	91 ± 2	83 ± 1	107 ± 2	97 ± 2	29 ± 3	47 ± 1	46 ± 1
16	T_2^{pred}	85 ± 4	87 ± 4	88 ± 4	79 ± 4	100 ± 5	91 ± 5	27 ± 1	46 ± 2	46 ± 2
17	ΔT_2	2.4	1.1	3.4	5.1	7.0	6.6	7.4	2.2	0.0
18	T_1	1634 ± 16	927 ± 5	1458 ± 13	993 ± 8	869 ± 5	705 ± 5	907 ± 3	532 ± 2	507 ± 1
19	T_1^{pred}	1580 ± 211	957 ± 75	1450 ± 176	1033 ± 94	888 ± 66	737 ± 47	758 ± 83	501 ± 28	505 ± 28
20	ΔT_1	3.4	-1.1	0.6	-3.9	-2.1	-4.3	19.7	6.2	0.4
21	T_2	97 ± 2	94 ± 1	99 ± 2	89 ± 1	112 ± 2	104 ± 2	33 ± 2	51 ± 1	51 ± 1
22	T_2^{pred}	93 ± 6	94 ± 6	95 ± 6	86 ± 5	107 ± 7	98 ± 6	31 ± 1	51 ± 2	51 ± 2
23	ΔT_2	4.3	0.0	4.2	3.5	4.7	6.1	6.5	0.0	0.0
24	CT	44 ± 4	44 ± 3	34 ± 4	55 ± 3	41 ± 4	35 ± 4	44 ± 3	50 ± 4	32 ± 3
25	CT^{pred}	43 ± 3	43 ± 3	34 ± 3	54 ± 3	40 ± 3	34 ± 3	42 ± 4	50 ± 3	33 ± 3
26	ΔCT	2.3	2.3	0.0	1.9	2.5	2.9	4.8	0.0	-3.0
27										
28										
29										
30										
31										
32										
33										
34										
35										
36										
37										
38										
39										
40										
41										
42										
43										
44										
45										
46										

Tab. 5. Measurement results for SPR comparison of specific soft tissue samples. Single-energy CT-values (CT) in HU , electron densities relative to water ($\hat{\rho}_e$), effective atomic numbers (Z_{eff}) and carbon ion ranges (r_s) in mm were measured for cubic 3D printed containers using the Peak-Finder system (Möhler et al. 2018). Predicted stopping power ratios using SECT (SPR^{SECT}) and DECT (SPR^{DECT}) are given as well as the experimental stopping power ratio (SPR) calculated using Eq. 1 and mean ion ranges in water $r_w = (66.22 \pm 0.04) mm$ ($N_w = 9$) and air $r_a = (84.00 \pm 0.01) mm$ ($N_a = 6$). Values are given as mean \pm standard deviation over N samples produced. Note: The muscle tissue samples was excluded from ion range measurements and SPR predictions due to air bubbles in the sample.

Tissue (N)	CT	$\hat{\rho}_e$	Z_{eff}	r_s	SPR^{SECT}	SPR^{DECT}	SPR
Kidney medulla (2)	47.3 ± 0.9	1.0293 ± 0.0009	8.03 ± 0.02	65.86 ± 0.00	1.0449 ± 0.0008	1.0221 ± 0.0008	1.0203 ± 0.0000
Kidney cortex (2)	47.5 ± 0.4	1.0252 ± 0.0002	8.02 ± 0.03	65.86 ± 0.03	1.0451 ± 0.0005	1.0182 ± 0.0000	1.0203 ± 0.0017
Prostate (3)	37.7 ± 2.2	1.0243 ± 0.0013	7.81 ± 0.03	65.91 ± 0.01	1.0358 ± 0.0020	1.0205 ± 0.0016	1.0174 ± 0.0004
Spleen (3)	59.7 ± 1.1	1.0283 ± 0.0015	8.17 ± 0.04	65.83 ± 0.03	1.0567 ± 0.0010	1.0191 ± 0.0022	1.0221 ± 0.0018
Grey matter (3)	43.5 ± 0.6	1.0248 ± 0.0013	8.00 ± 0.01	65.90 ± 0.02	1.0413 ± 0.0006	1.0181 ± 0.0013	1.0182 ± 0.0010
White matter (2)	37.5 ± 1.5	1.0237 ± 0.0008	7.84 ± 0.01	65.95 ± 0.01	1.0356 ± 0.0014	1.0194 ± 0.0006	1.0155 ± 0.0003
Liver (2)	55.2 ± 1.4	1.0313 ± 0.0015	8.02 ± 0.03	65.86 ± 0.08	1.0524 ± 0.0014	1.0242 ± 0.0019	1.0205 ± 0.0042
Pancreas (2)	33.5 ± 0.7	1.0256 ± 0.0009	7.63 ± 0.03	65.95 ± 0.07	1.0318 ± 0.0007	1.0246 ± 0.0005	1.0155 ± 0.0037

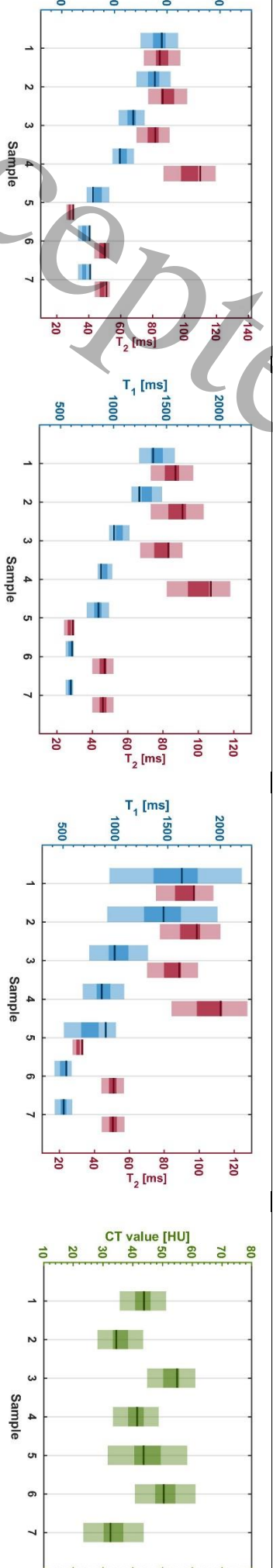
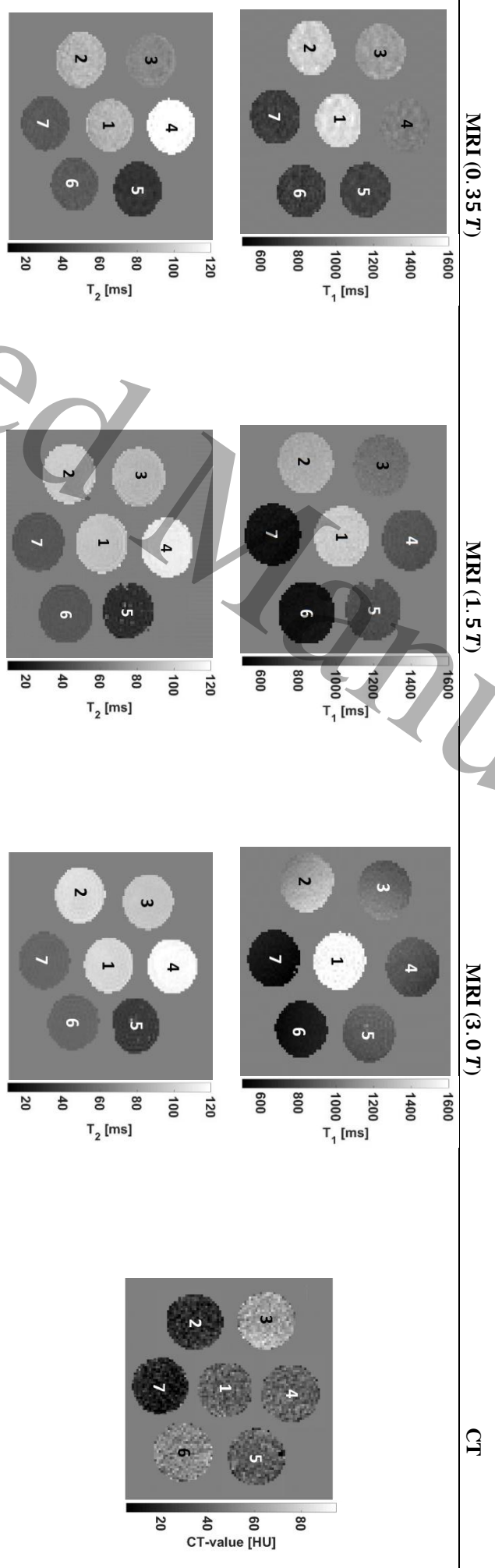


Fig. 1. Visualization of MR and CT contrast parameters of seven representative soft tissue samples (1: Kidney medulla, 2: Prostate, 3: Spleen, 4: Grey matter, 5: Muscle, 6: Liver, 7: Pancreas) as grey value maps (top) and bar plots (bottom) showing the 3σ range of predicted T_1 (T_2 , CT) values in light blue (red, green), the 1σ range in darker blue (red, green) and the experimentally measured value as a solid line.

4. Discussion

In this study, radiologically soft tissue equivalent phantom materials with individually adjusted CT values as well as T_1 and T_2 relaxation times were developed for three different MRI scanners with varying field strength (0.35, 1.5 and 3 T) using Ni-DTPA- and KCl-doped agarose gels.

A similar study using different materials has been published just recently (Singhrao et al. 2020a). Singhrao et al. used carrageenan-based phantom materials doped with a gadolinium-based MRI contrast agent (Gadofosveset), agarose, glass microspheres and calcium carbonate. The fitting procedure to determine CT -, T_1 - and T_2 values was similar as in our study and was also validated by specific tissue samples. However, although the MR contrast properties of the carrageenan-based materials were later quantified at three different field strengths (Singhrao et al. 2020b), an adjustment can only be performed at 3.0 T, where the calibration was performed. In our study, the calibration was performed at all three field strengths and individual fit models were calculated.

A first calibration of T_1 and T_2 values was performed based on agarose and Ni-DTPA concentrations without the addition of KCl. Here, the CT value is dependent on the agarose and Ni-DTPA concentrations needed for a specific T_1 and T_2 , and cannot be adjusted independently. Hence, a second calibration was performed with KCl being added to the samples to additionally adjust also the CT values. This led to a final set of equations describing T_1 , T_2 and CT values as a function of the agarose, Ni-DTPA and KCl concentration as well as equations describing the concentrations as a function of T_1 , T_2 and CT values. The fit parameters (table 4) of these functions represent the influence of the three ingredients on the respective imaging parameter. The latter equations were then used to determine the concentrations of agarose, Ni-DTPA and KCl for a set of specific soft tissue samples, using literature values of T_1 , T_2 and CT at 1.5 T (de Bazelaire et al. 2004; Bottomley et al. 1984; Schneider et al. 2000). These samples were then produced and measured with MRI as well as with CT. The resulting T_1 , T_2 and CT values were validated against the predictions of the derived equations. In addition, ion range measurements were performed to compare experimental SPR with predictions based on SECT and DECT. It has to be noted that since the MR-contrast of the specific tissue samples were optimized based on T_1 - and T_2 -values in the literature determined at 1.5 T, they provide true tissue-equivalent MR-contrast only for this magnetic field strength. Nevertheless, employing the specific T_1 - and T_2 -values for 1.5 T for all three magnetic field strengths allowed validating the consistency of predicted and measured contrast parameters, which might be compromised by fit uncertainties or problems in the specific tissue sample production or by uncertainties in the experimental determination of their contrast parameters.

The calibration of Ni-DTPA doped agarose gels provides an improvement of a previously published method (Tofts et al. 1993) using a simultaneous two-dimensional MLR instead of two separate one-dimensional linear regressions with one concentration being fixed in each fit. This approach then was extended to a three-dimensional MLR for the final calibration of agarose, Ni-DTPA, and KCl concentrations as a function of T_1 , T_2 and CT value. The calibration approach presented could also be applied using different materials changing T_1 , T_2 and the CT value, respectively. However, the adjustment of T_1 and T_2 values is limited to the range of data used in the calibration to assure calculated agarose and Ni-DTPA concentrations are positive. Since some MLR parameters were found to be negative, the insertion of values beyond the employed range could therefore lead to unphysical negative concentrations. For a wide applicability, contrast parameters from the literature of the most important soft tissues were included in the contrast calibration procedure. A limitation, however, is that a high concentration of agarose, such as for muscle ($[Ag] = 5.29\%$, $T_2 < 35\text{ ms}$) leads to a high viscosity of the gels and subsequently to problems in gel production and container filling. In addition, the range of achievable CT values is limited by the maximum solubility of KCl in water and the CT value of the employed agarose/Ni-DTPA mixture. In this study, CT values up to $(354 \pm 4)\text{ HU}$ were achieved, which is well covering literature values of soft tissues having positive CT values. For a simulation of bony structures with higher CT values, materials based on dipotassium phosphate (K_2HPO_4) and gypsum as described in (Niebuhr et al. 2016) may be used. The limitation with respect to higher CT values results from the water base of the gels. To simulate fatty tissues that typically have slightly negative CT values, various fatty materials such as Vaseline or oils are recommended, as shown previously in (Niebuhr et al. 2016).

Finally, for a lung equivalent material, petroleum jelly and Styrofoam based materials may be used as demonstrated in (Steinmann et al. 2018).

All measured T_1 , T_2 and CT values of the specific soft tissue samples (table 4) do not differ significantly from the values predicted by Eq. 6 and 7 using the fit parameters given in Tab. 3b. This demonstrates the consistency of the established contrast model with the contrasts of the specific soft tissue samples, which includes the technical reproducibility of production, imaging uncertainties and the uncertainties in the fit. Remaining deviations between measured and predicted values are within uncertainties resulting from the production and may be explained by small variations in agarose, Ni-DTPA and KCl concentrations as well as by uncertainties in the experimental determination of T_1 , T_2 and CT value. However, T_2 values at 1.5 and 3.0 T were constantly a few ms higher than predicted (mean: $+2.7 ms$ ($+2.6 ms$) at 1.5 T (3.0 T)). This systematic offset is most likely not only related to above-mentioned uncertainties, but may also be caused by small temperature variations between the measurement of the tissue and calibration samples, which may occur in spite of using the water flow phantom. In (Tofts et al. 1993), a T_2 temperature dependence of approximately $-1.4 \frac{\%}{^\circ C}$ was found for Ni-DTPA doped agarose gels of different concentrations, which would indicate an $\sim 2^\circ C$ lower temperature in the measurement of the soft tissue samples than in the calibration vessels. However, regarding the measures taken for temperature stability during MRI measurements, this appears rather unlikely and we therefore assume an increased temperature dependence of our gels due to the additional substitution of KCl. Although systematic, the deviations are still in the order of only a single standard deviation of the predicted T_2 values at 1.5 T and 3.0 T , respectively, and are therefore considered as not being significant.

Measurements of CT -values and T_1 and T_2 relaxation times at 1.5 T of the specific soft tissue samples after 5 months confirmed a long-term stability of the produced gels within a well acceptable range with a mean deviation of $(-0.8 \pm 1.6) \%$, $(-0.2 \pm 1.5) \%$ and $(-5.2 \pm 1.1) \%$ with respect to the first measurements of the CT -value, T_1 and T_2 , respectively. Slightly larger deviations in T_2 result most likely from small temperature deviations between the measurements. In this study, only small gel volumes (up to 50 ml) were used. However, the increased conductivity of the gels due to the use of Ni-DTPA and KCl could lead to image artifacts caused by standing waves in the MRI, if larger gel volumes are used (Erturk et al. 2009). The presence of Nickel ($Z = 28$) presumably also causes the deviation of SPR values between measurement and prediction when using SECT (mean $(-2.3 \pm 0.4) \%$). This deviation results from a wrong translation of CT values to SPR using a HLU that was calibrated for materials with atomic numbers < 20 . Such deviations were found earlier for iodine ($Z = 53$) containing contrast agents resulting in range errors of up to 2.5 % (Wertz and Jäkel 2004). In our study significant range deviations up to -3.3% (spleen sample) were found, whereas the higher value as compared to (Wertz and Jäkel 2004) might result from a higher Nickel concentration within the gels. Using DECT instead of SECT, deviations could be reduced to a mean error of $(0.2 \pm 0.3) \%$. With DECT, even more accurate predictions could be achieved using more complex evaluation methods, i.e. as described in (Möhler et al. 2016). The SPR prediction method used in our study (Hünemohr et al. 2014) was chosen for simplicity and technical availability. As the resulting range uncertainties are in the same order as the typical range uncertainties in ion beam RT of 2 to 3 % (Paganetti 2012), this demonstrates that the developed specific soft-tissue materials may also be employed in ion beam RT. In principle, similar effects may also occur in photon therapy due to different photon energies used in CT imaging and treatment delivery. To assure an accurate dose calculation for the developed materials, determination of correction factors might be necessary to perform full dosimetric end-to-end tests.

5. Conclusion

In this study, we presented anthropomorphic phantom materials with independently adjusted contrasts in CT and MRI. To our knowledge, this is the first method that allows adjusting independently CT values as well as T_1 and T_2 relaxation times at different relevant magnetic field strengths. After production, the specific soft tissue samples showed very good agreement with the predicted CT values as well as with T_1 and T_2 with mean deviations of less than 3.5 %. Finally, it has been shown that SECT-based SPR prediction overestimates measured SPRs by a mean of $(2.3 \pm 0.4) \%$, whereas a DECT-based prediction agrees well with the measurement with a mean deviation of $(0.2 \pm 0.3) \%$.

Acknowledgements

The authors acknowledge the German Research Council (DFG) for funding the MR-Linac device (grant no. DE 614/16-1). Furthermore, the project received financial support by the Federal Ministry of Education and Research (BMBF, ARTEMIS-project WP6, funding reference 13GW0436B).

References

- de Bazelaire, Cedric M. J., Guillaume D. Duhamel, Neil M. Rofsky, and David C. Alsop. 2004. "MR Imaging Relaxation Times of Abdominal and Pelvic Tissues Measured in Vivo at 3.0 T: Preliminary Results." *Radiology* 230(3):652–59.
- Bottomley, P. A., T. H. Foster, R. E. Argersinger, and L. M. Pfeifer. 1984. "A Review of Normal Tissue Hydrogen NMR Relaxation Times and Relaxation Mechanisms from 1-100 MHz: Dependence on Tissue Type, NMR Frequency, Temperature, Species, Excision, and Age." *Medical Physics* 11(4):425–48.
- Erturk, Sukru Mehmet, Angel Alberich-Bayarri, Karin A. Herrmann, Luis Marti-Bonmati, and Pablo R. Ros. 2009. "Use of 3.0-T MR Imaging for Evaluation of the Abdomen." *RadioGraphics* 29(6):1547–63.
- Hattori, Kengo, Yusuke Ikemoto, Wataru Takao, Seiichiro Ohno, Takashi Harimoto, Susumu Kanazawa, Masataka Oita, Koichi Shibuya, Masahiro Kuroda, and Hirokazu Kato. 2013. "Development of MRI Phantom Equivalent to Human Tissues for 3.0-T MRI." *Medical Physics* 40(3):32303.
- Hoffmann, Aswin, Bradley Oborn, Maryam Moteabbed, Susu Yan, Thomas Bortfeld, Antje Knopf, Herman Fuchs, Dietmar Georg, Joao Seco, Maria Francesca Spadea, Oliver Jäkel, Christopher Kurz, and Katia Parodi. 2020. "MR-Guided Proton Therapy: A Review and a Preview." *Radiation Oncology* 15(1):129.
- Hünemohr, Nora, Bernhard Krauss, Christoph Tremmel, Benjamin Ackermann, Oliver Jäkel, and Steffen Greilich. 2014. "Experimental Verification of Ion Stopping Power Prediction from Dual Energy CT Data in Tissue Surrogates." *Physics in Medicine and Biology* 59(1):83–96.
- Kim, Min-Joo, Seu-Ran Lee, Kyu-Ho Song, Hyeon-Man Baek, Bo-Young Choe, and Tae Suk Suh. 2020. "Development of a Hybrid Magnetic Resonance/Computed Tomography-Compatible Phantom for Magnetic Resonance Guided Radiotherapy." *Journal of Radiation Research* 61(2):314–24.
- Mann, P., M. Witte, T. Moser, C. Lang, A. Runz, W. Johnen, M. Berger, J. Biederer, and C. P. Karger. 2017. "3D Dosimetric Validation of Motion Compensation Concepts in Radiotherapy Using an Anthropomorphic Dynamic Lung Phantom." *Physics in Medicine and Biology* 62(2):573–95.
- Möhler, Christian, Tom Russ, Patrick Wohlfahrt, Alina Elter, Armin Runz, Christian Richter, and Steffen Greilich. 2018. "Experimental Verification of Stopping-Power Prediction from Single- and Dual-Energy Computed Tomography in Biological Tissues." *Physics in Medicine & Biology* 63(2):025001.
- Möhler, Christian, Patrick Wohlfahrt, Christian Richter, and Steffen Greilich. 2016. "Range Prediction for Tissue Mixtures Based on Dual-Energy CT." *Physics in Medicine and Biology* 61(11):N268-75.
- Niebuhr, N. I., W. Johnen, T. Guldaglar, A. Runz, G. Echner, P. Mann, C. Mohler, A. Pfaffenberger, O. Jakel, and S. Greilich. 2016. "Technical Note: Radiological Properties of Tissue Surrogates Used in a Multimodality Deformable Pelvic Phantom for MR-Guided Radiotherapy." *Medical Physics* 43(2):908–16.
- Nolden, M., S. Zelzer, A. Seitel, D. Wald, M. Müller, A. M. Franz, Daniel Maleike, Markus Fangerau, Matthias Baumhauer, Lena Maier-Hein, Klaus H. Maier-Hein, Hans-Peter Meinzer, and Ivo Wolf. 2013. "The Medical Imaging Interaction Toolkit: Challenges and Advances." *International Journal of Computer Assisted Radiology and Surgery* 8(4):607–20.
- Oborn, Bradley M., Stephen Dowdell, Peter E. Metcalfe, Stuart Crozier, Radhe Mohan, and Paul J. Keall. 2017. "Future of Medical Physics: Real-Time MRI-Guided Proton Therapy." *Medical Physics* 44(8):e77–90.

- 1
2
3 Paganelli, C., B. Whelan, M. Peroni, P. Summers, M. Fast, T. van de Lindt, J. McClelland, B. Eiben, P. Keall, T.
4 Lomax, M. Riboldi, and G. Baroni. 2018. "MRI-Guidance for Motion Management in External Beam
5 Radiotherapy: Current Status and Future Challenges." *Physics in Medicine and Biology* 63(22):22TR03.
6
7 Paganetti, Harald. 2012. "Range Uncertainties in Proton Therapy and the Role of Monte Carlo Simulations."
8 *Physics in Medicine and Biology* 57(11):R99–117.
9
10 Raaymakers, B. W., A. J. E. Raaijmakers, and J. J. W. Lagendijk. 2008. "Feasibility of MRI Guided Proton
11 Therapy: Magnetic Field Dose Effects." *Physics in Medicine and Biology* 53(20):5615–22.
12
13 Schneider, Uwe, Eros Pedroni, and Antony Lomax. 1996. "The Calibration of CT Hounsfield Units for
14 Radiotherapy Treatment Planning." *Physics in Medicine and Biology* 41(1):111–24.
15
16 Schneider, W., T. Bortfeld, and W. Schlegel. 2000. "Correlation between CT Numbers and Tissue Parameters
17 Needed for Monte Carlo Simulations of Clinical Dose Distributions." *Physics in Medicine and Biology*
18 45(2):459–78.
19
20 Singhrao, Kamal, Jie Fu, Yu Gao, Holden H. Wu, Yingli Yang, Peng Hu, and John H. Lewis. 2020a. "A
21 Generalized System of Tissue-Mimicking Materials for Computed Tomography and Magnetic Resonance
22 Imaging." *Physics in Medicine and Biology* 65(13):13NT01.
23
24 Singhrao, Kamal, Jie Fu, Holden H. Wu, Peng Hu, Amar U. Kishan, Robert K. Chin, and John H. Lewis. 2020b.
25 "A Novel Anthropomorphic Multimodality Phantom for MRI-Based Radiotherapy Quality Assurance
26 Testing." *Medical Physics* 47(4):1443–51.
27
28 Steinmann, Angela, R. Jason Stafford, Gabriel Sawakuchi, Zhifei Wen, Laurence Court, Clifton D. Fuller, and
29 David Followill. 2018. "Developing and Characterizing MR/CT-Visible Materials Used in QA Phantoms for
30 MRgRT Systems." *Medical Physics* 45(2):773–82.
31
32 Tofts, P. S., B. Shuter, and J. M. Pope. 1993. "Ni-DTPA Doped Agarose Gel--a Phantom Material for Gd-DTPA
33 Enhancement Measurements." *Magnetic Resonance Imaging* 11(1):125–33.
34
35 Wertz, Hansjörg and Oliver Jäkel. 2004. "Influence of Iodine Contrast Agent on the Range of Ion Beams for
36 Radiotherapy." *Medical Physics* 31(4):767–73.
37
38 Yoshimura, Koichi, Hirokazu Kato, Masahiro Kuroda, Atsushi Yoshida, Katsumi Hanamoto, Akio Tanaka,
39 Masatoshi Tsunoda, Susumu Kanazawa, Koichi Shibuya, Shoji Kawasaki, and Yoshio Hiraki. 2003.
40 "Development of a Tissue-Equivalent MRI Phantom Using Carrageenan Gel." *Magnetic Resonance in*
41 *Medicine* 50(5):1011–17.
42
43
44
45
46
47
48
49
50
51
52
53
54
55
56
57
58
59
60

2.4 Publication III

TECHNICAL NOTE: ON THE FEASIBILITY OF PERFORMING DOSIMETRY IN TARGET AND ORGAN AT RISK USING POLYMER DOSIMETRY GEL AND THERMOLUMINESCENCE DETECTORS IN AN ANTHROPOMORPHIC, DEFORMABLE, AND MULTIMODAL PELVIS PHANTOM

Authors: Mathieu Marot, Alina Elter, Philipp Mann, Andrea Schwahofer, Clemens Lang, Wibke Johnen, Stefan A. Körber, Bettina Beuthien-Baumann and Clarissa Gillmann

Status (12/2021): Published

Journal reference: *Medical Physics* (2021) 48:5501– 5510

DOI: 10.1002/mp.15096

Copyright: © 2021 American Association of Physicists in Medicine. Reproduced with permission. All rights reserved.

This paper was published Open Access. The original content of the publication may be used under the terms of a CC BY 4.0 licence (<https://creativecommons.org/licenses/by/4.0/>). No changes have been made.

Contribution: The first author of this publication is Mathieu Marot, who conducted his Master thesis within our department. The work investigates the feasibility to perform polymer gel dosimetry and thermoluminescence detector measurements within an anthropomorphic male pelvis phantom (ADAM-PETer). The work serves as an important preliminary work for subsequent end-to-end tests of MR-guided radiotherapy procedures using the same anthropomorphic phantom and a similar dosimeter setup (publication V). I significantly contributed to this work by being involved in the development of the main project idea, designing the 3D printed and polymer gel-filled prostate target in cooperation with Wibke Johnen and supervising the experimental conduction of the polymer gel dosimetry including the gel production, irradiation and evaluation. Furthermore, I supported Mathieu Marot and Clarissa Gillmann in the writing of the manuscript as well as in revising it according to the reviewer's comments.

Technical Note: On the feasibility of performing dosimetry in target and organ at risk using polymer dosimetry gel and thermoluminescence detectors in an anthropomorphic, deformable, and multimodal pelvis phantom

Mathieu Marot^{1,2,3}  | Alina Elter^{1,3,4}  | Philipp Mann^{1,3,5}  |
 Andrea Schwahofer^{1,3} | Clemens Lang^{1,3} | Wibke Johnen^{1,3} | Stefan A. Körber⁶ |
 Bettina Beuthien-Baumann^{7,8} | Clarissa Gillmann^{1,3,8} 

¹Department of Medical Physics in Radiation Oncology, German Cancer Research Center (DKFZ), Heidelberg, Germany

²Faculty of Medicine, University of Heidelberg, Heidelberg, Germany

³Heidelberg Institute for Radiation Oncology (HIRO), National Center for Radiation Research in Oncology (NCRO), Heidelberg, Germany

⁴Faculty of Physics and Astronomy, University of Heidelberg, Heidelberg, Germany

⁵HQ-Imaging GmbH, Heidelberg, Germany

⁶Department of Radiation Oncology, Heidelberg University Hospital, Heidelberg, Germany

⁷Department of Radiology, German Cancer Research Center (DKFZ), Heidelberg, Germany

⁸National Center for Tumor Diseases (NCT), Heidelberg, Germany

Correspondence

Mathieu Marot, Department of Medical Physics in Radiation Oncology, German Cancer Research Center (DKFZ), Im Neuenheimer Feld 280, 69120 Heidelberg, Germany.
 Email: m.mathieu@dkfz.de

Funding information

National Center for Tumor Diseases (NCT), Grant/Award Number: G886_G986_PoC_PSMA

Abstract

Objective: To assess the feasibility of performing dose measurements in the target (prostate) and an adjacent organ at risk (rectum) using polymer dosimetry gel and thermoluminescence detectors (TLDs) in an anthropomorphic, deformable, and multimodal pelvis phantom (ADAM PETER).

Methods: The 3D printed prostate organ surrogate of the ADAM PETER phantom was filled with polymer dosimetry gel. Nine TLD600 (LiF:Mg,Ti) were installed in 3 × 3 rows on a specifically designed 3D-printed TLD holder. The TLD holder was inserted into the rectum at the level of the prostate and fixed by a partially inflated endorectal balloon. Computed tomography (CT) images were taken and treatment planning was performed. A prescribed dose of 4.5 Gy was delivered to the planning target volume (PTV). The doses measured by the dosimetry gel in the prostate and the TLDs in the rectum (“measured dose”) were compared to the doses calculated by the treatment planning system (“planned dose”) on a voxel-by-voxel basis.

Results: In the prostate organ surrogate, the 3D- γ -index was 97.7% for the 3% dose difference and 3 mm distance to agreement criterium. In the center of the prostate organ surrogate, measured and planned doses showed only minor deviations (<0.1 Gy, corresponding to a percentage error of 2.22%). On the edges of the prostate, slight differences between planned and measured doses were detected with a maximum deviation of 0.24 Gy, corresponding to 5.3% of the prescribed dose. The difference between planned and measured doses in the TLDs was on average 0.08 Gy (range: 0.02–0.21 Gy), corresponding to 1.78% of the prescribed dose (range: 0.44%–4.67%).

This is an open access article under the terms of the Creative Commons Attribution License, which permits use, distribution and reproduction in any medium, provided the original work is properly cited.

© 2021 The Authors. *Medical Physics* published by Wiley Periodicals LLC on behalf of American Association of Physicists in Medicine

Conclusions: The present study demonstrates the feasibility of using polymer dosimetry gel and TLDs for 3D and 1D dose measurements in the prostate and the rectum organ surrogates in an anthropomorphic, deformable and multimodal phantom. The described methodology might offer new perspectives for end-to-end tests in image-guided adaptive radiotherapy workflows.

KEYWORDS

3D dosimetry, anthropomorphic phantom, polymer dosimetry gel, thermoluminescence dosimetry, TLD

1 | INTRODUCTION

In prostate cancer radiotherapy, a highly accurate dose deposition is of utmost importance due to the proximity of the prostate to radiation-sensitive organs at risk (OARs) like rectum and bladder. Image-guided and adaptive radiotherapy workflows using multimodal functional and anatomical imaging are expected to improve the accuracy of dose delivery. In particular, magnetic resonance imaging (MRI) has evolved as a promising technique for image guidance in prostate cancer radiotherapy.^{1,2}

Recent data additionally demonstrate the high potential of prostate-specific membrane antigen ligand positron emission tomography (PSMA-PET) for tumor delineation^{3,4} and detection of frequently occurring metastases in lymph nodes and bones.^{5,6} We therefore expect PSMA-PET imaging to become an increasingly important imaging modality for diagnosis and treatment planning of prostate cancer patients.

The clinical implementation of image-guided adaptive radiotherapy workflows is complex. The treatment planning chain consists of multiple steps including patient positioning, imaging, image co-registration, adaptation, and irradiation. Uncertainties may occur in any of these steps. The accumulation of uncertainties can be measured in workflow specific end-to-end tests. End-to-end tests require appropriate phantoms and the possibility to measure dose distributions from 1D to 3D. Most phantoms currently used in radiotherapy are static and only visible in computed tomography (CT), but not in MRI, nor in PET. Recently, a new multimodal (CT and MRI) phantom capable of simulating inter-fractional motion in a reproducible manner and measuring the dose in 3D, was introduced by Elter et al.⁷

However, coarse phantoms can hardly imitate uncertainties originating from the characteristic features of the human body. In that respect, anthropomorphic phantoms, for example, the ADAM phantom, that we recently introduced, are promising options.⁸ The ADAM phantom is an anthropomorphic, deformable and multimodal phantom of the male pelvis. It has successfully been used for end-to-end tests in MRI-guided radiotherapy⁹ and for an end-to-end empirical validation of dose accumulation in MRI-guided adaptive radiotherapy of prostate cancer.¹⁰

However, the ADAM phantom suffers from a few shortcomings: Since it was manually constructed, the design and shape of the organ surrogates are fixed. The phantom mimics human image contrast in CT and 1.5-T MRI, but an insertion of radioactive tracers for PET imaging is not possible. In addition, dosimetry is limited to 2D film measurements on the surfaces of the bladder and rectum organ surrogates.

To overcome these shortcomings, we recently developed an updated and extended version of ADAM, named ADAM PETER, where PETER stands for positron emission tomography (PET) extension radiotherapy.¹¹ ADAM PETER is completely based on 3D printing techniques allowing to change the design of the phantom into a completely modular structure. The formerly manually manufactured silicone organ surrogates were replaced by 3D printed organ shells that can be easily produced in high numbers for repetitive measurements.¹¹ In a first study, we demonstrated the phantom's suitability as multimodal, anthropomorphic model for CT, 3T MRI, and PET measurements.

In the present work, we present a methodology for how dosimetry can be performed in the new ADAM PETER phantom using polymer dosimetry gel in the prostate and an array of nine thermoluminescence detectors (TLDs) in the rectum. In a second step, we validate the accuracy of our approach by irradiating the phantom and comparing the dose planned by the treatment planning system with the dose measured by the dosimetry gel and the TLDs. Our described approach significantly extends the possibilities of dose measurements compared to the ADAM phantom, where dosimetry was limited to films in distinct pockets on the surfaces of bladder and rectum. We therefore believe that the new phantom and the results of our study might offer novel perspectives for end-to-end tests in image-guided and adaptive radiotherapy.

2 | MATERIALS AND METHODS

2.1 | Phantom specification

The design and construction of the new ADAM PETER phantom are detailed in Gillmann/Homolka et al.¹¹ Therefore, only a brief description is given here.

All parts of the phantom except the bladder are 3D printed. The phantom contains organ models for the prostate, the bladder, the rectum, and the hip bone that were derived from 3D segmentations of a CT scan of a prostate cancer patient. Two intraprostatic lesions, four iliac lymph node metastases and two bone metastases in the pelvis simulate prostate cancer as multifocal and metastatic disease. The flexible rectum traverses the phantom and is accessible from outside. The silicone organ model of the bladder includes imaging marker points. Bladder filling and content can be varied from outside via a syringe. Radiological properties (CT and 3T MRI) of cortical bone, bone marrow, and adipose tissue were simulated by heavy gypsum, a mixture of Vaseline and K_2HPO_4 and peanut oil, respectively. For soft tissues, agarose gels loaded with different concentrations of gadolinium-based contrast agent and sodium fluoride were developed (Table S1 available in the Supplementary Material). Along the outer case of the phantom, pink alignment lines were printed to allow reproducible positioning using the laser systems installed at imaging and radiotherapy units. Three Beekley spots mark the prostate isocenter. A 3D model of the ADAM PETER phantom is shown in Figure 1a.

Note: the original ADAM PETER design of the prostate organ surrogate contained two intraprostatic lesions since it was optimized for PET/MRI measurements. As the focus of the present study lies on dosimetry measurements, we now used a 3D printed prostate organ model without intraprostatic lesions. In that way, the complete volume of the prostate can be filled with dosimetry gel. A 3D model of the prostate organ surrogate is showcased in Figure 1b.

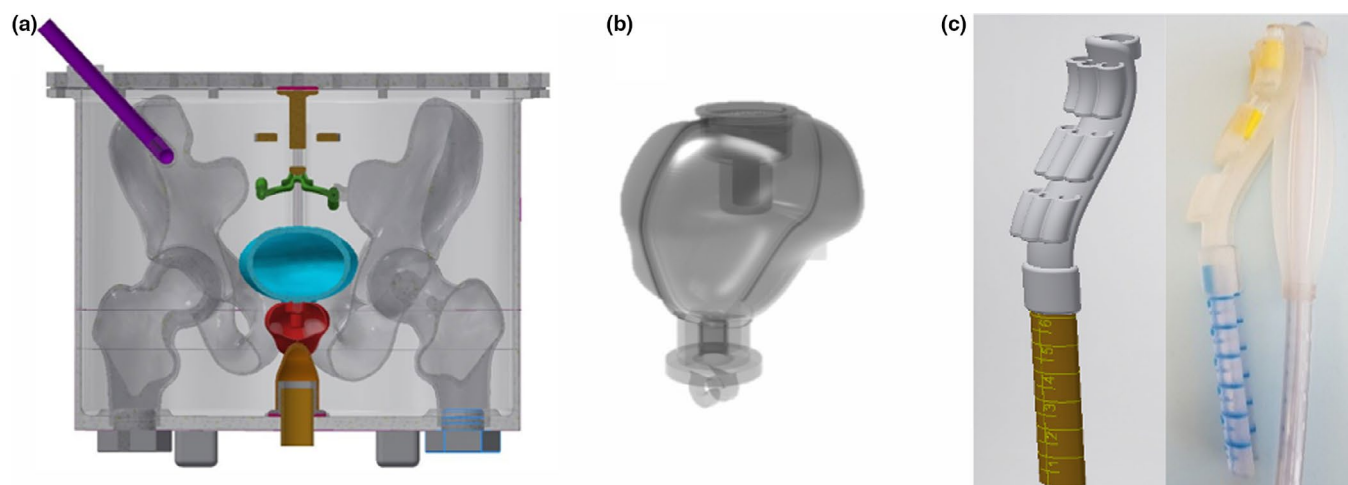


FIGURE 1 (a) 3D coronal cross section of the ADAM PETER phantom with the following organ surrogates highlighted in different colors: prostate (red), bladder (blue), rectum (orange), bone metastasis (purple), and four lymph node metastases (green). Further details on the phantom design and construction can be found in Gillmann/Homolka et al.¹¹ (b) 3D model of the prostate without intraprostatic lesions used in the present study. (c) Specifically designed 3D printed holder for an array of nine TLDs. 3D model (left) and picture of the TLD holder wrapped around the endorectal balloon (right) [Color figure can be viewed at wileyonlinelibrary.com]

2.2 | Dosimetry

For 3D dose measurements in the prostate, polyacrylamide gelatin gel fabricated at atmospheric conditions (PAGAT) was used.¹⁶ The gel contains monomers that polymerize locally depending on the absorbed dose.¹⁷ The degree of polymerization can be quantified as a shortening of T2 relaxation times in MRI.¹⁸ An exponential calibration curve relates the $R2=1/T2$ relaxation rate to a dose value. Polymer dosimetry gels offer a high spatial resolution in the order of millimeters.^{19,20} A study by Elter et al showed that the PAGAT dosimetry gel is compatible with the 3D print material (VeroClear™) used for the ADAM PETER prostate organ surrogate.²¹

In the rectum, 3D dosimetry using polymer dosimetry gel was not possible since the rectum is flexible and open to both sides. In addition, the dosimetry method in the rectum should be compatible with an endorectal balloon, whose use is common practice in prostate cancer radiotherapy. We therefore decided to use an array of TLDs due to the small dimension of the solid crystals. TLDs have proven to be a suitable tool for point-dose measurements and absolute dosimetry, achieving high accuracies with a mean standard deviation of 0.4%.²² The measurement setup is described in the next section.

2.3 | Measurement setup

For measurements, PAGAT dosimetry gel was produced. The process of gel manufacturing is described in detail by Deene et al.¹⁷ The dosimetry gel for the prostate and the calibration vials were prepared in one

single batch, so that any batch-to-batch variations can be ruled out. Prior to irradiation, both, prostate and calibration vials filled with dosimetry gel were stored in the same fridge at +4°C for 24 h. Four hours prior to irradiation, prostate and calibration vials were moved to the irradiation room for thermal stabilization. The phantom was then prepared for irradiation. The PAGAT-filled prostate organ surrogate was screwed onto the bottom of the water-filled bladder. Both organ surrogates were inserted into the phantom and secured in place using a dedicated string system. The remaining volume of the phantom was filled with peanut oil simulating fatty tissue. The irradiation of the calibration vials was performed immediately after phantom irradiation. After irradiation, the prostate and the calibration vials were wrapped in aluminum foil and kept at room temperature for 48 h until MRI acquisition. This workflow is identical to the one described in detail in Mann 2017. The volumes of the prostate (29.5 ml) and the calibration vials (26 ml) are very similar to avoid possible uncertainties due to different gel evaluation sizes.

Dosimetry measurements in the rectum were performed using TLDs. Therefore, nine TLD600 (LiF:Mg, Ti, Harshaw, Thermofisher Scientific, USA) were installed in 3x3 rows on a specifically designed 3D-printed TLD holder (Figure 1 (c-left)). The TLD holder was made of a combination of soft (Agilus30TM) and hard materials (VeroClearTM). The holder was attached to an endorectal balloon (Qfix Systems, MEDRAD PRO-TEKT) and inserted into the rectum at the level of the prostate (Figure 1 (c-right)). TLDs 1–6 were located directly posterior to the prostate while TLDs 7–9 were positioned below the prostate (Figure 2). Slightly blowing up the rectum balloon fixed the TLD holder in place.

2.4 | Imaging, treatment planning, and irradiation

The phantom ready for measurements was placed onto the treatment couch of a 6 MV linear accelerator (linac) (Artiste, Siemens Healthineers, Germany) in supine position. The treatment couch was rotated by 90 degrees and CT images (Figure 3a) were acquired using an in-room CT on rails (SOMATOM Emotion, Siemens

Healthineers, Germany). Treatment planning was performed using the software Raystation8A (Raysearch Laboratories, Stockholm, Sweden). The planning target volume (PTV) was defined as the whole prostate volume plus a 4-mm margin. Seven beams (beam angles: 0°, 50°, 100°, 155°, 205°, 260°, and 310°) were planned to deliver a prescribed dose of 4.5 Gy in one single fraction to the PTV (Figure 3b). The dose value of 4.5 Gy was chosen as polymer dosimetry gel performs best in a dose range of 0–6 Gy.²³ For the rectum, a dose constraint of 3.4 Gy maximum to 5% of the rectum volume was set. Irradiation was performed directly after treatment planning. The treatment couch was rotated back to the Linac and a cone-beam CT (CBCT) was acquired for position verification. For the dose calibration of the polymer dosimetry gel, eight vials of dosimetry gel were irradiated with doses from 0 Gy to 7 Gy in steps of 1 Gy. The vials were placed at 5-cm depth in a poly-methyl-methacrylate (PMMA) phantom, using a source skin distance (SSD) of 100 cm (reference conditions) according to Vening et al.¹⁶

2.5 | Dose evaluation

Two hours prior to MRI, the prostate and the calibration vials were placed into the same water circulation phantom adjusted to 20°C. MRI was performed at a 3T MRI (Prismafit, Siemens Healthineers, Germany). The T2 relaxation time of the gel was measured using a multi spin-echo sequence with 32 equidistant echo times in the range of 22.5 ms to 720 ms with an echo spacing of 22.5 ms and a repetition time of 10 000 ms. The acquisition was done with a 1-mm³ isotropic resolution and a pixel bandwidth of 130 Hz/pixel. Besides, a morphological high-resolution standard true fast imaging sequence with steady state precession (TrueFISP) of the prostate organ model was acquired for later co-registration of the MRI with the treatment planning CT. The MR images were evaluated using an in-house written gel dose evaluation tool based on Matlab code (Mathworks Inc, Natick).²⁴ The data from the eight calibration vials were used to establish a calibration curve between dose and R2-relaxation rate. For each calibration vial, a circular region of interest was defined to

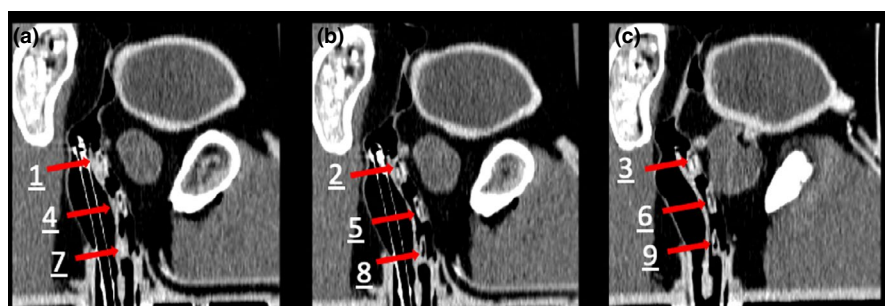


FIGURE 2 Positioning of the TLDs in the rectum visible on three consecutive sagittal slices (a, b, and c, respectively) of the treatment planning CT. The TLDs can be identified by the red arrows and the corresponding number [Color figure can be viewed at wileyonlinelibrary.com]

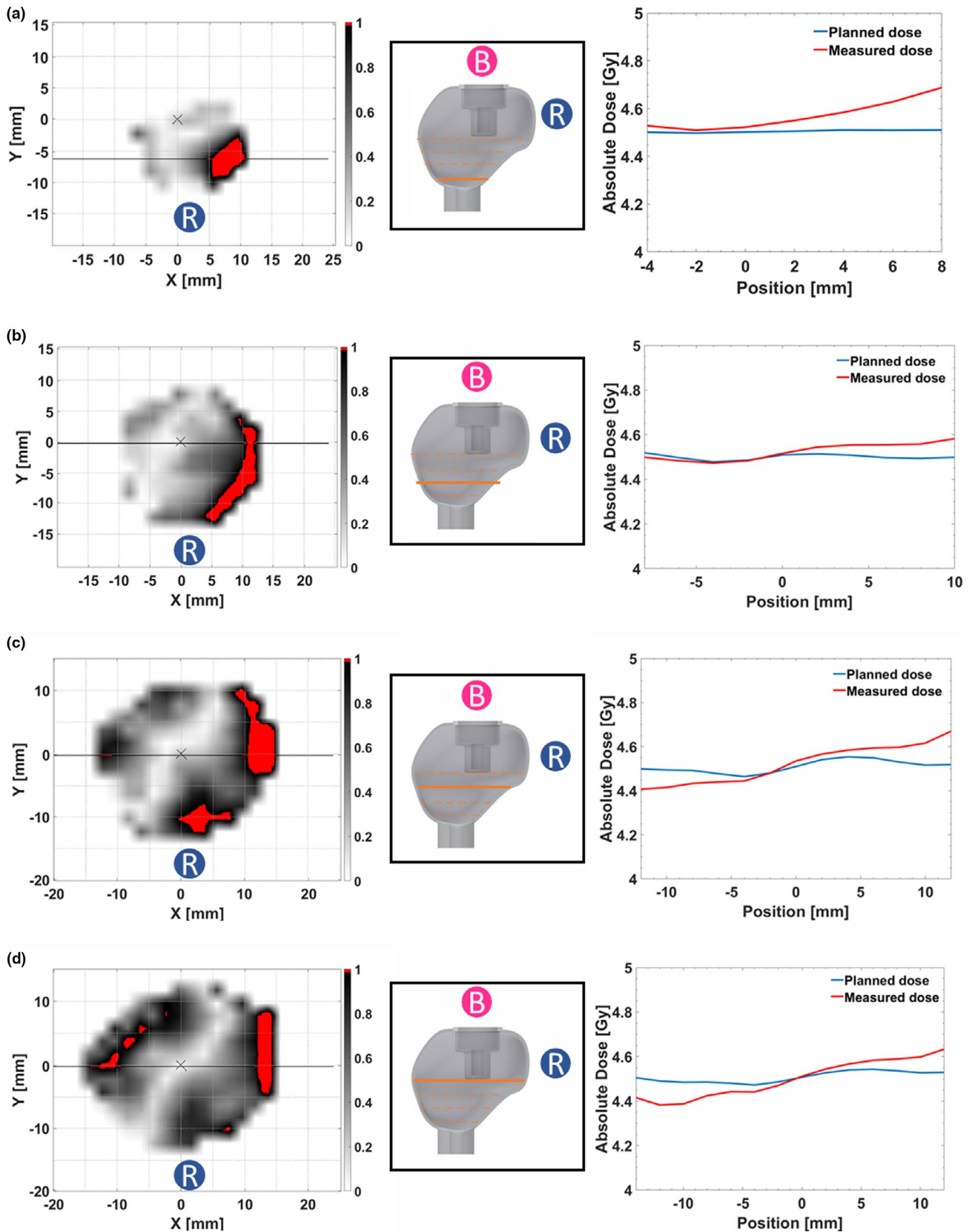


FIGURE 3 γ maps (left column) and left-right dose profiles (right column) at different trans-axial positions of the prostate (indicated by the orange line on the 3D prostate model) from bottom to top. The letters “B” and “R” represent the positions of the bladder and rectum relative to the prostate. The γ map shows the agreement rate between the planned and the measured dose for the 3%/3mm passing criterion. The color map indicates accepted points (white to black) and failed points (red). The black line on the γ maps corresponds to the LR dose profile plotted for each γ map. The dose profile is given as an absolute dose (Gray) as a function of the position (mm) for the planned (blue curve) and the measured dose (red curve) [Color figure can be viewed at wileyonlinelibrary.com]

determine the mean R2 value and the related standard deviation on the different images of the MR-acquisition. Using the eight mean R2-values from the calibration vials, a mono-exponential curve was fitted to obtain the calibration curve. Based on the calibration curve, the measured R2-relaxation rates in the prostate were transformed into a dose map. A detailed description of the gel dose evaluation process is given in Mann et al.²⁴

The TLDs were read-out using a hot gas reader (Harshow 5500, Thermofisher Scientific, USA) on the day of irradiation. The complete process of TLD reading is described in Schwahofer et al.²²

2.6 | Comparison of planned and measured doses

For a voxel-based comparison of planned versus measured doses in the prostate, several steps had to be taken: (1) The high-resolution morphological MR image of the prostate organ surrogate was co-registered with the treatment planning CT using the software Medical Imaging Interaction Toolkit (MITK, DKFZ, Germany).²⁵ (2) The deformation vector field of the co-registration was applied to the T2-relaxation map and hence to the dose map. (3) To decrease uncertainties, a renormalization of the measured dose was performed using the high dose region in the treatment plan as a reference point.^{14,15,26,27} (4) As a last step, a 3D comparison between the dose planned by the TPS (hereafter called planned dose) and the dose measured by the dosimetry gel (hereafter called measured dose) was performed with the software Verisoft (PTW, Freiburg, Germany).

A γ -index evaluation between planned and measured doses was performed with two passing criteria: the first one with 3% dose difference (DD) and 3-mm distance to agreement (DA) (3%/3 mm) and the second one with 5% DD and 3 mm DA (5%/3 mm). Dose

deviations refer to the local dose, and doses below 10% of the maximum dose were excluded.

For the dose evaluation in the rectum, the dose measured by the TLD was compared to the dose planned by the TPS at the position of the TLD visible on the treatment planning CT. If the TLD was visible on more than one CT slice, the dose was averaged.

For the measured doses of polymer gel and TLDs, the additional doses of the treatment planning CT and the CBCT were taken into account and were estimated to be 0.01 Gy each.

3 | RESULTS

The 3D γ indices of the planned and the measured dose distributions in the prostate were 97.7% for the 3%/3mm criteria and 99.6% for the 5%/3mm criteria. Figure 4 showcases γ maps (3%/3mm) of the measured and the planned doses on different trans-axial slices through the prostate. On the γ map, the dose distributions agree very well in the center of the prostate (white areas). Failed points (red areas) are observed only on the edges of the prostate. Dose profiles that compare the planned and the measured doses (Figure 4), show a homogeneous dose distribution throughout the prostate. The agreement of the measured and the planned doses is very high in the middle of the prostate with a deviation <0.1 Gy. On the edges of the prostate, measured and planned doses deviate slightly in the order of 0.24 Gy (corresponding to 5% of the prescribed dose).

The results from the punctual dose evaluation with TLDs in the rectum are displayed in Table 1. TLDs 1–6 were placed close to the prostate target. Here, doses in the range between 2.06 Gy and 4.20 Gy were measured. For TLDs 1–6, the average difference between the measured and the planned dose was 2.22% (range: 0.67%–4.67%). TLDs 7–9 were located below the prostate and measured doses between 0.18 Gy and 0.32 Gy.

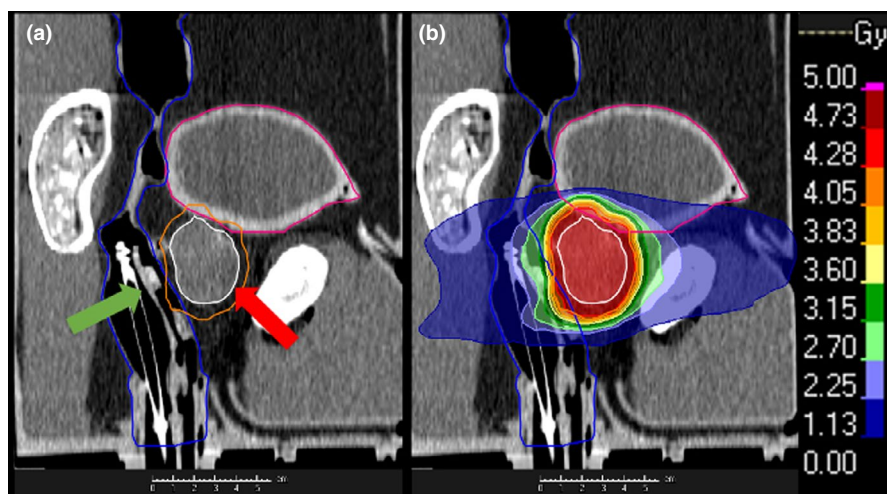


FIGURE 4 Imaging and treatment planning. (a): Median sagittal slice of the treatment planning CT indicating the position of the TLDs (green arrow) relative to the prostate (red arrow). (b): Radiotherapy treatment plan with a prescribed dose of 4.5 Gy to the prostate (color-coding on the right) on CT image (grayscale). Both images contain the following contours: GTV (white), PTV (orange), rectum (blue), bladder (pink) [Color figure can be viewed at wileyonlinelibrary.com]

TABLE 1 Comparison of planned and measured doses for the TLDs in the rectum

TLD N°	D _{planned} [Gy]	D _{measured} [Gy]	$\Delta = D_{\text{measured}} - D_{\text{planned}}$ [Gy]	$\square = \frac{ D_{\text{measured}} - D_{\text{planned}} }{D_{\text{prescribed}}}$ [%]
1	2.16	2.06	-0.1	2.22%
2	2.88	2.67	-0.21	4.67%
3	3.00	2.96	-0.04	0.89%
4	2.23	2.31	0.08	1.78%
5	3.18	3.32	0.14	3.11%
6	4.23	4.20	-0.03	0.67%
7	0.16	0.18	0.02	0.44%
8	0.25	0.29	0.04	0.89%
9	0.30	0.32	0.02	0.44%
Average difference			0.08	1.78%

Δ represents the dose difference between the measured and the planned doses in Gray. \square gives the dose difference between the measured and the planned dose in % relative to the prescribed dose (4.5 Gy). The normalization to the prescribed dose is done as the prescribed dose is a constant factor, while the planned dose is different for each TLD.

Here, the average difference between the measured and planned dose was 0.59% (range: 0.44%–0.89%). Regarding the absolute dose values in Gy, deviations of 0.02 Gy to 0.21 Gy (mean 0.08 Gy) were observed between measured and planned doses.

4 | DISCUSSION

Anthropomorphic phantoms are valuable tools for quality assurance in image-guided and adaptive radiotherapy. The new ADAM PETer phantom was designed and constructed for the simulation and optimization of the clinical workflow of PET/MRI-guided radiation treatment planning of prostate cancer patients. In a previous study, we demonstrated the suitability of the ADAM PETer phantom as multimodal, anthropomorphic model in CT-, 3T MRI- and PET-measurements.¹¹ In the present study, we assessed the potential of the ADAM PETer phantom for 3D dose measurements in the prostate and point-dose measurements in the rectum, using PAGAT dosimetry gel and TLDs, respectively.

4.1 | Methodology

Our data demonstrate the feasibility of this approach and suggest a high accuracy of the dosimetric methods employed. For the prostate, the 3D γ index evaluation indicated an agreement of 97.7% between planned and measured dose (3%/3 mm criterion). In particular in the prostate center, the measured dose overlaps almost perfectly with the planned dose. Slight discrepancies (maximum 5%) between measured and planned doses were observed only on the edges of the prostate organ surrogate. These discrepancies could potentially result from the wall effect,²¹

on the other hand they appear to have a nonrandom structure on the gamma maps (Figure 4). Further measurements should be done to investigate this effect. In general, however, our data confirm the study by Elter et al.²¹ that found a high compatibility of the PAGAT dosimetry gel with the 3D printing material of the prostate organ surrogate.

For dose measurements in the rectum, we used an array of nine TLDs. The TLDs showed an average dose difference of 0.08 Gy (1.78% of the prescribed dose) between planned and measured doses. In our study, the TLD dose evaluation shows less good results than in Mann et al., who found that the deviations were $\leq 0.02\%$ for a homogeneous irradiation.¹⁴ This difference in accuracy might be explained by the high dose gradient between prostate and rectum in our study: the highest discrepancies between planned and measured doses were found for TLDs 1–6, with a mean difference of 0.1 Gy (range: 0.03–0.21 Gy) and a maximum of 0.21 Gy for TLD 2. TLDs 1–6 were placed in the dose fall-off area directly posterior to the prostate (see Figures 2 and 3). Therefore, these TLDs measured relatively high doses (~65% of the prescribed dose) and experienced a strong dose gradient. For TLDs 7–9, the mean difference between planned and measured doses was very small: 0.03 Gy (range: 0.02–0.04 Gy). As TLDs 7–9 were placed below the prostate (Figure 2), they measured only low doses (~5% of the prescribed dose) and did not experience a strong dose gradient.

Polymer dosimetry gel and TLDs have already been combined in previous studies for dosimetry purposes, either for a dose comparison between the gel and the TLDs,^{12,13} or the TLDs were used to renormalize the gel dose measurement,^{14,15} but the present work seems to be the first combining gel and TLDs in a multimodal anthropomorphic phantom.

Several uncertainties are involved in the described methodology. First, there is the challenging handling of polymer dosimetry gel due to its hyper oxygen reactivity²⁸ and the required thermal stabilization for the irradiation.^{26,29} In addition, the dosimetric evaluation of the irradiated gel including MRI acquisition, dose calibration and co-registration of planning CT and MRI requires several steps, each containing individual sources of uncertainties. The rotation of the treatment couch between the treatment planning CT and the actual irradiation might have introduced a very slight positioning error of the phantom in the order of a few mm. As the 3D dose evaluation in the prostate is quite robust against positioning errors, this mainly affects the point dose evaluation in the TLDs and could explain some of our observed differences between planned and measured doses in the TLDs.

Overall, however, we consider these uncertainties to be relatively small, which is indicated by the good agreement of planned and measured doses in our experiment. In addition, our group profits from several years of experience in handling polymer dosimetry gel and TLDs. Therefore, all workflows for dosimetry studies are well established at our institution.^{7,14,21,22,24}

4.2 | 3D printed anthropomorphic phantoms for radiation dosimetry

Dosimetry measurements for treatment plan verification using more and more realistic anthropomorphic phantoms have become more accessible with the development of 3D printing methods. Advanced 3D printing methods allow to tailor the design and construction of anthropomorphic phantoms according to very specific needs since the phantom and the organs can be easily and reproducibly printed with different size, shape, or composition. Today, several anthropomorphic phantoms for different anatomical regions (i.e., head³⁰ and pelvis^{11,31}) have been developed to perform dose measurements using different dosimetry detectors (i.e., radiophotoluminescence glass dosimeters,³⁰ polymer dosimetry gel,⁷ TLDs,³² films¹⁰). However, to the best of our knowledge, the new ADAM PETER phantom is the first anthropomorphic phantom that (i) simulates prostate cancer as multifocal and metastatic disease including metastasis in lymph nodes and bones, (ii) has a modular setup in which organ surrogates can be exchanged within 15 min, (iii) allows for simulation of inter- and intrafractional organ motion and deformation, and (iv) is compatible not only with CT and MRI, but also with PET. Together with the here presented methodology of performing polymer gel and TLD dosimetry in prostate and rectum, ADAM PETER has a high potential for end-to-end tests in image-guided adaptive radiotherapy.

4.3 | Potential applications in image guided radiotherapy planning

The suitability of our previous ADAM phantom for image-guided and adaptive radiotherapy workflows has already been demonstrated by two independent studies at different institutions. Hoffmanns et al.⁹ used the previous ADAM phantom for end-to-end testing in MR-guided online adaptive radiotherapy. Bohoudi et al.¹⁰ performed a phantom-based end-to-end empirical validation of dose accumulation in MRI-guided adaptive radiotherapy simulating six MR-guided prostate stereotactic body radiotherapy treatment courses.

These studies demonstrate the phantom's general suitability for end-to-end testing in image-guided adaptive radiotherapy. However, in the previous ADAM phantom, dosimetry measurements were limited to films in distinct pockets at the surface of bladder and rectum. The new 3D printing technique of ADAM PETER now significantly extends these possibilities as it allows for performing 3D dose measurements in the prostate and point-dose measurements in the rectum. In addition, the prostate organ shell can be easily produced in high numbers, allowing for serial measurements, for example, using different adaptation methodologies. The compatibility with PET opens further perspectives. Assuming a compatibility of the dosimetry gel with PSMA ligands³³ or radioactive isotopes in general (which still has to be shown), the dosimetry gel and the radioactive isotope could be mixed before being filled into the prostate, potentially allowing for end-to-end tests in PET/MRI-guided radiotherapy. Another important aspect for end-to-end tests in image-guided and adaptive radiotherapy workflows is the possibility to induce organ motion and deformation. One approach for simulating organ motion in the previous ADAM phantom is described in Bohoudi et al.¹⁰ Bohoudi's approach could be transferred to the ADAM PETER phantom. In future studies, we will further investigate the possibility to induce reproducible organ motion and deformation in the ADAM PETER phantom.

4.4 | Conclusions and prospects

In the present study, we demonstrate the feasibility of using PAGAT dosimetry gel and TLDs for dose measurements in the prostate and the rectum organ surrogates of an anthropomorphic, deformable, and multimodal pelvis phantom. The described methodology might offer new perspectives for the simulation and optimization of image-guided adaptive radiotherapy workflows and ultimately end-to-end test.

ACKNOWLEDGMENTS

This work was funded by the National Center for Tumor Diseases (NCT), partner sites Heidelberg and Dresden (grant number: G886_G986_PoC_PSMA). Open Access funding enabled and organized by Projekt DEAL.

CONFLICT OF INTEREST

SAK reports grants from Viewray Inc., outside the submitted work. All other authors have no conflicts of interest to disclose.

DATA AVAILABILITY STATEMENT

The data that support the findings of this study are available from the corresponding author upon reasonable request.

ORCID

Mathieu Marot  <https://orcid.org/0000-0003-3984-8933>

Alina Elter  <https://orcid.org/0000-0002-0295-9931>

Philipp Mann  <https://orcid.org/0000-0002-2857-4861>

Clarissa Gillmann  <https://orcid.org/0000-0002-5977-6722>

REFERENCES

- McPartlin AJ, Li XA, Kershaw LE, et al. MRI-guided prostate adaptive radiotherapy – a systematic review. *Radiother Oncol.* 2016;119(3):371-380. <https://doi.org/10.1016/j.radonc.2016.04.014>
- Pollard JM, Wen Z, Sadagopan R, Wang J, Ibbott GS. The future of image-guided radiotherapy will be MR guided. *BJR.* 2017;90(1073):20160667. <https://doi.org/10.1259/bjr.20160667>
- Bettermann AS, Zamboglou C, Kiefer S, et al. [68Ga]-PSMA-11 PET/CT and multiparametric MRI for gross tumor volume delineation in a slice by slice analysis with whole mount histopathology as a reference standard – Implications for focal radiotherapy planning in primary prostate cancer. *Radiother Oncol.* 2019;141:214-219. <https://doi.org/10.1016/j.radonc.2019.07.005>
- Zamboglou C, Fassbender TF, Steffan L, et al. Validation of different PSMA-PET/CT-based contouring techniques for intraprostatic tumor definition using histopathology as standard of reference. *Radiother Oncol.* 2019;141:208-213. <https://doi.org/10.1016/j.radonc.2019.07.002>
- Knorr K, Eiber M, Maurer T, Wester H-J, Scheidhauer K. PET-CT and PET-MRI of the prostate: from 18F-FDG to 68Ga-PSMA. *Radiologe.* 2017;57(8):631-636. <https://doi.org/10.1007/s00117-017-0276-1>
- Freitag MT, Radtke JP, Hadaschik BA, et al. Comparison of hybrid 68Ga-PSMA PET/MRI and 68Ga-PSMA PET/CT in the evaluation of lymph node and bone metastases of prostate cancer. *Eur J Nucl Med Mol Imaging.* 2016;43(1):70-83. <https://doi.org/10.1007/s00259-015-3206-3>
- Elter A, Dorsch S, Mann P, et al. End-to-end test of an online adaptive treatment procedure in MR-guided radiotherapy using a phantom with anthropomorphic structures. *Phys Med Biol.* 2019;64(22):225003. <https://doi.org/10.1088/1361-6560/ab4d8e>
- Niebuhr NI, Johnen W, Echner G, et al. The ADAM-pelvis phantom—an anthropomorphic, deformable and multimodal phantom for MRgRT. *Phys Med Biol.* 2019;64(4):04NT05. <https://doi.org/10.1088/1361-6560/aafd5f>
- Hoffmans D, Niebuhr N, Bohoudi O, Pfaffenberger A, Palacios M. An end-to-end test for MR-guided online adaptive radiotherapy. *Phys Med Biol.* 2020;65(12):125012. <https://doi.org/10.1088/1361-6560/ab8955>
- Bohoudi O, Lagerwaard FJ, Bruynzeel AME, et al. End-to-end empirical validation of dose accumulation in MRI-guided adaptive radiotherapy for prostate cancer using an anthropomorphic deformable pelvis phantom. *Radiother Oncol.* 2019;141:200-207. <https://doi.org/10.1016/j.radonc.2019.09.014>
- Gillmann C, Homolka N, Johnen W, et al. Technical Note: ADAM PETer – An anthropomorphic, deformable and multimodality pelvis phantom with positron emission tomography extension for radiotherapy. *Med Phys.* 2021;48(4):1624-1632. <https://doi.org/10.1002/mp.14597>
- Guillerminet C, Gschwind R, Makovicka L, Spevacek V, Soukoup M, Novotny J. Comparative study of polyacrylamid gels and thermoluminescent dosimeters used in external radiotherapy. *Radiat Meas.* 2005;39(1):39-42. <https://doi.org/10.1016/j.radmeas.2004.06.003>
- Wong CJ, Ackerly T, He C, et al. Small field size dose-profile measurements using gel dosimeters, gafchromic films and micro-thermoluminescent dosimeters. *Radiat Meas.* 2009;44(3):249-256. <https://doi.org/10.1016/j.radmeas.2009.03.012>
- Mann P, Schwahofer A, Karger CP. Absolute dosimetry with polymer gels—a TLD reference system. *Phys Med Biol.* 2019;64(4):045010. <https://doi.org/10.1088/1361-6560/aafd41>
- Schwahofer A, Mann P, Spindeldreier CK, Karger CP. On the feasibility of absolute 3D dosimetry using LiF thermoluminescence detectors and polymer gels on a 0.35T MR-LINAC. *Phys Med Biol.* 2020;65(21):215002. <https://doi.org/10.1088/1361-6560/aba6d7>
- Venning A, Hill B, Subramanian B, Healy B, Baldock C. Investigation of the PAGAT polymer gel dosimeter using magnetic resonance imaging. *Phys Med Biol.* 2005;50:3875-3888. <https://doi.org/10.1088/0031-9155/50/16/015>
- Deene YD, Vergote K, Claeys C, Wagter CD. The fundamental radiation properties of normoxic polymer gel dosimeters: a comparison between a methacrylic acid based gel and acrylamide based gels. *Phys Med Biol.* 2006;51(3):653-673. <https://doi.org/10.1088/0031-9155/51/3/012>
- Baldock C, De Deene Y, Doran S, et al. Polymer gel dosimetry. *Phys Med Biol.* 2010;55(5):R1-R63. <https://doi.org/10.1088/0031-9155/55/5/R01>
- Sandilos P, Angelopoulos A, Baras P, et al. Dose verification in clinical imrt prostate incidents. *Int J Radiat Oncol Biol Phys.* 2004;59(5):1540-1547. <https://doi.org/10.1016/j.ijrobp.2004.04.029>
- Vergote K, Deene YD, Bussche EV, Wagter CD. On the relation between the spatial dose integrity and the temporal instability of polymer gel dosimeters. *Phys Med Biol.* 2004;49(19):4507-4522. <https://doi.org/10.1088/0031-9155/49/19/005>
- Elter A, Dorsch S, Mann P, Runz A, Johnen W, Karger CP. Compatibility of 3D printing materials and printing techniques with PAGAT gel dosimetry. *Phys Med Biol.* 2019;64(4):04NT02. <https://doi.org/10.1088/1361-6560/aafef0>
- Schwahofer A, Feist H, Georg H, Häring P, Schlegel W. Experimental determination of the photon-energy dependent dose-to-water response of TLD600 and TLD700 (LiF:Mg, Ti) thermoluminescence detectors. *Z Med Phys.* 2017;27(1):13-20. <https://doi.org/10.1016/j.zemedi.2016.02.003>
- Matrosic C, McMillan A, Holmes J, Bednarz B, Culbertson W. Dosimetric comparison of DEFEL and PAGAT formulae paired with an MRI acquisition. *J Phys Conf Ser.* 2017;847: <https://doi.org/10.1088/1742-6596/847/1/012012>
- Mann P, Witte M, Moser T, et al. 3D dosimetric validation of motion compensation concepts in radiotherapy using an

- anthropomorphic dynamic lung phantom. *Phys Med Biol*. 2016;62(2):573-595. <https://doi.org/10.1088/1361-6560/aa51b1>
25. Nolden M, Zelzer S, Seitel A, et al. The Medical Imaging Interaction Toolkit: challenges and advances : 10 years of open-source development. *Int J Comput Assist Radiol Surg*. 2013;8(4):607-620. <https://doi.org/10.1007/s11548-013-0840-8>
 26. Deene YD, Vandecasteele J. On the reliability of 3D gel dosimetry. *J Phys: Conf Ser*. 2013;444:012015. <https://doi.org/10.1088/1742-6596/444/1/012015>
 27. Vandecasteele J, De Deene Y. On the validity of 3D polymer gel dosimetry: I. Reproducibility study. *Phys Med Biol*. 2013;58(1):19-42. <https://doi.org/10.1088/0031-9155/58/1/19>
 28. Deene YD, Hurley C, Venning A, et al. A basic study of some normoxic polymer gel dosimeters. *Phys Med Biol*. 2002;47(19):3441-3463. <https://doi.org/10.1088/0031-9155/47/19/301>
 29. De Deene Y, Pittomvils G, Visalatchi S. The influence of cooling rate on the accuracy of normoxic polymer gel dosimeters. *Phys Med Biol*. 2007;52(10):2719-2728. <https://doi.org/10.1088/0031-9155/52/10/006>
 30. Kamomae T, Shimizu H, Nakaya T, et al. Three-dimensional printer-generated patient-specific phantom for artificial in vivo dosimetry in radiotherapy quality assurance. *Physica Med*. 2017;44:205-211. <https://doi.org/10.1016/j.ejmp.2017.10.005>
 31. Pappas E, Kalaitzakis G, Boursianis T, et al. Dosimetric performance of the Elekta Unity MR-linac system: 2D and 3D dosimetry in anthropomorphic inhomogeneous geometry. *Phys Med Biol*. 2019;64(22):225009. <https://doi.org/10.1088/1361-6560/ab52ce>
 32. Babaloui S, Jafari S, Polak W, et al. Development of a novel and low-cost anthropomorphic pelvis phantom for 3D dosimetry in radiotherapy. *J Contemp Brachytherapy*. 2020;12(5):470-479. <https://doi.org/10.5114/jcb.2020.100380>
 33. Beuthien-Baumann B, Koerber SA. PET imaging in adaptive radiotherapy of prostate tumors. *Q J Nucl Med Mol Imaging*. 2018;62(4):404-410. <https://doi.org/10.23736/S1824-4785.18.03080-7>

SUPPORTING INFORMATION

Additional supporting information may be found online in the Supporting Information section.

How to cite this article: Marot M, Elter A, Mann P, et al. Technical Note: On the feasibility of performing dosimetry in target and organ at risk using polymer dosimetry gel and thermoluminescence detectors in an anthropomorphic, deformable, and multimodal pelvis phantom. *Med Phys*. 2021;48:5501–5510. <https://doi.org/10.1002/mp.15096>

2.5 Publication IV

GEL DOSIMETRY AS A TOOL FOR CLINICAL IMPLEMENTATION OF IMAGE-GUIDED RADIOTHERAPY

Authors: Alina Elter, Dorsch Stefan, Mathieu Marot, Clarissa Gillmann, Wibke Johnen, Armin Runz, C. Katharina Spindeldreier, Sebastian Klüter, Christian P. Karger and Philipp Mann

Status (12/2021): Peer-reviewed with pending publication

Journal reference: *Journal of Physics: Conference Series*

DOI: –

Copyright: This is the Author's Original version of the manuscript as submitted and peer-reviewed for publication in the Journal of Physics: Conference Series. The paper will be published open access.

Contribution: This manuscript describes a variety of phantoms equipped with polymer dosimetry gel that are used for different quality assurance tests in image-guided radiotherapy. As first and main author, I have contributed significantly to the presented experiments including the preparation and post-processing steps with support of the co-authors. I have written the manuscript, prepared all graphics and revised the manuscript based on the reviewer's comments with support from Prof. Christian P. Karger.

Gel dosimetry as a tool for clinical implementation of image-guided radiotherapy

A Elter^{1,2,4}, S Dorsch^{1,2,4}, M Marot^{1,4}, C Gillmann^{1,4}, W Johnen^{1,4}, A Runz^{1,4}, C K Spindeldreier^{3,4}, S Klüter^{3,4}, C P Karger^{1,4} and P Mann^{1,4,5}

¹ Department of Medical Physics in Radiation Oncology, German Cancer Research Center (DKFZ), INF 280, 69120 Heidelberg, Germany

² Faculty of Physics and Astronomy, University of Heidelberg, Heidelberg, Germany

³ Department of Radiation Oncology, University Hospital Heidelberg, INF 400, 69120 Heidelberg, Germany

⁴ National Center for Radiation Research in Oncology (NCRO), Heidelberg Institute for Radiation Oncology (HIRO), Heidelberg, Germany

⁵ HQ-Imaging GmbH, Heidelberg, Germany

E-Mail: a.elter@dkfz.de

Abstract. The implementation of new image-guided radiotherapy (IGRT) treatment techniques requires the development of new quality assurance (QA) methods including geometric and dosimetric validation of the applied dose in 3D. Polymer gels (PG) provide a promising tool to perform such tests. However, to be used in a large variety of clinical applications, the PG must be flexibly applicable. In this work, we present a variety of phantoms used in clinical routine to perform both hardware and workflow tests in IGRT. This includes the validation of isocenter accuracy in magnetic resonance (MR)-guided RT (MRgRT) and end-to-end tests of online adaptive treatment techniques for inter- and intra-fraction motion management in IGRT. The phantoms are equipped with one or more PG containers of different materials including 3D printed containers to allow for 3D dosimetry in arbitrarily shaped structures. The proposed measurement techniques and phantoms provide a flexible application and show a clear benefit of PG for 3D dosimetry in combination with end-to-end tests in many clinical QA applications.

1. Introduction

New radiotherapy (RT) treatment techniques, such as image-guided RT (IGRT), applied in clinical routine increase tumor-conformity while sparing surrounding organs at risk (OAR). However, the increasing complexity of such techniques requires the development of new quality assurance (QA) procedures ensuring correct dose delivery. Especially for new hybrid machines combining magnetic resonance imaging (MRI) and conventional RT (so-called MR-Linacs), the implementation of new QA protocols is of great interest. These protocols range from single component testing to the validation of new motion management and adaptive treatment strategies (such as gating and daily plan adaptation). However, the complexity of such tests requires dedicated detectors allowing to test (i) geometric and (ii) dosimetric accuracy of the 3D dose distribution in (iii) phantoms, which are visible in MRI. One promising method meeting requirements (i)-(iii) are so-called polymer gels (PG) [1]. To be used in a larger variety of clinical QA procedures, the PG applications should be as flexible as possible including the use of arbitrarily shaped gel containers to simulate anthropomorphic structures. Furthermore, a geometrical evaluation of the gel directly after irradiation instead of after the long stabilization times of

the gel's polymerization processes of up to 48h [2] is of high importance for the evaluation of geometrical parameters. In this paper, we present a set of dedicated phantoms that can be equipped with arbitrary 3D printed gel containers [3] and that are used at the German Cancer Research Center (DKFZ) and University Hospital in Heidelberg, Germany, for a variety of clinical QA procedures of advanced treatment techniques. The experimental PG workflow as validated in [2] was applied in this work.

2. Polymer gel

2.1. Fabrication

As PG, the PAGAT (PolyAcrylamide Gelatin gel fabricated at ATmospheric conditions) was used and in-house produced following the protocol described elsewhere [2].

2.2. Gel containers

We used three different types of gel containers: (i) borosilicate glass flasks and (ii) Barex™ (VELOX GmbH, Hamburg, Germany) containers, which are two well established materials for the use with PG, but which are also limited in size and shape. Hence, we have developed a method to (iii) 3D print gel containers in arbitrary shapes using the VeroClear™ printing material of the Objet500 Connex 3 3D printer (Stratasys, Eden Prairie, USA) [3].

2.3. Evaluation

Gel evaluation was performed either (i) purely geometrically directly after irradiation on a 0.35T MR-Linac (ViewRay Inc., Ohio, USA) or (ii) dosimetrically 48h after irradiation on a diagnostic 3T Prisma^{fit} (Siemens Healthineers, Erlangen, Germany). For this, a turbospin- or multispin-echo sequence with 1/32 equidistant echoes acquired with an isotropic image resolution of 1 mm³ was used for (i)/(ii). For quantitative dose comparison, a 3D γ evaluation with a passing criterion of 3%/3mm (dose difference/distance-to-agreement) was employed, taking only dose levels larger than 10% of the maximum dose into account.

3. Clinical applications

A schematic overview of the phantoms presented in this paper is shown in Figure 1. Each phantom is equipped with one or more PG containers to either perform 3D geometric and/or dosimetric measurements in different scenarios.

3.1. 3D isocenter accuracy measurement in MRgRT

To test the alignment of imaging and irradiation isocenter in MRgRT, we used an in-house developed QA phantom [4]. The phantom is equipped with a spherical PG-filled glass flask of 8cm diameter (Fig. 1a). The phantom was aligned with the imaging isocenter of the MRI using dedicated fiducials (Fig. 1b, red marking) while the irradiation isocenter was measured by a star shot irradiation of the PG container. The PG was then geometrically evaluated in 3D using a T₂-weighted turbo spin echo sequence directly after irradiation without moving the phantom to determine the radius of the irradiation isocircle (IC_r) and the distance between the imaging and irradiation isocenter (IC_d). Results showed a mean IC_r/ IC_d of (0.4±0.1)mm/ (0.4±0.6)mm, which were well within the tolerance levels of 0.5mm and 1mm, respectively [4].

3.2. End-to-end tests of online adaptive IGRT procedures

3.2.1. Inter-fractional motion. With the introduction of new IGRT devices, the online adaption of treatment plans in case of inter-fractional anatomy changes became feasible. To validate these techniques, we used two deformable phantoms that can be equipped with 3D printed and PG-filled structures to validate the dose delivery.

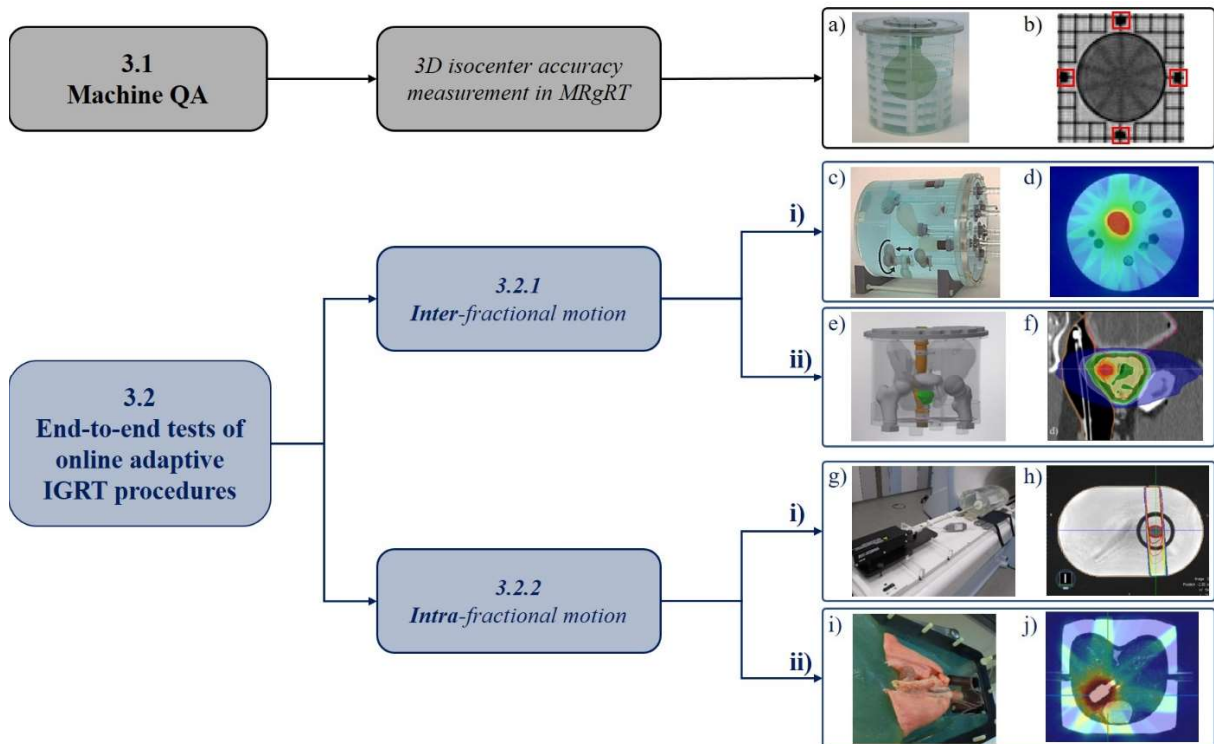


Figure 1: Schematic overview of the phantoms presented in this paper: a) a picture of the phantom for 3D isocenter accuracy measurements in MRgRT including the gel container (green) and b) the geometric PG evaluation including fiducials (red) for a correct positioning in the imaging isocenter. Pictures of the phantoms used for end-to-end tests of online adaptive IGRT procedures are given in c), e), g), and i) together with the respective treatment plan in d), f), h), and j).

i. AQUARIUM. To validate the online plan adaption process in MRgRT the AQUARIUM (Anthropomorphic Quality Assurance phantom to study Interfractional Uncertainties in MRgRT) [5] was equipped with two PG-filled structures (OAR, tumor) as well as structures filled with anthropomorphic imaging contrast (Fig. 1c). PG containers were either 3D printed or made of Barex™. By a reproducible shift and rotation of the inner structures, a patient's inter-fractional anatomy change was simulated and the applied dose to the tumor and OAR with and without an adaption of the treatment plan was evaluated in 3D. Results showed a very good agreement of PG evaluation with calculated treatment plans with passing rates >93% in 3D γ -analyses. The online plan adaption successfully compensated under-/over-dosages (down to 45%/ up to 180% of the prescribed dose) in the tumor/OAR that occurred without plan adaption.

ii. ADAM-PETer. Inter-fractional motion was simulated in a realistic setup using the ADAM-PETer phantom (Fig. 1e) [6]. To test a fractionated prostate irradiation scheme at a conventional linear accelerator (Artiste, Siemens Healthineers, Erlangen, Germany) with a microboost irradiation of an intraprostatic lesion (Fig. 1f), the phantom was equipped with a 3D printed and PG-filled prostate. The treatment fractions were irradiated directly after each other with the same PG container in the phantom. Between fractions, the position of the prostate was altered by changing the filling of an endorectal balloon. As expected, an under-dosage and a dose smearing within the microboost-volume were measured. Additionally, we could demonstrate significant inter-fractional shifts of the microboost volume of up to 5mm by the gel evaluation.

3.2.2. Intra-fractional motion. In case of intra-fractional patient motion (e.g. breathing), new IGRT treatment methods such as gating or tracking may be used for compensation. To test and validate

an existing gating procedure at the MR-Linac, two motion phantoms were equipped with a PG-filled Barex™ container simulating the tumor.

i. Geometric motion phantom. In a first experiment, the gating procedure at a clinical MR-Linac was simulated with a geometrical motion phantom consisting of a water-filled cylindrical case ($d=22\text{cm}$, $l=50\text{cm}$) holding a movable smaller water-filled cylinder ($d=9\text{cm}$, $l=50\text{cm}$) that can be loaded with the PG-filled Barex™ tumor (Fig. 1g). The phantom motion was based on a \cos^4 trajectory with a peak-to-peak amplitude of 1.5cm. The gel was evaluated dosimetrically. Results for a gated treatment showed a homogenous target coverage similar to that of a static case with high 3D γ passing rates of $>98.6\%$. Irradiation without motion compensation resulted in poor dose coverage with a γ_{3D} passing rate of 68.6%.

ii. Porcine lung phantom. To test the gated treatment at a clinical MR-Linac in a realistic setup, we used a porcine lung phantom (Fig. 1i) [2]. The PG tumor was sewed onto the mediastinum of the lung, which moved according to a real patient's breathing pattern. The target structure could be tracked by MRI throughout the entire treatment session. Additionally, homogeneous dose coverage without significant under or over-dosage was found indicating a successful gated irradiation. Dosimetric evaluation yielded a high 3D γ passing rate of 95.9%.

4. Discussion and Conclusion

In this paper, we present a variety of phantoms equipped with PG, which were used in clinical routine to perform both hardware and workflow tests in IGRT. This includes 3D isocenter alignment measurements at a clinical MR-Linac and end-to-end tests of online adaptive treatment procedures for both inter- and intra-fractional motion management. One important step to achieve a realistic setting is the use of 3D printed PG containers. This allows for adapting and extending existing phantoms to applications that require 3D dose measurements in irregularly shaped structures, e.g. for the simulation of specific organ sites. Furthermore, experiments have also shown that a geometric evaluation of the PG is possible directly after the irradiation. If, however, a full dosimetric evaluation is required, it is a common procedure in PG dosimetry to await the stabilization time and to normalize the required calibration curve at a reference point with a known dose determined e.g. by an ionization chamber (IC). However, due to the lack of bores in our anthropomorphic phantoms, independent absolute dose measurements with an IC were not possible. Hence, we based the reference dose on the treatment plan. To overcome this limitation, a recently developed technique combining thermoluminescence detectors (TLD) with PG can be used. Due to their compact design, TLDs can be attached on the surface of various phantom structures (OARs and/or tumor) serving as a reference system for absolute dosimetry [7,8]. Overall, the presented techniques and phantoms provide a flexible application of PG for 3D dosimetry in complex radiotherapy treatment techniques.

5. Acknowledgements

This work was supported by the EMPIR programme co-financed by the Participating States and from the European Union's Horizon 2020 research and innovation programme. We would like to thank the German Research Council (DFG) for the funding of the MR-Linac device.

References

- [1] Baldock C et al. 2010 *Phys. Med. Biol.* **55** R1-63
- [2] Mann P et al. 2017 *Phys. Med. Biol.* **62** 573-95
- [3] Elter A et al. 2019 *Phys. Med. Biol.* **64** 04NT02
- [4] Dorsch S et al. 2019 *Phys. Med. Biol.* **64** 205011
- [5] Elter A et al. 2019 *Phys. Med. Biol.* **64** 225003
- [6] Gillmann C et al. 2021 *Med. Phys.* **48** 1624-32
- [7] Mann P et al. 2019 *Phys. Med. Biol.* **64** 45010
- [8] Schwahofer A et al. 2020 *Phys. Med. Biol.* **65** 215002

2.6 Publication V

END-TO-END TEST OF AN ONLINE ADAPTIVE TREATMENT PROCEDURE IN MR-GUIDED RADIOTHERAPY USING A PHANTOM WITH ANTHROPOMORPHIC STRUCTURES

Authors: Alina Elter, Dorsch Stefan, Philipp Mann, Armin Runz, Wibke Johnen, C. Katharina Spindeldreier, Sebastian Klüter and Christian P. Karger

Status (12/2021): Published

Journal reference: *Physics in Medicine & Biology* **64** (2019) 225003

DOI: 10.1088/1361-6560/ab4d8e

Copyright: © Institute of Physics and Engineering in Medicine. Reproduced with permission. All rights reserved.

This paper was published Open Access. The original content of the publication may be used under the terms of a CC BY 3.0 unported license (<https://creativecommons.org/licenses/by/3.0/>). No changes have been made.

Contribution: This work presents a new phantom with reproducibly adjustable structures that are filled with anthropomorphic imaging contrast and polymer dosimetry gel for 3D dose evaluation in the target and a simulated organ at risk. I used this phantom to perform an end-to-end test of an online adaptive treatment procedure in MR-guided radiotherapy. While the phantom development was part of my preceding Master thesis, I developed the specific internal structures used in this end-to-end test and performed all measurements and evaluations within the PhD project. I conducted all steps of the end-to-end test including phantom development, pre-treatment imaging, treatment planning, on-site imaging, treatment plan adaption, irradiation and dose evaluation with the support of the co-authors. Furthermore, I have performed the post-processing and quantitative analysis of the results. Finally, I have written the manuscript, prepared all graphics and revised the manuscript based on the reviewer's comments with support from Dr. Stefan Dorsch, Dr. Philipp Mann and Prof. Christian P. Karger.

OPEN ACCESS



PAPER

End-to-end test of an online adaptive treatment procedure in MR-guided radiotherapy using a phantom with anthropomorphic structures

RECEIVED
3 July 2019REVISED
30 September 2019ACCEPTED FOR PUBLICATION
14 October 2019PUBLISHED
15 November 2019

Original content from this work may be used under the terms of the [Creative Commons Attribution 3.0 licence](https://creativecommons.org/licenses/by/4.0/).

Any further distribution of this work must maintain attribution to the author(s) and the title of the work, journal citation and DOI.



A Elter^{1,2,4}, S Dorsch^{1,2,4}, P Mann^{1,4,5}, A Runz^{1,4}, W Johnen^{1,4}, C K Spindeldreier^{3,4}, S Klüter^{3,4} and C P Karger^{1,4}

¹ Department of Medical Physics in Radiation Oncology, German Cancer Research Center (DKFZ), INF 280, 69120 Heidelberg, Germany

² Faculty of Physics and Astronomy, University of Heidelberg, Heidelberg, Germany

³ Department of Radiation Oncology, University Hospital Heidelberg, INF 400, 69120 Heidelberg, Germany

⁴ National Center for Radiation Research in Oncology (NCRO), Heidelberg Institute for Radiation Oncology (HIRO), Heidelberg, Germany

⁵ HQ-Imaging GmbH, Heidelberg, Germany

E-mail: a.elter@dkfz.de

Keywords: magnetic resonance-guided (adaptive) radiotherapy (MRgRT), inter-fractional motion, end-to-end test, deformable anthropomorphic phantom, 3D gel dosimetry (PAGAT)

Abstract

Online adaptive treatment procedures in magnetic resonance (MR)-guided radiotherapy (MRgRT) allow compensating for inter-fractional anatomical variations in the patient. Clinical implementation of these procedures, however, requires specific end-to-end tests to validate the treatment chain including imaging, treatment planning, positioning, treatment plan adaption and accurate dose delivery. For this purpose, a new phantom with reproducibly adjustable anthropomorphic structures has been developed. These structures can be filled either with contrast materials providing anthropomorphic image contrast in MR and CT or with polymer dosimetry gel (PG) allowing for 3D dose measurements. To test an adaptive workflow at a 0.35 T MR-Linac, the phantom was employed in two settings simulating inter-fractional anatomical variations within the patient. The settings included two PG-filled structures representing a tumour and an adjacent organ at risk (OAR) as well as five additional structures. After generating a treatment plan, three irradiation experiments were performed: (i) delivering the treatment plan to the phantom in reference setting, (ii) delivering the treatment plan after changing the phantom to a displaced setting without adaption, and (iii) adapting the treatment plan online to the new setting and delivering it to the phantom. PG measurements revealed a homogeneous tumour coverage and OAR sparing for experiment (i) and a significant under-dosage in the PTV (down to 45% of the prescribed dose) and over-dosage in the OAR (up to 180% relative to the planned dose) in experiment (ii). In experiment (iii), a uniform dose in the PTV and a significantly reduced dose in the OAR was obtained, well-comparable to that of experiment (i) where no adaption of the treatment plan was necessary. PG measurements were well comparable with the corresponding treatment plan in all irradiation experiments. The developed phantom can be used to perform end-to-end tests of online adaptive treatment procedures at MR-Linac devices before introducing them to patients.

1. Introduction

One of the major advantages of radiation therapy (RT) is the possibility to deliver a highly conformal dose distribution to the tumour while sparing the surrounding normal tissue. However, for such high precision treatments, precise knowledge of the actual tumour position and the surrounding organs at risk (OARs) is essential (Verhey *et al* 1982). Changes in patient anatomy between treatment planning and radiation delivery as well as between treatment fractions (Barker *et al* 2004, Sonke *et al* 2019), the so-called inter-fractional motion, are

therefore one of the most prominent uncertainties in RT. Conventionally, this is accounted for by restricting the anatomical changes by means of immobilization aids (Verhey *et al* 1982) and by adding safety margins around the tumour volume (van Herk 2004), which however, increases the irradiated normal tissue volume.

The development of online adaptive radiotherapy procedures using image-guidance has the potential of correcting for anatomical changes over the treatment course (Dawson and Sharpe 2006, Martinez *et al* 2001, Kontaxis *et al* 2015, Green *et al* 2019) and can be used to reduce margin sizes potentially leading to less side effects in normal tissue (Kron 2008) as well as the safe application of dose escalation to the tumour (Yan *et al* 1997). Mostly, image-guidance is performed by x-ray imaging using on-board kilo voltage cone beam computed tomography (kV-CBCT) (Jaffray *et al* 2002). However, kV-CBCT provides only poor soft tissue contrast and thus tumour visibility (Njeh 2008) and its applicability for identifying daily changes of the tumour and OAR is limited. To improve the soft-tissue contrast and to reduce the patient's exposure to ionizing radiation (Chang *et al* 1987), new hybrid devices have been introduced recently by combining a conventional linear accelerator (Linac) with magnetic resonance (MR) imaging for MR-guided radiotherapy (MRgRT) (Lagendijk *et al* 2008, Fallone *et al* 2009, Keall *et al* 2014, Paganelli *et al* 2018, Klüter 2019). With these MR-Linac machines, it is now possible to identify anatomical changes of soft tissue structures with much higher precision and based on online (i.e. while the patient is on the treatment couch) acquired images, the treatment plan may be adapted to the new anatomical situation.

Due to the complex adaption, end-to-end tests are needed to validate the entire chain of treatment planning, positioning, imaging and image registration, plan adaption and irradiation. Such workflow-specific end-to-end tests evaluate the accumulation of uncertainties throughout the treatment procedure which may not be detected by component-by-component testing only (Zakjevskii *et al* 2016). Such end-to-end tests are already well established in conventional radiotherapy using phantoms such as the StereoPHAN™ (Sun Nuclear Corp, Melbourne, FL, USA) or Lucy 3D® QA Phantom (Standard Imaging Inc, Middleton, WI, USA) in stereotactic radiosurgery (Sarkar *et al* 2016). However, typical phantom inserts are static and only visible in CT, but not in MRI. For MR-Linac systems several MRI compatible phantoms are already available to perform end-to-end testing in case of intra-fractional motion, such as breathing motion, e.g. the QUASAR™ MRI^{4D} phantom (Modus Medical Devices Inc, London, ON, Canada). To our knowledge, however, no phantom is commercially available yet being capable of simulating inter-fractional anatomical changes in a realistic and reproducible manner and being visible in both MRI and CT. While tests of image registration algorithms can be realized by a deformable phantom, the validation of dose delivery requires the use of dosimeters in 1D to 3D. A promising method to perform 3D dose measurements is the use of polymer gels (PG) (Schreiner 2006, Baldock *et al* 2010). PGs are based on radiation sensitive chemicals, which polymerize as a function of the absorbed dose when being irradiated. The resulting change in mass density and relaxation rate can be evaluated using either x-ray computed tomography (CT) (Hilts *et al* 2000) or MR imaging (MRI) (Venning *et al* 2005). PGs offer a high spatial resolution enabling measurements of steep dose gradients as they occur e.g. in intensity-modulated radiation therapy (IMRT) (Sandilos *et al* 2004, Vergote *et al* 2004). Moreover, they exhibit minimal influences by magnetic fields on their radiation response (Lee *et al* 2017), and radiation absorption properties equivalent to that of soft tissues (Baldock *et al* 2010, Schreiner 2015). In addition, structures mimicking various anthropomorphic imaging contrasts in CT and MRI are required to provide realistic conditions for image registration algorithms and treatment planning.

In this study, we developed a new phantom with reproducibly adjustable anthropomorphic structures that can be filled either with PG or anthropomorphic imaging contrast materials. This phantom was used to perform an end-to-end test of an online adaptive treatment procedure at a 0.35 T MR-Linac (Mutic and Dempsey 2014, Klüter 2019).

2. Materials and methods

2.1. Phantom

2.1.1. Phantom design

For use in end-to-end tests of online adaptive treatment workflows in MRgRT, a phantom was designed according to the following requirements: (i) the phantom contains adjustable irregular geometric structures that can be reproducibly shifted and rotated. (ii) These structures provide anthropomorphic imaging contrasts in CT as well as in MRI. (iii) 1D, 2D or 3D detectors for dose measurements can be inserted into the structures. While (i) and (ii) are necessary to test the performance of image registration algorithms used for treatment plan adaption, (iii) enables verification of beam guidance and dose delivery.

The 'Anthorpomorphic QUality AssuRance phantom to study Interfractional Uncertainties in MRgRT (AQUARIUM)' consists of a polymethyl-methacrylate (PMMA) cylinder (diameter: 25 cm, height: 25 cm, wall-thickness: 0.5 cm) which was filled with milliporous water enriched with 3.6 g l⁻¹ sodium chloride (NaCl) and 1.25 g l⁻¹ copper sulphate (CuSO₄) to increase the conductivity (American Association of Physicists in Medicine 2010) and to reduce T_1 relaxation. Up to eleven reproducibly shiftable and rotatable hollow PMMA rods fixed to

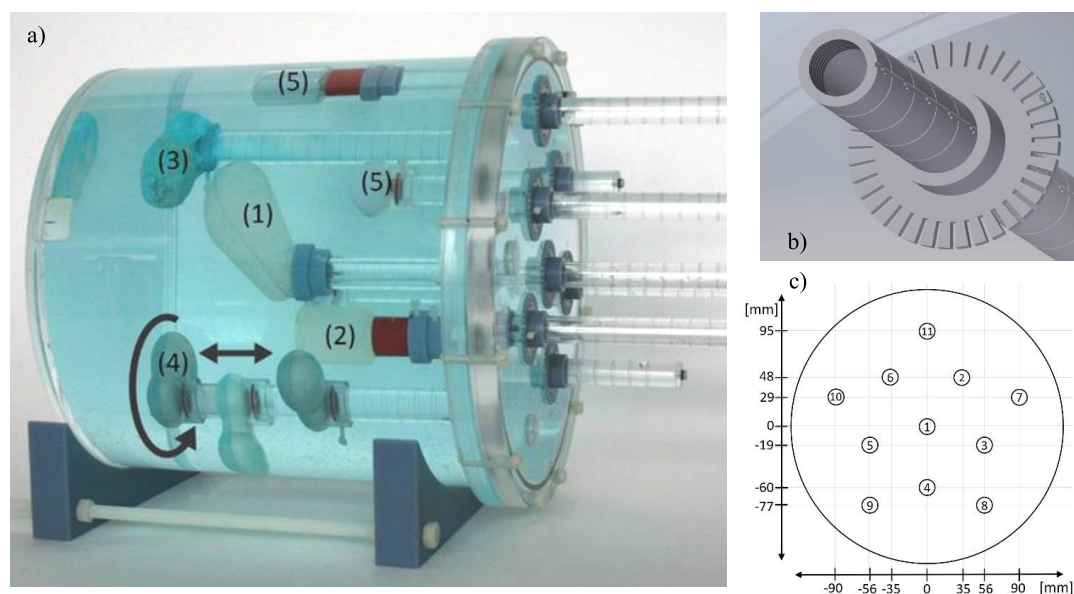


Figure 1. The AQUARIUM including the inserted structures (a): (1) the PG-filled tumour, (2) the PG-filled OAR, (3) CT contrast element 'bone', (4) CT contrast element 'air' displayed as a multi-exposure image, including an exemplary shift and rotation of the element, and (5) exemplary MR contrast elements; the longitudinal and angular scales (10 mm and 10° partitions) to shift and rotate the structures (b), and the arrangement and numbering of the insert positions on the phantom lid (c).

various structures can be inserted into the phantom (figure 1). In addition, thimble ionization chambers can be led through the rods into the structures to perform absolute dose measurements.

2.1.2. Phantom structures

In this study, seven structures were designed and filled with different anthropomorphic image contrast materials or with PG, respectively. Five structures were 3D printed with the Objet500 Connex 3 3D printer (Stratasys, Eden Prairie, USA) using the VeroClear™ printing material, which has been shown to be compatible with PG (Elter *et al* 2019). For the other two, PG compatible Bares™ (VELOX GmbH, Hamburg, Germany) container were used (Mann *et al* 2017). The following structures have been fabricated:

- (i) *CT contrast.* To simulate bone, 1250 g l^{-1} dipotassium phosphate (K_2HPO_4) and 1.6 g l^{-1} CuSO_4 was solved in water (Niebuhr *et al* 2016) and filled into a 3D printed element (figures 2(a), (f) and (k)). Three layers of gypsum bandages (Cellona, REF 20 110, Lohmann & Rauscher International, Rengsdorf, Germany) were additionally attached to the structure to ensure a high attenuation and were impregnated with a clear lacquer to protect the gypsum from the surrounding water (Lackspray Spezial SaBesto, Würth, Künzelsau, Germany). An identical 3D printed element was left air-filled to simulate low CT contrast (figures 2(b), (g) and (l)).
- (ii) *MR contrast.* Three different MRI contrasts were produced using Ni-DTPA doped agarose gel (Tofts *et al* 1993) with a 50 mM Ni-DTPA solution and filled into two 3D printed spheres with a diameter of 20 mm (44.2% Ni-DTPA solution, 1.6% Agarose, 54.2% water resulting in relaxation rates similar to fat) and 25 mm (15.6% Ni-DTPA solution, 3.3% Agarose, 81.1% water resulting in relaxation rates similar to muscle) (figures 2(c), (h) and (m)), respectively, and a Bares™ vial (12.2% Ni-DTPA solution, 1.3% agarose, 86.5% water resulting in relaxation rates similar to prostate tissue).
- (iii) *PG container.* Two PG containers providing water-equivalent contrast were prepared. A 3D printed irregularly shaped container served as a tumour (figures 2(d), (i) and (n)). Additionally, a PG filled Bares™ container was used to simulate an organ at risk (OAR) (figures 2(e), (j) and (o)).

2.2. Polymer gel dosimetry

For 3D dosimetry, the PAGAT (PolyAcrylamide Gelatin gel fabricated at ATmospheric conditions) PG was used (Venning *et al* 2005). When being irradiated, the gel polymerizes as a function of the absorbed dose, which locally alters the relaxation rate R_2 of the transverse magnetization in MRI (Baldock *et al* 2010). The PAGAT gel was selected as it shows a small dose rate dependence (De Deene *et al* 2006) and can be produced in-house at low costs under atmospheric conditions. For conversion of R_2 -values to dose, a calibration was performed using

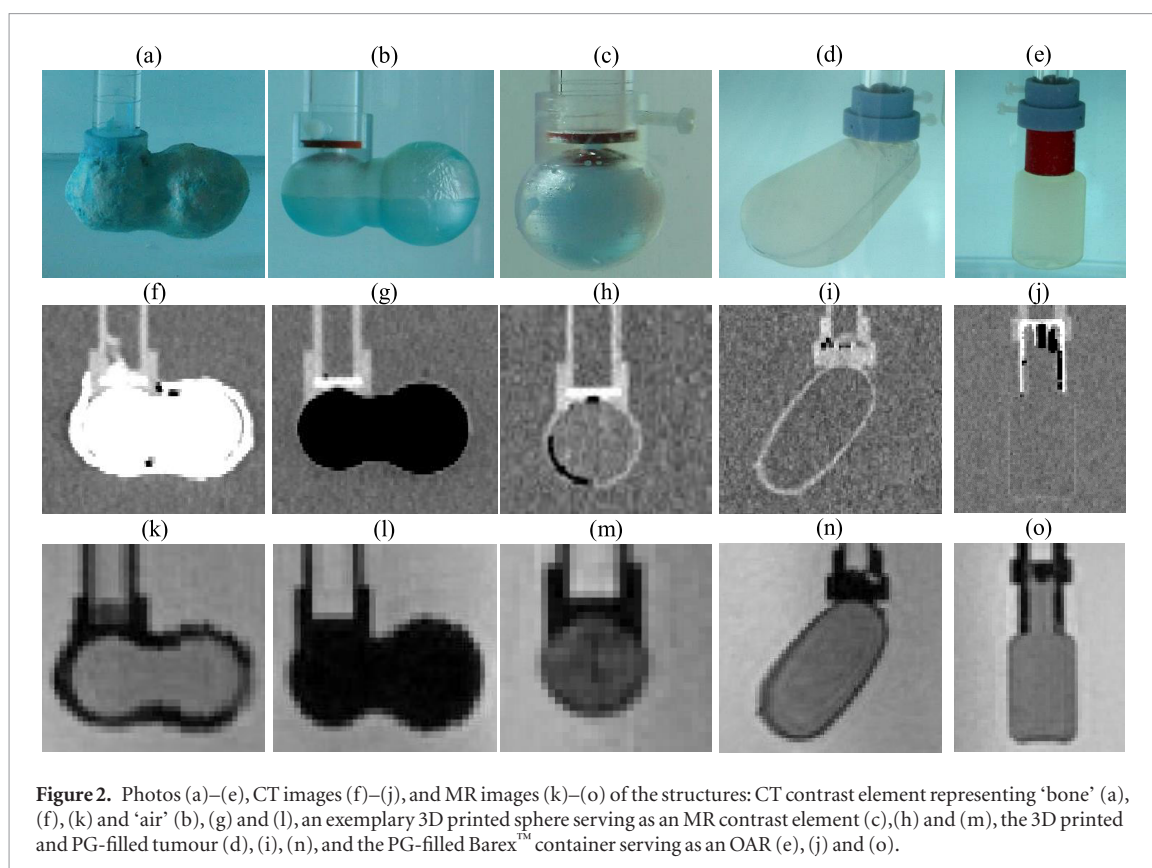


Figure 2. Photos (a)–(e), CT images (f)–(j), and MR images (k)–(o) of the structures: CT contrast element representing ‘bone’ (a), (f), (k) and ‘air’ (b), (g) and (l), an exemplary 3D printed sphere serving as an MR contrast element (c), (h) and (m), the 3D printed and PG-filled tumour (d), (i), (n), and the PG-filled BarexTM container serving as an OAR (e), (j) and (o).

eight additional PG-filled BarexTM vials being irradiated with doses from 0 to 7 Gy in steps of 1 Gy under reference conditions (Venning *et al* 2005, Mann *et al* 2017).

2.2.1. Fabrication

The PG is based on two monomers (2.5% w/w acrylamide and 2.5% w/w N,N'-methylene-bis-acrylamide) which are added as active components to a gelatin matrix (6% w/w Gelatin, 300 bloom, SIGMA Aldrich). Due to the high reactivity of the PG with oxygen the gel was flushed with nitrogen for 1 min to reduce the amount of dissolved oxygen (De Deene *et al* 2002) and 5 mM bis[tetrakis(hydroxymethyl)phosphonium] chloride (THPC) was added as an antioxidant. To protect the gel from light-induced polymerization (Koeva *et al* 2009), the gel containers were enwrapped in aluminum foil. Afterwards, they were placed in a desiccator, which was flushed with nitrogen for 10 min and stored in a refrigerator at 4 °C for 20–24 h. The gel containers were then removed 4 h prior to irradiation to adapt to room temperature.

2.2.2. MRI evaluation

48 h after irradiation, the gel containers were evaluated on a diagnostic 3T Magnetom Prisma^{fit} (Siemens Healthineers, Erlangen, Germany). For temperature constancy within ± 0.1 °C during MRI measurement, the containers were placed in a dedicated water-flow phantom (Mann *et al* 2017). For quantitative R_2 measurement, the phantom was scanned within a 64-channel head/neck coil using a multispin-echo sequence with 32 equidistant echoes and echo times of $TE = 22.5\text{--}720.0$ ms and an echo spacing of 22.5 ms. The scans were performed with a repetition time $TR = 10000$ ms to avoid influences of T_1 -relaxation, a resolution of $1.0 \times 1.0 \times 1.0$ mm³, and a band width of $BW = 130$ Hz/pixel. Furthermore, an additional high-resolution ($0.5 \times 0.5 \times 0.5$ mm³) 3D-image was acquired for registration purposes to compare the measured 3D PG dose distribution with the planned dose (see section 2.2.3). This was performed with a standard true fast imaging sequence with steady state precession (TrueFISP) (Scheffler and Hennig 2003, Chavhan *et al* 2008) as implemented by the MRI vendor using the parameters $TR = 11.68$ ms, $TE = 5.84$ ms, number of averages = 2, and a flip angle of 70°. For this scan, the water flow in the phantom was turned off to avoid flow artifacts.

2.2.3. Post-processing

The MR data was transferred to a personal computer and processed using an in-house developed Matlab (The Mathworks Inc., Natick, USA)-based PG evaluation tool (Mann *et al* 2017) to pixel wise calculate the spin-spin relaxation rate $R_2 = 1/T_2$ and generate R_2 maps. An edge conserving total variation filter (Rudin *et al* 1992) was used for noise reduction while steep dose gradients are conserved (Mann 2017). Absolute dose maps were

generated using the mono-exponential calibration curve, which was previously renormalized according to the high dose region in the treatment plan (De Deene and Vandecasteele 2013, Vandecasteele and De Deene 2013, Mann *et al* 2017). Afterwards, co-registration of the MR-images for PG evaluation to the planning MR-images of the MR-Linac was performed on the image processing platform MITK (Nolden *et al* 2013) using a point-based *RigidClosedForm3D* b-Spline 3rd order interpolation algorithm as implemented by the software and three uniquely defined landmarks on the surface of the gel containers. A 3D γ -map analysis (Low *et al* 1998) was performed of the TPS-calculated and measured dose distributions in the commercial software VeriSoft (PTW, Freiburg, Germany) using a passing criterion of 3%/3 mm (dose difference with respect to the local dose/distance-to-agreement) and taking only dose levels larger than 10% of the maximum dose into account. The results of the γ -map analysis are presented as passing rates, i.e. the percentage of evaluated voxels that meets the gamma criterion.

2.3. Online adaptive MRgRT

2.3.1. General treatment workflow

The online adaptive treatment workflow to be tested in this study is visualized in figure 3. In this possible adaption workflow, first CT and MR scans of the patient are performed (pre-treatment imaging) with the MRI being acquired at the MR-Linac. For treatment planning, the CT is registered to the MRI and an electron density map (pseudo-CT) is created for dose calculation. Structures used for planning are now delineated based on the pre-treatment MRI and a treatment plan is calculated based on the generated pseudo-CT. For the actual treatment, the patient is positioned again on the couch of the MR-Linac and an additional MRI (termed as online MRI) is acquired at each treatment session (Raaymakers *et al* 2017). To correct for anatomical changes, the treatment plan is adapted online to the current patient anatomy using the information of the online MRI and the previously generated treatment plan. For this, the pre-treatment MRI is registered deformably to this online MRI and the contours are transferred (Paganelli *et al* 2018). Using the resulting deformation, the electron density map is deformed accordingly to generate a pseudo-CT of the actual anatomical situation. Changes of the tumour position are first corrected by a setup correction. If there are further clinically relevant anatomical changes, the initial treatment plan is adapted and the new treatment plan is delivered to the patient.

2.3.2. End-to-end test of an online adaptive MRgRT treatment procedure

The AQUARIUM was used to perform an end-to-end test of an online adaptive treatment procedure at a clinical 0.35 T MR-integrated 6 MV flattening filter free linear accelerator (MR-Linac, MRIdian[®] Linac, ViewRay, Inc., Oakwood Village, OH, USA). For this, the AQUARIUM was used in two different settings (table 1). As a preparation, a pre-treatment CT and MRI of the phantom in the reference setting were acquired and a treatment plan was generated. After planning, the AQUARIUM was positioned again at the MR-Linac and after an image-based setup correction, it was irradiated with a nominal dose rate of 630 MU/min under three different conditions: (i) the AQUARIUM being in the reference setting, (ii) after changing the AQUARIUM setting to the displaced setting without adapting the treatment plan, and (iii) after changing the AQUARIUM setting to the displaced setting and adapting the treatment plan online to the new phantom setting. For each experiment (i)–(iii), a new set of PG containers for both tumour volume and OAR was used and the AQUARIUM setting was exactly reproduced. The different steps of the treatment workflow including the online adaption are described in the following.

2.3.2.1. CT imaging

A pre-treatment CT was acquired for treatment planning at a SOMATOM confidence RT Pro (Siemens Healthineers, Erlangen, Germany) scanner using the following parameters: voltage 120 kVp, current 216 mAs, slice thickness 1 mm, and a resolution of $1 \times 1 \text{ mm}^2$.

2.3.2.2. MR imaging

A pre-treatment MRI was performed directly at the MR-Linac ($B_0 = 0.35 \text{ T}$) for treatment planning using the surface flex coil with 12 receiver channels of the MR-Linac system. A standard TrueFISP sequence as implemented by the vendor was applied with a field of view (FOV) of $35.0 \times 36.0 \times 40.0 \text{ cm}^3$, TR = 1.45 ms, TE = 3.35 ms, BW = 537 Hz/pixel, slice thickness = 0.15 cm, resolution of $0.15 \times 0.15 \text{ cm}^2$, flip angle = 60° , and an acquisition time of 92 s.

2.3.2.3. Treatment planning

For treatment planning, the pre-treatment CT of the AQUARIUM in reference setting was registered to the corresponding pre-treatment MRI. As the configuration of the AQUARIUM was exactly the same in both images, a rigid registration was used to simulate optimal irradiation conditions. An intensity modulated radiotherapy (IMRT) treatment plan was calculated using the treatment planning system (TPS) of the MR-Linac with a dose

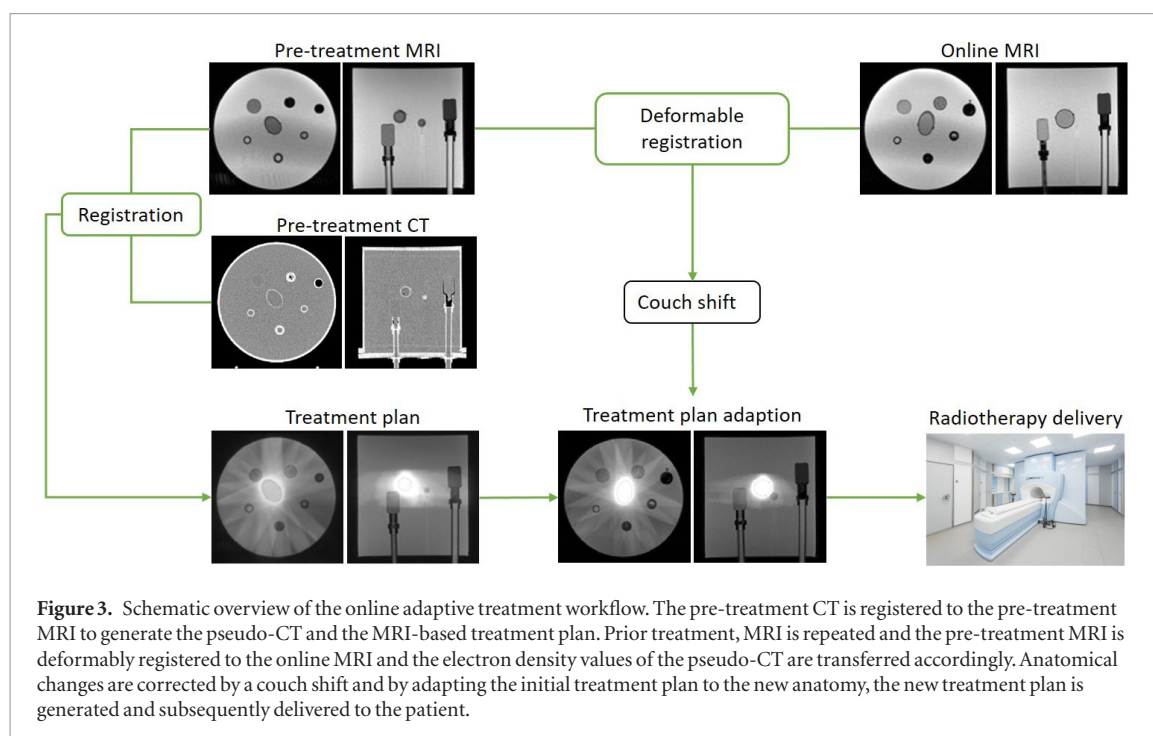


Table 1. Setting of the AQUARIUM structures used for measurement (ii) and (iii) relative to the reference setting (measurement (i)). The changes are given as longitudinal shifts (Δz) and rotations ($\Delta\alpha$) of each rod (see figure 1(b)).

Rod	Structure	Modified setting relative to reference setting	
		Δz [mm]	$\Delta\alpha$ [°]
1	PG-filled tumour	0.0	-40
2	MR contrast sphere 25 mm	10.0	0
3	CT contrast 'bone'	10.0	-70
4	MR contrast sphere 20 mm	10.0	0
5	CT contrast 'air'	-10.0	50
6	PG-filled OAR	-10.0	0
7	MR contrast Barex™ vial	-10.0	0

calculation grid of 0.2 cm. The treatment plan was optimized to irradiate the PG-filled tumour at the centre of the phantom with nineteen equally spaced beams prescribing a homogenous dose of 4 Gy. The PG in the target was delineated as the gross target volume (GTV) and a uniform margin of 3 mm was added to define the planning target volume (PTV). The following objectives were used for optimization: $V_{4.00 \text{ Gy}} \geq 50\%$, $V_{3.80 \text{ Gy}} > 95\%$, $V_{4.28 \text{ Gy}} < 1\%$ of the PTV and $V_{1.00 \text{ Gy}} < 30\%$, $V_{2.00 \text{ Gy}} < 1.00 \text{ cm}^3$ of the OAR ($V_{x \text{ Gy}}$ being the volume in % or cm^3 receiving more than x Gy). The dose volume parameters achieved for the initial treatment plan with the AQUARIUM in reference position are displayed in table 2. The dose calculation was performed based on the electron density of the pseudo-CT.

2.3.2.4. Irradiation workflow

Prior to irradiation, an additional MRI was acquired using the same parameters as for the pre-treatment MRI. Subsequently, irradiations were performed under the three different conditions:

- (i) *The AQUARIUM in reference setting.* The AQUARIUM in the reference setting was aligned at the MR-Linac by means of the laser-system and moved to the isocentre position. Then, an online MRI was acquired and a setup correction was derived by rigidly registering the planning to the online MRI. After realizing the setup correction by a couch shift, the PG tumour was irradiated without any adaption of the treatment plan.
- (ii) *The AQUARIUM in displaced setting without plan adaption.* In the second experiment, the PG container were replaced and the configuration of the AQUARIUM was changed to the displaced setting (table 1). After positioning of the AQUARIUM at the MR-Linac, an online MRI was acquired and the

Table 2. Dose volume objectives used for treatment plan optimization and the actually values obtained for the treatment plans of the three irradiation experiments (i)–(iii).

	PTV			OAR	
	$V_{4.00\text{ Gy}} [\%]$	$V_{3.80\text{ Gy}} [\%]$	$V_{4.28\text{ Gy}} [\%]$	$V_{1.00\text{ Gy}} [\%]$	$V_{2.00\text{ Gy}} [\text{cm}^3]$
Treatment plan optimization	≥ 50.00	> 95.00	< 1.00	< 30.00	< 1.00
(i) reference setting	54.08	98.11	0.00	23.41	0.13
(ii) displaced setting without plan adaption	20.74	43.80	0.16	40.58	1.47
(iii) displaced setting with plan adaption	52.12	97.47	0.00	32.22	0.00

planning MRI was registered to the online MRI using the intensity-based deformable registration algorithm as implemented by the vendor (Bohoudi *et al* 2017) to transfer the contours of the treatment plan to the actual MRI data set. For this, the advanced registration mode of the system was used with the following parameters: deformation in both ways, tissue stiffness = 1, number of pyramids = 2, downsampling method = minimum, final grid size = 6, max. final iterations = 10, max. intermediate iterations = 8, and contour smoothing = 2. After applying an image-derived couch shift, the treatment plan was delivered without any adaption. Finally, the dose distribution was recalculated on the actual MRI without reoptimization using the respective pseudo-CT.

- (iii) *The AQUARIUM in displaced setting with plan adaption.* In the third experiment, the PG container were again replaced while keeping the displaced setting of the AQUARIUM (table 1). The deformable registration was performed in the same way as in (ii) and after applying an image-based couch shift, the treatment plan was adapted to the new configuration of the AQUARIUM using the same optimization objectives as for the initial treatment plan. The adapted treatment plan was then delivered to the phantom.

3. Results

3.1. Deformable image registration

Qualitative evaluation revealed that the deformable image registration algorithm was able to deform the planning MRI of the AQUARIUM in the reference setting to the online MRI of the AQUARIUM in the displaced setting. All shifted and rotated structures were accurately matched. The corresponding deformation vector field was then applied to the contours and the treatment planning CT to generate the pseudo-CT required for dose calculation on the actual geometry. No artefacts were found in the deformed images. All deformed contours matched well the corresponding structures in the online MRI, in the deformed planning MRI, and in the pseudo-CT.

3.2. Treatment plan evaluation

The dose volume parameters of the three treatment plans delivered to the AQUARIUM are depicted in table 2 and figure 4 displays the corresponding dose volume histograms (DVH). While all dose objectives were met for the AQUARIUM in reference setting (i), application of the same plan for the displaced setting (ii) lead to a clear under-dosage of the PTV (43.80% at 3.80 Gy) and an over-dosage in the OAR (40.58% at 1.00 Gy). In contrast, applying the adapted plan to the AQUARIUM in the displaced setting (iii), the dose distribution was restored and the dose objectives in the PTV were met. In addition, the over-dosage in the OAR was reduced again (32.22% at 1.00 Gy).

3.3. PG evaluation

Figure 5 displays representative dose profiles for the PG-filled tumour and OAR measured in the AQUARIUM in reference setting when delivering the initial treatment plan (i). No significant dose deviation from the prescribed dose was found in the tumour and the dose volume parameters of the OAR met the objectives used for plan optimization. This is also reflected by the dose calculation, which agrees well with the measurement. Comparing measurement and calculation results in 3D passing rates of the γ -index of 96.4% and 93.7% with only a few voxels with absolute dose differences of up to 0.25 Gy and 0.12 Gy for the tumour and the OAR, respectively.

Figure 6 shows representative dose profiles for the PG-filled tumour and OAR measured in the AQUARIUM in displaced setting when delivering the initial treatment plan (ii). As a result, a significant under-dosage down to 45% of the planned dose was measured in the PG tumour while the OAR experienced a large over-dosage of up to 180% of the initially planned dose. These results correspond well with the dose distribution recalculated for the new geometry. Comparing measurement and calculation results in 3D passing rates of 96.1% and 94.7% with only a few voxels with absolute dose differences of up to 0.30 Gy and 0.18 Gy in the PG tumour and OAR, respectively.

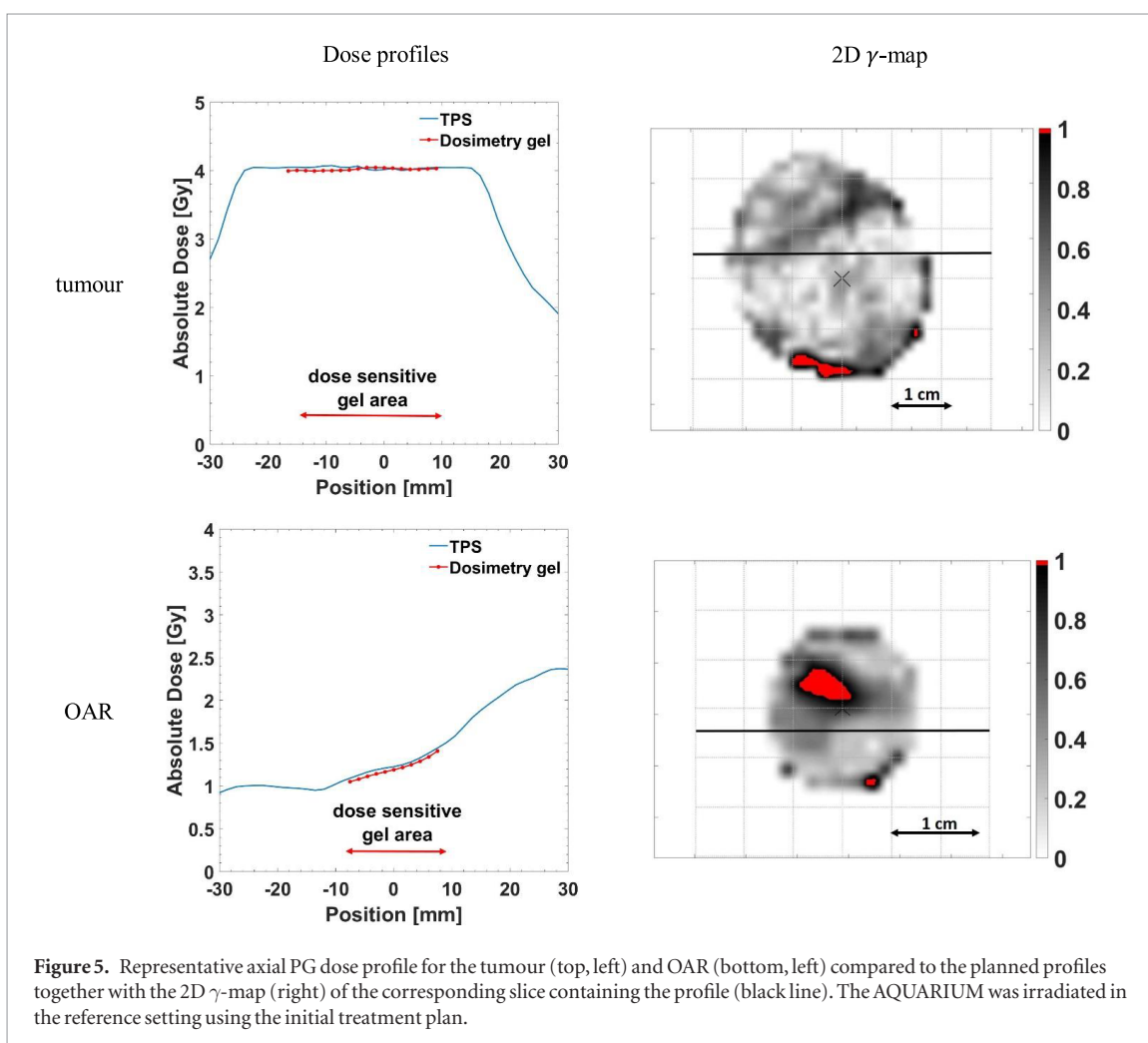
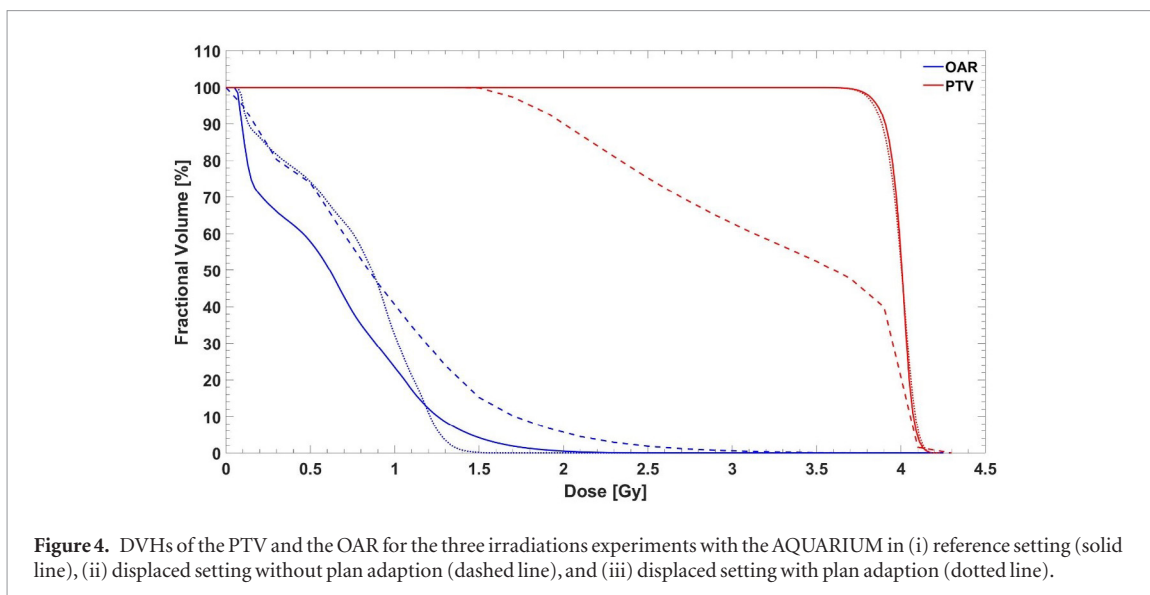
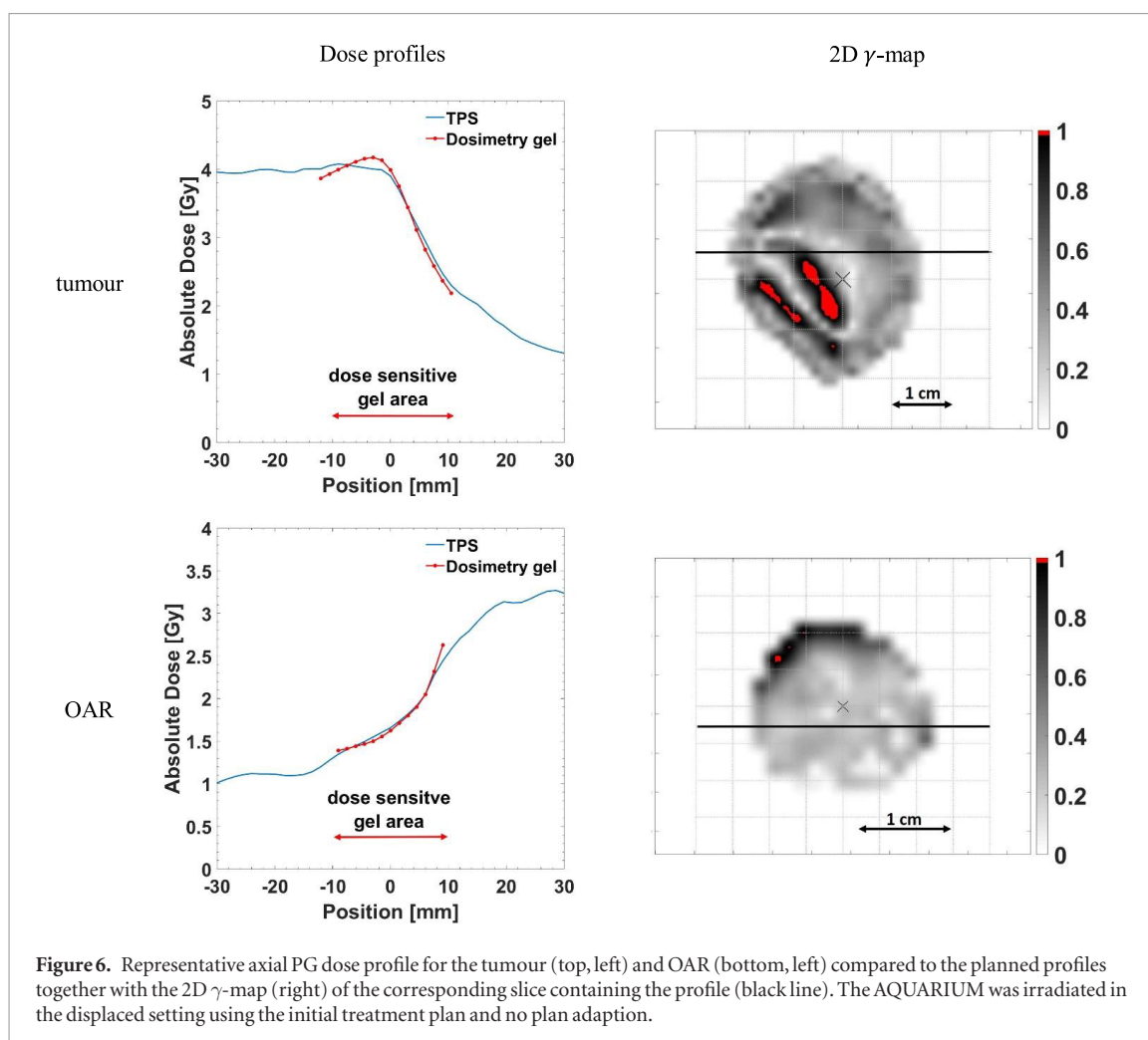


Figure 7 shows representative dose profiles for the PG-filled tumour and OAR measured in the AQUARIUM in displaced setting when delivering the adapted treatment plan (iii). The online re-optimization of the treatment plan restored the dose distribution. No significant dose deviation from the prescribed dose was found in the tumour and the dose levels in the OAR were comparable to the case, when the AQUARIUM was irradiated in the reference setting using the initial treatment plan. This is also reflected by the dose calculation, which agrees well with the measurement. Comparing measurement and calculation results in 3D passing rates of 93.1% and 94.1% with only a few voxels with absolute dose difference of up to 0.25 Gy and 0.12 Gy in the PG tumour and OAR, respectively.

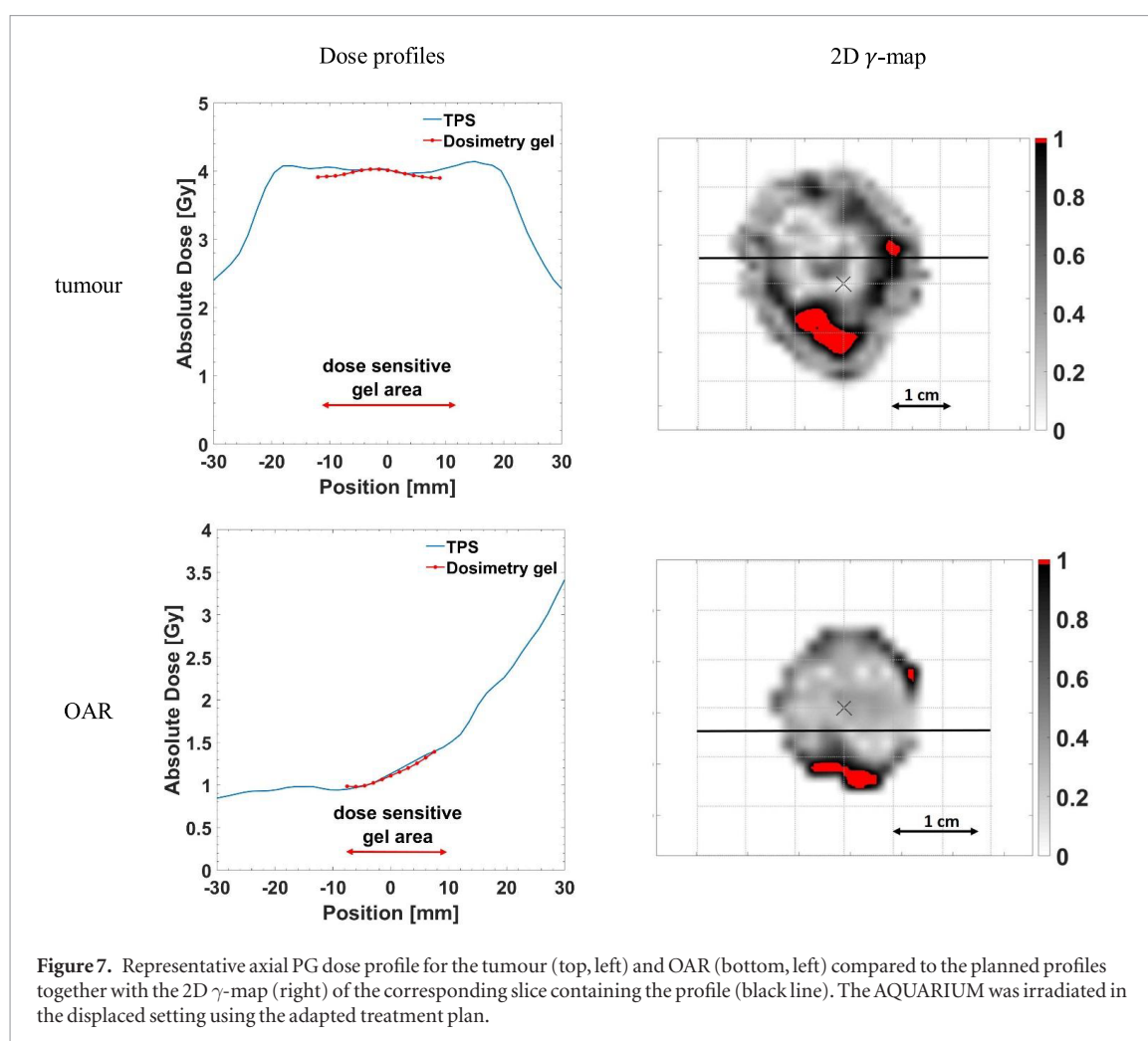


4. Discussion

In this study, an end-to-end test of an online adaptive treatment workflow was performed at an MR-Linac using the newly developed AQUARIUM. The new phantom allows simulating the complete workflow including the validation of the implemented image registration algorithms, the online adaption of the treatment plan and the verification of the dose delivery. To our knowledge, already existing phantoms (e.g. StereoPHANTM by Sun Nuclear Corp, Lucy 3D[®] QA Phantom by Standard Imaging Inc, QUASARTM MRI^{4D} by Modus Medical Devices Inc., Niebuhr *et al* 2019) used for end-to-end testing in various radiotherapy treatment procedures are either static, do not resemble anthropomorphic image contrasts in CT and MRI, focused on intra-fractional motion, or are not able to simulate anatomical changes in a highly reproducible way. As compared to the existing phantoms, the AQUARIUM is capable of simulating inter-fractional anatomical changes in a realistic and reproducible manner and it provides anthropomorphic imaging contrasts in both CT and MRI. In this work, the image registration algorithm was challenged by using adjustable irregular geometric structures having anthropomorphic image contrast. The reproducible setting of the structure configuration is ensured by scales allowing for adjustments with an accuracy of better than 1 mm and 2.5°, respectively, if settings defined by the scale marks are used (figure 1(b)). For dose measurements, it is possible to use 3D polymer gels, ionization chambers or thermoluminescence detectors (TLD) that can be inserted or attached to the tumour or OAR structures.

Experiments in this study were performed at the ViewRay MRIdian[®] Linac machine using a magnetic field strength of $B_0 = 0.35$ T. However, the use of the AQUARIUM is not limited to this device. All phantom materials are as well compatible with higher magnetic field strengths used in other MR-Linac devices. This makes the phantom a versatile tool for comparative end-to-end tests at different MR-Linac centres. However, higher magnetic field strengths might induce additional image artefacts in specific imaging sequences not being observed at $B_0 = 0.35$ T. These image artefacts could have an impact on the image registration accuracy and would have to be evaluated when using the AQUARIUM at higher field strengths.

In this work, three irradiation experiments were performed. While experiment (i) acts as a reference measurement under ideal conditions, where no adaption was necessary, (ii) represents a negative control demonstrating



the effect on the dose distribution, when geometrical changes are not considered by treatment plan adaptations. Experiment (iii), finally, represents an end-to-end test of the clinically intended adaptive treatment workflow.

In this study, the parameters of the deformable image registration algorithm were optimized to cope with the geometrical changes in the AQUARIUM. To register the pre-treatment CT with the pre-treatment MRI, a rigid registration was chosen, since there were no displacements within the phantom. Hence, the two images were perfectly aligned after registration allowing for treatment planning under ideal conditions. This was also the case for the registration of the pre-treatment to the online MRI in experiment (i). In the irradiation experiments (ii) and (iii), the pre-treatment and the online MRI were registered deformably and the parameters of the algorithm were optimized until all structures were fully aligned and the treatment planning contours were deformed using the resulting deformation vector fields. In this study, the choice of the downsampling method had the largest impact on registration quality. Similar to a real patient treatment, where a physician has to check the transferred contours prior treatment, we also checked this for the new phantom geometry. However, the systematic evaluation of the registration algorithms as well as the identification of its limitations was beyond the scope of this study and requires further work. This also includes testing of the deformable registration algorithm for other scenarios such as tumour growth or shrinkage, which may be simulated using the AQUARIUM with differently shaped and sized 3D printed tumour structures. For this purpose also flexible inserts may be inserted to the AQUARIUM to simulate organ deformations (Niebuhr *et al* 2019).

Comparing the results of the 3D dose measurements clearly demonstrates the benefit of the online treatment plan adaption for the shifts and rotations of the phantom structures employed in our study: The deteriorated dose distribution within the PTV and the significant increased dose within the OAR obtained in experiment (ii) were completely restored by the adapted treatment plan in experiment (iii) leading to a uniform dose in the PTV and a significantly reduced dose in the OAR. Both dose distributions agree well with those of the reference experiment (i), where no adaption was necessary. This is also reflected by the dose volume parameters (table 2) and the DVH (figure 4).

For the present study, it was important to capture the dose distribution within the tumour and OAR in 3D. As this is not feasible with point-like detectors such as ionization chambers or TL-detectors, PG was used. As the dosimetric accuracy of PG is usually lower than that of standard detectors, high efforts were taken to be as

accurate as possible. Interestingly, measured and planned dose distributions agreed very well for the standard irradiation as well as in the new geometry in experiment (ii) and (iii). This is demonstrated by the γ passing rates of 96.4%, 96.1%, and 93.1% in the tumour and 93.7%, 94.7%, and 94.1% in the OAR for irradiation (i)–(iii), respectively. Maximum deviations relative to the planned dose were in the order of 0.1–0.3 Gy, which can be considered as small for PG measurements (Baldock *et al* 2010) and are within the overall dose resolution of gels (Baldock *et al* 2001, 2010). The registration of the measured dose distributions within the PG containers to the phantom images allows for a geometric validation of the planned dose distribution. The good agreement between measured and calculated dose confirms that our PG measurements are reliable and that the combination of the AQUARIUM with PG-filled structures can be used to perform full end-to-end tests of adaptive treatment procedures at MR-Linac devices. Moreover, due to its generality, the method can also be applied to verify image-guided treatment workflows at other modern image-guided radiotherapy devices, such as conventional Linacs, Tomotherapy (Mackie *et al* 1999), or Cyberknife (Kilby *et al* 2010) machines.

For the 3D dose evaluation, it should be kept in mind that the calibration curve was normalized based on a reference point within the calculated dose distribution for the AQUARIUM, which is a standard procedure in PG dosimetry (De Deene and Vandecasteele 2013). A recently published method by Mann *et al* (2019) suggested a new method, which uses TLDs within the same experiment to normalize the calibration curve. In principle, this method can also be adapted to the present experimental setup by additionally attaching several TLDs around both the OAR and target structures. Since both PG and TLDs measure time-integrated doses (De Deene and Vandecasteele 2013, Murthy 2013), such a combined dosimetric system within the AQUARIUM may also be used to simulate a whole fractionated treatment scheme with anatomical changes between the fractions being corrected by online adaptations of the treatment plan.

As a major draw-back, quantitative PAGAT dosimetry requires up to 48 hours until the polymerization process stabilizes (Vandecasteele and De Deene 2013). It is therefore not feasible to evaluate the PG at the MR-Linac directly after irradiation. However, as recently shown by Dorsch *et al* (2019), evaluation of geometrical parameters such as isocenter alignment and image distortions directly after irradiation is feasible and exhibits results comparable to those of films. This would allow the visualization of sharp dose gradients, e.g. an under-dosage within OARs directly after irradiation as long as no absolute dose levels are required.

In our treatment simulation there was no independent online quality assurance (QA) of the adapted treatment plan. Although this is a required step in patient treatment, the PG measurements in the AQUARIUM confirmed that the re-optimization of the treatment plan and dose delivery was correctly performed. In this study, we developed an end-to-end test for the whole chain of an online adaptive treatment workflow and successfully performed a dosimetric validation.

5. Conclusion

In this study, a new phantom with adjustable anthropomorphic structures has been developed. The phantom was used to perform an end-to-end test of an online adaptive treatment procedure at a 0.35 T MR-Linac by simulating the complete workflow including the validation of image registration, treatment plan adaption and dose delivery. 3D dosimetry gel measurements confirmed that the adapted treatment plan resulted in dose distributions in the tumour and the OAR that were well-comparable to a static case, where no adaption of the treatment plan was necessary. The developed phantom can be used to perform end-to-end tests of online adaptive treatment procedures at MR-Linac devices before introducing them to patients.

Acknowledgments

This work was supported by the EMPIR programme co-financed by the Participating States and from the European Union's Horizon 2020 research and innovation programme. We would like to thank the German Research Council (DFG) for the funding of the MR-Linac device. In addition, the authors would like to thank Professor Dr K Kopka for providing the lab space to produce the polymer gel.

ORCID iDs

A Elter  <https://orcid.org/0000-0002-0295-9931>

S Dorsch  <https://orcid.org/0000-0002-8185-8644>

P Mann  <https://orcid.org/0000-0002-2857-4861>

References

American Association of Physicists in Medicine 2010 AAPM Report No. 100 Acceptance Testing and Quality Assurance Procedures for Magnetic Resonance Imaging Facilities (College Park, MD: American Association of Physicists in Medicine)

- Baldock C, De Deene Y, Doran S, Ibbott G, Jirasek A, Lepage M, McAuley K B, Oldham M and Schreiner L J 2010 Polymer gel dosimetry *Phys. Med. Biol.* **55** R1–63
- Baldock C, Lepage M, Bäck S Å J, Murry P J, Jayasekera P M, Porter D and Kron T 2001 Dose resolution in radiotherapy polymer gel dosimetry: effect of echo spacing in MRI pulse sequence *Phys. Med. Biol.* **46** 449–60
- Barker J L et al 2004 Quantification of volumetric and geometric changes occurring during fractionated radiotherapy for head-and-neck cancer using an integrated CT/linear accelerator system *Int. J. Radiat. Oncol. Biol. Phys.* **59** 960–70
- Bohoudi O, Bruynzeel A M E, Senan S, Cuijpers J P, Slotman B J, Lagerwaard F J and Palacios M A 2017 Fast and robust online adaptive planning in stereotactic MR-guided adaptive radiation therapy (SMART) for pancreatic cancer *Radiother. Oncol.* **125** 439–44
- Chang A E, Matory Y L, Dwyer A J, Hill S C, Girton M E, Steinberg S M, Knop R H, Frank J A, Hyams D and Doppman J L 1987 Magnetic resonance imaging versus computed tomography in the evaluation of soft tissue tumors of the extremities *Ann. Surg.* **205** 340–48
- Chavhan G B, Babyn P S, Jankharia B G, Cheng H M and Shroff M M 2008 Steady-state MR imaging sequences: physics, classification, and clinical applications *Radiograph.* **28** 1147–60
- Dawson L A and Sharpe M B 2006 Image-guided radiotherapy: rationale, benefits, and limitations *Lancet Oncol.* **7** 848–58
- De Deene Y and Vandecasteele J 2013 On the reliability of 3D Gel dosimetry *J. Phys.: Conf. Ser.* **444** 012015
- De Deene Y, Hurley C, Venning A, Vergote K, Mather M, Healy B J and Baldock C 2002 A basic study of some normoxic polymer gel dosimeters *Phys. Med. Biol.* **47** 3441–63
- De Deene Y, Vergote K, Claeys C and De Wagter C 2006 The fundamental radiation properties of normoxic polymer gel dosimeters: a comparison between a methacrylic acid based gel and acrylamide based gels *Phys. Med. Biol.* **51** 653–73
- Dorsch S, Mann P, Elter A, Runz A, Spindeldreier C K, Klüter S and Karger C P 2019 Measurement of isocenter alignment accuracy and image distortion of an 0.35 T MR-linac system *Phys. Med. Biol.* **64** 205011
- Elter A, Dorsch S, Mann P, Runz A, Johnen W and Karger C P 2019 Compatibility of 3D printing materials and printing techniques with PAGAT gel dosimetry *Phys. Med. Biol.* **64** 04NT02
- Fallone B G, Murray B, Rathee S, Stanescu T, Steciw S, Vidakovic S, Blosser E and Tymofichuk D 2009 First MR images obtained during megavoltage photon irradiation from a prototype integrated linac-MR system *Med. Phys.* **36** 2084–8
- Green O L, Henke L E and Hugo G D 2019 Practical clinical workflows for online and offline adaptive radiation therapy *Semin. Radiat. Oncol.* **29** 219–27
- Hilts M, Audet C, Duzenli C and Jirasek A 2000 Polymer gel dosimetry using x-ray computed tomography: a feasibility study *Phys. Med. Biol.* **45** 2559–71
- Jaffray D A, Siewerdsen J H, Wong J W and Martinez A A 2002 Flat-panel cone-beam computed tomography for image-guided radiation therapy *Int. J. Radiat. Oncol. Biol. Phys.* **53** 1337–49
- Keall P J, Barton M and Crozier S 2014 The Australian magnetic resonance imaging-linac program *Semin. Radiat. Oncol.* **24** 203–6
- Kilby W, Dooley J R, Kuduvalli G, Sayeh S and Maurer C R 2010 The CyberKnife® robotic radiosurgery system in 2010 *Technol. Cancer Res. Trea.* **9** 433–52
- Klüter S 2019 Technical design and concept of a 0.35 T MR-linac *Clin. Transl. Radiat. Oncol.* **18** 98–101
- Koeva V I, Olding T, Jirasek A, Schreiner L J and McAuley K B 2009 Preliminary investigation of the NMR, optical and x-ray CT dose-response of polymer gel dosimeters incorporating cosolvents to improve dose sensitivity *Phys. Med. Biol.* **54** 2779–90
- Kontaxis C, Bol G H, Lagendijk J J W and Raaymakers B W 2015 A new methodology for inter- and intrafraction plan adaptation for the MR-linac *Phys. Med. Biol.* **60** 7485–97
- Kron T 2008 Reduction of margins in external beam radiotherapy *J. Med. Phys.* **33** 41–42
- Lagendijk J J W, Raaymakers B W, Raaijmakers A J E, Overweg J, Brown K J, Kerkhof E M, van der Put R W, Hardemark B, van Vulpen M and van der Heide U A 2008 MRI/linac integration *Radiother. Oncol.* **86** 25–9
- Lee H J, Roed Y, Venkataraman S, Carroll M and Ibbott G S 2017 Investigation of magnetic field effects on the dose-response of 3D dosimeters for magnetic resonance - image guided radiation therapy applications *Radiother. Oncol.* **125** 426–32
- Low D A, Harms W B, Mutic S and Purdy J A 1998 A technique for the quantitative evaluation of dose distributions *Med. Phys.* **25** 656–61
- Mackie T R, Balog J, Ruchala K, Shepard D, Aldridge S, Fitchard E, Reckwerdt P, Olivera G, McNutt T and Mehta M 1999 Tomotherapy *Semin. Radiat. Oncol.* **9** 108–17
- Mann P 2017 Development and implementation of 3D-dosimetric end-to-end tests in adaptive radiation therapy of moving tumors *PhD Thesis* Ruperto-Carola University of Heidelberg
- Mann P, Schwahofer A and Karger C P 2019 Absolute dosimetry with polymer gels—a TLD reference system *Phys. Med. Biol.* **64** 45010
- Mann P, Witte M, Moser T, Lang C, Runz A, Johnen W, Berger M, Biederer J and Karger C P 2017 3D dosimetric validation of motion compensation concepts in radiotherapy using an anthropomorphic dynamic lung phantom *Phys. Med. Biol.* **62** 573–95
- Martinez A A, Yan D, Lockman D, Brabbins D, Kota K, Sharpe M, Jaffray D A, Vicini F and Wong J 2001 Improvement in dose escalation using the process of adaptive radiotherapy combined with three-dimensional conformal or intensity-modulated beams for prostate cancer *Int. J. Radiat. Oncol. Biol. Phys.* **50** 1226–34
- Murthy K V R 2013 Thermoluminescence and its applications: a review *Defect Diffus. Forum* **347** 35–73
- Mutic S and Dempsey J F 2014 The viewray system: magnetic resonance-guided and controlled radiotherapy *Semin. Radiat. Oncol.* **24** 196–99
- Niebuhr N I, Johnen W, Echner G, Runz A, Bach M, Stoll M, Giske K, Greilich S and Pfaffenberger A 2019 The ADAM-pelvis phantom—an anthropomorphic, deformable and multimodal phantom for MRgRT *Phys. Med. Biol.* **64** 04NT05
- Niebuhr N I, Johnen W, Guldaglar T, Runz A, Echner G, Mann P, Mohler C, Pfaffenberger A, Jakel O and Greilich S 2016 Technical note: radiological properties of tissue surrogates used in a multimodality deformable pelvic phantom for MR-guided radiotherapy *Med. Phys.* **43** 908–16
- Njeh C F 2008 Tumor delineation: the weakest link in the search for accuracy in radiotherapy *J. Med. Phys.* **33** 136–40
- Nolden M et al 2013 The medical imaging interaction toolkit: challenges and advances *Int. J. Comput. Assist. Radiol. Surg.* **8** 607–20
- Paganelli C et al 2018 MRI-guidance for motion management in external beam radiotherapy: current status and future challenges *Phys. Med. Biol.* **63** 22TR03
- Raaymakers B W et al 2017 First patients treated with a 1.5 T MRI-linac: clinical proof of concept of a high-precision, high-field MRI guided radiotherapy treatment *Phys. Med. Biol.* **62** L41–50
- Rudin L I, Osher S and Fatemi E 1992 Nonlinear total variation based noise removal algorithms *Physica D* **60** 259–68
- Sandilos P et al 2004 Dose verification in clinical IMRT prostate incidents *Int. J. Radiat. Oncol. Biol. Phys.* **59** 1540–7
- Sarkar V, Huang L, Huang Y J, Szegeedi M W, Rassiah-Szegeedi P, Zhao H and Salter B J 2016 Head to head comparison of two commercial phantoms used for SRS QA *J. Radiosurg. SBRT* **4** 213–23
- Scheffler K and Hennig J 2003 Is TrueFISP a gradient-echo or a spin-echo sequence? *Magn. Reson. Med.* **49** 395–7
- Schreiner L J 2006 Dosimetry in modern radiation therapy: limitations and needs *J. Phys.: Conf. Ser.* **56** 1

- Schreiner L J 2015 True 3D chemical dosimetry (gels, plastics): development and clinical role *J. Phys.: Conf. Ser.* **573** 012003
- Sonke J, Aznar M and Rasch C 2019 Adaptive radiotherapy for anatomical changes *Semin. Radiat. Oncol.* **29** 245–57
- Tofts P S, Shuter B and Pope J M 1993 Ni-DTPA doped agarose gel—a phantom material for Gd-DTPA enhancement measurements *Magn. Reson. Imaging* **11** 125–33
- van Herk M 2004 Errors and margins in radiotherapy *Semin. Radiat. Oncol.* **14** 52–64
- Vandecasteele J and De Deene Y 2013 On the validity of 3D polymer gel dosimetry: I. Reproducibility study *Phys. Med. Biol.* **58** 19–42
- Venning A J, Hill B, Brindha S, Healy B J and Baldock C 2005 Investigation of the PAGAT polymer gel dosimeter using magnetic resonance imaging *Phys. Med. Biol.* **50** 3875–88
- Vergote K, De Deene Y, Duthoy W, De Gerssem W, De Neve W, Achten E and De Wagter C 2004 Validation and application of polymer gel dosimetry for the dose verification of an intensity-modulated arc therapy (IMAT) treatment *Phys. Med. Biol.* **49** 287–305
- Verhey L J, Goitein M, McNulty P, Munzenrider J E and Suit H D 1982 Precise positioning of patients for radiation therapy *Int. J. Radiat. Oncol. Biol. Phys.* **8** 289–94
- Yan D, Vicini F, Wong J and Martinez A 1997 Adaptive radiation therapy *Phys. Med. Biol.* **42** 123–32
- Zakjevskii V V, Knill C S, Rakowski J T and Snyder M G 2016 Development and evaluation of an end-to-end test for head and neck IMRT with a novel multiple-dosimetric modality phantom *J. Appl. Clin. Med. Phys.* **17** 497–510

2.7 Publication VI

END-TO-END TEST FOR FRACTIONATED ONLINE ADAPTIVE MR-GUIDED RADIOTHERAPY USING A DEFORMABLE ANTHROPOMORPHIC PELVIS PHANTOM

Authors: Alina Elter, Carolin Rippke, Wibke Johnen, Philipp Mann, Emily Hellwich, Andrea Schwahofer, Stefan Dorsch, Carolin Buchele, Sebastian Klüter and Christian P. Karger

Status (12/2021): Accepted

Journal reference: *Physics in Medicine & Biology*

DOI: 10.1088/1361-6560/ac3e0c

Copyright: © Institute of Physics and Engineering in Medicine. Reproduced with permission. All rights reserved.

This Accepted Manuscript is available for reuse under a CC BY-NC-ND 3.0 license (<https://creativecommons.org/licenses/by-nc-nd/3.0/>) after the 12 month embargo period provided that all the terms of the license are adhered to. This is the Accepted Manuscript version of an article accepted for publication in *Physics in Medicine and Biology*. IOP Publishing Ltd is not responsible for any errors or omissions in this version of the manuscript or any version derived from it. The Version of Record is available online at <https://doi.org/10.1088/1361-6560/ac3e0c>. No changes have been made.

Contribution: In this study, an end-to-end test for fractionated online adaptive MR-guided radiotherapy was performed using the anthropomorphic male pelvis phantom ADAM-PETer. For this, I have adapted the phantom with the support of Wibke Johnen to perform (i) polymer gel dosimetry and thermoluminescence detector measurements in the prostate and (ii) polymer gel dosimetry measurements in the rectum. Five treatment fractions were applied to the phantom with different bladder and rectum fillings, which represents a realistic patient situation. I conducted all preparations, measurements and evaluations with support of the co-authors. This included the preparation and evaluation of the dosimetry gel, the calibration and evaluation of thermoluminescence detectors, treatment planning and adaption in cooperation with Carolin Rippke, the irradiation as well as the final analysis of the results. Furthermore, I have written the manuscript, prepared all graphics and revised the manuscript based on the reviewer's comments with support from Prof. Christian P. Karger.

ACCEPTED MANUSCRIPT

End-to-end test for fractionated online adaptive MR-guided radiotherapy using a deformable anthropomorphic pelvis phantom

To cite this article before publication: Alina Elter *et al* 2021 *Phys. Med. Biol.* in press <https://doi.org/10.1088/1361-6560/ac3e0c>

Manuscript version: Accepted Manuscript

Accepted Manuscript is “the version of the article accepted for publication including all changes made as a result of the peer review process, and which may also include the addition to the article by IOP Publishing of a header, an article ID, a cover sheet and/or an ‘Accepted Manuscript’ watermark, but excluding any other editing, typesetting or other changes made by IOP Publishing and/or its licensors”

This Accepted Manuscript is © 2021 Institute of Physics and Engineering in Medicine.

During the embargo period (the 12 month period from the publication of the Version of Record of this article), the Accepted Manuscript is fully protected by copyright and cannot be reused or reposted elsewhere.

As the Version of Record of this article is going to be / has been published on a subscription basis, this Accepted Manuscript is available for reuse under a CC BY-NC-ND 3.0 licence after the 12 month embargo period.

After the embargo period, everyone is permitted to use copy and redistribute this article for non-commercial purposes only, provided that they adhere to all the terms of the licence <https://creativecommons.org/licenses/by-nc-nd/3.0>

Although reasonable endeavours have been taken to obtain all necessary permissions from third parties to include their copyrighted content within this article, their full citation and copyright line may not be present in this Accepted Manuscript version. Before using any content from this article, please refer to the Version of Record on IOPscience once published for full citation and copyright details, as permissions will likely be required. All third party content is fully copyright protected, unless specifically stated otherwise in the figure caption in the Version of Record.

View the [article online](#) for updates and enhancements.

End-to-end test for fractionated online adaptive MR-guided radiotherapy using a deformable anthropomorphic pelvis phantom

A Elter^{1,2,4}, C Rippke^{3,4,5}, W Johnen^{1,4}, P Mann^{1,4}, E Hellwich^{1,4}, A Schwahofer^{1,4}, S Dorsch^{1,4}, C Buchele^{3,4,5}, S Klüter^{3,4} and C P Karger^{1,4}

¹ Department of Medical Physics in Radiation Oncology, German Cancer Research Center (DKFZ), INF 280, 69120 Heidelberg, Germany

² Faculty of Physics and Astronomy, Heidelberg University, Heidelberg, Germany

³ Department of Radiation Oncology, University Hospital Heidelberg, INF 400, 69120 Heidelberg, Germany

⁴ National Center for Radiation Research in Oncology (NCRO), Heidelberg Institute for Radiation Oncology (HIRO), Heidelberg, Germany

⁵ Medical Faculty, Heidelberg University, Heidelberg, Germany

E-mail: a.elter@dkfz.de

Received xxxxxx

Accepted for publication xxxxxx

Published xxxxxx

Abstract

Objective: In MR-guided radiotherapy (MRgRT) for prostate cancer treatments inter-fractional anatomy changes such as bladder and rectum fillings may be corrected by an online adaption of the treatment plan. To clinically implement such complex treatment procedures, however, specific end-to-end tests are required that are able to validate the overall accuracy of all treatment steps from pre-treatment imaging to dose delivery.

Approach: In this study, an end-to-end test of a fractionated and online adapted MRgRT prostate irradiation was performed using the so-called ADAM-PETer phantom. The phantom was adapted to perform 3D polymer gel (PG) dosimetry in the prostate and rectum.

Furthermore, thermoluminescence detectors (TLDs) were placed at the center and on the surface of the prostate for additional dose measurements as well as for an external dose renormalization of the PG. For the end-to-end test, a total of five online adapted irradiations were applied in sequence with different bladder and rectum fillings, respectively.

Main results: A good agreement of measured and planned dose was found represented by high γ -index passing rates (3%/3 mm criterion) of the PG evaluation of 98.9% in the prostate and 93.7% in the rectum. TLDs used for PG renormalization at the center of the prostate showed a deviation of -2.3%.

Significance: The presented end-to-end test, which allows for 3D dose verification in the prostate and rectum, demonstrates the feasibility and accuracy of fractionated and online-adapted prostate irradiations in presence of inter-fractional anatomy changes. Such tests are of high clinical importance for the commissioning of new image-guided treatment procedures such as online adaptive MRgRT.

Keywords: Magnetic resonance-guided (adaptive) radiotherapy (MRgRT), inter-fractional motion, fractionated treatment, end-to-end test, deformable anthropomorphic pelvis phantom, 3D gel dosimetry (PAGAT), thermoluminescence detectors (TLD)

1. Introduction

Magnetic resonance (MR-) guided radiotherapy (RT, MRgRT) aims to deliver high treatment doses for tumour control while optimally sparing surrounding healthy tissue in presence of inter- and intra-fractional anatomical changes. Two MRgRT systems are currently available commercially, the 1.5 T Unity system (Elekta Instrument AB Stockholm, Sweden) (Raaymakers et al. 2017, Raaymakers et al. 2009, Winkel et al. 2019) and the 0.35 T MRIdian Linac (Viewray, USA) (Klüter 2019, Mutic and Dempsey 2014). The excellent soft tissue contrast without additional radiation exposure from MR imaging (Chang et al. 1987) allows adapting the treatment plan according to the actual anatomical situation found in the online acquired MR images. This online adaption of the treatment plan prior to each fraction may enable the application of higher doses to the tumour while reducing safety margins that conventionally account for anatomical changes during the course of the treatment (van Herk 2004). Hence, an online adaption of the treatment plan may increase the radiation effectiveness of the tumour and decrease the risk of severe side effects by the reduction of the irradiated normal tissue volume. Especially RT treatments of the prostate may benefit largely from MR-guided online adaptive irradiations by sparing bladder and rectum as the main organs at risk (OAR), which are constantly changing their fillings (Tetar et al. 2019, Tocco et al. 2020).

Due to the complex treatment chain of adaptive MRgRT, it is essential to perform end-to-end tests to validate the accumulated accuracy of all steps from pre-treatment imaging to dose delivery. Such tests require phantoms allowing for reproducible changes of anatomical structures (inter- or intra-fractional changes) that have to be compensated by adapting the treatment plan, for anthropomorphic and artefact-free imaging contrast in computed tomography (CT) and MR imaging (MRI), and for accurate dose measurements to validate the dose delivery in 1D to 3D.

First end-to-end tests for online adaptive MRgRT treatments have already been published (Elter et al. 2019b, Hoffmans et al. 2020, Pappas et al. 2019, Stark et al. 2020). In Stark et al. (2020) a static and homogenous phantom without the possibility to change the geometry of inner structures was applied to test the online adaptive workflow in case of inter-fractional motion. Hoffmans et al. (2020) applied the anthropomorphic male pelvis phantom ADAM (Niebuhr et al. 2019) equipped with small pieces of radiochromic films at the interfaces of organ structures and performed a fractionated and online adapted irradiation of the prostate with different bladder and rectum fillings of the phantom for each fraction. However, the use of radiochromic film samples only allowed to measure the delivered dose at some selected positions in 2D. Pappas et al. applied polymer dosimetry gel in an anthropomorphic head phantom, however, this phantom again was static. In our previous study (Elter et al. 2019b), polymer gel (PG)-filled inserts were applied in the AQUARIUM phantom to measure the applied dose to the target volume as well as to an OAR-representing structure in 3D. While this phantom simulated inter-fractional anatomy changes highly reproducible, it did not represent real anthropomorphic geometries and, moreover, the end-to-end test included only a single fraction.

Other studies have suggested the use of thermoluminescence detectors (TLDs) to renormalize the absolute PG dose distribution (Mann et al. 2019, Schwahofer et al. 2020) as well as to combine PG and TLDs for dose measurements within the updated version of the ADAM phantom (ADAM-PETER, Marot et al. (2021)). Marot et al. (2021) applied the same phantom as used in the present study equipped with a PG-filled prostate and TLDs in the rectum. However, the phantom was used only statically without employing MR-guidance or online adaption of the treatment plan. As a main result, the study demonstrated the feasibility of PG and TLD measurement in the complex ADAM-PETER phantom.

In this study, the ADAM-PETER was equipped with PG-filled prostate and rectum inserts as well as with additional TLDs for point dose measurements at the center and on the surface of the prostate. An end-to-end test for a fractionated and online adapted MRgRT treatment in presence of inter-fractional anatomy changes was performed using (i) a deformable anthropomorphic pelvis phantom, (ii) dose measurements by 3D polymer gel dosimeters and TLDs in the prostate as well as in the rectum, (iii) simulated organ deformation and MR-based online-adaption of the treatment plan, and (iv) a fractionated irradiation.

2. Materials and Methods

2.1 Phantom

The experiment was carried out using the so-called ADAM-PETer (Anthropomorphic, Deformable And Multimodal pelvis phantom with positron emission tomography (PET) Extension for Radiotherapy), which was initially designed to perform a variety of different end-to-end tests in radiotherapy (Gillmann et al. 2021, Marot et al. 2021). In the present study, however, no PET measurements were performed and the included lymph node system was not used. The phantom is anthropomorphic with respect to organ shapes and imaging contrast in CT and MRI and allows for the insertion of different dosimeters. In this study, two small adaptations were made for the prostate and the rectum:

- (i) The prostate (figure 1a, volume 24 ml) was 3D printed with the Objet500 Connex3 3D printer (Stratasys, USA) using the VeroClear™ material that has been shown to be compatible with the PG used in this work (Elter et al. 2019a). At the center of the prostate, a holder has been included, which allows for insertion and removal of a TLD from the outside. This TLD allows for a renormalization of the dose distribution measured with PG (Mann et al. 2019, Schwahofer et al. 2020). Two additional TLDs enclosed in dedicated PMMA capsules were attached to the surface of the prostate using an additional 3D printed holder.
- (ii) A silicone rectum (figure 1b) as used in the original version of the ADAM phantom (Niebuhr et al. 2019) was inserted into the phantom due to a better long term stability as compared to the flexible 3D printed version described for ADAM-PETer (Gillmann et al. 2021). An additional 3D printed PG container (figure 1b, volume 8.5 ml) was placed in the rectum at the height of the prostate.

During the irradiation experiment, the bladder and the rectum balloon were filled with six different water (100 – 200 ml) and air volumes (0 – 20 ml), respectively, using externally attached syringes (table 1). The first set of fillings served for pre-irradiation imaging and treatment planning while the other five induced anatomical changes for the five treatment fractions.



Figure 1: CAD-drawings of the 3D printed prostate including the central TLD holder (1) and the two TLD holders on the surface (2) (a) as well as the ADAM-PETer phantom configured with the bladder (3), prostate (4) and rectum (5) including the 3D printed rectum insert (6) (b).

Table 1: Bladder and rectum fillings of the ADAM-PETer used for pre-irradiation imaging and treatment planning and for the five treatment fractions, respectively.

	Bladder (water) [ml]	Rectum balloon (air) [ml]
Pre-irradiation	170	15
Fraction 1	185	20
Fraction 2	150	5
Fraction 3	200	15
Fraction 4	100	10
Fraction 5	170	20

2.2 Dosimeter preparation

Two detector systems were used in this work: (i) PAGAT (PolyAcrylamide Gelatin gel fabricated at ATmospheric conditions) dosimetry gel and (ii) TLDs that are used to renormalize the PG dose distribution as described earlier (Mann et al. 2019, Schwahofer et al. 2020).

PAGAT exhibits a small dose-rate dependence and allows for in-house production at low costs and under atmospheric conditions (De Deene et al. 2006). The PG is evaluated by MRI employing a quantitative map of the R_2 relaxation rate (Baldock et al. 2010). The entire PG experiment workflow from production to evaluation is described in detail elsewhere (Elter et al. 2021). The PG was filled into the 3D printed prostate and rectum inserts and in addition, a set of ten Barex™ (VELOX GmbH, Germany) containers were filled with PG of the same production batch and were irradiated with known doses from 0 to 9 Gy in steps of 1 Gy to perform a R_2 -dose calibration for absolute dosimetry.

TLDs (TLD600, LiF:Mg,Ti, Harshaw, Thermofisher Scientific, USA) were inserted at the center and on the surface of the prostate for additional point dose measurements. The calibration and evaluation procedure of the TLDs has been described earlier (Schwahofer et al. 2020).

2.3 End-to-end testing

Using the ADAM-PETer phantom equipped with PG and TLDs for dose measurement, an end-to-end test was performed for a fractionated and online adapted MRgRT treatment. In this study, the MRIdian Linac system was used, which combines a 0.35 T MRI system with a 6 MV flattening filter free linear accelerator (Linac, MR-Linac). For the end-to-end test, an initial treatment plan was generated based on the pre-irradiation MR and CT images. The actual treatment was delivered in five directly consecutive fractions with the bladder and rectum filling being changed prior to each fraction (table 1) and for each fraction, the initial treatment plan was adapted according to an online MR image of the respective fraction. A schematic overview of the online adaptive workflow applied in this work is shown in figure 2.

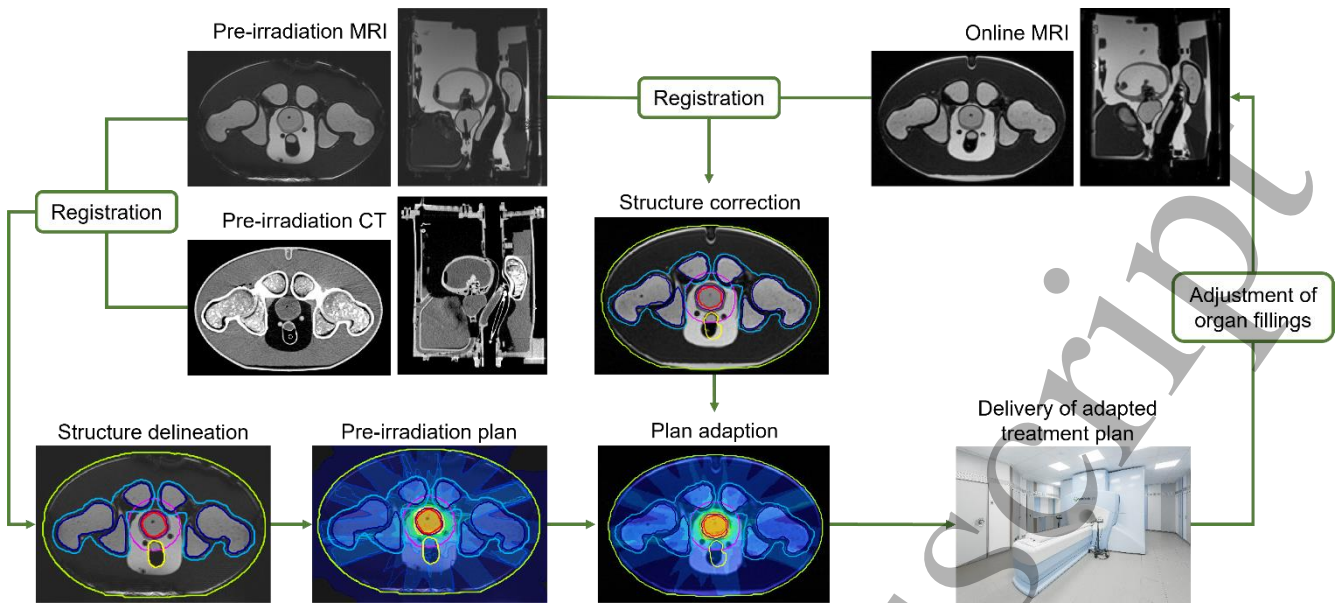


Figure 2: Schematic overview of the online adaptive treatment workflow applied in this study. The pre-irradiation CT is registered to the pre-irradiation MRI, treatment structures are delineated and the initial pre-irradiation plan calculated based on the pre-irradiation images. Prior to each fraction, the MRI is repeated and the pre-irradiation MRI registered to the online MRI. Treatment structures are corrected and the treatment plan is adapted according to the actual geometries before irradiation of each treatment fraction. The online adaption process is repeated for each fraction with bladder and rectum fillings being adjusted.

2.3.1 Pre-irradiation imaging.

Initial CT and MR images of the phantom were acquired for treatment planning using the pre-irradiation bladder and rectum balloon fillings (table 1). CT imaging was performed at a SOMATOM confidence RT Pro (Siemens Healthineers, Germany) scanner with a voltage of 120 kVp, exposure of 500 mAs and voxel size of $1 \times 1 \times 1 \text{ mm}^3$. Pre-irradiation MR imaging was performed at the MR-Linac ($B_0 = 0.35 \text{ T}$) using a clinical planning true fast imaging sequence with steady state precession (TrueFISP) sequence (Chavhan et al. 2008, Scheffler and Hennig 2003) as implemented by the vendor with a field of view (FOV) of $35.0 \times 36.0 \times 40.0 \text{ cm}^3$, a repetition time $TR = 1.45 \text{ ms}$, echo time $TE = 3.35 \text{ ms}$, band width $BW = 537 \text{ Hz/pixel}$ and a voxel size $VS = 1.5 \times 1.5 \times 1.5 \text{ mm}^3$. PG-filled inserts and TLDs were replaced after pre-irradiation imaging.

2.3.2 Treatment planning.

Treatment planning was performed using the treatment planning system (TPS) of the MR-Linac. For this, the pre-irradiation CT was rigidly registered to the pre-irradiation MRI and the skin and bone contours were delineated based on the CT image due to better visibility, while the contours of prostate, bladder and rectum were based on the MRI. The PG insert within the rectum was not separately delineated, but was considered as part of the rectum structure. An intensity-modulated radiotherapy (IMRT) plan was generated using a set of 15 beams. Dose was calculated with the TPS's (Viewray, USA) Monte Carlo algorithm considering the magnetic field with a dose grid resolution of 0.2 cm and prediction uncertainty of 0.5 %.

To dosimetrically visualize a potentially incomplete coverage of the planning target volume (PTV) within the PG, the PTV was defined to be 0.2 cm smaller than the PG volume of the prostate. A uniform dose of 5 Gy delivered in 5 fractions was prescribed to the PTV applying the following objectives for optimization according to clinically applied values (ClinicalTrials.gov NCT04845503): $V_{5.00 \text{ Gy}} \geq 50 \%$, $V_{5.35 \text{ Gy}} < 2 \%$, $V_{4.75 \text{ Gy}} > 95 \%$ of the PTV and $V_{5.13 \text{ Gy}} < 0.20 \text{ cm}^3$ of both the rectum and the bladder ($V_{x \text{ Gy}}$ being the volume in % or in cm^3 receiving more than $x \text{ Gy}$). The planned dose of 5 Gy was chosen due to the optimal dose resolution of the PAGAT gel at 0 – 6 Gy (Matrosic et al. 2017).

2.3.3 Irradiation.

Prior to each irradiation, the bladder and rectum balloon fillings were adjusted according to table 1 and an online MRI was acquired at the MR-Linac using the same sequence as for pre-irradiation imaging (section 2.3.1). The pre-irradiation MRI was then registered to the online MRI using the intensity-based deformable

algorithm as implemented by the vendor (Bohoudi et al. 2017). All contours were then transferred to the online MRI using automatic deformation followed by a manual correction of the skin, prostate, bladder and rectum structures. Rectum and bladder correction were restricted to a 2 cm margin around the previous PTV structure. The treatment plan was re-optimized according to the actual anatomical geometry using the same dose prescription and constraints as used for the initial treatment plan (section 2.3.2). This procedure was repeated for all five fractions using the same PG inserts and TLDs in the phantom.

2.3.4 Quality assurance (QA) procedures. Prior to each irradiation, the online-adapted treatment plan was checked by the so-called adaptive QA tool (AQA) of the MR-Linac system, which performs a secondary dose calculation and evaluates the number of monitor units (MU) and plan segments per fraction compared to the initial pre-irradiation plan (Klüter et al. 2021). The secondary dose calculation is compared to the primary by a 3D γ -analysis (Low et al. 1998) using a 2 %/1 mm (dose difference with respect to the local dose/distance-to-agreement) criterion. In addition, the adapted treatment plan of fraction 1 was recalculated to a solid water phantom and the dose at the isocenter was retrospectively verified with an ionization chamber (A1SL, Standard Imaging, Inc., USA).

2.4 Dosimeter evaluation

The PG containers were evaluated 48 h after irradiation on a diagnostic 3 T Magnetom Prisma^{fit} MRI scanner (Siemens Healthineers, Germany). For this, the containers were placed in a dedicated water flow phantom to ensure a temperature stability of ± 0.1 °C (Elter et al. 2021, Mann et al. 2017). A quantitative R_2 map was acquired with a 64-channel head/neck coil using a multiple spin echo sequence with 32 equidistant echoes ($TE = 25 - 800$ ms), $TR = 7000$ ms, $BW = 130$ Hz/pixel and $VS = 1 \times 1 \times 1$ mm³. In addition, a high resolution standard TrueFISP sequence with $TR = 11.66$ ms, $TE = 5.83$ ms, $BW = 130$ Hz/pixel, number of averages = 2, flip angle = 70° and $VS = 0.5 \times 0.5 \times 0.5$ mm³ was acquired to register the images of the MR evaluation with the images used for treatment planning.

TLDs were read out directly after irradiation using a hot gas reader (Harshow 5500, Thermofisher Scientific, USA) with a time temperature profile of 10 °C/s up to 350 °C. The signal was gathered by a photomultiplier and exported in an ASCII file (Schwahofer et al. 2017).

2.5 Post processing

To compare the measured and planned dose distributions, a dose accumulation of the adapted treatment plans of the five fractions was performed using the treatment planning system RayStation 10A (Raysearch Laboratories, Sweden). For this, the online MR image of each fraction were registered to the pre-irradiation MRI, which served as reference, using a hybrid deformable image registration algorithm as implemented by the vendor with the prostate structure being selected as a so-called controlling structure (Weistrand and Svensson 2015). The resulting deformation vector fields were then applied to the dose distribution of the respective fraction and the resulting dose distributions were summed. For comparison of planned and measured dose distributions, the accumulated dose distribution was then rescaled by the relative difference found in the QA measurement of fraction 1 (sections 2.3.4 & 3.1.3).

Evaluation of the TLDs was performed within the in-house developed software ‘TLD Analyzer’ (Schwahofer 2016). To compare the measured dose of the TLDs with that of the plan, the accumulated and scaled dose of the treatment plan was averaged over three slices, which included the respective TLD in the pre-irradiation MRI.

The post-processing of the MR images for PG evaluation was performed using the in-house developed evaluation tool based on the image processing platform MITK (Elter et al. 2021, Nolden et al. 2013). After generation of a $R_2 = 1/T_2$ map, an edge conserving total variation filter (Rudin et al. 1992) was applied and a dose map was created by means of a mono-exponential calibration curve. The measured dose maps of the PG inserts in the prostate and rectum were separately mapped to the accumulated planned dose distribution based on a rigid registration of the respective morphological images. For this, the point-based closed-form MITK registration algorithm RigidClosedForm3D with three uniquely defined landmarks on the surface of the PG containers and a b-Spline 3rd order interpolation algorithm was used. The PG calibration curve was then linearly renormalized using two reference points of the dose distribution in the high and low dose region, respectively, and new dose distributions were generated accordingly (Vandecasteele and De Deene 2013). The measured dose of the central TLD of the prostate served as an external reference in the high dose region (for details, see Mann et al. (2019) and Schwahofer

et al. (2020)), while the PG was renormalized to the treatment plan in the low dose region of the rectum insert. Since the PG-based dose is not available directly at the central TLD position of the prostate, a neighbouring point with the same planned dose was chosen to renormalize the PG-dose distribution. Finally, a 3D γ -analysis (Low et al. 1998) was performed using a 3 %/3 mm (2 %/2 mm) criterion (dose difference with respect to the local dose/distance-to-agreement) disregarding dose values below 10 % of the maximum dose.

3. Results

3.1 Treatment plan evaluation

3.1.1 Dose statistics. The dose statistics for the calculated pre-irradiation plan and the adapted treatment plans of the five delivered fractions are given in table 2. Each plan was scaled to the total planned dose of 5 Gy. Prescribed objectives for optimization were always met.

Table 2: Dose statistics including the minimum, mean and maximum dose as well as the actually realized dose volume objectives (V_x) of the pre-irradiation plan and the five adapted treatment plans of the five fractions.

Structure		Min [Gy]	Mean [Gy]	Max [Gy]	$V_{5.00\text{ Gy}}/V_{5.35\text{ Gy}}/V_{4.75\text{ Gy}}/V_{5.13\text{ Gy}}$
PTV	Pre-irradiation plan	3.44	4.96	5.23	50.0 %/0.0 %/95.2 % / -
	Fraction 1	4.26	4.99	5.30	50.0 %/0.0 %/96.9 % / -
	Fraction 2	4.39	4.99	5.26	50.0 %/0.0 %/98.5 % / -
	Fraction 3	4.20	4.99	5.25	50.0 %/0.0 %/97.7 % / -
	Fraction 4	4.49	4.99	5.29	50.0 %/0.0 %/98.7 % / -
	Fraction 5	4.31	4.99	5.34	50.0 %/0.0 %/96.9 % / -
Rectum	Pre-irradiation plan	0.01	0.28	2.07	-/-/-/0.0 cm ³
	Fraction 1	0.01	0.28	2.34	-/-/-/0.0 cm ³
	Fraction 2	0.01	0.29	2.49	-/-/-/0.0 cm ³
	Fraction 3	0.01	0.29	2.42	-/-/-/0.0 cm ³
	Fraction 4	0.01	0.28	2.53	-/-/-/0.0 cm ³
	Fraction 5	0.01	0.29	2.67	-/-/-/0.0 cm ³
Bladder	Pre-irradiation plan	0.04	0.24	4.56	-/-/-/0.0 cm ³
	Fraction 1	0.03	0.23	4.50	-/-/-/0.0 cm ³
	Fraction 2	0.04	0.27	4.74	-/-/-/0.0 cm ³
	Fraction 3	0.03	0.24	4.61	-/-/-/0.0 cm ³
	Fraction 4	0.05	0.31	4.55	-/-/-/0.0 cm ³
	Fraction 5	0.04	0.24	4.40	-/-/-/0.0 cm ³

3.1.2 Dose volume histograms. Dose volume histograms (DVH) of the online-adapted treatment plan accumulated over five fractions in comparison to the pre-irradiation treatment plan are shown in figure 3. An improved coverage of the prostate and PTV as well as a better sparing of OARs was achieved in the accumulated adapted treatment plans compared to the pre-irradiation plan.

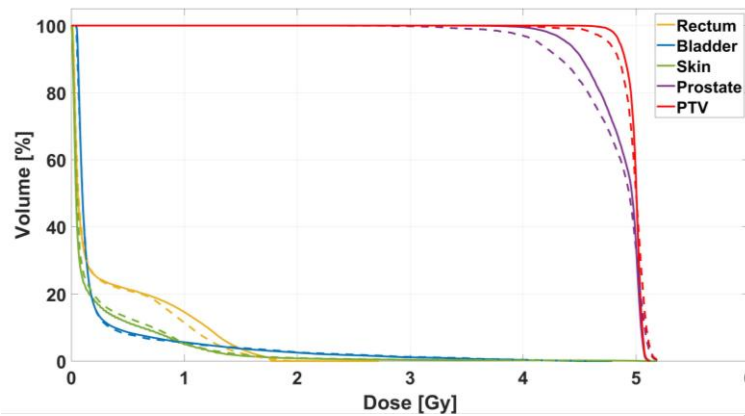


Figure 3: DVHs of the accumulated adapted treatment plans (solid line) and pre-irradiation treatment plan (dashed line) for the rectum (yellow), bladder (blue), skin (green), prostate (purple) and PTV (red) structures.

3.1.3 Quality assurance.

The AQA-tool revealed γ -passing rates of the secondary dose calculation of $> 97\%$ for all adapted treatment plans. Furthermore, the average deviation in the number of MUs per fraction and treatment segments relative to the pre-irradiation plan was found to be $-0.2 \pm 6.4\%$ and $-0.3 \pm 6.0\%$, respectively. The additional dose verification measurement of fraction 1 resulted in a relative difference of -3.1% between measured and planned dose, which was then used to rescale the online-adapted treatment plan accumulated over the five fractions.

3.2 Dosimeter evaluation

3.2.1 TLD evaluation.

The results of the TLD measurements in the prostate are given in table 3. A maximum deviation of -0.11 Gy and -4.7% with respect to the planned dose was found at the surface. The measured dose of the central TLD of 4.75 Gy was used for dose renormalization of the PG.

Table 3: Measured and planned dose of the three TLD measurements at the center (high dose region) and the surface (dose gradient) of the prostate.

TLD position	Measured dose [Gy]	Planned dose [Gy]	Deviation [%]
Center	4.75	4.86	-2.3
Surface 1	2.24	2.35	-4.7
Surface 2	2.01	2.04	-1.5

3.2.2 PG evaluation.

Representative dose profiles at different heights for the PG-filled prostate together with respective 2D γ -maps are shown in figure 4. No significant dose deviation of measured and planned dose was found as shown by the high 3D passing rates of the γ -index of 98.9% ($3\%/3\text{ mm}$) and 91.4% ($2\%/2\text{ mm}$), respectively. A total of 6436 voxels was evaluated and only few voxels exhibited absolute deviations up to 0.4 Gy .

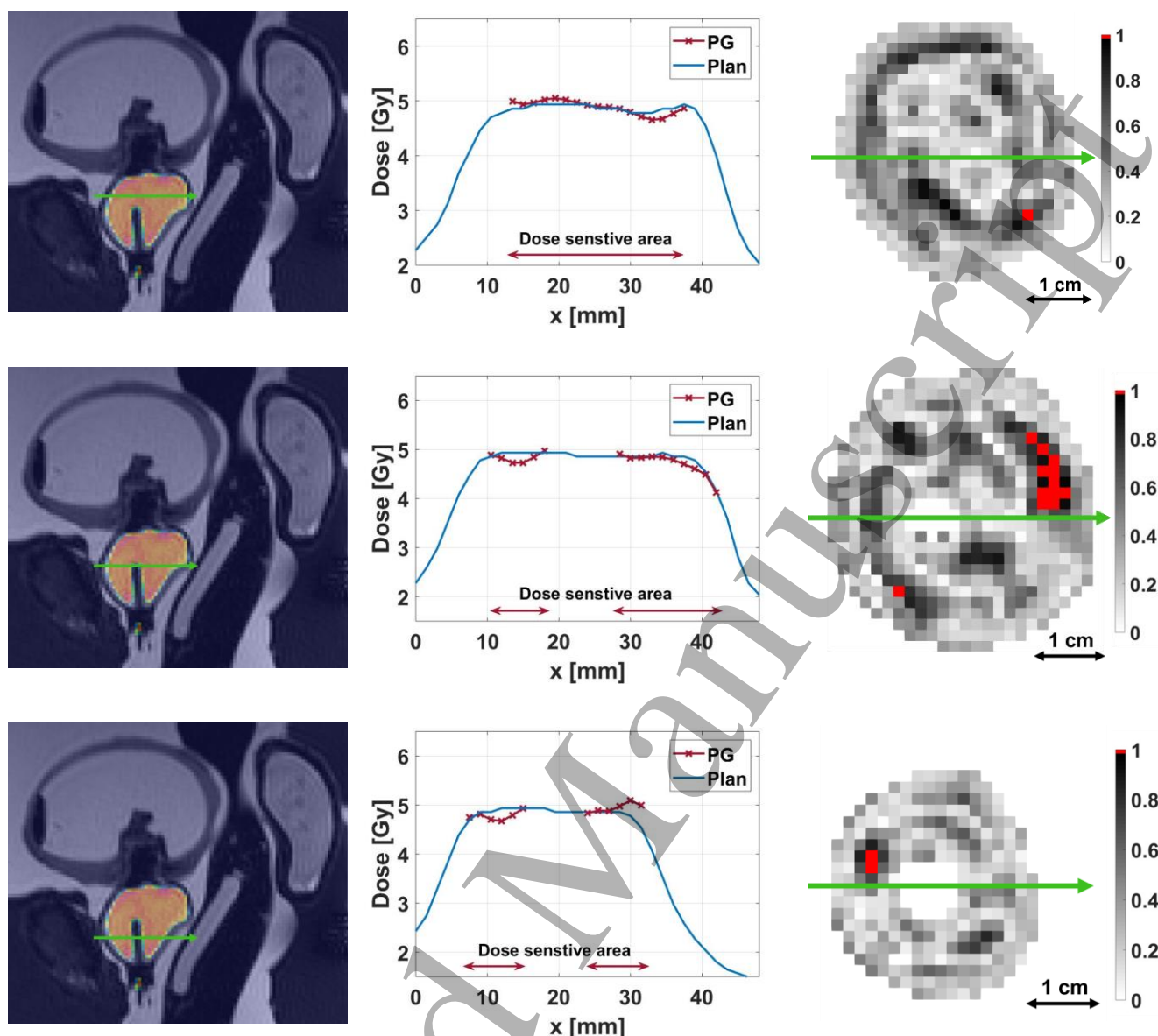


Figure 4: Comparison of measured and planned dose profiles (center) through the prostate at three representative heights. The position of the profiles is indicated in the sagittal MR images with the overlaid measured dose distribution (left) and in the transversal 2D γ -maps (3 %/3 mm, right). Voxels violating the γ -criterion are indicated in red.

Representative dose profiles of two different orientations for the PG-filled rectum insert together with respective 2D γ -maps are shown in figure 5. A good agreement of planned and measured dose was found as indicated by 3D passing rates of the γ -index of 93.7 % (3 %/3 mm) and 80.0 % (2 %/2 mm) with a total of 1853 voxels being evaluated.

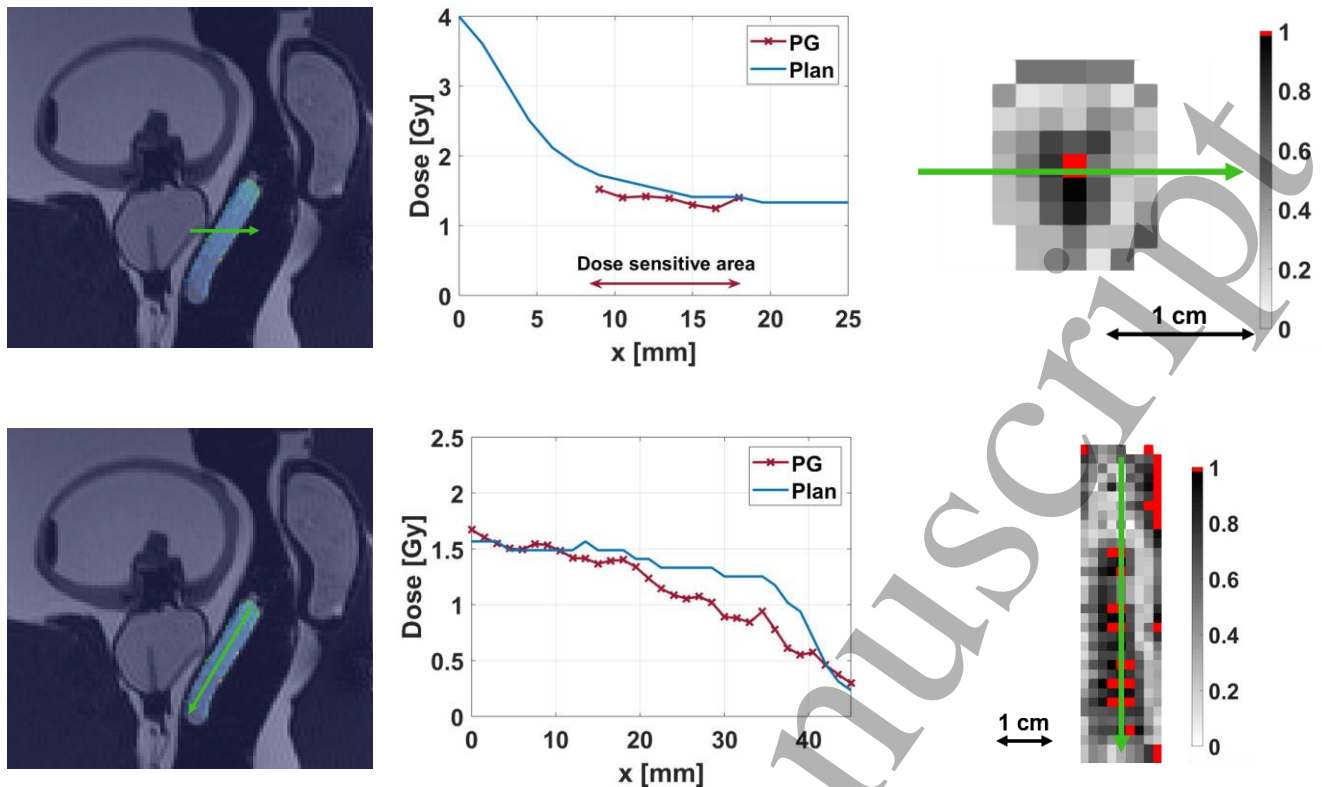


Figure 5: Representative measured and planned dose profiles (center) through the rectum insert for two different orientations as indicated by the green arrows in the PG dose map overlaid on the reference MRI (left, sagittal view) and the corresponding 2D γ -maps (3 %/3 mm, right). Voxels violating the γ -criterion are indicated in red.

4. Discussion

In this study, a successful end-to-end test of a fractionated and online adapted MRgRT treatment was performed using the ADAM-PETER phantom. The ADAM-PETER was adapted to perform 3D dosimetry using PG in the prostate and the rectum as well as additional point measurements using TLDs at the center and on the surface of the prostate. To our knowledge, this is the first study that applies a deformable phantom with anthropomorphic imaging contrast in CT and MRI to accurately simulate inter-fractional anatomy changes for an end-to-end test of multiple fractions while being able to measure the applied dose in 3D. Previous studies have either used static phantoms without anthropomorphic geometries, have performed point-like or 2D dose measurements or applied one treatment fraction only (Elter et al. 2019b, Hoffmans et al. 2020, Pappas et al. 2019, Stark et al. 2020). The performed test included all steps of an online adapted MRgRT treatment from pre-irradiation MRI and CT imaging, treatment planning, inter-fractional anatomy changes, the corresponding online adaption of the treatment plan, dose delivery to specific QA measurements.

Due to the complexity of the presented workflow including PG and TLD measurements, the end-to-end test may not be suited for regular patient-specific QA purposes on a weekly or monthly basis. We therefore propose such measurements as end-to-end tests in the commissioning phase of new treatment techniques such as MR-guided treatments at a MR-Linac. Here, PGs provide a promising tool for 3D dose evaluations with a high dosimetric and geometric accuracy. Conventionally used dosimetry systems (e.g. ionization chambers, films) do typically not allow for a 3D dose evaluation and therefore lack the possibility to fully represent steep dose gradients as present in complex dose distributions. Hence, they may not be able to detect geometrical errors in the dose delivery.

Bladder and rectum fillings of the five fractions were adapted to typical medium to high bladder and empty rectum fillings in clinical prostate irradiations, e.g. implemented by drinking instructions to the patient before irradiation (Alongi et al. 2020, Bruynzeel et al. 2019, Tetar et al. 2019). Therefore, the bladder filling was mostly varied between a base level of 150 ml corresponding to a full, but not expanded, bladder and a maximum filling of 200 ml. However, a rather small bladder filling of 100 ml in fraction 4 was included in the current study to simulate scenario of a nearly empty bladder. To simulate an empty rectum, only air fillings of the rectal balloon were used, although

1
2
3
4
5
6
7
8
9
10
11
12
13
14
15
16
17
18
19
20
21
22
23
24
25
26
27
28
29
30
31
32
33
34
35
36
37
38
39
40
41
42
43
44
45
46
47
48
49
50
51
52
53
54
55
56
57
58
59
60

water fillings are generally possible (Niebuhr et al. 2019). Besides this, bladder and rectum fillings were randomly selected within the range of technically feasible fillings.

Dose measurements in this study showed a very good agreement with the accumulated treatment plan represented by very high 3D passing rates of the γ -index (3 %/ 3 mm criterion) of 98.9 % in the PG-filled prostate and 93.7 % in the PG-filled rectum insert, as well as maximum deviations of the TLD measurements to the accumulated treatment plan of -4.7 %.

While the chosen threshold level of 10 % of the local maximum dose does not influence the γ -analysis in the high dose region of the prostate, it might slightly influence the passing rate of the rectum due to the lower dose level and the included dose gradient.

The deviations in the TLD measurements on the surface of the prostate may result from small positioning uncertainties in the dose gradient region or small uncertainties in the TLD dose calibration process.

Both PG and TLDs are generally considered to accumulate the applied dose (De Deene and Baldock 2004, Murthy 2013). However, first studies have shown a dependency of the gel response on the dose fractionation scheme, which can be corrected by a dose renormalization (Karlsson et al. 2007). In this study, a so-called two point renormalization was performed using two reference points in the high and low dose region, respectively (Vandecasteele and De Deene 2013), since the delivered dose distribution was evaluated in both the high dose (prostate) and low dose (rectum insert) region. While a normalization to an external dose measurement using a TLD was possible in the homogenous dose region of the prostate (Mann et al. 2019, Schwahofer et al. 2020), this was not feasible in the dose gradient region of the rectum insert. In the dose gradient, a slight shift in position between a possible TLD and the PG would directly lead to a large shift in the applied dose of up to 0.1 Gy/mm. Furthermore, a second independent dose measurement using TLDs or ionization chambers positioned within the rectum insert was not feasible as the anatomy of the ADAM-PETer phantom is not perfectly reproducible. Hence, the PG was renormalized to the treatment plan in the low dose region of the rectum insert. Remaining deviations in the PG response may result from the dose delivery as well as from the 15 radiation beams, each using multiple IMRT segments, since PG response to fractionated irradiations was earlier found to be dose dependent (Karlsson et al. 2007). The small PG volumes, which were necessary for technical reasons, may also have been affected by effects from the container material on the PG response as well as by slight variations in temperature gradients during the cooling process after production or during irradiation.

Due to the optimal dose resolution of the PG at 0 – 6 Gy (Matrosic et al. 2017), a uniform dose of 5 Gy delivered in 5 fractions (1 Gy per fraction) was prescribed to the prostate in this end-to-end test as compared to 5×7.5 Gy applied in the clinical study used as reference (ClinicalTrials.gov NCT04845503). As the absolute dose output of the treatment device is regularly checked by routine QA measurements e.g. using ionization chambers in simple water phantoms, the dose prescription of complex workflow tests as presented in this study may be scaled without significantly compromising the accuracy of the measurement.

In the dose verification measurement of fraction 1 with an ionization chamber, a difference to the planned dose of -3.1 % was found. This may result from slight variations in the MR-Linac output calibration, but also from systematic errors in the dose calculation and the delivery of the IMRT plan with 15 beams and > 30 segments per fraction. Due to the low absolute dose applied of 1 Gy per fraction, this leads to small numbers of monitor units per segment, which may additionally increase the uncertainty of the dose delivery. In addition, positioning errors, volume effects or disregarding the plan-specific reference field in the ionization chamber measurement may also contribute to the overall uncertainty. Furthermore, an additional systematic error source cannot be excluded. The QA measurement was performed for one fraction only, since all treatments were applied on the same day in direct succession and all adaptations were based in the same pre-irradiation plan. Therefore, no significant deviation between the fractions was expected.

Uncertainties in the accumulated dose distribution may result from the deformable registration required for each of the five fractions. In the air-filled rectum these uncertainties may increase further as the interface of air and water-equivalent material may increase the dosimetric effect of small registration errors and moreover disturbs the secondary electron equilibrium.

Furthermore, the AQA-tool revealed a variation of monitor units and number of segments with a corresponding standard deviation in the order of 6 %. However, this variation, which may appear to be large, is not surprising due to the independent re-optimization of the treatment plan for each fraction.

As a result, the DVH (figure 3) shows a slightly better coverage of the PTV for the accumulated adapted treatment plan compared to the pre-irradiation plan. This is in good agreement with the dose statistics in table 2 and might result from a slightly different organ positioning during the treatment compared to the pre-irradiation scenario allowing for a better optimization of the treatment plan.

Overall, the presented end-to-end test demonstrated the feasibility and accuracy of fractionated and online-adapted prostate irradiations in presence of inter-fractional anatomy changes. In all fractions, optimal sparing of the rectum as most important OAR was achieved. Due to the anthropomorphic imaging contrast of the phantom in CT and MRI, the experimental setup is of similar complexity as that in patients and it may therefore also be used in future experiments to validate so-called MR-only treatment planning techniques.

5. Conclusion

In this study, we presented a successful end-to-end test of a fractionated and online adapted MR-guided radiotherapy treatment using a deformable pelvis phantom with anthropomorphic imaging contrast in CT and MR. 3D polymer dosimetry gel and thermoluminescence detectors allowed for comprehensive dose measurements in the prostate as well as in the rectum. A good agreement of measured and planned dose was found. γ -index passing rates (3 %/3 mm) of 98.9 % and 93.7 % were found for the prostate and rectum, respectively, and point measurements with thermoluminescence detectors revealed deviations of -2.3 % at the center and up to -4.7 % on the surface of the prostate.

Acknowledgements

The authors acknowledge the German Research Council (DFG) for funding the MR-Linac device (grant no. DE 614/16-1).

References

- Alongi, F., Rigo, M., Figlia, V., Cuccia, F., Giaj-Levra, N., Nicosia, L., Ricchetti, F., Sicignano, G., De Simone, A., Naccarato, S., Ruggieri, R. and Mazzola, R. (2020) '1.5 T MR-guided and daily adapted SBRT for prostate cancer: feasibility, preliminary clinical tolerability, quality of life and patient-reported outcomes during treatment', *Radiation Oncology*, 15(69).
- Baldock, C., De Deene, Y., Doran, S., Ibbott, G., Jirasek, A., Lepage, M., McAuley, K. B., Oldham, M. and Schreiner, L. J. (2010) 'Polymer gel dosimetry', *Physics in Medicine and Biology*, 55(5), R1-63.
- Bohoudi, O., Bruynzeel, A. M. E., Senan, S., Cuijpers, J. P., Slotman, B. J., Lagerwaard, F. J. and Palacios, M. A. (2017) 'Fast and robust online adaptive planning in stereotactic MR-guided adaptive radiation therapy (SMART) for pancreatic cancer', *Radiotherapy and Oncology*, 125(3), 439-444.
- Bruynzeel, A. M. E., Tetar, S. U., Oei, S. S., Senan, S., Haasbeek, C. J. A., Spoelstra, F. O. B., Piet, A. H. M., Meijnen, P., Bakker van der Jagt, M. A. B., Fraikin, T., Slotman, B. J., van Moorselaar, R. J. A. and Lagerwaard, F. J. (2019) 'A Prospective Single-Arm Phase 2 Study of Stereotactic Magnetic Resonance Guided Adaptive Radiation Therapy for Prostate Cancer: Early Toxicity Results', *International journal of radiation oncology, biology, physics*, 105(5), 1086-1094.
- Chang, A. E., Matory, Y. L., Dwyer, A. J., Hill, S. C., Girton, M. E., Steinberg, S. M., Knop, R. H., Frank, J. A., Hyams, D. and Doppman, J. L. (1987) 'Magnetic resonance imaging versus computed tomography in the evaluation of soft tissue tumors of the extremities', *Annals of surgery*, 205(4), 340-348.
- Chavhan, G. B., Babyn, P. S., Jankharia, B. G., Cheng, H. M. and Shroff, M. M. (2008) 'Steady-State MR Imaging Sequences: Physics, Classification, and Clinical Applications', *RadioGraphics*, 28(4), 1147-1160.
- ClinicalTrials.gov NCT04845503 (2021) 'Stereotactic MRI-guided Radiation Therapy for Localized prostatic Cancer', [online], available: <https://ClinicalTrials.gov/show/NCT04845503>].
- De Deene, Y. and Baldock, C. (2004) 'Third International Conference on Radiotherapy Gel Dosimetry', *Journal of Physics: Conference Series*, 3.
- De Deene, Y., Vergote, K., Claeys, C. and De Wagter, C. (2006) 'The fundamental radiation properties of normoxic polymer gel dosimeters: a comparison between a methacrylic acid based gel and acrylamide based gels', *Physics in Medicine and Biology*, 51(3), 653-673.
- Elter, A., Dorsch, S., Mann, P., Runz, A., Johnen, W. and Karger, C. P. (2019a) 'Compatibility of 3D printing materials and printing techniques with PAGAT gel dosimetry', *Physics in Medicine and Biology*, 64(04NT02).
- Elter, A., Dorsch, S., Mann, P., Runz, A., Johnen, W., Spindeldreier, C. K., Klüter, S. and Karger, C. P. (2019b) 'End-to-end test of an online adaptive treatment procedure in MR-guided radiotherapy using a phantom with anthropomorphic structures', *Physics in Medicine and Biology*, 64(225003).
- Elter, A., Dorsch, S., Thomas, S., Hentschke, C. M., Floca, R. O., Runz, A., Karger, C. P. and Mann, P. (2021) 'PAGAT gel dosimetry for everyone: gel production, measurement and evaluation', *Biomedical Physics & Engineering Express*, 7(057001).

- Gillmann, C., Homolka, N., Johnen, W., Runz, A., Echner, G., Pfaffenberger, A., Mann, P., Schneider, V., Hoffmann, A. L., Troost, E. G. C., Koerber, S. A., Kotzerke, J. and Beuthien-Baumann, B. (2021) 'Technical Note: ADAM PETER – An anthropomorphic, deformable and multimodality pelvis phantom with positron emission tomography extension for radiotherapy', *Medical Physics*, 48(4), 1624-1632.
- Hoffmans, D., Niebuhr, N., Bohoudi, O., Pfaffenberger, A. and Palacios, M. (2020) 'An end-to-end test for MR-guided online adaptive radiotherapy', *Physics in Medicine and Biology*, 65(125012).
- Karlsson, A., Gustavsson, H., Månsson, S., McAuley, K. B. and Bäck, S. A. J. (2007) 'Dose integration characteristics in normoxic polymer gel dosimetry investigated using sequential beam irradiation', *Physics in Medicine and Biology*, 52(15), 4697-4706.
- Klüter, S. (2019) 'Technical design and concept of a 0.35 T MR-Linac', *Clinical and Translational Radiation Oncology*, 18, 98-101.
- Klüter, S., Schrenk, O., Renkamp, C. K., Gliessmann, S., Kress, M., Debus, J. and Hörner-Rieber, J. (2021) 'A practical implementation of risk management for the clinical introduction of online adaptive Magnetic Resonance-guided radiotherapy', *Physics and Imaging in Radiation Oncology*, 17, 53-57.
- Low, D. A., Harms, W. B., Mutic, S. and Purdy, J. A. (1998) 'A technique for the quantitative evaluation of dose distributions', *Medical Physics*, 25(5), 656-661.
- Mann, P., Schwahofer, A. and Karger, C. P. (2019) 'Absolute dosimetry with polymer gels-a TLD reference system', *Physics in Medicine and Biology*, 64(45010).
- Mann, P., Witte, M., Moser, T., Lang, C., Runz, A., Johnen, W., Berger, M., Biederer, J. and Karger, C. P. (2017) '3D dosimetric validation of motion compensation concepts in radiotherapy using an anthropomorphic dynamic lung phantom', *Physics in Medicine and Biology*, 62(2), 573-595.
- Marot, M., Elter, A., Mann, P., Schwahofer, A., Lang, C., Johnen, W., Körber, S. A., Beuthien-Baumann, B. and Gillmann, C. (2021) 'Technical Note: On the feasibility of performing dosimetry in target and organ at risk using polymer dosimetry gel and thermoluminescence detectors in an anthropomorphic, deformable, and multimodal pelvis phantom', *Medical Physics*, 48(9), 5501-5510.
- Matrosic, C., McMillan, A., Holmes, J., Bednarz, B. and Culberson, W. (2017) 'Dosimetric comparison of DEFGEL and PAGAT formulae paired with an MRI acquisition', *Journal of Physics: Conference Series*, 847(12012).
- Murthy, K. V. R. (2013) 'Thermoluminescence and its Applications: A Review', *Defect and Diffusion Forum*, 347, 35-73.
- Mutic, S. and Dempsey, J. F. (2014) 'The ViewRay system: magnetic resonance-guided and controlled radiotherapy', *Seminars in Radiation Oncology*, 24(3), 196-199.
- Niebuhr, N. I., Johnen, W., Echner, G., Runz, A., Bach, M., Stoll, M., Giske, K., Greilich, S. and Pfaffenberger, A. (2019) 'The ADAM-pelvis phantom—an anthropomorphic, deformable and multimodal phantom for MRgRT', *Physics in Medicine and Biology*, 64(04NT05).

- 1
2
3 Nolden, M., Zelzer, S., Seitel, A., Wald, D., Müller, M., Franz, A. M., Maleike, D., Fangerau, M., Baumhauer,
4 M., Maier-Hein, L., Maier-Hein, K. H., Meinzer, H. P. and Wolf, I. (2013) 'The Medical Imaging
5 Interaction Toolkit: challenges and advances', *International Journal of Computer Assisted Radiology and
6 Surgery*, 8(4), 607-620.
7
- 8
9 Pappas, E., Kalaitzakis, G., Boursianis, T., Zoros, E., Zourari, K., Pappas, E. P., Makris, D., Seimenis, I.,
10 Efstathopoulos, E. and Maris, T. G. (2019) 'Dosimetric performance of the Elekta Unity MR-linac system:
11 2D and 3D dosimetry in anthropomorphic inhomogeneous geometry', *Physics in Medicine and Biology*,
12 64(225009).
13
- 14
15 Raaymakers, B. W., Jürgenliemk-Schulz, I. M., Bol, G. H., Glitzner, M., Kotte, A. N. T. J., van Asselen, B., de
16 Boer, J. C. J., Bluemink, J. J., Hackett, S. L., Moerland, M. A., Woodings, S. J., Wolthaus, J. W. H., van
17 Zijp, H. M., Philippens, M. E. P., Tijssen, R., Kok, J. G. M., de Groot-van Breugel, E. N., Kiekebosch, I.,
18 Meijers, L. T. C., Nomden, C. N., Sikkes, G. G., Doornaert, P. A. H., Eppinga, W. S. C., Kasperts, N.,
19 Kerkmeijer, L. G. W., Tersteeg, J. H. A., Brown, K. J., Pais, B., Woodhead, P. and Lagendijk, J. J. W.
20 (2017) 'First patients treated with a 1.5 T MRI-Linac: clinical proof of concept of a high-precision, high-
21 field MRI guided radiotherapy treatment', *Physics in Medicine and Biology*, 62(23), L41-L50.
22
- 23
24 Raaymakers, B. W., Lagendijk, J. J. W., Overweg, J., Kok, J. G. M., Raaijmakers, A. J. E., Kerkhof, E. M., van
25 der Put, R. W., Meijsing, I., Crijns, S. P. M., Benedosso, F., van Vulpen, M., de Graaff, C. H. W., Allen, J.
26 and Brown, K. J. (2009) 'Integrating a 1.5 T MRI scanner with a 6 MV accelerator: proof of concept',
27 *Physics in Medicine and Biology*, 54(N229).
28
- 29
30 Rudin, L. I., Osher, S. and Fatemi, E. (1992) 'Nonlinear total variation based noise removal algorithms', *Physica
31 D: Nonlinear Phenomena*, 60(1-4), 259-268.
32
- 33
34 Scheffler, K. and Hennig, J. (2003) 'Is TrueFISP a gradient-echo or a spin-echo sequence?', *Magnetic Resonance
35 in Medicine*, 49(2), 395-397.
36
- 37
38 Schwahofer, A. (2016) 'Establishing a process for the use of thermoluminescence dosimetry (TLD) in
39 radiotherapy - an approach concerning the entire range of diagnostic and therapeutic photon energies', *PhD
40 Thesis*, (Medical Faculty of Ruprecht-Karls-University Heidelberg).
41
- 42
43 Schwahofer, A., Feist, H., Georg, H., Häring, P. and Schlegel, W. (2017) 'Experimental determination of the
44 photon-energy dependent dose-to-water response of TLD600 and TLD700 (LiF:Mg,Ti)
45 thermoluminescence detectors', *Zeitschrift für medizinische Physik*, 27(1), 13-20.
46
- 47
48 Schwahofer, A., Mann, P., Spindeldreier, C. K. and Karger, C. P. (2020) 'On the feasibility of absolute 3D
49 dosimetry using LiF thermoluminescence detectors and polymer gels on a 0.35T MR-LINAC', *Physics in
50 Medicine and Biology*, 65(215002).
51
- 52
53 Stark, L. S., Andratschke, N., Baumgartl, M., Bogowicz, M., Chamberlain, M., Dal Bello, R., Ehrbar, S., Girbau
54 Garcia, Z., Guckenberger, M., Krayenbühl, J., Pouymayou, B., Rudolf, T., Vuong, D., Wilke, L.,
55 Zamburlini, M. and Tanadini-Lang, S. (2020) 'Dosimetric and geometric end-to-end accuracy of a magnetic
56 resonance guided linear accelerator', *Physics and Imaging in Radiation Oncology*, 16, 109-112.
57
- 58
59 Tetar, S. U., Bruynzeel, A. M. E., Lagerwaard, F. J., Slotman, B. J., Bohoudi, O. and Palacios, M. A. (2019)
60 'Clinical implementation of magnetic resonance imaging guided adaptive radiotherapy for localized prostate
cancer', *Physics and Imaging in Radiation Oncology*, 9, 69-76.

- 1
2
3
4 Tocco, B. R., Kishan, A. U., Ma, T. M., Kerkmeijer, L. G. W. and Tree, A. C. (2020) 'MR-Guided Radiotherapy
5 for Prostate Cancer', *Frontiers in oncology*, 10(616291).
6
7 van Herk, M. (2004) 'Errors and margins in radiotherapy', *Seminars in Radiation Oncology*, 14(1), 52-64.
8
9
10 Vandecasteele, J. and De Deene, Y. (2013) 'On the validity of 3D polymer gel dosimetry: I. reproducibility study',
11 *Physics in Medicine and Biology*, 58(1), 19-42.
12
13
14 Weistrand, O. and Svensson, S. (2015) 'The ANACONDA algorithm for deformable image registration in
15 radiotherapy', *Medical Physics*, 42(1), 40-53.
16
17
18 Winkel, D., Bol, G. H., Kroon, P. S., van Asselen, B., Hackett, S. S., Werensteijn-Honingh, A. M., Intven, M. P.
19 W., Eppinga, W. S. C., Tijssen, R. H. N., Kerkmeijer, L. G. W., de Boer, H. C. J., Mook, S., Meijer, G. J.,
20 Hes, J., Willemsen-Bosman, M., de Groot-van Breugel, E. N., Jürgenliemk-Schulz, I. M. and Raaymakers,
21 B. W. (2019) 'Adaptive radiotherapy: The Elekta Unity MR-linac concept', *Clinical and Translational
22 Radiation Oncology*, 18, 54-59.
23
24
25
26
27
28
29
30
31
32
33
34
35
36
37
38
39
40
41
42
43
44
45
46
47
48
49
50
51
52
53
54
55
56
57
58
59
60

3 DISCUSSION

In this thesis, end-to-end tests were developed and implemented to validate online adaptive MRgRT treatment procedures at the 0.35 T MRIdian Linac. The recent clinical introduction of MR-Linacs allows to improve the treatment accuracy of RT treatments using daily online acquired MR images of the patient anatomy. These online images may be used to correct the patient positioning and, more importantly, to adapt the treatment plan to the actual patient geometry and for motion compensation during the treatment. With the improved accuracy, OAR toxicity may be reduced while the dose to the target per treatment fraction may be increased (so-called *dose escalation*). However, the correct and precise dose delivery in such a scenario has to be verified on a regular basis using dedicated machine- and patient-specific QA procedures. Furthermore, end-to-end tests are required to validate the feasibility and accuracy of the entire treatment workflow. A crucial part of such tests is the identification of remaining uncertainties, which may not be detected by solely testing each single step of the workflow. Especially for complex procedures such as online adaptive MRgRT, end-to-end tests are essential to deduce the potential and possible limitations of this novel treatment technique. To implement these tests, dedicated phantoms that realistically represent the patient in terms of anthropomorphic geometry, radiation attenuation and image contrast are required. A further challenge for the development of end-to-end testing phantoms is the integration of measurement systems that may verify the delivered dose distribution with high geometric and dosimetric accuracy.

For the final implementation of end-to-end tests for online adaptive MRgRT, several methods were developed within the scope of this thesis. This includes the standardization of PG experiments for 3D dose measurements (publication I) and the development of anthropomorphic phantom materials (publication II). These methods were validated in a clinical environment (publication II & III) and finally, several end-to-end tests of IgRT procedures were introduced and clinically implemented (publications IV-VI) focusing on online adaptive MRgRT. Within this section, the main results of the six publications, which comprise this thesis, will be discussed and put into a general context.

3.1 Methodological developments

3.1.1 3D dose verification

A crucial part for the implementation of end-to-end tests is the applied dose measurement system. In the ideal case, dose measurements allow for a highly accurate 3D dose evaluation. Hence, PGs provide a promising tool for end-to-end tests. However, this method is normally associated with many uncertainties especially related to the complex experimental workflow [151]. For PAGAT gels, these uncertainties may originate from the production process (e.g. chemical impurities or unwanted chemical reaction processes), from irradiation and storage (e.g. temperature and dose rate variations), as well as from the MRI evaluation (e.g. temperature variations or magnetic field

inhomogeneities). In literature, several different PGs with different properties were applied to different workflows and each PG requires specific measures to minimize uncertainties [121]. This limits the feasibility of PG experiments and further complicates their clinical introduction. Therefore, a standardized protocol for the experimental workflow to conduct PAGAT gel dosimetry was presented in publication I. Such a standardization is highly important to track and minimize uncertainties and to allow for a wide range of applications. Hence, it is a prerequisite for the reproducible use of PGs in advanced end-to-end tests of new RT treatment techniques. However, despite the standardized workflow and a dedicated calibration procedure, an external renormalization of the PG response has to be performed in order to conduct absolute dosimetry [122]. Such a renormalization of the calibration curve may be performed using the treatment plan or an external dose reference measurement, e.g. using TLDs [145, 146]. By renormalizing the dose to an external reference, a high dosimetric accuracy of PG experiments with an overall uncertainty of $< 4\%$ can be achieved with the workflow reported in publication I [144, 146]. The presented workflow was applied for various QA measurements in publications III-VI. However, PAGAT experiments require experimental times of several days from gel production to evaluation (approximately one week for a single PG experiment), well-equipped laboratories for gel production, and access to an MRI device for gel evaluation. The required time might be reduced if only geometrical aspects are analyzed, since they are insensitive to chemical stabilization of the PG after irradiation [152]. For dosimetric purposes in regular QA, other dosimetry systems, e.g. ionization chamber arrays, may present an alternative as they allow an online read-out. Nevertheless, PG dosimetry in anthropomorphic phantoms provide a valuable method for the commissioning of new radiotherapy treatment techniques such as MRgRT.

3.1.2 Phantoms with anthropomorphic attenuation and imaging contrast

Besides a 3D dose measurement system, a phantom for end-to-end testing in MRgRT should have the same attenuation properties and image contrast in CT and MRI as patients. In general, anthropomorphic attenuation properties are associated with CT-values as relative attenuation coefficients for photon therapy, or with SPRs for proton and ion therapy, which may be derived from CT-values using dedicated HLUTs (for a further discussion on attenuation properties see section 3.2.1). However, typical phantom materials presented in literature represent either anthropomorphic CT or MRI contrast, do not allow for an individual adjustment towards specific contrast values [148, 153], or do not account for different relaxation times at the magnetic field strength of the applied MRI [154]. Therefore, phantom materials with individually adjustable CT as well as MRI contrast at three different field strengths were developed and presented in publication II. The chosen magnetic field strengths (0.35, 1.5 and 3.0 T) cover the full range of potentially applied field strengths in MRgRT, i.e. diagnostic MRI devices and MR-Linacs. The developed system of equations allows for the prediction of required concentrations of chemical ingredients for given CT, T_1 and T_2 values at each magnetic field strength and vice versa. This enables the preparation of phantom materials with defined image contrast (CT and MRI) to represent soft tissues. An exception is the simulation of materials with very low to negative CT-values or CT-values > 350 HU. The limitation on positive CT-values is due to the water base ($CT_{\text{water}} = 0$ HU) of the materials and the fact that the chemical ingredients used for varying the CT-value (KCl) or MRI contrast (agarose and Ni-DTPA) increase the CT-value. However, soft

tissues with negative CT-values may easily be simulated using oil or Vaseline [148], which is applied in the ADAM-PETer phantom [150] used in publications III, IV and VI. On the other hand, high CT-values beyond the soft tissue range are limited by the solubility of KCl in the developed method. Hence, other materials such as K_2HPO_4 and gypsum have to be used for the simulation of bony structures in end-to-end testing phantoms [148]. This was done in the AQUARIUM and ADAM-PETer (publications III-VI). Furthermore, the MRI contrast of the developed materials is limited towards low T_2 values ($T_2 < 30$ ms), since high agarose concentrations are required for lower values, which would lead to a very high viscosity of the gels resulting in a poor mixing ability and the formation of air bubbles. Nevertheless, the range of achievable imaging parameters well covers the range of most important soft tissues with positive CT-values (section 3.2.1).

3.1.3 Simulation of anatomical changes in phantoms

The simulation of realistic anatomical changes is essential to perform end-to-end tests of complex adaptive image-guided treatment procedures. Depending on the tested workflow, the anatomical changes may include inter- or intra-fractional motion. While two phantoms capable of simulating intra-fractional motion were presented in publication IV, this thesis focusses on inter-fractional motion to investigate the feasibility and accuracy of treatment plan adaptations (publications III-VI). In both types of motion, the anatomical changes may be simulated either by rather simple non-anthropomorphic phantoms or by phantoms that represent realistic anthropomorphic geometries. Purely geometric phantoms such as the AQUARIUM (publications IV & V) typically benefit from an easy use and from a high reproducibility of the applied change, allowing for repeated measurements under identical conditions. Hence, errors and uncertainties in the tested workflow that can be attributed to the respective motion pattern may be detected. End-to-end tests using such geometrical phantoms are therefore essential to generally validate the feasibility of a specific workflow and to successively identify specific limitations. However, these phantoms are typically not able to simulate realistic anatomical changes in patients due to the lack of an anthropomorphic geometry. To overcome this limitation, anthropomorphic phantoms such as the ADAM-PETer representing a male pelvis may be used (publications III, IV & VI). End-to-end tests using such realistic phantoms are necessary to validate a specific image-guided workflow under clinical conditions. However, just as in the patient, an identical geometry of the phantom cannot be guaranteed in repeated experiments. Hence, errors occurring in a single measurement may not be reproducible. Therefore, both geometric phantoms allowing for high reproducibility as well as realistic anthropomorphic phantoms should be used in end-to-end tests for new image-guided treatment procedures before introducing them into clinical practice.

3.2 Validation of methods

3.2.1 Phantoms with anthropomorphic attenuation and imaging contrast

To validate the developed phantom materials, nine specific soft tissue materials were produced according to CT and MRI (1.5 T) literature values (publication II). A good agreement of the imaging parameters of the phantom materials with literature values was found, which is demonstrated in figure 7 for the example of T_1 and T_2 values at 1.5 T for six representative soft

tissue samples. Using these material samples the consistency of predicted and measured parameters could be validated with mean deviations of less than 3.5 %. The deviations may result from fit uncertainties of the developed equations to predict weights of the material’s chemical ingredients as well as contrast parameters. Furthermore, uncertainties in the phantom material production and in the experimental determination of measured contrast parameters may have influenced the measured imaging parameters. For an application in end-to-end testing phantoms, an anthropomorphic image contrast between different tissue types is particularly important, whereby a deviation of the absolute imaging parameters in the range of a few percent should not have a significant influence. In addition, the materials must be stable over time without significant changes in image contrast. This was confirmed by a repeated measurement of CT, T_1 and T_2 values at 1.5 T after five months resulting in mean deviations of -0.8 ± 1.6 %, -0.2 ± 1.5 % and -5.2 ± 1.1 %, respectively.

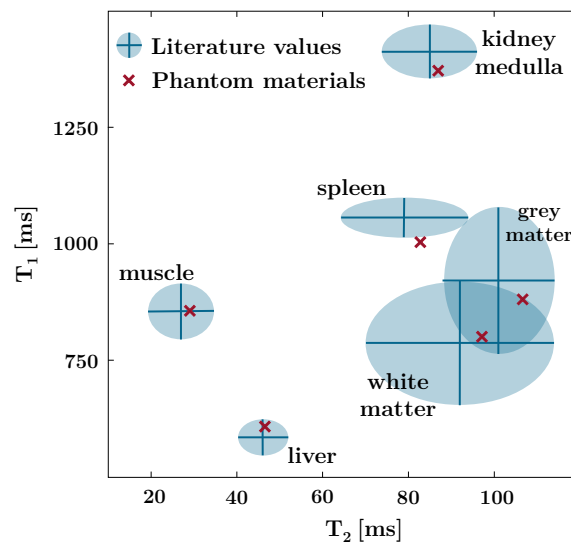


Figure 7: Comparison of T_1 and T_2 values of the developed phantom materials at 1.5 T with literature values [155, 156] for six representative soft tissues. The values of the phantom materials and the literature values (mean \pm standard deviation) are indicated in red and blue, respectively. The phantom materials were optimized for the mean of the corresponding literature value.

Although anthropomorphic attenuation is generally given by anthropomorphic CT-values, deviations can occur in materials with high- Z components ($Z > 20$), if their amount is higher than in human tissues. This is due to a typical calibration of clinical HLUTs based on materials with $Z < 20$. These deviations may be especially significant in proton and ion therapy due to the different dependence of the attenuation coefficient (CT) and SPR on the material’s atomic number and ionization potential as well as due to the finite range of protons and ions. As the developed materials contain a significant amount of Nickel ($Z_{Ni} = 28$), the SPR of the specific soft tissue samples was experimentally determined and compared with predictions via single- and dual-energy CT. This resulted in an SPR over-estimation using single-energy CT and a clinical HLUT (mean deviation of 2.3 ± 0.4 %), but in a good agreement of measurements and predictions via DECT (mean deviation of 0.2 ± 0.3 %). Hence, the developed materials are well suited to develop phantoms for future end-to-end tests of MR-guided ion therapy, if treatment planning is based on DECT measurements.

A HLUT is similarly used in photon therapy to convert CT-values to electron densities, which are needed to calculate the dose distribution. The high- Z components of the developed phantom materials may therefore also impact the dose calculation in conventional photon RT. This may require the determination of a specific correction factor. However, since the depth dependence of the photon dose is much less than for ions (figure 2), the impact of high- Z components in the developed materials is considered to be negligible for the application in photon therapy.

3.2.2 Advanced dosimetry in an anthropomorphic pelvis phantom

To assure feasibility of performing dosimetry using PG and TLDs in complex deformable phantoms such as the ADAM-PETer, a test measurement was performed and presented in publication III. This study served as important preliminary work for the final end-to-end test presented in publication VI by using the same phantom, but a much simplified treatment workflow. The high accuracy of both dosimetry systems within the complex setup was demonstrated by an overall good agreement of measured and planned doses with maximum deviations of less than 5 % in PG regions close to the container wall or TLD measurements in regions experiencing strong dose gradients. Larger deviations in peripheral regions of the PG volume may be caused by so-called wall effects (e.g. interaction of the PG with the container material or partial volume effects during MRI evaluation), or by generally slight dosimetric fluctuations in the PG evaluation, which were corrected in the central region by a PG renormalization to the treatment plan. Using the treatment plan for PG renormalization in a relatively small central volume of interest could have led to a misleadingly good agreement between measured and planned dose in this volume but poorer agreement in more distant regions. To avoid a dependence of the measurement on the treatment plan, the PG renormalization may be performed using additional external point-like dose measurements (e.g. TLDs [145, 146], publication VI). The rather simple treatment workflow applied in this test allowed for a thorough evaluation of the dosimetry systems without significant influences from organ deformations and advanced treatment procedures. A large margin of 4 mm to generate the PTV from the prostate structure ensured a uniform irradiation of the PG volume even for slight displacements despite having kept internal organs untouched between treatment planning and delivery (no adjustment of bladder and rectum fillings). As the treatment plan was calculated based on an in-room CT-on-rails system, only the treatment couch was rotated for treatment delivery without moving the phantom itself. Hence, potential displacements of the phantom as well as of internal structures were minimized and consequently, no treatment plan adaption was required.

3.3 End-to-end tests

End-to-end tests of complex RT treatment procedures are required to demonstrate their feasibility, to investigate the overall uncertainty, as well as to determine possible limitations. As all developed tests presented in this thesis combine advanced dosimetry systems such as PG and TLDs with complex (anthropomorphic) phantoms, they are typically not suited for regular QA measurements on a weekly or monthly basis, but rather for verifications of the specific workflow on longer time scales (e.g. yearly). Moreover, these tests are especially important in the commissioning phase of

new image-guided treatment devices, such as MR-Linacs, and of new treatment workflows, e.g. online adaptive MRgRT in presence of inter-fractional anatomical changes.

3.3.1 3D polymer dosimetry gel in clinical QA phantoms

A summary of phantoms equipped with PG for 3D dose measurements as applied for various QA purposes at DKFZ and UKHD was presented in publication IV. For such versatile applications from machine-related QA to end-to-end tests in case of inter- as well as intra-fractional motion, the use of PG must be as flexible as possible. This includes for example 3D printed PG containers in order to measure the dose in anthropomorphically-shaped volumes as well as a geometrical evaluation of the dose response directly after irradiation instead of full dosimetric evaluations after typical waiting times in the order of several days [152]. While the versatility of the presented phantoms and workflows demonstrates a wide applicability of PG for various QA purposes, all workflows share a high complexity due to elaborated PG experiments, in some cases combined with complex anthropomorphic phantoms. Therefore, these tests are not recommended to be performed routinely on a weekly or monthly basis, but rather for the commissioning of new image-guided treatment techniques such as online adaptive MRgRT. For this purpose, the implementation of PG dosimetry into clinical QA phantoms offers a great possibility for accurate 3D dose measurements in a wide range of scenarios.

3.3.2 Online adaptive MRgRT using a highly reproducible geometric phantom

In publication V, an end-to-end test of an online adaptive MRgRT treatment was performed using the AQUARIUM phantom. For this test, the water-filled phantom was equipped with several geometric structures fixed to reproducibly shiftable and rotatable rods. The structures were filled with PG or anthropomorphic image contrast in CT or MRI. The dose was measured in 3D using PG in the target structure and in an OAR. The high reproducibility of the phantom inserts allowed to compare three different irradiation scenarios: (i) delivering the treatment plan to the phantom in a reference setting without changing its geometry, (ii) delivering the same treatment plan after displacing the phantom's internal structures without a plan adaption, and (iii) performing a treatment plan adaption and delivering this reoptimized plan to the phantom in the displaced setting. Scenario (i) served as a reference by representing the optimal, but typically unrealistic, case where no inter-fractional anatomy change has occurred and no adaption of the treatment plan was required. On the contrary, a displacement of internal structures was simulated in scenarios (ii) and (iii). While irradiation (ii) showed a worst-case scenario, where the geometry significantly changed but no adaption was performed, the actually tested workflow of an MR-guided online plan adaption to account for this changed geometry was applied in irradiation (iii). The end-to-end test performed in this study demonstrated the feasibility to uniformly cover the target with a prescribed dose while significantly reducing the dose to the OAR in case of structure displacements by online adapting the treatment plan. The dose evaluation in both target and OAR structures of irradiation (iii) was well-comparable to the reference scenario (irradiation (i)). In contrast, a significant under-dosage in the PTV and over-dosage in the OAR was found in irradiation (ii), demonstrating the strong necessity to adapt the treatment plan. In conventional RT, such changes in the dose distribution due to geometrical variations of internal organs may either remain undetected or force

the treatment to be postponed, if an online plan adaption is technically not feasible. In all three irradiation scenarios of this study, the PG evaluation agreed well with the respective treatment plan (in irradiation (ii), the treatment plan was recalculated to the displaced phantom setting based on the online MRI, but was not adapted). The γ -index analysis (3 %/3 mm criterion) resulted in passing rates > 93 % for target and OAR structures in all three irradiations, respectively. Only small maximum deviations between measured and planned dose of 0.1 – 0.3 Gy were found, which is in the order of the PG’s dose resolution [121, 127]. However, a limitation of the AQUARIUM is that the internal structures are made of rigid materials, which do not allow deformations occurring e.g. by varying bladder and rectum fillings. In addition, the structures were surrounded by water which may lead to an unrealistic image contrasts as compared to patients. This may influence the accuracy of automated contouring and image registration algorithms. Therefore, this setup may not fully reflect the complexity of online adaptive treatments in patients. However, the end-to-end test using the AQUARIUM successfully demonstrated the overall necessity and technical feasibility to perform online adaptive MRgRT procedures at the MRIdian Linac with a high accuracy.

3.3.3 Multi-fractional online adaptive MRgRT using a pelvis phantom

A second end-to-end test of an online adaptive MRgRT procedure was performed using the anthropomorphic and deformable ADAM-PETer phantom. This time, treatment plan adaption and delivery over five fractions was simulated with varying bladder and rectum fillings. The accumulated dose was measured in 3D in the prostate as well as a rectum insert. Furthermore, TLDs were placed at the center and on the surface of the prostate for additional point-like dose measurements. In the preceding studies (publications III-V), the PG dose was normalized to the treatment plan, which is a standard procedure in PG dosimetry. Here, the dose measurement of the central TLD was used as a renormalization reference in the high-dose region to avoid the dependence of the dose evaluation on the treatment plan [145, 146]. However, the treatment plan still had to be used as a reference in the low-dose region, since an additional measurement, e.g. using a TLD, was not feasible in the low-dose region of the rectum. This is due to the phantom’s technical construction as well as the present dose gradient, which would not allow to simultaneously measure the same dose in the PG and the additional reference TLD. In this study, the renormalized PG dose maps and TLD measurements agreed well with the treatment plan being accumulated over the five applied treatment fractions. High passing rates of 98.9 % and 93.7 % were found for the PG evaluation of the prostate and rectum insert, respectively, when performing a γ -index analysis using a 3 %/3 mm criterion. Only few voxels of the PG evaluation in the prostate showed deviations up to 0.4 Gy. Slightly higher deviations of up to 0.5 Gy were found in the PG evaluation of the rectum insert. The increased deviation in the rectum may result from a dependency of the PG response on the dose fractionation scheme [157] as well as the small container size [121]. While the fractionation effect may be corrected by a renormalization of the PG dose, the dependency was shown to vary with the applied total dose [157]. Hence, increased deviations may occur in regions with dose levels between the two reference points used for the PG renormalization. The small container size of the rectum insert, which was technically required, may have led to an increased effect of PG interactions with the container material and of temperature gradients during PG storage times. Furthermore, TLD measurements showed a maximum

deviation of 0.1 Gy corresponding to 2.3 % at the center of the prostate and 4.7 % on the surface. These deviations may result from small variations in the TLD dose calibration or small positioning errors of the TLDs on the prostate surface within the dose gradient. In addition, the measured dose of both PG and TLDs may be influenced by slight variations in the calibration of the MR-Linac output, systematic errors in the dose calculation or in the various post-processing procedures. In addition, the DIRs of online MRIs and adapted dose maps to accumulate the dose of the treatment fractions may lead to uncertainties in the treatment plan used as reference for the measurement. In this end-to-end test, a comparison of different irradiation scenarios or dose measurement systems by successive experiments with the same phantom geometry was not possible, since the phantom's anatomy is not exactly reproducible. However, the test simulates the online adaptive MR-guided treatment scenario under highly realistic conditions. It therefore successfully demonstrated the feasibility and accuracy of online adapted MR-guided prostate irradiations, which is especially important for the commissioning of such new treatment techniques.

4 CONCLUSION

In this thesis, end-to-end tests for online adaptive MR-guided radiotherapy were developed and implemented at a 0.35 T MR-Linac. The recent introduction of MRgRT devices allows for online plan adaption and motion compensation and hence a potential increase of the dose in the tumor while sparing surrounding healthy tissue. However, such complex workflows need to be thoroughly validated before clinical implementation. This includes dedicated end-to-end tests that validate the feasibility and overall accuracy of the workflow, while identifying potential limitations. In the ideal case, such end-to-end tests should simulate patient treatments as realistically as possible and measure the applied dose distribution with high geometric and dosimetric accuracy. Several methods for the final implementation of end-to-end tests for online adaptive MRgRT, were therefore developed and validated in this thesis. This includes the standardization of 3D dosimetry using polymer gel and the development of anthropomorphic phantom materials. Finally, a set of end-to-end tests to validate complex image-guided radiotherapy procedures was established focusing on online adaptive MR-guided treatments in case of inter-fractional anatomy changes.

End-to-end testing phantoms to validate MRgRT procedures should comprise in the ideal case an accurate 3D dosimetry system, phantom materials with anthropomorphic radiological properties in CT and MRI as well as the possibility to simulate realistic anatomical changes. In the first part of this thesis, methods were therefore developed to be integrated into new as well as already existing end-to-end testing phantoms. This includes a standardized protocol to use PAGAT dosimetry gel, which allows for an accurate and reproducible conduction and evaluation of gel experiments. For an easy and consistent post-processing of such experiments, a dedicated open-source software tool was developed. Furthermore, phantom materials with individually adjustable CT and MRI contrast at three different magnetic field strengths (0.35, 1.5 and 3.0 T) were developed. These gel-like phantom materials exhibit anthropomorphic radiological properties in the range of soft tissues with positive CT-values.

In a next step, the developed methods were clinically validated. In this context, the radiological tissue equivalence of the developed phantom materials was demonstrated by comparing predicted and measured imaging parameters of nine specific soft tissue samples, which revealed mean deviations of less than 3.5 %. It was furthermore shown that the materials may be used for future MR-guided ion therapy applications, if treatment planning is performed based on dual-energy CT. In addition, the feasibility of using advanced dosimetry systems (polymer gel and thermoluminescence detectors) in an anthropomorphic and deformable pelvis phantom was demonstrated. Polymer gel measurements in the prostate resulted in a good agreement with the treatment plan with a passing rate of the 3D γ -index analysis (3 %/3 mm criterion) of 97.7 %. TLD measurement resulted in a mean deviation from the treatment plan of 1.78 %.

In the third part of this thesis, end-to-end tests of complex treatment procedures were developed and clinically implemented. First, a set of clinically applied quality assurance phantoms equipped with polymer dosimetry gel for dose evaluation was presented, which demonstrated the variable application of polymer gels for various quality assurance purposes. Finally, two end-to-end tests for online adaptive MR-guided radiotherapy in case of inter-fractional motion were developed and implemented at the 0.35 T MR-Linac using (i) a highly reproducible geometric phantom applying a single treatment fraction and (ii) a deformable and anthropomorphic pelvis phantom applying a total of five treatment fractions in a highly realistic setting with varying bladder and rectum fillings. These two tests demonstrated the feasibility to perform online adaptive MR-guided treatments with high accuracy in case of inter-fractional anatomy changes. Passing rates of the γ -index analysis (3 %/3 mm criterion) of 93.1 % (i) and 98.9 % (ii) were found when comparing the respective polymer gel measurement of the target structure with the online adapted treatment plan. Such end-to-end tests are of high importance for the commissioning of new image-guided treatment devices such as MR-Linacs and the implementation of complex treatment procedures such as online treatment plan adaption.

LIST OF FIGURES

Figure 1: Schematic visualization of a margin reduction.	2
Figure 2: Characteristic depth-dose profiles of photons, electrons and protons in water.....	4
Figure 3: Characteristic profiles of longitudinal and transversal magnetization relaxation.	7
Figure 4: Workflow development from conventional to adaptive image-guided radiotherapy. ...	10
Figure 5: Online adaptive treatment workflow at the MRIdian Linac at UKHD.	14
Figure 6: Thematic overview of the six publications (I-VI).....	21
Figure 7: Comparison of T_1 and T_2 values of phantom materials with literature.	120

LIST OF PUBLICATIONS

Journal articles

Alina Elter, Carolin Rippke, Wibke Johnen, Philipp Mann, Emily Hellwich, Andrea Schwahofer, Stefan Dorsch, Carolin Buchele, Sebastian Klüter and Christian P. Karger (2021) 'End-to-end test for fractionated online adaptive MR-guided radiotherapy using a deformable anthropomorphic pelvis phantom', *accepted, Phys. Med. Biol.*, <https://doi.org/10.1088/1361-6560/ac3e0c>

Alina Elter, Stefan Dorsch, Sarina Thomas, Clemens M. Hentschke, Ralf O. Floca, Armin Runz, Christian P. Karger and Philipp Mann (2021) 'PAGAT gel dosimetry for everyone: gel production, measurement and evaluation', *Biomed. Phys. Eng. Express* **7** 057001

Alina Elter, Emily Hellwich, Stefan Dorsch, Martin Schäfer, Armin Runz, Sebastian Klüter, Benjamin Ackermann, Stephan Brons, Christian P. Karger and Philipp Mann (2021) 'Development of phantom materials with independently adjustable CT- and MR-contrast at 0.35, 1.5 and 3 T', *Phys. Med. Biol.* **66** 045013

Mathieu Marot, Alina Elter, Philipp Mann, Andrea Schwahofer, Clemens Lang, Wibke Johnen, Stefan A. Körber, Bettina Beuthien-Baumann and Clarissa Gillmann (2021) 'Technical Note: On the feasibility of performing dosimetry in target and organ at risk using polymer dosimetry gel and thermoluminescence detectors in an anthropomorphic, deformable, and multimodal pelvis phantom', *Med. Phys.*, 48:5501– 5510

Alina Elter, Dorsch Stefan, Philipp Mann, Armin Runz, Wibke Johnen, C. Katharina Spindeldreier, Sebastian Klüter and Christian P. Karger (2019) 'End-to-end test of an online adaptive treatment procedure in MR-guided radiotherapy using a phantom with anthropomorphic structures', *Phys. Med. Biol.* **64** 225003

Alina Elter, Dorsch Stefan, Philipp Mann, Armin Runz, Wibke Johnen, Christian P. Karger (2019) 'Compatibility of 3D printing materials and printing techniques with PAGAT gel dosimetry', *Phys. Med. Biol.* **64** 04NT02

Stefan Dorsch, Philipp Mann, Alina Elter, Armin Runz, Sebastian Klüter, Christian P. Karger (2019) 'Measurement of isocenter alignment accuracy and image distortion of a 0.35 T MR-Linac System', *Phys. Med. Biol.* **64** 205011

Stefan Dorsch, Philipp Mann, Alina Elter, Armin Runz, C. Katharina Spindeldreier, Sebastian Klüter and Christian P. Karger (2019) 'Polymer gel-based measurements of the isocenter accuracy in an MR-LINAC', *J. Phys. Conf. Ser.* 1305 012007

Christian Möhler, Tom Russ, Patrick Wohlfahrt, Alina Elter, Armin Runz, Christian Richter and Steffen Greilich (2018) ‘Experimental verification of stopping-power prediction from single- and dual-energy computed tomography in biological tissues’, *Phys. Med. Biol.* **63** 025001

Alina Elter, Dorsch Stefan, Mathieu Marot, Clarissa Gillmann, Wibke Johnen, Armin Runz, C. Katharina Spindeldreier, Sebastian Klüter, Christian P. Karger and Philipp Mann ‘Gel dosimetry as a tool for clinical implementation of image-guided radiotherapy’, *peer-reviewed as conference paper of the 2021 IC3DDose virtual meeting, publication pending*

Conference contributions

Oral contributions

Alina Elter – **Invited Talk:** End-to-end-Tests for adaptive MRgRT. In: *Virtual satellite symposium of Virtual 8th MR in RT Symposium, online congress (2021)*

Alina Elter – **Invited Talk:** MR-guided radiotherapy: working at the boundary of MR physics and RT physics. In: *3rd European Congress of Medical Physics, online congress (2021)*

Alina Elter, Emily Hellwich, Stefan Dorsch, Martin Schäfer, Armin Runz, Sebastian Klüter, Benjamin Ackermann, Stephan Brons, Christian P. Karger, Philipp Mann – **Talk:** Development of anthropomorphic phantom materials for end-to-end testing in MR-guided ion therapy. In: *Virtual 8th MR in RT Symposium, online congress (2021)*

Stefan Dorsch, Philipp Mann, Alina Elter, Armin Runz, C. Katharina Spindeldreier, Sebastian Klüter, Christian P. Karger – **Talk:** Measurement of isocenter accuracy and image distortion in MRgRT. In: *Virtual 8th MR in RT Symposium, online congress (2021)*

Alina Elter, Emily Hellwich, Stefan Dorsch, Martin Schäfer, Armin Runz, Sebastian Klüter, Christian P. Karger, Philipp Mann – **Talk:** Entwicklung von Phantommaterialien mit individuell anpassbaren CT Werten sowie T₁- und T₂- Zeiten bei drei verschiedenen Feldstärken. In: *51. Jahrestagung der Deutschen Gesellschaft für Medizinische Physik (e.DGMP), online congress (2020)*

Emily Hellwich, Alina Elter, Stefan Dorsch, Philipp Mann, Julian Emmerich, Martin Schäfer, Armin Runz, C. Katharina Renkamp, Jeschua Geist, Christian P. Karger, Jürgen Debus, Sebastian Klüter – **Talk:** Quantification and reduction of susceptibility artefacts for a quality assurance phantom in MRgRT. In: *Annual conference of the European Society for Radiotherapy & Oncology (ESTRO), online congress (2020)*

Stefan Dorsch, Philipp Mann, Alina Elter, Armin Runz, C. Katharina Spindeldreier, Sebastian Klüter, Christian P. Karger – **Talk:** Messung der Isozentrumsgenauigkeit und Bildverzerrung in der MRgRT. In: *51. Jahrestagung der Deutschen Gesellschaft für Medizinische Physik (e.DGMP), online congress (2020)*

Alina Elter, Dorsch Stefan, Philipp Mann, Armin Runz, Wibke Johnen, Christian P. Karger – **Talk:** Development of a deformable phantom for validation of adaptive irradiation methods in MRgRT. In: *38th annual conference of the European Society for Radiotherapy & Oncology (ESTRO), Milano, Italy (2019)*

Alina Elter, Dorsch Stefan, Philipp Mann, Sebastian Klüter, Christian P. Karger – **Talk:** Validation of adaptive irradiation procedures for MR-guided radiotherapy using a novel deformable phantom. In: *24th International Conference on Medical Physics, Santiago de Chile, Chile (2019)*

Alina Elter, Dorsch Stefan, Philipp Mann, Armin Runz, Wibke Johnen, Sebastian Klüter, Christian P. Karger – **Talk:** Validierung adaptiver Bestrahlungsprozeduren für die MR-geführte Strahlentherapie mittels eines neuartigen deformierbaren Phantoms. In: *50. Jahrestagung der Deutschen Gesellschaft für Medizinische Physik (DGMP), Stuttgart, Germany (2019)*

Alina Elter, Dorsch Stefan, Philipp Mann, Armin Runz, Clemens Lang, Christian P. Karger – **Talk:** 3D Polymer Gel Dosimetrie – Eignung von Druckmaterialien und -druckverfahren für den Bau neuer Phantome. In: *49. Jahrestagung der Deutschen Gesellschaft für Medizinische Physik (DGMP), Nürnberg, Germany (2018)*

Stefan Dorsch, Philipp Mann, Alina Elter, Armin Runz, Sebastian Klüter, Christian P. Karger – **Talk:** Polymer gel-based measurements of the isocenter accuracy in an MR-LINAC. In: *10th International Conference: 3D and Advanced Dosimetry (IC3DDose), Shanghai, China (2018)*

Poster contributions

Alina Elter, Carolin Rippke, Wibke Johnen, Philipp Mann, Emily Hellwich, Stefan Dorsch, Carolin Buchele, Sebastian Klüter, Christian P. Karger – **Poster:** Investigation of dosimetry gel fractionation effects for end-to-end tests of complex MR-guided treatment scenarios. In: *Joint Conference of the ÖGMP, DGMP and SGSMP, online congress (2021)*

Alina Elter, Philipp Mann, Emily Hellwich, Dorsch Stefan, Christian P. Karger – **Poster:** Absolute gel dosimetry without dose renormalization employing fractionated calibration. In: *Annual conference of the European Society for Radiotherapy & Oncology (ESTRO), online congress (2021)*

Anna Fischer, Alina Elter, Philipp Mann, Stefan Dorsch, Regula Gnirs, Juliane Hörner-Rieber, Oliver Schenk, C. Katharina Spindeldreier, Christian P. Karger – **Poster:** Performance of deformable image registration for the integration of diagnostic MR images to treatment. In: *Virtual 8th MR in RT Symposium, online congress (2021)*

Emily Hellwich, Alina Elter, Stefan Dorsch, Philipp Mann, Julian Emmerich, Armin Runz, Martin Schäfer, Jeschua Geist, Sebastian Klüter, C. Katharina Renkamp, Christian P. Karger, Jürgen Debus – **Poster:** Quantification and reduction of susceptibility artefacts for a quality assurance phantom in MRgRT. In: *Virtual 8th MR in RT Symposium, online congress (2021)*

Emily Hellwich, Alina Elter, Stefan Dorsch, Philipp Mann, Julian Emmerich, Martin Schäfer, Anahita Bakhtiari Moghaddam, Armin Runz, C. Katharina Renkamp, Jeschua Geist, Christian P. Karger, Jürgen Debus, Sebastian Klüter – **Poster:** Quantification and reduction of susceptibility artefacts for a quality assurance phantom in MRgRT. In: *Joint Conference of the ÖGMP, DGMP and SGSMP, online congress (2021)*

Alina Elter, Philipp Mann, Dorsch Stefan, Armin Runz, Martin Schäfer, Christian P. Karger – **Poster:** Development of materials with independently adjustable MR- and CT-contrast to validate pseudo CTs. In: *Annual conference of the European Society for Radiotherapy & Oncology (ESTRO), online congress (2020)*

Mathieu Marot, Alina Elter, Philipp Mann, Andrea Schwahofer, Clemens Lang, Wibke Johnen, Stefan A. Körber, Bettina Beuthien-Baumann, Clarissa Gillmann – **Poster:** End-to-end empirical validation of 3D dose distributions using an anthropomorphic pelvis phantom. In: *Annual conference of the European Society for Radiotherapy & Oncology (ESTRO), online congress (2020)*

Anna Fischer, Alina Elter, Philipp Mann, Stefan Dorsch, Regula Gnirs, Juliane Hörner-Rieber, Oliver Schenk, C. Katharina Spindeldreier, Christian P. Karger – **Poster:** Untersuchung der deformierbaren Bildregistrierung zur Integration diagnostischer MRT-Bilder in die Bestrahlungsplanung. In: *51. Jahrestagung der Deutschen Gesellschaft für Medizinische Physik (e.DGMP), online congress (2020)*

Stefan Dorsch, Philipp Mann, Alina Elter, Armin Runz, Sebastian Klüter, Christian P. Karger – **Poster:** Polymer gel-based tests for geometric accuracy in a 0.35 T MR-LINAC. In: *38th annual conference of the European Society for Radiotherapy & Oncology (ESTRO), Milano, Italy (2019)*

Wibke Johnen, Armin Runz, Noa Homolka, Nina I. Niebuhr, Philipp Mann, Bettina Beuthien-Baumann, Clarissa Gillmann, Asja Pfaffenberger, Alina Elter, Aswin L. Hoffmann, Esther Troost, Stefan A. Körber, Gernot Echner – **Poster:** Update ADAM-pelvis phantom: New possibilities to simulate treatment scenarios in radiotherapy. In: *38th annual conference of the European Society for Radiotherapy & Oncology (ESTRO), Milano, Italy (2019)*

Stefan Dorsch, Philipp Mann, Alina Elter, Armin Runz, Sebastian Klüter, Christian P. Karger – **Poster:** Polymer gel-based measurements of radiation isocenter accuracy in magnetic fields. In: *6th MR in RT Symposium, Utrecht, the Netherlands (2018)*

Honors and awards

- | | |
|----------------|---|
| April 2021 | 2 nd prize of the Young Investigator Session 2021 of <i>Virtual 8th MRinRT Symposium</i> |
| September 2020 | IOP trusted reviewer status in recognition of an exceptionally high level of peer review competency awarded by <i>IOP Publishing</i> |
| September 2020 | Registration fee grant of <i>51. Jahrestagung der Deutschen Gesellschaft für Medizinische Physik (e.DGMP)</i> |
| September 2019 | Travel grant for <i>24th International Conference on Medical Physics, Santiago de Chile, Chile</i> awarded by <i>Deutsche Akademische Austauschdienst e. V. (DAAD)</i> |
| September 2019 | Travel grant of <i>50. Jahrestagung der Deutschen Gesellschaft für Medizinische Physik (DGMP), Stuttgart, Germany</i> |
| February 2019 | Publication V featured in IOP Publishing ltd.'s magazine " <i>physics world</i> ": 3D printing enables gel dosimetry in complex phantoms |

BIBLIOGRAPHY

1. Fidler, M.M., I. Soerjomataram, and F. Bray, *A global view on cancer incidence and national levels of the human development index*. International Journal of Cancer, 2016. **139**(11): p. 2436-2446.
2. Wild, C., E. Weiderpass, and B.W. Stewart, *World cancer report cancer research for cancer prevention*. 2020, Lyon: International Agency for Research on Cancer World Health Organization Press.
3. Robert-Koch-Institut and G.d.e.K.i.D. eV., *Krebs in Deutschland 2015/2016*. 2019.
4. Baumann, M., et al., *Radiation oncology in the era of precision medicine*. Nature reviews. Cancer, 2016. **16**(4): p. 234-249.
5. Baskar, R., et al., *Cancer and radiation therapy: current advances and future directions*. International journal of medical sciences, 2012. **9**(3): p. 193-199.
6. Lomax, M.E., L.K. Folkes, and P. O'Neill, *Biological Consequences of Radiation-induced DNA Damage: Relevance to Radiotherapy*. Clinical Oncology, 2013. **25**(10): p. 578-585.
7. Emami, B., et al., *Tolerance of normal tissue to therapeutic irradiation*. International Journal of Radiation Oncology, Biology, Physics, 1991. **21**(1): p. 109-122.
8. Bentzen, S.M., et al., *Quantitative Analyses of Normal Tissue Effects in the Clinic (QUANTEC): an introduction to the scientific issues*. International Journal of Radiation Oncology, Biology, Physics, 2010. **76**(3 Suppl): p. S3-S9.
9. Landberg, T., et al., *Report 62*. Journal of the International Commission on Radiation Units and Measurements, 1999. **os32**.
10. Landberg, T., et al., *Report 50*. Journal of the International Commission on Radiation Units and Measurements, 1993. **os26**.
11. van Herk, M., *Errors and margins in radiotherapy*. Seminars in Radiation Oncology, 2004. **14**(1): p. 52-64.
12. Karger, C.P., *Klinische Strahlenbiologie*, in *Medizinische Physik: Grundlagen – Bildgebung – Therapie – Technik*, W. Schlegel, C.P. Karger, and O. Jäkel, Editors. 2018, Springer Berlin Heidelberg: Berlin, Heidelberg. p. 451-472.
13. Taylor, A. and M.E.B. Powell, *Intensity-modulated radiotherapy--what is it?* Cancer imaging : the official publication of the International Cancer Imaging Society, 2004. **4**(2): p. 68-73.
14. Schlegel, W. and P. Kneschaurek, *Inverse Bestrahlungsplanung*. Strahlentherapie und Onkologie, 1999. **175**(5): p. 197-207.
15. Webb, S., *The physical basis of IMRT and inverse planning*. The British Journal of Radiology, 2003. **76**(910): p. 678-689.
16. Karzmark, C.J. and N.C. Pering, *Electron linear accelerators for radiation therapy: history, principles and contemporary developments*. Physics in Medicine and Biology, 1973. **18**(3): p. 321-354.
17. Schlegel, W., *Bestrahlungsgeräte der Teletherapie*, in *Medizinische Physik: Grundlagen – Bildgebung – Therapie – Technik*, W. Schlegel, C.P. Karger, and O. Jäkel, Editors. 2018, Springer Berlin Heidelberg: Berlin, Heidelberg. p. 405-424.

-
18. Schlegel, W. and J. Bille, *Medizinische Strahlenphysik 2*. 2002, Berlin, Heidelberg: Springer Berlin Heidelberg.
 19. Okumura, Y., T. Kitagawa, and T. Kitabatake, *Scattering Foil Device for High-Energy Electron-Beam Therapy*. *Radiology*, 1969. **93**(3): p. 667-670.
 20. Greilich, S. and J.-M. Osinga-Blättermann, *Strahlenphysik*, in *Medizinische Physik: Grundlagen – Bildgebung – Therapie – Technik*, W. Schlegel, C.P. Karger, and O. Jäkel, Editors. 2018, Springer Berlin Heidelberg: Berlin, Heidelberg. p. 3-35.
 21. Paganetti, H., *Proton therapy physics*. Series in medical physics and biomedical engineering. 2012, Boca Raton, Fla. [u.a.]: Taylor & Francis. 684.
 22. Krämer, M., et al., *Treatment planning for heavy-ion radiotherapy: physical beam model and dose optimization*. *Physics in Medicine and Biology*, 2000. **45**(11): p. 3299-3317.
 23. Brown, A. and H. Suit, *The centenary of the discovery of the Bragg peak*. *Radiotherapy and Oncology*, 2004. **73**(3): p. 265-268.
 24. Takada, K., *Qualitative Comparison of Proton Beams and Other Radiotherapy Beams*, in *Proton Beam Radiotherapy: Physics and Biology*, K. Tsuboi, T. Sakae, and A. Gerelchuluun, Editors. 2020, Springer Singapore: Singapore. p. 73-82.
 25. Brock, K.K., et al., *Use of image registration and fusion algorithms and techniques in radiotherapy: Report of the AAPM Radiation Therapy Committee Task Group No. 132*. *Medical Physics*, 2017. **44**(7): p. e43-e76.
 26. Czajkowski, P. and T. Piotrowski, *Registration methods in radiotherapy*. *Reports of Practical Oncology & Radiotherapy*, 2019. **24**(1): p. 28-34.
 27. Rosenman, J.G., et al., *Image Registration: An Essential Part of Radiation Therapy Treatment Planning*. *International Journal of Radiation Oncology, Biology, Physics*, 1998. **40**(1): p. 197-205.
 28. Hounsfield, G.N., *Computerized transverse axial scanning (tomography): Part 1. Description of system*. *The British Journal of Radiology*, 1973. **46**(552): p. 1016-1022.
 29. Kachelrieß, M., *Computertomographie*, in *Medizinische Physik: Grundlagen – Bildgebung – Therapie – Technik*, W. Schlegel, C.P. Karger, and O. Jäkel, Editors. 2018, Springer Berlin Heidelberg: Berlin, Heidelberg. p. 153-203.
 30. Chang, A.E., et al., *Magnetic resonance imaging versus computed tomography in the evaluation of soft tissue tumors of the extremities*. *Annals of surgery*, 1987. **205**(4): p. 340-348.
 31. Stolzmann, P., *Strahlenexposition*, in *Wie funktioniert CT?* 2011, Springer, Berlin, Heidelberg. p. 197-200.
 32. Schneider, U., E. Pedroni, and A. Lomax, *The calibration of CT Hounsfield units for radiotherapy treatment planning*. *Physics in Medicine and Biology*, 1996. **41**(1): p. 111-124.
 33. Paganetti, H., *Range uncertainties in proton therapy and the role of Monte Carlo simulations*. *Physics in Medicine and Biology*, 2012. **57**(11): p. R99-R117.
 34. Schaffner, B. and E. Pedroni, *The precision of proton range calculations in proton radiotherapy treatment planning: experimental verification of the relation between CT-HU and proton stopping power*. *Physics in Medicine and Biology*, 1998. **43**(6): p. 1579-1592.

35. Yang, M., et al., *Comprehensive analysis of proton range uncertainties related to patient stopping-power-ratio estimation using the stoichiometric calibration*. Physics in Medicine and Biology, 2012. **57**(13): p. 4095-4115.
36. Yang, M., et al., *Theoretical variance analysis of single- and dual-energy computed tomography methods for calculating proton stopping power ratios of biological tissues*. Physics in Medicine and Biology, 2010. **55**(5): p. 1343-1362.
37. Hünemohr, N., et al., *Experimental verification of ion stopping power prediction from dual energy CT data in tissue surrogates*. Physics in Medicine and Biology, 2014. **59**(1): p. 83-96.
38. Möhler, C., et al., *Experimental verification of stopping-power prediction from single- and dual-energy computed tomography in biological tissues*. Physics in Medicine and Biology, 2018. **63**(025001).
39. Ladd, M.E., et al., *Magnetresonanztomographie und -spektroskopie*, in *Medizinische Physik*. 2018, Springer Spektrum, Berlin, Heidelberg. p. 205-283.
40. Brown, R.W., et al., *Magnetic Resonance Imaging*. 2nd ed. Physical Principles and Sequence Design. 2014, Hoboken, New Jersey: Wiley Blackwell.
41. Reiser, M.F., W. Semmler, and H. Hricak, *Magnetic Resonance Tomography*. 1st ed. 2008, Berlin, Heidelberg: Springer Berlin Heidelberg. 1510.
42. Brix, G., et al., *Basics of Magnetic Resonance Imaging and Magnetic Resonance Spectroscopy*, in *Magnetic Resonance Tomography*, M.F. Reiser, W. Semmler, and H. Hricak, Editors. 2008, Springer Berlin Heidelberg: Berlin, Heidelberg. p. 3-167.
43. Cheng, H.-L.M., et al., *Practical medical applications of quantitative MR relaxometry*. Journal of Magnetic Resonance Imaging, 2012. **36**(4): p. 805-824.
44. Cercignani, M. and M.A. Horsfield, *The physical basis of diffusion-weighted MRI*. Journal of the Neurological Sciences, 2001. **186**: p. S11-S14.
45. Glover, G.H., *Overview of functional magnetic resonance imaging*. Neurosurgery clinics of North America, 2011. **22**(2): p. 133-139.
46. Le Bihan, D., *Molecular diffusion nuclear magnetic resonance imaging*. Magnetic resonance quarterly, 1991. **7**(1): p. 1-30.
47. Bieri, O. and K. Scheffler, *Fundamentals of balanced steady state free precession MRI*. Journal of Magnetic Resonance Imaging, 2013. **38**(1): p. 2-11.
48. Chavhan, G.B., et al., *Steady-State MR Imaging Sequences: Physics, Classification, and Clinical Applications*. RadioGraphics, 2008. **28**(4): p. 1147-1160.
49. Scheffler, K. and J. Hennig, *Is TrueFISP a gradient-echo or a spin-echo sequence?* Magnetic Resonance in Medicine, 2003. **49**(2): p. 395-397.
50. Meiboom, S. and D. Gill, *Modified Spin-Echo Method for Measuring Nuclear Relaxation Times*. Review of Scientific Instruments, 1958. **29**: p. 688-691.
51. Hennig, J., A. Nauerth, and H. Friedburg, *RARE imaging: A fast imaging method for clinical MR*. Magnetic Resonance in Medicine, 1986. **3**(6): p. 823-833.
52. Jaffray, D.A., *Image-guided radiotherapy: from current concept to future perspectives*. Nature Reviews Clinical Oncology, 2012. **9**(12): p. 688-699.
53. Verellen, D., M.D. Ridder, and G. Storme, *A (short) history of image-guided radiotherapy*. Radiotherapy and Oncology, 2008. **86**(1): p. 4-13.

-
54. van Herk, M., *Different Styles of Image-Guided Radiotherapy*. Seminars in Radiation Oncology, 2007. **17**(4): p. 258-267.
 55. Jäkel, O., *Bildgebung für die Strahlentherapie*, in *Medizinische Physik: Grundlagen – Bildgebung – Therapie – Technik*, W. Schlegel, C.P. Karger, and O. Jäkel, Editors. 2018, Springer Berlin Heidelberg: Berlin, Heidelberg. p. 473-484.
 56. MacKay, R.I., *Image Guidance for Proton Therapy*. Clinical Oncology, 2018. **30**(5): p. 293-298.
 57. Raaymakers, B.W., A.J.E. Raaijmakers, and J.J.W. Lagendijk, *Feasibility of MRI guided proton therapy: magnetic field dose effects*. Physics in Medicine and Biology, 2008. **53**(20): p. 5615-5622.
 58. Echner, G., *Patientenlagerung und -positionierung*, in *Medizinische Physik: Grundlagen – Bildgebung – Therapie – Technik*, W. Schlegel, C.P. Karger, and O. Jäkel, Editors. 2018, Springer Berlin Heidelberg: Berlin, Heidelberg. p. 515-524.
 59. Xing, L., J. Siebers, and P. Keall, *Computational Challenges for Image-Guided Radiation Therapy: Framework and Current Research*. Seminars in Radiation Oncology, 2007. **17**(4): p. 245-257.
 60. Mosleh-Shirazi, M.A., et al., *A cone-beam megavoltage CT scanner for treatment verification in conformal radiotherapy*. Radiotherapy and Oncology, 1998. **48**(3): p. 319-328.
 61. Pouliot, J., et al., *Low-dose megavoltage cone-beam CT for radiation therapy*. International Journal of Radiation Oncology, Biology, Physics, 2005. **61**(2): p. 552-560.
 62. Jaffray, D.A., et al., *Flat-panel cone-beam computed tomography for image-guided radiation therapy*. International Journal of Radiation Oncology, Biology, Physics, 2002. **53**(5): p. 1337-1349.
 63. Bostel, T., et al., *Prospective feasibility analysis of a novel off-line approach for MR-guided radiotherapy*. Strahlentherapie und Onkologie, 2018. **194**(5): p. 425-434.
 64. Karlsson, M., et al., *Dedicated Magnetic Resonance Imaging in the Radiotherapy Clinic*. International Journal of Radiation Oncology, Biology, Physics, 2009. **74**(2): p. 644-651.
 65. Jaffray, D.A., et al., *A Facility for Magnetic Resonance-Guided Radiation Therapy*. Seminars in Radiation Oncology, 2014. **24**(3): p. 193-195.
 66. Raaymakers, B.W., et al., *Integrating a 1.5 T MRI scanner with a 6 MV accelerator: proof of concept*. Physics in Medicine and Biology, 2009. **54**(N229).
 67. Mutic, S. and J.F. Dempsey, *The ViewRay system: magnetic resonance-guided and controlled radiotherapy*. Seminars in Radiation Oncology, 2014. **24**(3): p. 196-199.
 68. Fallone, B.G., et al., *First MR images obtained during megavoltage photon irradiation from a prototype integrated linac-MR system*. Medical Physics, 2009. **36**(6): p. 2084-2088.
 69. Keall, P.J., M. Barton, and S. Crozier, *The Australian magnetic resonance imaging-linac program*. Seminars in Radiation Oncology, 2014. **24**(3): p. 203-206.
 70. Jiang, S.B., *Technical aspects of image-guided respiration-gated radiation therapy*. Medical Dosimetry, 2006. **31**(2): p. 141-151.
 71. Kubo, H.D. and B.C. Hill, *Respiration gated radiotherapy treatment: a technical study*. Physics in Medicine and Biology, 1996. **41**(1): p. 83-91.

72. Tacke, M.B., et al., *Real-time tumor tracking: Automatic compensation of target motion using the Siemens 160 MLC*. Medical Physics, 2010. **37**(2): p. 753-761.
73. Fast, M.F., et al., *Dynamic tumor tracking using the Elekta Agility MLC*. Medical Physics, 2014. **41**(11).
74. Shirato, H., et al., *Four-dimensional treatment planning and fluoroscopic real-time tumor tracking radiotherapy for moving tumor*. International Journal of Radiation Oncology, Biology, Physics, 2000. **48**(2): p. 435-442.
75. Shirato, H., et al., *Physical aspects of a real-time tumor-tracking system for gated radiotherapy*. International Journal of Radiation Oncology, Biology, Physics, 2000. **48**(4): p. 1187-1195.
76. Kuo, J.S., et al., *The CyberKnife stereotactic radiosurgery system: description, installation, and an initial evaluation of use and functionality*. Neurosurgery, 2008. **62**(suppl_2): p. 1235-1239.
77. Meeks, S.L., et al., *Optically Guided Patient Positioning Techniques*. Seminars in Radiation Oncology, 2005. **15**(3): p. 192-201.
78. Schlosser, J., K. Salisbury, and D. Hristov, *Telerobotic system concept for real-time soft-tissue imaging during radiotherapy beam delivery*. Medical Physics, 2010. **37**(12): p. 6357-6367.
79. Green, O.L., et al., *Implementation of Real-Time, Real-Anatomy Tracking and Radiation Beam Control on the First MR-IGRT Clinical System*. International Journal of Radiation Oncology, Biology, Physics, 2015. **93**(3).
80. Spindeldreier, C.K., et al., *MR-guided radiotherapy of moving targets*. Der Radiologe, 2021.
81. Keall, P.J., et al., *The first clinical implementation of electromagnetic transponder-guided MLC tracking*. Medical Physics, 2014. **41**(020702).
82. Depuydt, T., et al., *Treating patients with real-time tumor tracking using the Vero gimbaled linac system: Implementation and first review*. Radiotherapy and Oncology, 2014. **112**(3): p. 343-351.
83. Nuyttens, J.J., et al., *Lung tumor tracking during stereotactic radiotherapy treatment with the CyberKnife: Marker placement and early results*. Acta Oncologica, 2006. **45**(7): p. 961-965.
84. Green, O.L., L.E. Henke, and G.D. Hugo, *Practical Clinical Workflows for Online and Offline Adaptive Radiation Therapy*. Seminars in Radiation Oncology, 2019. **29**(3): p. 219-227.
85. Schlegel, W., et al., *Bestrahlungsverfahren*, in *Medizinische Physik: Grundlagen – Bildgebung – Therapie – Technik*, W. Schlegel, C.P. Karger, and O. Jäkel, Editors. 2018, Springer Berlin Heidelberg: Berlin, Heidelberg. p. 525-577.
86. Acharya, S., et al., *Online Magnetic Resonance Image Guided Adaptive Radiation Therapy: First Clinical Applications*. International Journal of Radiation Oncology, Biology, Physics, 2016. **94**(2): p. 394-403.
87. Kurz, C., et al., *Medical physics challenges in clinical MR-guided radiotherapy*. Radiation Oncology, 2020. **15**(93).
88. Winkel, D., et al., *Adaptive radiotherapy: The Elekta Unity MR-linac concept*. Clinical and Translational Radiation Oncology, 2019. **18**: p. 54-59.

-
89. Bol, G.H., et al., *Fast online Monte Carlo-based IMRT planning for the MRI linear accelerator*. Physics in Medicine and Biology, 2012. **57**(5): p. 1375-1385.
 90. Wang, Y., et al., *A GPU-accelerated Monte Carlo dose calculation platform and its application toward validating an MRI-guided radiation therapy beam model*. Medical Physics, 2016. **43**(7): p. 4040-4052.
 91. Gngr, G., et al., *Time Analysis of Online Adaptive Magnetic Resonance-Guided Radiation Therapy Workflow According to Anatomical Sites*. Practical Radiation Oncology, 2021. **11**(1): p. e11-e21.
 92. Archambault, Y., et al., *Making on-line adaptive radiotherapy possible using artificial intelligence and machine-learning for efficient daily re-planning*. Medical Physics International, 2020. **9**(2): p. 77-86.
 93. Sibolt, P., et al., *Clinical implementation of artificial intelligence-driven cone-beam computed tomography-guided online adaptive radiotherapy in the pelvic region*. Physics and Imaging in Radiation Oncology, 2021. **17**: p. 1-7.
 94. Rogowski, P., et al., *Feasibility and Early Clinical Experience of Online Adaptive MR-Guided Radiotherapy of Liver Tumors*. Cancers, 2021. **13**(7).
 95. Intven, M.P.W., et al., *Online adaptive MR-guided radiotherapy for rectal cancer; feasibility of the workflow on a 1.5T MR-linac: clinical implementation and initial experience*. Radiotherapy and Oncology, 2021. **154**: p. 172-178.
 96. Boldrini, L., et al., *Online adaptive magnetic resonance guided radiotherapy for pancreatic cancer: state of the art, pearls and pitfalls*. Radiation Oncology, 2019. **14**(1): p. 71.
 97. Schellhammer, S.M., et al., *Integrating a low-field open MR scanner with a static proton research beam line: proof of concept*. Physics in Medicine and Biology, 2018. **63**(23LT01).
 98. Debus, J. *The ARTEMIS- Project Heidelberg*. in *Virtual 8th MR in RT Symposium 2021*. 2021.
 99. Klter, S., *Technical design and concept of a 0.35 T MR-Linac*. Clinical and Translational Radiation Oncology, 2019. **18**: p. 98-101.
 100. Bohoudi, O., et al., *Fast and robust online adaptive planning in stereotactic MR-guided adaptive radiation therapy (SMART) for pancreatic cancer*. Radiotherapy and Oncology, 2017. **125**(3): p. 439-444.
 101. Smit, K., et al., *Towards reference dosimetry for the MR-linac: magnetic field correction of the ionization chamber reading*. Physics in Medicine and Biology, 2013. **58**(17): p. 5945-5957.
 102. Spindeldreier, C.K., et al., *Radiation dosimetry in magnetic fields with Farmer-type ionization chambers: determination of magnetic field correction factors for different magnetic field strengths and field orientations*. Physics in Medicine and Biology, 2017. **62**(16): p. 6708-6728.
 103. van Asselen, B., et al., *A formalism for reference dosimetry in photon beams in the presence of a magnetic field*. Physics in Medicine and Biology, 2018. **63**(125008).
 104. Almond, P.R., et al., *AAPM's TG-51 protocol for clinical reference dosimetry of high-energy photon and electron beams*. Medical Physics, 1999. **26**(9): p. 1847-1870.

105. Miften, M., et al., *Tolerance limits and methodologies for IMRT measurement-based verification QA: Recommendations of AAPM Task Group No. 218*. Medical Physics, 2018. **45**(4): p. e53-e83.
106. Ginn, J.S., et al., *Characterization of spatial distortion in a 0.35 T MRI-guided radiotherapy system*. Physics in Medicine and Biology, 2017. **62**(11): p. 4525-4540.
107. Yan, Y., et al., *A methodology to investigate the impact of image distortions on the radiation dose when using magnetic resonance images for planning*. Physics in Medicine and Biology, 2018. **63**(085005).
108. Chen, C.-C., et al., *Quality Assurance of Clinical MRI Scanners Using ACR MRI Phantom: Preliminary Results*. Journal of Digital Imaging, 2004. **17**(4): p. 279-284.
109. Gao, Y., et al., *Technical Note: Validation of an automatic ACR phantom quality assurance tool for an MR-guided radiotherapy system*. Medical Physics, 2021. **48**(4): p. 1540-1545.
110. Price, R.R., et al., *Quality assurance methods and phantoms for magnetic resonance imaging: Report of AAPM nuclear magnetic resonance Task Group No. 1*. Medical Physics, 1990. **17**(2): p. 287-295.
111. Snyder, J.E., et al., *Commissioning of a 1.5T Elekta Unity MR-linac: A single institution experience*. Journal of Applied Clinical Medical Physics, 2020. **21**(7): p. 160-172.
112. Dorsch, S., et al., *Measurement of isocenter alignment accuracy and image distortion of an 0.35 T MR-Linac system*. Physics in Medicine and Biology, 2019. **64**(205011).
113. Tijssen, R.H.N., et al., *MRI commissioning of 1.5T MR-linac systems – a multi-institutional study*. Radiotherapy and Oncology, 2019. **132**: p. 114-120.
114. Agazaryan, N., T.D. Solberg, and J.J. DeMarco, *Patient specific quality assurance for the delivery of intensity modulated radiotherapy*. Journal of Applied Clinical Medical Physics, 2003. **4**(1): p. 40-50.
115. Rhein, B. and P. Häring, *3D Quality Assurance Systems*, in *New Technologies in Radiation Oncology*, W. Schlegel, T. Bortfeld, and A.-L. Grosu, Editors. 2006, Springer Berlin Heidelberg: Berlin, Heidelberg. p. 411-423.
116. Mönnich, D., et al., *Quality assurance of IMRT treatment plans for a 1.5 T MR-linac using a 2D ionization chamber array and a static solid phantom*. Physics in Medicine and Biology, 2020. **65**(16NT01).
117. Smit, K., et al., *Performance of a multi-axis ionization chamber array in a 1.5 T magnetic field*. Physics in Medicine and Biology, 2014. **59**(7): p. 1845-1855.
118. Li, H.H., et al., *Patient-Specific Quality Assurance for the Delivery of ^{60}Co Intensity Modulated Radiation Therapy Subject to a 0.35T Lateral Magnetic Field*. International Journal of Radiation Oncology, Biology, Physics, 2015. **91**(1): p. 65-72.
119. Houweling, A.C., et al., *Performance of a cylindrical diode array for use in a 1.5 T MR-linac*. Physics in Medicine and Biology, 2016. **61**(3): p. N80-N89.
120. de Vries, J.H.W., et al., *Characterization of a prototype MR-compatible Delta4 QA system in a 1.5 tesla MR-linac*. Physics in Medicine and Biology, 2018. **63**(02NT02).
121. Baldock, C., et al., *Polymer gel dosimetry*. Physics in Medicine and Biology, 2010. **55**(5): p. R1-63.
122. Vandecasteele, J. and Y. De Deene, *On the validity of 3D polymer gel dosimetry: I. reproducibility study*. Physics in Medicine and Biology, 2013. **58**(1): p. 19-42.

-
123. Vandecasteele, J. and Y. De Deene, *On the validity of 3D polymer gel dosimetry: II. Physico-chemical effects*. Physics in Medicine and Biology, 2013. **58**(1): p. 43-61.
124. Vandecasteele, J. and Y. De Deene, *On the validity of 3D polymer gel dosimetry: III. MRI-related error sources*. Physics in Medicine and Biology, 2013. **58**(1): p. 63-85.
125. Oldham, M., *3D dosimetry by optical-CT scanning*. Journal of Physics: Conference Series, 2006. **56**: p. 58-71.
126. Hilts, M., et al., *Polymer gel dosimetry using x-ray computed tomography: a feasibility study*. Physics in Medicine and Biology, 2000. **45**(9): p. 2559-2571.
127. Baldock, C., et al., *Dose resolution in radiotherapy polymer gel dosimetry: effect of echo spacing in MRI pulse sequence*. Physics in Medicine and Biology, 2001. **46**(2): p. 449-460.
128. De Deene, Y. and C. Baldock, *Optimization of multiple spin-echo sequences for 3D polymer gel dosimetry*. Physics in Medicine and Biology, 2002. **47**(17): p. 3117-3141.
129. Mather, M.L., A.K. Whittaker, and C. Baldock, *Ultrasound evaluation of polymer gel dosimeters*. Physics in Medicine and Biology, 2002. **47**(9): p. 1449-1458.
130. Venning, A.J., et al., *Investigation of the PAGAT polymer gel dosimeter using magnetic resonance imaging*. Physics in Medicine and Biology, 2005. **50**(16): p. 3875-3888.
131. Elter, A., et al., *PAGAT gel dosimetry for everyone: gel production, measurement and evaluation*. Biomedical Physics & Engineering Express, 2021. **7**(057001).
132. Klüter, S., et al., *A practical implementation of risk management for the clinical introduction of online adaptive Magnetic Resonance-guided radiotherapy*. Physics and Imaging in Radiation Oncology, 2021. **17**: p. 53-57.
133. Menten, M.J., et al., *Automatic reconstruction of the delivered dose of the day using MR-linac treatment log files and online MR imaging*. Radiotherapy and Oncology : Journal of the European Society for Therapeutic Radiology and Oncology, 2020. **145**: p. 88-94.
134. Torres-Xirau, I., et al., *3D dosimetric verification of unity MR-linac treatments by portal dosimetry*. Radiotherapy and Oncology, 2020. **146**: p. 161-166.
135. Low, D.A., et al., *A technique for the quantitative evaluation of dose distributions*. Medical Physics, 1998. **25**(5): p. 656-661.
136. Pappas, E., et al., *Dosimetric performance of the Elekta Unity MR-linac system: 2D and 3D dosimetry in anthropomorphic inhomogeneous geometry*. Physics in Medicine and Biology, 2019. **64**(225009).
137. Hoffmans, D., et al., *An end-to-end test for MR-guided online adaptive radiotherapy*. Physics in Medicine and Biology, 2020. **65**(125012).
138. Stark, L.S., et al., *Dosimetric and geometric end-to-end accuracy of a magnetic resonance guided linear accelerator*. Physics and Imaging in Radiation Oncology, 2020. **16**: p. 109-112.
139. Baldock, C., C.P. Karger, and H. Zaidi, *Gel dosimetry provides the optimal end-to-end quality assurance dosimetry for MR-linacs*. Medical Physics, 2020. **47**(8): p. 3259-3262.
140. De Deene, Y., et al., *The fundamental radiation properties of normoxic polymer gel dosimeters: a comparison between a methacrylic acid based gel and acrylamide based gels*. Physics in Medicine and Biology, 2006. **51**(3): p. 653-673.
141. Elter, A., et al., *Compatibility of 3D printing materials and printing techniques with PAGAT gel dosimetry*. Physics in Medicine and Biology, 2019. **64**(04NT02).

142. Mann, P., et al., *3D dosimetric validation of motion compensation concepts in radiotherapy using an anthropomorphic dynamic lung phantom*. Physics in Medicine and Biology, 2017. **62**(2): p. 573-595.
143. Mann, P., et al., *Feasibility of markerless fluoroscopic real-time tumor detection for adaptive radiotherapy: development and end-to-end testing*. Physics in Medicine and Biology, 2020. **65**(115002).
144. Mann, P., *Development and implementation of 3D-dosimetric end-to-end tests in adaptive radiation therapy of moving tumors*, in *Combined Faculties for the Natural Sciences and for Mathematics*. 2017, Ruperto-Carola University Heidelberg: Heidelberg, Germany.
145. Schwahofer, A., et al., *On the feasibility of absolute 3D dosimetry using LiF thermoluminescence detectors and polymer gels on a 0.35T MR-LINAC*. Physics in Medicine and Biology, 2020. **65**(215002).
146. Mann, P., A. Schwahofer, and C.P. Karger, *Absolute dosimetry with polymer gels—a TLD reference system*. Physics in Medicine and Biology, 2019. **64**(45010).
147. Elter, A., *Development and application of a deformable phantom to validate adaptive treatment procedures in MR-guided radiotherapy*, in *Department of Physics and Astronomy*. 2018, Heidelberg University: Heidelberg, Germany.
148. Niebuhr, N.I., et al., *Technical Note: Radiological properties of tissue surrogates used in a multimodality deformable pelvic phantom for MR-guided radiotherapy*. Medical Physics, 2016. **43**(2): p. 908-916.
149. Niebuhr, N.I., et al., *The ADAM-pelvis phantom—an anthropomorphic, deformable and multimodal phantom for MRgRT*. Physics in Medicine and Biology, 2019. **64**(04NT05).
150. Gillmann, C., et al., *Technical Note: ADAM PETer – An anthropomorphic, deformable and multimodality pelvis phantom with positron emission tomography extension for radiotherapy*. Medical Physics, 2021. **48**(4): p. 1624-1632.
151. De Deene, Y. and A. Jirasek, *Uncertainty in 3D gel dosimetry*. Journal of Physics: Conference Series, 2015. **573**(012008).
152. Dorsch, S., et al., *Feasibility of polymer gel-based measurements of radiation isocenter accuracy in magnetic fields*. Physics in Medicine & Biology, 2018. **63**(11): p. 11NT02-11NT02.
153. Steinmann, A., et al., *Developing and characterizing MR/CT-visible materials used in QA phantoms for MRgRT systems*. Medical Physics, 2018. **45**(2): p. 773-782.
154. Singhrao, K., et al., *A generalized system of tissue-mimicking materials for computed tomography and magnetic resonance imaging*. Physics in Medicine and Biology, 2020. **65**(13NT01).
155. de Bazelaire, C.M.J., et al., *MR imaging relaxation times of abdominal and pelvic tissues measured in vivo at 3.0 T: preliminary results*. Radiology, 2004. **230**(3): p. 652-659.
156. Bottomley, P.A., et al., *A review of normal tissue hydrogen NMR relaxation times and relaxation mechanisms from 1-100 MHz: dependence on tissue type, NMR frequency, temperature, species, excision, and age*. Medical physics, 1984. **11**(4): p. 425-448.
157. Karlsson, A., et al., *Dose integration characteristics in normoxic polymer gel dosimetry investigated using sequential beam irradiation*. Physics in Medicine and Biology, 2007. **52**(15): p. 4697-4706.

ACKNOWLEDGEMENTS

At this point I would like to express my sincere thanks to all the people who have contributed in many different ways to the success of this thesis. While I will name only a small selection here, I am truly grateful to each and every one of you.

I especially thank Prof. Dr. Joao Seco and Prof. Dr. Christian P. Karger for kindly accepting to act as referees for my dissertation, being my first and second supervisor with the faculty as well as guiding me through the project as part of my ‘Thesis Advisory Committee’.

In addition, I am deeply thankful to Prof. Dr. Christian P. Karger for all the valuable discussions and the exceptional support during the project.

Dr. Philipp Mann and Dr. Stefan Dorsch – *tada*, it’s done. Thank you!

Many thanks to Dr. Sebastian Klüter for being the completing part of my ‘Thesis Advisory Committee’ and helping me out with all clinic-related questions, together with the rest of the medical physics team at UKHD.

I kindly thank Wibke Johnen and Armin Runz for your support concerning technical constructions and 3D printing, as well as Wibke Johnen, Carolin Rippke and Emily Hellwich for your patient help with long measurement sessions or the support in the lab.

Thanks as well to Dr. Stephan Brons and Benjamin Ackermann for the support concerning measurements at HIT.

I am furthermore very grateful for the warm and fun working atmosphere during my time at DKFZ, which was supported by everyone in my office, the E40-2 group as well as the E-040 department.

And finally, a very special thanks to my family, my friends and Robert for a final proof reading of the thesis – and especially for all the support and love through each phase of my life.